



**POLITECNICO DI MILANO**

Faculty of Engineering

Department of Chemistry, Materials  
and Chemical Engineering “G. Natta”

Doctoral Program in Materials Engineering

---

**Carbon Nanostructures for Electrochemical Energy  
Conversion and Storage Applications**

Doctoral Dissertation of:  
**Mazdak Hashempour Igderi**

Supervisor:  
Prof. **Antonello Vincenzo**

Tutor:  
Prof. **Massimiliano Bestetti**

The Chair of the Doctoral Program:  
Prof. **Chiara Castiglioni**

March 2015 – Cycle XXVII



# **Carbon Nanostructures for Electrochemical Energy Conversion and Storage Applications**

By

**Mazdak Hashempour Igderi**

A dissertation submitted in partial fulfillment  
of the requirements for the degree of

Doctor of Philosophy  
in Materials Engineering

at

**Politecnico di Milano**

2015



## **Abstract**

In the current dissertation, under the general framework of “Carbon nanostructures for electrochemical energy conversion and storage applications”, a range of activities with main focus on synthesis and electrochemical characterization of carbon nanostructured materials have been carried out. Accordingly, the thesis has been divided into three chapters and a summary of each activity will be presented in the following as the objective and results of a chapter.

(i) Chemical vapor deposition (CVD) direct growth of carbon nanotubes (CNTs) on stainless steel (SS) and their application for the bipolar plates of proton exchange membrane fuel cells (PEMFCs): in this part, a systematic study of the parameters affecting the direct growth of CNTs on SS is presented and the suitability of the resulting material for working in electrochemical environments is investigated. CNTs were successfully grown on SS via a simple CVD method and without application of any external catalyst after fine tuning all the surface characteristics of SS as well as the growth parameters. It was found out that during the controlled atmosphere heating of SS up to CNT growth temperature, its surface undergoes nano-scale modifications and the type of the subsequently grown filamentous carbon shows a direct relation to the size of surface nano-features formed as a result of certain pretreatments on SS such as polishing, etching, heating condition and atmosphere. CNTs were the dominant growth products where the average size of SS surface nano-features was below 60 nm. Due to the surface modifications of the SS during the high temperature CVD treatment in carbonaceous atmosphere, a reduced corrosion resistance of the SS was found to occur. In particular, chromium depletion of SS due to chromium carbide formation and an accelerated sensitization caused an infirm behavior of the material in electrochemical

media, appearing in the form of intergranular corrosion. Accordingly, although problems such as electrical contact resistance of bare SS in corrosive environment (that is feeble mainly due to passive oxide layer) were addressed, the CNT coating provided by this method was evaluated insufficient as for a corrosion barrier in the electrochemical media such as bipolar plates of PEMFCs.

(ii) Investigation on different carbon nanostructures as the catalyst support of the PEMFCs: in this part, fabrication of Pt electrocatalyst supported on different carbon materials, namely, CNT, reduced graphene oxide (RGO) and hybrid CNT–RGO is demonstrated using a rapid and single step microwave–assisted polyol process (MWAPP), and the activity of Pt towards the oxygen reduction reaction (ORR) is studied on different supports. Due to direct relation of the abundance of defects on the support and Pt concentration and dispersion, inherently inert CNTs showed the lowest and RGO with large number of defects showed the highest concentration of the deposited catalyst. Accordingly, a Pt nanoparticle (NP) size trend as follows was found on different supports: RGO–Pt < CNT–RGO–Pt < CNT–Pt. XPS studies, demonstrated the highest content of oxygen on RGO–Pt and the lowest on CNT–Pt while the composite support had an intermediate oxygen content, resulting in a C/O ratio trend of the supports in the following order: RGO–Pt (7.26) < CNT–RGO–Pt (17.49) < CNT–Pt (21.32). These observations supported the assumption of the higher conductivity of CNT support than the RGO. Moreover, the high resolution XPS results, demonstrated the highest content of  $sp^2$  component of C 1s spectra on CNT compared to others, whereas all the oxygen functional groups were more abundant on RGO. In particular, the biggest jump in the content of a certain functional group from CNT to RGO was realized for HO–C=O (carboxyl) groups. The chemical state of the catalyst was also found to be affected by the support type and in particular, by its initial oxygen content, so as the highest and lowest metallic Pt ( $Pt^0$ ) contents were observed on CNT–Pt and RGO–Pt, respectively. In almost all these XPS studies, CNT–RGO–Pt showed concentrations between CNT–Pt and RGO–Pt. Area specific activity evaluation of the samples towards ORR showed a clear outperformance of all the lab-made samples compared to the commercial Vulcan XC72–30%Pt over the entire kinetic region. In

particular, the specific activities of RGO–Pt, CNT–RGO–Pt and CNT–Pt samples at  $E = 0.90 V_{\text{RHE}}$ , were 2.25, 2.3 and 3.13 times higher than the commercial sample, respectively. Regarding the mass specific activity, the effect of electrical conductivity found to become more important and RGO–Pt showed the poorest behavior. However, CNT–Pt and CNT–RGO–Pt showed 58% and 80% improvements compared to the commercial sample at  $E = 0.90 V_{\text{RHE}}$ . CNT–RGO–Pt support showed particularly high mass activity due to simultaneous benefitting from the conductivity of CNTs working as nano–interconnects between RGO sheets, and wettability and surface area factors of RGO. It was finally concluded that hybridizing the 1D and 2D support families (CNT–RGO), shared the features of individual components of the hybrid, so as to result at the same time in high area and mass specific activities outrunning the performance of commercial catalysts.

(iii) Investigation on different carbon nanostructures as the active materials for the supercapacitors: this part is mainly concentrating on the electrochemical behavior of CNT and RGO as the active materials for the electrochemical double layer capacitors (EDLCs) or supercapacitors, compared to activated carbon (A.C.) as the commercially available material for this application. Furthermore, different combinations of these three carbon species were investigated to have a clearer understanding of the potentials and risks of hybridization strategy for preparation of the supercapacitor carbon based active materials. Along with thorough microstructural characterizations, electrical conductivity measurements were also carried out on all materials using a lab-made facility, demonstrating orders of magnitude higher conductivities of CNTs ( $332 \text{ S m}^{-1}$ ) and RGO ( $1 \text{ S m}^{-1}$ ) compared to A.C. ( $10 \mu\text{S m}^{-1}$ ). Supercapacitor electrodes were prepared via the so-called “paste method” from the desired compositions of active materials in three main classes including A.C.–CNT, A.C.–RGO and A.C.–CNT–RGO. Electrochemical characterization of the electrodes was carried out using cyclic voltammetry (CV), cyclic charge–discharge (CD) and electrochemical impedance spectroscopy (EIS) techniques in a  $1 \text{ M Na}_2\text{SO}_4$  solution and parameters related to EDLC performance such as specific capacitance ( $C_s$ ), internal resistance ( $R_i$ ), energy density ( $E_s$ ), power density ( $P_s$ ), relaxation time ( $\tau_0$ ), ideality of the

performance and lifetime were evaluated. Specific capacitance and energy density studies showed that a big contribution in the deficiency of pure A.C. electrodes was originating from the lack of electrical conductivity. Addition of more conductive species (i.e., both CNT and RGO) could address this problem. In A.C.–CNT class a maximum was observed in the  $C_s$  and  $E_s$  in the intermediate compositions (CNT contents) below which the composite suffered from low conductivity and above which, the lower specific surface area CNTs was limiting the capacitance. In A.C.–RGO class however, a continuous increase of both specific capacitance and energy was observed by RGO content due to simultaneous improvement of conductivity and almost similar surface area. A.C.–CNT–RGO class showed the lowest dependence on the composition of the added constituents since a good conductivity (supplied by the constant 25% CNT content) and an acceptable surface area (provided by different contents RGO and A.C.) guaranteed and almost always high capacitance. Studies on the rate capability, power performance, frequency response and internal resistance of the electrodes showed a superior behavior of pure CNT electrodes (a  $\tau_0=0.19$  s,  $R_i=0.83$   $\Omega$  and a  $P_{s,max}=22$   $\text{kWkg}^{-1}$  at matched impedance condition) or those containing a high content of CNTs. RGO (with a  $\tau_0=6.31$  s,  $R_i=6.38$   $\Omega$  and a  $P_{s,max}=5.6$   $\text{kWkg}^{-1}$  at matched impedance condition for pure RGO) was behaving better than A.C. (a  $\tau_0>100$  s and a  $P_{s,max}=4.1$   $\text{kWkg}^{-1}$  at matched impedance condition) in this respect, but still more sensitive to rate compared to CNTs. Composite three component electrodes of A.C.–CNT–RGO class benefited from low ionic diffusivity resistance of mesopores of CNTs along with high surface area of RGO, presenting high rate capability and energy density at the same time ( $\tau_0\approx 1$  s,  $R_i\approx 1.4$   $\Omega$  and a  $P_{s,max}\approx 10$   $\text{kWkg}^{-1}$  steadily all over the range composition). Moreover, the A.C.–CNT–RGO class also showed the highest degree of ideality in performance with ideality factors (IF)  $>0.9$  over the entire CD current range (quite close to unity as the ideal capacitor). Finally, durability studies showed one of the few infirmities of the composite electrodes compared to pure ones. The negative effect of hybridization on durability was considered to be originating from the integrity loss of the active film, including mechanical and electrical interconnections of the constituents, generating heterogeneity in electronic and ionic properties of the entire electrode. In this respect, the

larger the morphological dissimilarities of the initial constituents, the higher the susceptibility to durability shortcomings. From another point of view, however, this can be looked at as a technical problem in the electrode preparation process that can be improved by optimization of the paste treatment and binder materials as well as possibly some stabilization post treatments.

# Contents

<b>Abstract</b> .....	<b>i</b>
<b>List of Figures</b> .....	<b>x</b>
<b>List of Tables</b> .....	<b>xvi</b>
<b>1 Direct growth of carbon nanotubes on stainless steel</b> .....	<b>1</b>
1.1 Introduction.....	1
1.1.1 Objective.....	4
1.2 Experimental .....	5
1.2.1 Materials and preparation.....	5
1.2.2 CNT/CNF Synthesis .....	6
1.2.3 Microstructural characterization .....	8
1.2.4 Electrochemical characterization and corrosion measurements .....	9
1.3 Results and discussion .....	9
1.3.1 Synthesis of CNTs/CNFs.....	9
1.3.1.1 Effect of surface morphology .....	9
1.3.1.2 Effect of surface etching .....	20
1.3.1.3 Effect of growth time.....	28
1.3.1.4 Effect of surface oxidation-reduction.....	28
1.3.2 Corrosion evaluation .....	32
1.3.2.1 Microstructural characterization before corrosion.....	32
1.3.2.2 Electrochemical characterization .....	35
1.3.2.2.1 Potentiodynamic tests .....	35
1.3.2.2.2 Potentiostatic tests .....	36
1.3.2.3 Microstructural characterization after corrosion tests.....	38
1.4 Conclusion .....	48
<b>2 Carbon nanostructures as catalyst support of fuel cells</b> .....	<b>52</b>

2.1	Introduction .....	52
2.1.1	<i>Fuel cells and materials challenges</i> .....	52
2.1.2	<i>Support materials</i> .....	53
2.1.2.1	Carbonaceous supports .....	54
2.1.2.1.1	Carbon blacks and graphite materials .....	54
2.1.2.1.2	Activated carbon .....	57
2.1.2.1.3	Mesoporous carbons .....	59
2.1.2.1.4	Carbon fibers and nanofibers .....	62
2.1.2.1.5	Carbon nanotubes .....	64
2.1.2.1.6	Carbon nanohorns, nano onions and nanocoils.....	67
2.1.2.1.7	Nanodiamonds and doped diamonds.....	69
2.1.2.1.8	Graphene and reduced graphene oxide.....	71
2.1.2.2	Composite carbonaceous supports.....	76
2.1.2.3	Non-carbonaceous supports.....	76
2.1.3	<i>Interactions between carbon support and catalyst</i> .....	77
2.1.4	<i>Objective</i> .....	82
2.2	Experimental .....	84
2.2.1	<i>Carbon supports preparation</i> .....	84
2.2.1.1	CNTs synthesis.....	84
2.2.1.2	CNTs purification .....	86
2.2.1.3	GO synthesis .....	86
2.2.2	<i>Catalyst synthesis</i> .....	87
2.2.3	<i>Microstructural characterization</i> .....	88
2.2.4	<i>Electrode preparation</i> .....	89
2.2.5	<i>Electrochemical characterization</i> .....	90
2.3	Results and discussion .....	91
2.3.1	<i>Supports preparation</i> .....	91
2.3.2	<i>Catalyst synthesis on supports</i> .....	94
2.3.2.1	TEM studies .....	95
2.3.2.2	TGA studies .....	98
2.3.2.3	XRD studies.....	101

2.3.2.4	XPS studies .....	103
2.3.2.4.1	Survey scans .....	103
2.3.2.4.2	Narrow scans .....	107
2.3.2.4.2.1	Carbon narrow scans .....	108
2.3.2.4.2.2	Platinum narrow scans .....	112
2.3.3	Electrochemical characterization .....	116
2.3.3.1	Electrochemical surface area (ECSA).....	116
2.3.3.2	Oxygen reduction reaction (ORR) .....	121
2.3.3.2.1	Electrocatalytic activity .....	125
2.4	Conclusion .....	131
<b>3</b>	<b>Carbon nanostructures as active materials of supercapacitors .....</b>	<b>135</b>
3.1	Introduction .....	135
3.1.1	Carbon-based electrode materials.....	137
3.1.1.1	Activated carbons (A.C.s).....	137
3.1.1.2	CNTs .....	140
3.1.1.3	Graphene and reduced graphene oxide .....	141
3.1.1.4	Templated ordered mesoporous carbons .....	144
3.1.1.5	Other carbons.....	146
3.1.2	Objective.....	146
3.2	Experimental .....	148
3.2.1	Carbon supports preparation .....	148
3.2.1.1	CNTs synthesis and purification .....	148
3.2.1.2	GO synthesis .....	148
3.2.1.3	GO reduction .....	150
3.2.2	Microstructural characterization .....	150
3.2.3	Electrode preparation .....	151
3.2.4	Electrodes classification .....	154
3.2.5	Electrochemical characterization .....	155
3.2.6	Conductivity measurement .....	158
3.3	Results and discussion .....	160

3.3.1	<i>Microstructural characterization of the active materials</i> .....	160
3.3.1.1	TEM studies .....	160
3.3.1.2	XRD studies.....	162
3.3.1.3	TGA studies.....	163
3.3.1.4	SEM studies of the pastes.....	164
3.3.2	<i>Electrical characterization</i> .....	173
3.3.2.1	Conductivity measurement.....	173
3.3.3	<i>Electrochemical characterization</i> .....	176
3.3.3.1	Specific capacitance and energy density.....	176
3.3.3.1.1	A.C. – CNT electrodes.....	180
3.3.3.1.2	A.C. – RGO electrodes.....	182
3.3.3.1.3	A.C. – CNT – RGO electrodes.....	183
3.3.3.2	Rate capability.....	185
3.3.3.3	Ideality of the performance.....	190
3.3.3.4	Durability.....	194
3.3.3.5	Frequency response and relaxation time based on EIS.....	196
3.3.3.5.1	A.C. – CNT electrodes.....	200
3.3.3.5.2	A.C. – RGO electrodes.....	201
3.3.3.5.3	A.C. – CNT – RGO electrodes.....	202
3.3.3.6	Power performance.....	203
3.3.3.6.1	Power density.....	203
3.3.3.6.2	Internal resistance and matched impedance power ( $P_{max}$ ).....	206
3.3.3.7	Ragone plots.....	210
3.4	Conclusion.....	212
<b>References</b> .....		<b>217</b>
<b>Appendix A</b> .....		<b>243</b>
Catalyst amount calculation and ink composition.....		243
Vulcan 30wt% Pt.....		243
CNT-Pt.....		244
RGO-Pt.....		245
CNT-RGO-Pt.....		246

## List of Figures

Fig. 1.1 SEM surface micrographs of (a) sample A1 and (b) sample P1 before CNT growth. ....	10
Fig. 1.2 Low (50x50 $\mu\text{m}$ scan, left column) and high (1x1 $\mu\text{m}$ scan, right column) resolution AFM images of the samples of groups A and P before and after the reducing atmosphere heating; (a, b) group A samples before reducing atmosphere heating, (c, d) group P samples before reducing atmosphere heating, (e, f) group A samples after reducing atmosphere heating, (g, h) group P samples after reducing atmosphere heating. ....	12
Fig. 1.3 Nano-hills diameter distribution for as-received and polished samples before (A and P) and after (A Red and P Red) reducing atmosphere heating. ....	12
Fig. 1.4 SEM micrographs of the samples (a) A1, (b) higher magnification of A1, (c) P1, (d) and (e) higher magnifications of P1. ....	14
Fig. 1.5 SEM micrographs of the samples (a) A2, (b) higher magnification of A2, (c) P2, (d) higher magnifications of P2. ....	16
Fig. 1.6 XRD patterns of bare stainless steel, CNT on stainless steel (A1) and CNF on stainless steel (OR). ....	16
Fig. 1.7 TEM micrographs of carbon nanostructures in group A. ....	18
Fig. 1.8 AFM images of as-received and polished samples after different etching durations. AE (a, b) and PE (e, f) samples are etched in HCl for 5 min and AES (c, d) and PES (g, h) are etched in the same solution for 10 min (left column images are 50x50 $\mu\text{m}$ low resolution scans and right column images are 1x1 $\mu\text{m}$ high resolution scans). ....	22
Fig. 1.9 Nano-hills diameter distribution for A, AE, AES, P, PE, and PES samples. ....	22
Fig. 1.10 SEM micrographs of samples AE1 (a, b), AE2 (c, d) and AES2 (e, f) in different magnifications. ....	23
Fig. 1.11 SEM micrographs of the samples PE1 (a, b), PE2 (c, d) and PES2 (e, f) in different magnifications. ....	25
Fig. 1.12 Low (50x50 $\mu\text{m}$ scan, left column) and high (1x1 $\mu\text{m}$ scan, right column) resolution AFM images of the samples of groups AE and AES after the reducing atmosphere heating; (a, b) group AE samples after reducing atmosphere heating, (c, d) group AES samples after reducing atmosphere heating. ....	26

Fig. 1.13 Nano-hills diameter distribution for A, AE, AES samples after reducing atmosphere heating..	26
Fig. 1.14 Low (50x50 $\mu\text{m}$ scan, left column) and high (1x1 $\mu\text{m}$ scan, right column) resolution AFM images of the samples of groups OR; (a, b) after oxidation treatment step and (c, d) after reduction step followed by the primary oxidation. ....	29
Fig. 1.15 Nano-hills diameter distribution for OR samples. ....	29
Fig. 1.16 SEM micrographs of sample OR in different magnifications. ....	31
Fig. 1.17 SEM micrographs of as-grown samples showing (a) CNTs and (b) CNFs. ....	32
Fig. 1.18 XRD patterns of as-received and as-grown samples. ....	33
Fig. 1.19 SEM micrographs of 316 SS substrates stripped from (a, b) CNT and (c, d) CNF. ....	34
Fig. 1.20 Potentiodynamic curves of 316 SS, 316 SS+CNT, 316 SS+CNF and SS-NH samples in 1 M $\text{H}_2\text{SO}_4$ + 2 ppm HF solution at 80°C. ....	36
Fig. 1.21 Potentiostatic curves of 316 SS, 316 SS+CNT and 316 SS+CNF samples in 1 M $\text{H}_2\text{SO}_4$ + 2 ppm HF solution at 80°C, (a) saturated with $\text{H}_2$ , at -0.1 V vs. SCE, and (b) saturated with $\text{O}_2$ , at 0.6 V vs. SCE. ....	37
Fig. 1.22 XRD patterns of corroded samples. ....	39
Fig. 1.23 (a) SEM micrograph of 316 SS after 10000 s potentiostatic test under anodic environment conditions, (b) higher magnification of (a). ....	40
Fig. 1.24 SEM micrographs of "CNT on 316 SS" sample after 10000 s potentiostatic corrosion test under the anodic environment conditions showing three different zones and different magnifications of each zone. ....	41
Fig. 1.25 SEM micrographs of "CNF on 316 SS" sample after 10000 s potentiostatic corrosion test under the anodic environment conditions showing four different zones and different magnifications of each zone. ....	43
Fig. 1.26 SEM micrographs of 316 SS+CNT stripped sample after 10000 s of potentiostatic corrosion test under the anodic environment conditions. (a) Secondary electron mode, (b) back scattered mode, (c) point analysis locations and (d) EDS results at three different zones, compared to pristine 316 SS. ....	45
Fig. 1.27 SEM micrographs of cross sectioned stripped 316 SS+CNT samples (a) etched with Nital 2% before corrosion test and (b) without etching after 10000 s of potentiostatic corrosion test under the anodic environment conditions. ....	46
Fig. 1.28 (a) SEM micrograph of an etched (Nital 2%) cross section of a stripped CNT sample before corrosion test and (b) EDS line scan results from point A to point B. ....	47

Fig. 2.1 Primary particle of carbon black. (Grivei, E., TIMCAL Belgium) .....	55
Fig. 2.2 Microstructure of activated carbon (Norit®).....	58
Fig. 2.3 Microstructure of ordered mesoporous carbon [187].....	60
Fig. 2.4 The ideal pore size of OMC for easy access of the reactants to the catalyst [196].....	61
Fig. 2.5 (a) HRTEM images of CNOs produced by the arc discharge in water [293], (b) The icosahedral-quasicrystal-like model of an onion carbon particle constructed with the classical molecular dynamics technique [294].....	67
Fig. 2.6 (a) A magnified TEM micrograph of CNOs with inset representing a simulated single CNH and (b) lower magnification of the same, showing an aggregate of CNHs making a “Duhlia”. Inset schematically showing the same [295].....	68
Fig. 2.7 TEM micrograph of a CNC with inset on right showing the multi-walled structure of the coil (from [310]) and the inset on left, showing a simulated model of the coil [298].....	69
Fig. 2.8 (a) The conversion of a “carbon onion” (multi-walled concentric fullerene-like balls) into a diamond using particle beams. A growing diamond is seen inside concentric graphitic layers [314], (b) a nanodiamond crystal. ....	70
Fig. 2.9 Classification grid for the categorization of different graphene types according to three fundamental properties: number of graphene layers, average lateral dimension, and atomic carbon/oxygen ratio [335].....	73
Fig. 2.10 Illustration of the amphoteric character of carbon materials [419].....	79
Fig. 2.11 (a) high magnification and (b) high resolution TEM images of CNTs synthesized by CVD method after purification.....	92
Fig. 2.12 TGA of as synthesized and purified CNTs.....	93
Fig. 2.13 TEM micrograph of a few layered GO sheet.....	93
Fig. 2.14 schematic representation of Pt synthesis on different supports using MWAPP.....	94
Fig. 2.15 TEM micrographs of the CNT supported Pt catalysts (a) high magnification TEM of the the distribution of Pt NPs on the CNTs, (b) HRTEM of Pt and CNT, (c and d) FFTs of CNT and Pt, respectively.....	95
Fig. 2.16 Morphology and corresponding particle size distribution of (a and b) CNT-Pt, (c and d) RGO-Pt and (e and f) CNT-RGO-Pt systems.....	97

Fig. 2.17 TGA studies on (a) CNT–Pt, (b) RGO–Pt, (c) CNT–RGO–Pt and (d) overlay of the three systems. ....	99
Fig. 2.18 XRD patterns of CNT and GO as the starting support materials before Pt synthesis. ....	102
Fig. 2.19 XRD patterns of the three support-catalyst systems. ....	102
Fig. 2.20 XPS surveys of the three support-catalyst systems. ....	105
Fig. 2.21 (a) Mass concentration of the elements present in different supports based on quantification results (averaged) of the XPS survey and (b) C/O ratio calculated from the same. ....	106
Fig. 2.22 High-resolution deconvoluted XPS spectra of C 1s for (a) CNT–Pt, (b) RGO–Pt (c) CNT–RGO–Pt and (d) comparison plot of chemical states of Pt in different supports. ....	110
Fig. 2.23 High-resolution deconvoluted XPS spectra of Pt 4f for (a) CNT–Pt, (b) RGO–Pt (c) CNT–RGO–Pt and (d) comparison plot of chemical states of Pt in different supports. ....	113
Fig. 2.24 Cyclic voltammograms of different support-catalyst systems for ECSA determination carried out at 20 mVs <sup>-1</sup> in de-aerated 0.1 M HClO <sub>4</sub> . ....	118
Fig. 2.25 Bar charts of (a) Pt loading and (b) ECSA of different support-catalyst systems. ....	118
Fig. 2.26 loading of different oxidation states of Pt, (Pt <sup>0</sup> , Pt <sup>2+</sup> and Pt <sup>4+</sup> ), on the electrodes tested for ECSA and ORR determination. ....	120
Fig. 2.27 A typical anodic sweep of the ORR polarization curve carried out at different rotation rates. Measurement of the diffusion and kinetic controlled currents is shown schematically at E = 0.40 V <sub>RHE</sub> and E = 0.90 V <sub>RHE</sub> , respectively. ....	121
Fig. 2.28 ORR polarization curves recorded during the anodic sweep (0.05V to 1.1 V <sub>RHE</sub> ) at 20 mV s <sup>-1</sup> . Electrode rotation rate. ....	123
Fig. 2.29 activity plots of different support-catalyst systems (a and b) Tafel plots of mass and area specific activities, respectively, and (c and d) the values of mass and area specific activities at E = 0.9 V <sub>RHE</sub> . ....	127
Fig. 3.1 Specific power against specific energy, also called a Ragone plot, for various electrical energy storage devices. If a supercapacitor is used in an electric vehicle, the specific power shows how fast one can go, and the specific energy shows how far one can go on a single charge. Times shown are the time constants of the devices, obtained by dividing the energy density by the power [468]. ....	136
Fig. 3.2 Illustration of the preparation steps of supercapacitor electrodes. ....	153
Fig. 3.3 Schematic presentation of the cell used for electrochemical measurements. ....	156

Fig. 3.4 Diagram of the protocol adopted for comprehensive electrochemical characterization of the electrodes.....	157
Fig. 3.5 Schematic of the conductivity measurement cell.....	159
Fig. 3.6 HMTEM and HRTEM micrographs of (a and b) CNT, (c and d) RGO and (e and f) A.C. ....	161
Fig. 3.7 XRD patterns of purified CNTs, GO, and RGO prepared via thermal reduction under $N_2+H_2$ (RGO(NH)) or $N_2+H_2+C_2H_4$ (RGO(NHC)) atmosphere.....	162
Fig. 3.8 TGA results of the purified CNTs and RGO. ....	163
Fig. 3.9 SEM micrographs of pure A.C. electrode paste in two magnifications. ....	164
Fig. 3.10 SEM micrographs of A.C.–5%CNT electrode paste in different magnifications.....	165
Fig. 3.11 SEM micrographs of A.C.–25%CNT electrode paste in different magnifications. ....	167
Fig. 3.12 SEM micrographs of pure CNT electrode paste in different magnifications. ....	167
Fig. 3.13 SEM micrographs of A.C.–5% RGO electrode paste in different magnifications. ....	168
Fig. 3.14 SEM micrographs of A.C.–25% RGO electrode paste in different magnifications. ....	169
Fig. 3.15 SEM micrographs of pure RGO electrode paste in different magnifications.....	170
Fig. 3.16 SEM micrographs of A.C.–25%CNT–25%RGO electrode paste in different magnifications.....	171
Fig. 3.17 SEM micrographs of RGO–25%CNT electrode paste in different magnifications.....	172
Fig. 3.18 Results of the dried paste thickness measurement via SEM as a function of the paste composition. ....	173
Fig. 3.19 Conductivity measurements of the raw initial materials. ....	174
Fig. 3.20 Conductivity measurements of the paste electrodes of supercapacitors. ....	176
Fig. 3.21 Specific capacitance of a typical electrode calculated via CV at different scan rates and CD at different currents. ....	177
Fig. 3.22 Demonstration of the methodology used for specific capacitance and energy calculation based on the CD technique.....	178
Fig. 3.23 Specific capacitance (a, c, and d) and specific energy (b) of A.C.–CNT electrodes.....	180

Fig. 3.24 Specific capacitance (a, c, and d) and specific energy (b) of A.C.–RGO electrodes.....	183
Fig. 3.25 Specific capacitance (a, c, and d) and specific energy (b) of A.C.–CNT–RGO electrodes. ....	185
Fig. 3.26 CVs of (a) pure A.C., (b) pure CNT, (c) pure RGO, (d) A.C.–50%CNT and (e) A.C.–50%RGO electrodes normalized by scan rate and electrode mass for rate capability studies.....	187
Fig. 3.27 CVs of (a) A.C.–25%CNT–5%RGO, (b) A.C.–25%CNT–15%RGO, (c) A.C.–25%CNT–25%RGO and (d) RGO–25%CNT electrodes normalized by scan rate and electrode mass for rate capability studies. ....	190
Fig. 3.28 Ideality factor ( $IF$ ) of different electrodes as a function of CD current. ....	192
Fig. 3.29 Specific capacitance change over a 10000 CD life cycle testing. ....	195
Fig. 3.30 The EIS results of a typical supercapacitor, (a) Nyquist presentation with inset magnifying the high frequency region, (b) real and imaginary capacitance obtained by elaboration of the raw EIS data, as a function of the frequency. ....	198
Fig. 3.31 EIS results of A.C.–CNT class electrodes presented in the form of (a) real and (b) imaginary capacitances as functions of frequency.....	200
Fig. 3.32 EIS results of A.C.–RGO class electrodes presented in the form of (a) real and (b) imaginary capacitances as functions of frequency.....	201
Fig. 3.33 EIS results of A.C.–CNT–RGO class electrodes presented in the form of (a) real and (b) imaginary capacitances as functions of frequency. ....	202
Fig. 3.34 Relaxation time $\tau_0$ of different classes of electrodes as a function of the composition. ....	203
Fig. 3.35 Power performance of different classes of supercapacitor electrodes as a function of discharge specific current. ....	205
Fig. 3.36 Supercapacitor electrical equivalent circuit adopted from [548]. ....	207
Fig. 3.37 (a) internal resistance of a typical sample calculated at different CD currents, (b) average internal resistance of different electrodes as a function of the composition and (c) the power of matched impedance for different electrodes as a function of the composition. ....	210
Fig. 3.38 Ragone plots of different classes of electrodes as electrochemical energy storage devices. ....	212

## List of Tables

Table 1-1 List of the samples with different preparation steps used in this work. During the growth step of either CNT or CNF, the flow rate of N <sub>2</sub> , H <sub>2</sub> and C <sub>2</sub> H <sub>4</sub> was maintained at 100, 5 and 20 sccm, respectively. During the reduction step after oxidation in air for CNF synthesis, the flow rate of N <sub>2</sub> and H <sub>2</sub> were 100 and 50 sccm.....	7
Table 2-1 Quantification results (averaged) of the XPS survey spectra of different support–catalyst systems.....	106
Table 2-2 Position constraints used for deconvolution of C 1s components. ....	108
Table 2-3 Quantification results (averaged) of high-resolution deconvoluted XPS spectra of C 1s of different support–catalyst systems. ....	110
Table 2-4 Quantification results (averaged) of high-resolution deconvoluted XPS spectra of Pt 4f of different support–catalyst systems. ....	114
Table 2-5 Detailed table showing peak positions and percentage contributions obtained from deconvolution of the high resolution XPS spectra of all the support–catalyst systems studied.....	114
Table 2-6 Comparison of the mass-specific ( $I_m$ ) and area-specific activities ( $I_s$ ) of different support–catalyst systems for the ORR at $E = 0.90$ V versus RHE determined from the anodic sweep (0.05 V to 1.10 V) at $20 \text{ mV s}^{-1}$ . ....	127
Table 2-7 Potential based activity indicators of different samples.....	129
Table 3-1 Compositions of the supercapacitor electrodes prepared and characterized.....	155

# 1 *Direct growth of carbon nanotubes on stainless steel*

## 1.1 Introduction

Carbon nanotubes have arrived in such popularity and have been paid so great attention by researchers in two last decades that trying to enumerate a full and detailed list of their characteristics, synthesis techniques and possible applications is out of might and sight of this work. Consideration of numerous synthesis methods, each with its own features and parameters, makes us to suffice to a review of the literature finely related to the approach corresponding to the scope of our work.

Amongst various carbon nanotube/fiber (CNT/CNF) synthesis methods, chemical vapor deposition (CVD) has been recognized as a versatile and robust method due to several advantages such as capability to produce dense and uniform deposit, reproducibility, good adhesion, adjustable deposition rates, ability to control crystal structure, surface morphology and orientation of the CVD products, reasonable cost and wide scope in selection of chemical precursors [1]. Although new research directions have been established under the topic of “structural nanoparticle catalysts” trying to grow CNTs on unusual substrates such as noble metals [2–6], ceramics [7,8] and semiconducting nanoparticles [9–12], the *3d* transition metals like iron, cobalt and nickel are predominantly used as catalyst for CNT growth [13–15]. Researches in this area can be divided in two main groups: 1) *Indirect* growth of CNTs on a noble substrate decorated with transition metal catalyst particles and 2) *Direct* growth of CNTs on a catalytic substrate. Different substrates such as aluminum [16], copper [17–22], silicon [23–28], ceramics and ceramic templates [29–33], and different

substrate decoration techniques –such as varieties of physical vapor deposition techniques [34–39], electrodeposition [16,17], sol-gel [40,41], co-reduction of precursors [42,43], impregnation [44,45], incubation [46], thermal decomposition of carbonyl complexes [47,48], metal-organic chemical vapor deposition [49–54]– have been investigated in the so-called *indirect* method.

On the other hand, attempts to investigate the direct growth of CNTs on a catalytic substrate are a negligible proportion of the literature. Few attempts on cobalt substrate [55,56], some on nickel [27,55,57–59] and some on stainless steel with iron as the main catalytic element [60–70] form the relevant literature.

Basically, CVD uses a controlled atmosphere containing a carbonaceous species at a suitable temperature to decompose the carbon precursor on a catalytic surface and subsequently, by supersaturating the catalyst particle, make the extra carbon to precipitate in a certain crystalline form, namely, graphite [71]. In this regard, proper preparation of the catalyst layer on the surface of the substrate to be covered by CNTs is a vital step. Accordingly, the availability of substrate materials showing catalytic activity for CNT synthesis translates into an effective facilitation of the synthesis by elimination of a crucial step, namely, catalyst preparation, and therefore, to economic justification as well [72]. Considering potential applications like electrodes for supercapacitors [73–76] and fuel cells [77–81], electrodes for capacitive deionization [82,83] and capacitive mixing for extracting energy from salinity difference of water resources [84–86], field emission probes [23,55,87–89], sensors [90–92], catalyst support for wastewater treatment [66] and low friction applications [93–95], stainless steel can be considered as a potential candidate for direct growth of CNT, due to its high content of iron as the catalyst element. Direct growth of CNT on a catalytic substrate may offer in principle important advantages, in particular a strong bonding to the substrate and consequently lower contact resistance and improved electron/thermal transport properties, then promising improved efficiency in many of the above mentioned applications.

Direct growth of CNTs on stainless steel has been recently studied by using enhanced CVD methods such as direct current plasma enhanced CVD

(DCPECVD) [93], radio frequency plasma enhanced CVD (RFPECVD) [96,97], microwave plasma enhanced CVD (MWPECVD) [55] and plasma enhanced hot filament CVD (PEHFCVD) [95]. These methods benefit from the possibility of relatively low operating temperature and rely on surface treatment by plasma for the formation of nanoparticle like roughness providing catalytic sites. Obviously, PECVD systems are more costly compared to traditional CVD equipment.

Vander Wal et al. tried to grow CNTs directly on 304 stainless steel meshes with different surface pretreatments such as oxidation, oxidation-reduction and laser ablation oxidation [67]. They investigated the effect of different types and flow rates of precursor gases such as acetylene ( $C_2H_2$ ) /benzene mixture and CO/benzene mixture on the CNT formation and showed that CO was less active than the others. They also showed that the oxidation pretreatment followed by adequate reduction is a critical point in the synthesis of uniform CNTs. The effectiveness of oxidation-reduction pretreatment on CNT growth was also confirmed by others [66,68,69]. Chemical etching of the stainless steel substrate was another preparation method used successfully for CNT growth by several researchers [61–64]. Nevertheless, possible pretreatments are not limited to chemical etching and alternatives such as micro-shot-peening [70] and ion bombardment [65] were also tested with good results in terms of CNT growth. Recently, attempts have been made to directly grow CNTs on stainless steel without any special pretreatment by CVD using acetylene as precursor gas [60]. In this respect, the industrial application of the CVD technique is confronted with safety and health issues raised by the use of dangerous carbon sources such as acetylene, xylene and benzene which are the precursors most frequently used in the literature. Using species such as ethylene can significantly decrease the associated risk, though not eliminating it completely. However, the lower relative reactivity of ethylene compared to gases such as acetylene [98,99] is a serious drawback to be overcome by optimizing the growth process parameters.

### 1.1.1 Objective

In this work we intend to directly grow CNTs and CNFs on stainless steel using ethylene as the carbon source via a simple CVD method without use of any extra catalyst layer. It will be shown that pretreatment steps such as ion bombardment, etching, oxidation-reduction, etc. are not necessary to achieve simple growth of entangled CNT layers. Growth mechanism will also be studied and elucidated relying on detailed topographic and statistical investigation of the surface nano-features. As a complementary step, different pretreatment methods reported in the literature are applied and experimentally tested, characterizing the results of each pretreatment in terms of both modification of the surface nanostructure, before the growth step, and the influence of each treatment on the structure of the final products, after growth.

The other side of our motivation behind this work, is directed towards the suitability of the produced material for one of the major field of interest for application of this material, namely electrochemical energy conversion and storage. As briefly reviewed before, many of the potential applications for CNTs are related to the electrochemical performance of the electrode made of CNTs (in our particular, stainless steel/CNT electrode), that in any instance, may imply exposure of the electrode to an electrochemically aggressive environments. Accordingly, the investigation on the corrosion behavior of such materials is a necessary step to confirm their viability for those applications. However, to the best of our knowledge, an in-depth study on the corrosion response of stainless steel/CVD grown CNT has not been performed yet. Thus, in this work we also aim to explore the changes in the substrate caused by the CNT growth which then may affect its corrosion behavior, as expected in view of the well-established vulnerability of stainless steel to corrosion upon high temperature exposure to carbon rich environments [100–103]. More precisely, this work is intended to investigate the corrosion behavior of 316 stainless steel coated with different types of filamentous carbon materials, namely, CNT and CNF, directly grown on the substrate by CVD method. Since these types of conductive carbon do not form a dense and compact layer, the occasion is offered for studying the effects of CNT/CNF growth conditions on the

corrosion behavior of stainless steel. Electrochemical testing for corrosion assessment was conducted under conditions simulating the working environment of bipolar plates (BPs) in polymer electrolyte membrane fuel cells (PEMFCs) [81]. Actually, the highly corrosive environment in which BPs should work, namely high acidity and relatively high temperature, makes this instance stand out as an upper limit in terms of the severity of the corrosion conditions within the aforementioned applications. Hence, any possible weakness of the system which could not possibly appear in milder corrosion conditions was more likely to be revealed herein.

## 1.2 Experimental

### 1.2.1 Materials and preparation

Stainless steel (type 316) sheets cut into the size 15×15×1 mm were used as catalytic substrate. Different pretreatment procedures were used, including: grinding and polishing, etching with hydrochloric acid solution, and oxidation–reduction process.

The preparation of mirror polished samples was performed by sequential grinding with SiC abrasive paper, 600 , 800, 1200 and 2000 grit, followed by a final polishing with alumina powder 0.3 μm.

For those samples planned to be used in the etched state, dipping into concentrated hydrochloric acid (Sigma-Aldrich, puriss. p.a., ≥32%) for different durations of 5 and 10 min was carried out to achieve different etching levels and test their effects on subsequent CNT growth.

Careful cleaning including 10 min sonication in acetone and 10 min sonication in distilled water followed by nitrogen drying was applied to all of the samples (as-received, mirror polished and etched) to remove organic and inorganic contaminants. Then, samples were transferred to the CVD reactor.

### 1.2.2 CNT/CNF Synthesis

The reactor was a horizontal quartz tube (ISO 4793-1980, diameter 20 mm, length 880 mm) heated in a temperature controlled electrical furnace (Carbolite, mod. Endotherm VST 24-16). The tube was coupled to a gas flow control system (flow meter, Brooks Instrument BV, Model 5878). 316 SS substrates were fixed on an alumina stage and then placed into the quartz tube at a location calibrated for temperature control.

As the shielding and carrier gas, nitrogen was used in all tests. Except for the case of oxidation-reduction pretreatment, in all other tests the tube containing the samples was first purged with the carrier gas (continuous flow of 100 sccm) and hydrogen (5 sccm) at room temperature and then heated up to 760 °C. The heating rate was 15 °C/min and the temperature was checked with a thermocouple (Delta Ohm HD2108.1). The temperature profile in the flow direction along the furnace axis was evaluated by point by point measurement, showing a trapezoidal shape. Accordingly, the central zone of the furnace, of about 20 cm length, was isothermal and then selected as the convenient place for sample location. After reaching the desired temperature, a 10 min hold time was allowed to achieve a stabilized temperature. During the whole heating up and holding time, the nitrogen and hydrogen gases flowed constantly (for brevity, this step will be referred to in the following as “reducing atmosphere heating”). After stabilizing the temperature, ethylene (C<sub>2</sub>H<sub>4</sub>) was fed into the tube with a flow rate of 20 sccm. Following the admission of ethylene, the process time was set to either 10 or 20 min to assess the effect of growth time.

The samples subjected to the oxidation-reduction pretreatment were placed in the appropriate location in the tube, as noted above, and heated up to the desired temperature in air at atmospheric pressure. The tube was then connected to the nitrogen line (100 sccm) and all connections sealed. Tube reactor was purged with nitrogen for 10 min to fully remove the air and then hydrogen was introduced (50 sccm) for 20 min to reduce the oxidized samples. After this step, ethylene was allowed to flow in the reactor along with the other gases similar to all other samples.

By the end of the growth period, the ethylene flow was interrupted while hydrogen and nitrogen were left to flow continuously to prevent oxidation during cooling down.

Table 1-1 summarizes all of the preparation and synthesis conditions for the different samples referred to hereafter. For reference, A stands for as-received samples without etching, AE for as-received and moderately etched (5 min) samples, AES for as-received and strongly etched (10 min) samples, P for polished samples without etching, PE for polished and moderately etched (5 min) samples, PES for polished and strongly etched (10 min) samples and OR for oxidized-reduced samples.

**Table 1-1 List of the samples with different preparation steps used in this work. During the growth step of either CNT or CNF, the flow rate of N<sub>2</sub>, H<sub>2</sub> and C<sub>2</sub>H<sub>4</sub> was maintained at 100, 5 and 20 sccm, respectively. During the reduction step after oxidation in air for CNF synthesis, the flow rate of N<sub>2</sub> and H<sub>2</sub> were 100 and 50 sccm.**

Condition → ----- Samples ↓	Surface finish	Etching time in HCl 32% (min)	Oxidation-Reduction	Growth time (min)
A1	As-received	NA	No	10
A2	As-received	NA	No	20
AE1	As-received	5	No	10
AE2	As-received	5	No	20
AES2	As-received	10	No	20
P1	Mirror polished	NA	No	10
P2	Mirror polished	NA	No	20
PE1	Mirror polished	5	No	10
PE2	Mirror polished	5	No	20
PES2	Mirror polished	10	No	20
OR	As-received	NA	Yes	10

The mass gain of the samples (hereafter referred to as deposited carbon) was calculated from the mass difference before and after the CVD treatment

by using a Sartorius M2P electronic microbalance with an accuracy of 0.001 mg.

Finally, to study the effect of the CVD process temperature on the electrochemical behavior of the sample in the absence of any carbonaceous gas, a series of 316 SS samples were treated in the tubular furnace under the same thermal and atmospheric conditions mentioned for CNT growth, but without ethylene admission.

### **1.2.3 Microstructural characterization**

Deposited carbon layers were characterized for phase analysis by grazing incidence X-ray diffraction (XRD) technique using an 1830 PW Philips X-ray generator equipped with a PW 3020 Philips goniometer and a PW 3710 Philips control unit. The radiation used was Cu K $\alpha$ , with scan step time of 0.50 s and step size ( $2\theta$ ) of  $0.02^\circ$  having the sample in the thin film geometry arrangement at  $0.5^\circ$  glancing angle and with rotating detector.

Surface topographic characterization was performed using an NT-MDT Solver Pro Atomic Force Microscope (AFM) instrument operated in contact mode with dedicated software. Evaluation of the surface nano-features was performed based on the DFL (deflection related signal) images of the AFM. DFL signals which are the difference signal between top and bottom halves of the AFM photodiode can be used to perform a more precise topography imaging. Contact silicon cantilevers (CSG 10) with tip radius of 10 nm curvature were used to probe the surface. Further elaboration and analysis on AFM data was made by WSXM (v5.3) software [104].

Microstructural characterizations of as-received, as-grown and corroded samples were carried out using scanning electron microscope (SEM, using either a Zeiss EVO 50 EP equipped with energy dispersive X-ray (EDX) or a Stereoscan 360 Cambridge SEM instrument). Nanostructures of CNTs and CNFs were further characterized with a transmission electron microscope (Philips CM200 FEG TEM). CNT and CNF specimens for TEM analysis were obtained by scratching as-grown samples while being immersed in a small volume of ethanol and sonicating the suspension for 60 min.

### 1.2.4 *Electrochemical characterization and corrosion measurements*

The corrosion behavior of coated and uncoated samples was studied by performing potentiodynamic and potentiostatic tests, using a standard three-electrode cell set-up, in 1 M H<sub>2</sub>SO<sub>4</sub> + 2 ppm HF solution, at 80°C. As the working electrode, different samples were used, namely, the bare as-received 316 SS, nitrogen heat treated 316 SS (SS-NH) and CNTs or CNFs coated 316 SS. A platinum coated titanium sheet was used as the counter electrode and a saturated calomel electrode (SCE) as the reference electrode. Electrochemical tests were conducted using a Modulab system (Solartron Analytical).

Potentiodynamic experiments were performed in the potential range from –0.5 to 1 V vs. SCE at a scan rate of 1 mV s<sup>-1</sup> in deaerated electrolyte saturated with nitrogen. Potentiostatic tests were carried out at potentials of –0.1 V and 0.6 V vs. SCE in an H<sub>2</sub> or O<sub>2</sub> saturated electrolytes, respectively, in the attempt to simulate the polarization conditions of the cathode and anode in a real fuel cell system [105–107]. Before each experiment, samples were left immersed in the electrolyte for 60 min to allow equilibration with the corrosive environment. Open Circuit potential (OCP) measurements in all cases showed a steady trend.

## 1.3 Results and discussion

### 1.3.1 *Synthesis of CNTs/CNFs*

#### 1.3.1.1 *Effect of surface morphology*

Fig. 1.1 (a) and (b) show the SEM micrographs of bare 316 SS in the as-received (a) and mirror polished (b) states. According to the micrographs in Fig. 1.1, protruding grains could be distinguished at the surface of as-received samples, while after polishing the surface appears obviously smooth and featureless.

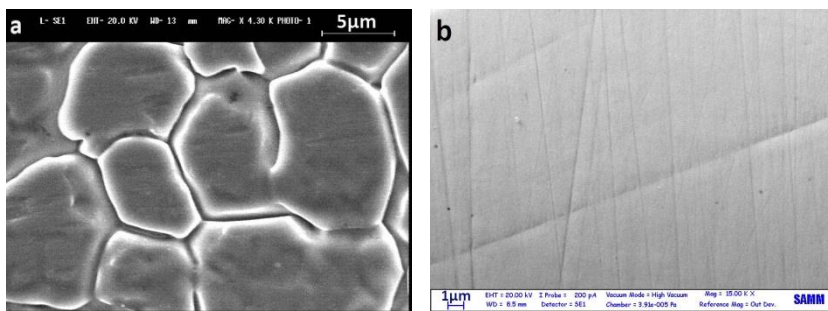
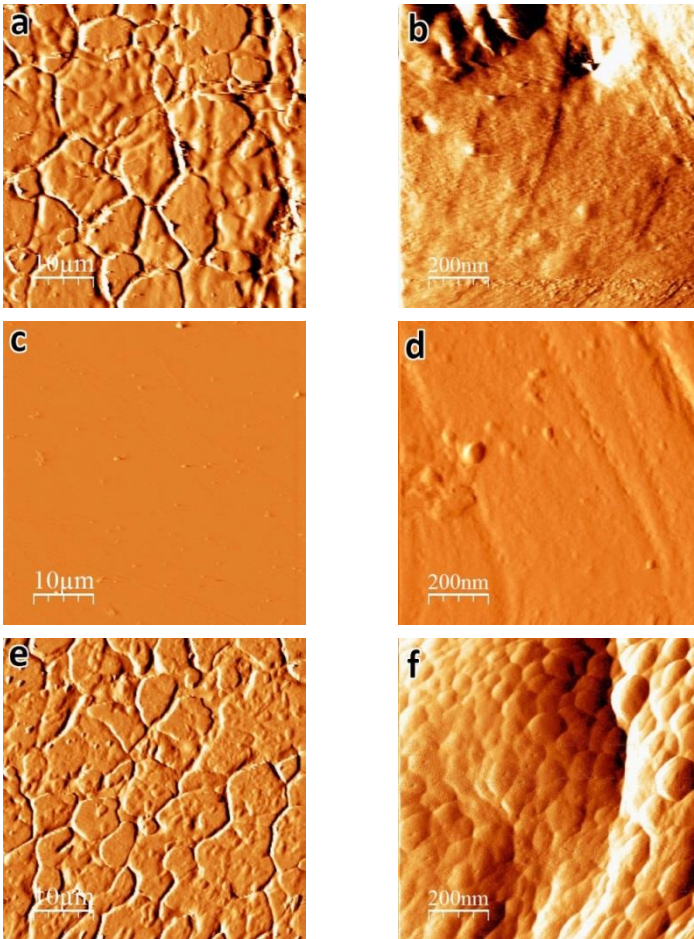


Fig. 1.1 SEM surface micrographs of (a) sample A1 and (b) sample P1 before CNT growth.

For confidence, a polished sample was subjected to metallographic etching with Beraha's (I) reagent ( $\text{H}_2\text{O}$ : 100 ml,  $\text{HCl}$ : 20 ml,  $\text{K}_2\text{S}_2\text{O}_5$ : 0.5 g,  $\text{NH}_4\text{HF}_2$ : 2.4 g) [108] and observed under the optical microscope. The etched sample revealed the same granular morphology as in the as-received sample.

For a more thorough investigation on the effects of surface features on CNT growth, low and high resolution AFM scans were performed and the results are shown in Fig. 1.2. In order to clarify the role of the heat pretreatment under controlled atmosphere on the evolution of the morphology of the catalytic substrate, AFM characterization was accompanied by detailed statistical analysis of nano-features lateral sizes which will be discussed herein. According to AFM results, prior to reducing atmosphere heating, a very fine nanoscale roughness characterizes the surface of group A samples (Fig. 1.2 (b)) while these features are eliminated to a great extent in the case of group P samples (Fig. 1.2 (d)). Fig. 1.3 shows the normal (Gaussian) distribution of nano-features lateral size for as-received and polished samples before and after the reducing atmosphere heating. Apparently, the as-received sample had a very narrow distribution of nano-hills diameter, with the frequency peak in the range of 7 nm, while the polished sample had almost thoroughly lost its surface features and no meaningful statistical analysis could be performed. The AFM analysis also confirms the strong

effect of polishing on the original samples (Fig. 1.2 (c and d)). Obviously, concerning the effect of the substrate surface morphology on the CNT



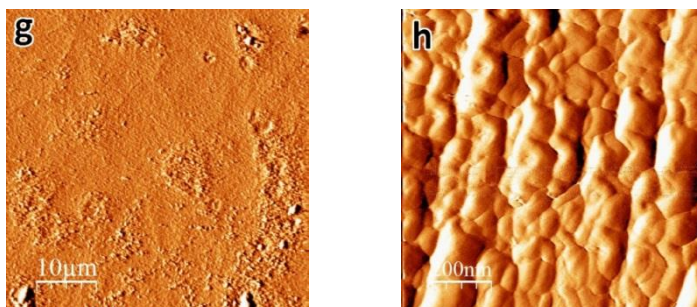


Fig. 1.2 Low ( $50 \times 50 \mu\text{m}$  scan, left column) and high ( $1 \times 1 \mu\text{m}$  scan, right column) resolution AFM images of the samples of groups A and P before and after the reducing atmosphere heating; (a, b) group A samples before reducing atmosphere heating, (c, d) group P samples before reducing atmosphere heating, (e, f) group A samples after reducing atmosphere heating, (g, h) group P samples after reducing atmosphere heating.

growth, mainly the nanoscale features are of interest rather than micro or macro scale features. In this regard, the granular microstructure with large grain sizes of  $10\text{--}20 \mu\text{m}$  and grain boundary depth of around  $0.5 \mu\text{m}$  of as-received samples (Fig. 1.2 (a)), will not be considered further in this study.

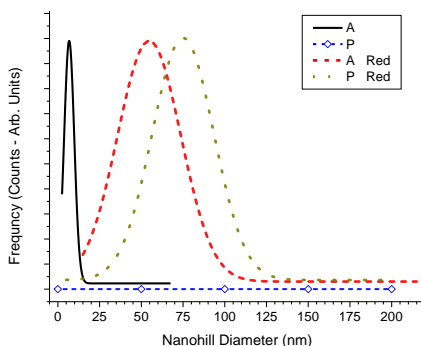
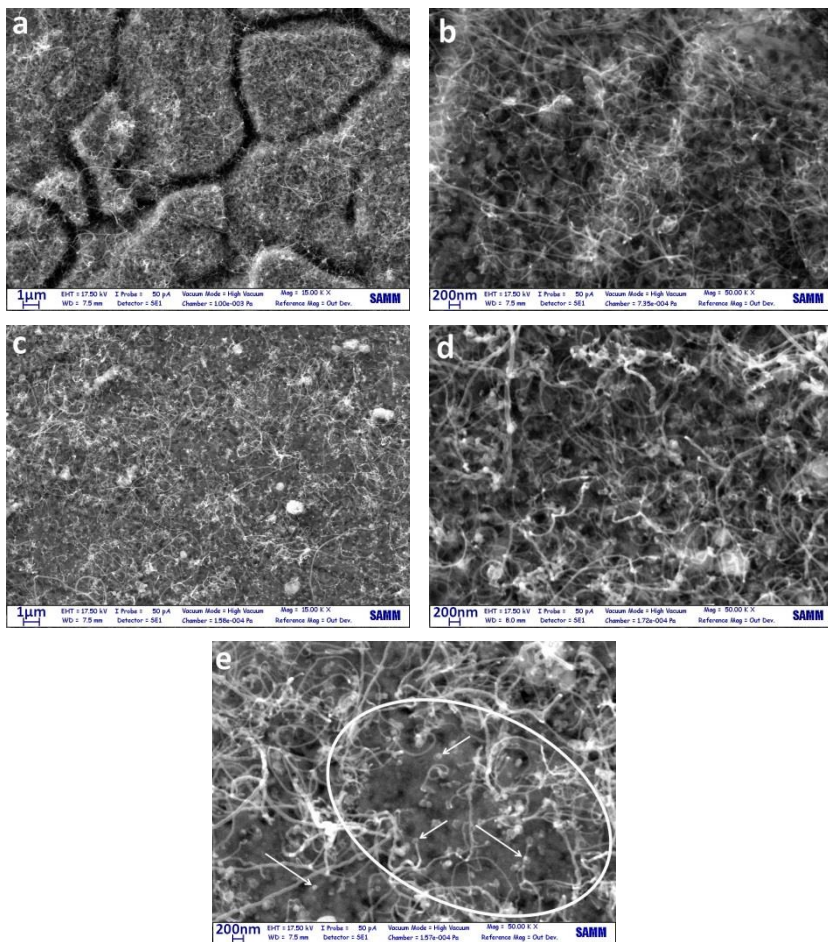


Fig. 1.3 Nano-hills diameter distribution for as-received and polished samples before (A and P) and after (A Red and P Red) reducing atmosphere heating.

Fig. 1.4 shows SEM micrographs of A1 (a, b) and P1 (c, d, e) samples. Both at low and high magnifications (Fig. 1.4 (a and b)), sample A1 shows a uniform and homogeneous coverage of CNTs. On the contrary, in the case of sample P1, some bare areas can be distinguished (for instance, within the area encircled by the ellipse drawn in Fig. 1.4 (e)). Comparing CNTs of samples A1 and P1 (Fig. 1.4 (b) and (d), respectively), smaller diameter and greater homogeneity along the tubes length could be recognized for sample A1. Furthermore, sample A1 shows an almost exclusive formation of CNT, while in sample P1 the presence of carbon nanofiber (CNF) is not negligible.

Since most of the nanoscale roughness of the surface was removed by polishing, formation of proper sites for filamentous carbon growth relies mainly on the surface evolution during the preliminary steps of synthesis. Attention should be paid to the morphological evolution caused by the heat treatment in flowing hydrogen in order to clarify the differences in CNT growth on polished and unpolished samples. As AFM images suggest, while the microstructures of samples of group A and P (Fig. 1.2 (e) and (g), respectively) did not show remarkable changes, the nanostructures of these samples (Fig. 1.2 (f) and (h), respectively) experienced significant modifications. Fine and uniform granular features with an average lateral diameter of 55 nm formed on group A and a semi-granular less uniform nanostructure formed on group P samples after reduction under hydrogen. Nano-hills of group P possess an average diameter of 75 nm which is larger compared to group A (Fig. 1.3).

The surface restructuring revealed by AFM and leading to nanostructure formation is apparently a complex phenomenon resulting from the interplay and compromise between different competing and concurrent factors. The environmental conditions, i.e. high temperature and reducing atmosphere, will probably activate surface reconstruction processes –as a result of oxide reduction and associated with hydrogen adsorption– leading to atomic and



**Fig. 1.4** SEM micrographs of the samples (a) A1, (b) higher magnification of A1, (c) P1, (d) and (e) higher magnifications of P1.

nanoscale chemical and structural rearrangement at the surface. Surface energy driven processes will nonetheless overlap with thermally activated processes, such as phase separation and transformation –in particular, carbide precipitation – and recrystallization, which in turn are particularly

sensitive to the thermo-mechanical history of the substrate material. The rather elusive and definitely complex nature of these phenomena require a devoted and focused investigation, which was outside the scope of the present work.

Since these nano-features would serve as the catalytic sites for the CNT growth [60,61,65–68,96], there would be a direct relation between the diameter of the tubes and those of the catalyst particles. Larger nano-hills would favor the growth of thicker CNTs or, rather, CNFs. Further, if in some regions these nano-hills are not formed or there are relatively large flat zones, the growth of filamentous carbon is disfavored in those areas. Non-catalytic sites will instead be covered by amorphous carbon or graphite [67,89].

Fig. 1.5 shows the SEM images of A2 (a, b) and P2 (c, d) samples experiencing 20 min exposure to carbon source. It can be seen that by increasing the growth time, the uniformity of the coverage was maintained for unpolished samples and improved for the polished ones. Furthermore, the diameter of carbon filaments increased compared to 10 min growth time CNTs, which complies with both an increase in the number of walls of CNTs and an increase in the proportion of CNFs in the total product.

Fig. 1.6 shows the XRD patterns of stainless steel before and after growth of different filamentous carbon products. Bare stainless steel shows characteristic peaks of austenite phase at  $2\theta$  equal to  $43.38^\circ$ ,  $50.23^\circ$  and  $74.40^\circ$  corresponding to (111), (200) and (220) planes of FCC austenite, respectively. Weak peaks corresponding to a thin oxide layer on the pristine steel can also be recognized. After growth of CNT/CNF, characteristic peaks of hexagonal graphite were observed at  $2\theta$  angles equal to  $26.09^\circ$  and  $44.57^\circ$  corresponding to (002) and (101) crystallographic planes, respectively, along with weaker peaks such as (004) plane at  $54.21^\circ$ , (102) plane at  $50.79^\circ$  and (100) plane at  $42.21^\circ$  which are all present but not marked to avoid confusion. According to the peak at  $26.09^\circ$ , the interplanar spacing of (002) planes in the CNT is 0.341 nm. Although some recent theories such as re-ordering of chaotic carbon even discuss the possibility of

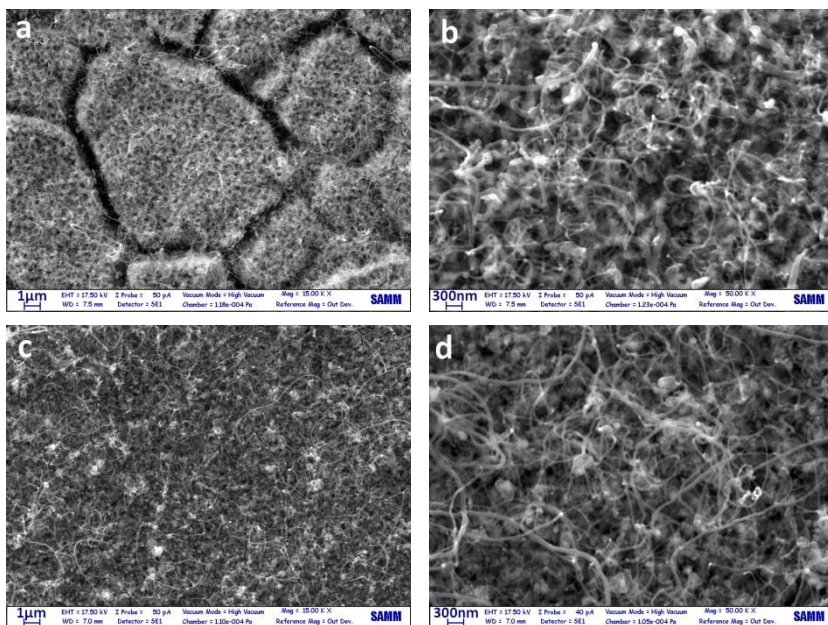


Fig. 1.5 SEM micrographs of the samples (a) A2, (b) higher magnification of A2, (c) P2, (d) higher magnifications of P2.

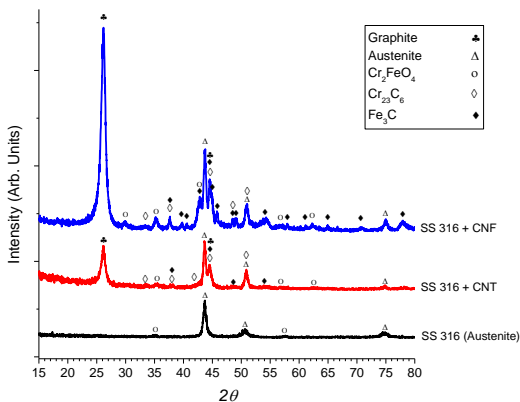


Fig. 1.6 XRD patterns of bare stainless steel, CNT on stainless steel (A1) and CNF on stainless steel (OR).

formation of carbon nanocrystals with preferred orientation within the amorphous carbon matrix seeding the growth of crystalline carbon species such as CNTs [109], evidences such as presence of metals and metal carbides peaks in XRD patterns, suggest more likely growth mechanisms as follows. Notably, XRD pattern of the OR sample showed the presence of cementite and possibly a small fraction of chromium carbide, though overlapping of carbides peaks (and of graphite) does not allowed unequivocal conclusions. The presence of very weak reflections that could be attributed either to iron or chromium carbides was also recognized in the A1 sample. Metallic carbides are formed during the exposure of stainless steel to ethylene at high temperature. Similar combination of iron and chromium carbides with filamentous carbon and  $\text{Cr}_2\text{FeO}_4$  has been reported in the literature concerning the metal dusting corrosion of stainless steel [110–112]. Moreover, iron carbide, cementite, was reported to be the effective nature of the catalyst in CNT growth by different authors [98,113,114]. Applicability of either of these viewpoints to our case should be discussed on the basis of the TEM images.

Fig. 1.7 shows the TEM micrographs of carbon nanostructures in group A samples. It confirms that MWCNTs with up to 30 walls are formed with inner diameter less than 10 nm and outer diameter up to 50 nm. However, the products are not limited to CNTs and some CNFs are formed also (Fig. 1.7 (a)). Generally, without using a precisely engineered catalyst, avoiding the formation of CNFs seems to be difficult. Interplanar spacing of 0.33 nm can be observed between the tube walls (Fig. 1.7 (d)) in good agreement with the value calculated from the XRD peak of (002) planes of hexagonal graphite. Two different types of catalyst particles could be observed in the micrographs. The first one (Fig. 1.7 (b)) is a thin conical shaped nanorod with an average diameter less than 10 nm similar to the inner diameter of CNTs. The second type (Fig. 1.7 (c)) includes relatively large particles encapsulated at the tips of CNTs with an average diameter of 50 nm similar to or slightly larger than the outer diameter of CNTs.

Instances of the first type (Fig. 1.7 (b)) are believed by several groups to be the proof of *base growth* mode [60,115]. In our case, catalyst nano-hills which are naturally parts of the substrate surface seem to have injected these shoot shaped materials either by partial break-up or by undergoing a quasi-liquid transformation resulting in catalyst transfer into the tube channel. In either case, the catalyst particle inside the tube seems to be in a quasi-liquid [60,114] or fluctuating crystalline [113] state after standing out from the surface, making it easily deformable under the stretching forces of the tube walls.

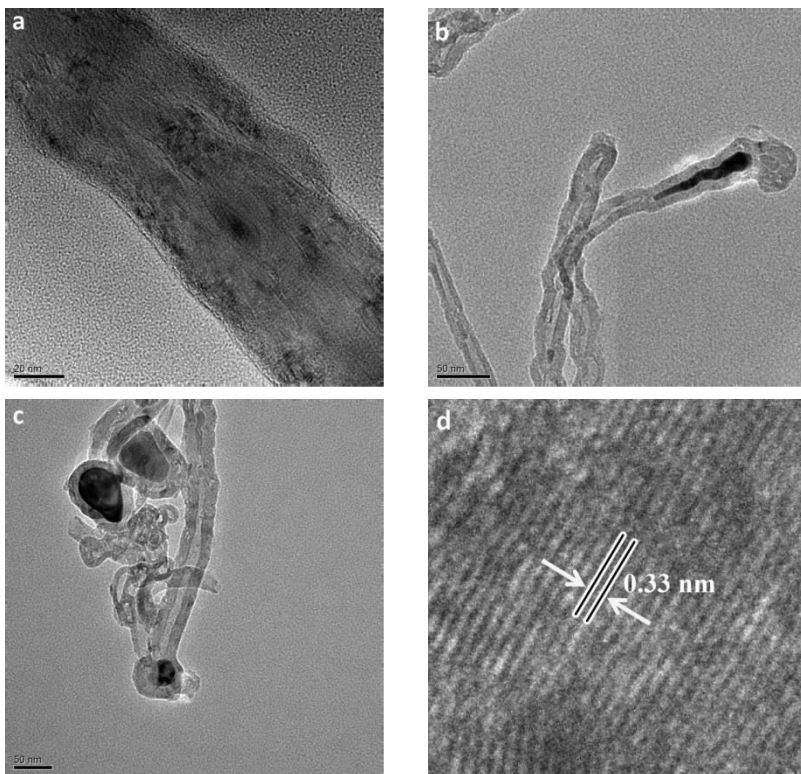


Fig. 1.7 TEM micrographs of carbon nanostructures in group A.

Regarding the second type (Fig. 1.7 (c)), the presence of catalyst nanoparticles at the tips of CNTs is mainly interpreted as an evidence of *tip growth* mode in the literature [41,116,117]. Based on proposed explanation in an early work by Baker et al. [71] as well as in some later works, growth mode depends mainly on the interaction of the catalyst and the support and low adhesion would favor catalyst particle detachment from the substrate and sticking to the CNT tip giving rise to the tip growth mode. However, in our case the catalyst-substrate interaction is supposed to be strong since the catalyst is actually the same as and integrated with the substrate. Therefore, the question can be as follows. How could relatively large particles be detached from the substrate to pursue the tip growth mode? There are very early discussions on the phenomenology of “metal dusting” describing it as “localized or general overall surface damage, in potentially carburizing and reducing gas environments with or without oxygen, in the temperature range of 450°-800°C” with a variety of damage products such as graphite mixed with metal, metal carbides and metal oxides, generally called as dust [118]. Although this type of damage is categorized as a gaseous corrosion with localized damage (e.g., deep pits), its sidelong symptoms such as graphite coverage on the surface [119], break-up of the bulk metallic structure into powder or dust [120,121], formation of metallic carbides [112] and growth of filamentous carbon [122] are all present in this work suggesting that the very elementary stages of dusting are involved in the formation of nanoscale catalyst particles broken-up from the substrate. According to Szakálos [110], a sequence of dusting mechanisms can lead to CNT/CNF formation. Namely, in the case of austenitic steels which cannot form cementite, primarily graphite nucleates and deposits on the austenite surface. Then, by carbon interstitial diffusion into the sub-layer, graphite tends to grow within the near surface material. Consequently, graphite saturation will cause deformation and break-up of the metal surface. This graphite deposition and particle break-up was described as the “type II-mechanism” of dusting. Subsequently, the broken-up particles can play the role of catalyst particles for the filamentous carbon growth (the “type IV-mechanism” according to Szakálos nomenclature). In this regard, the required catalyst particles for the tip growth mode observed in Fig. 1.7 (c),

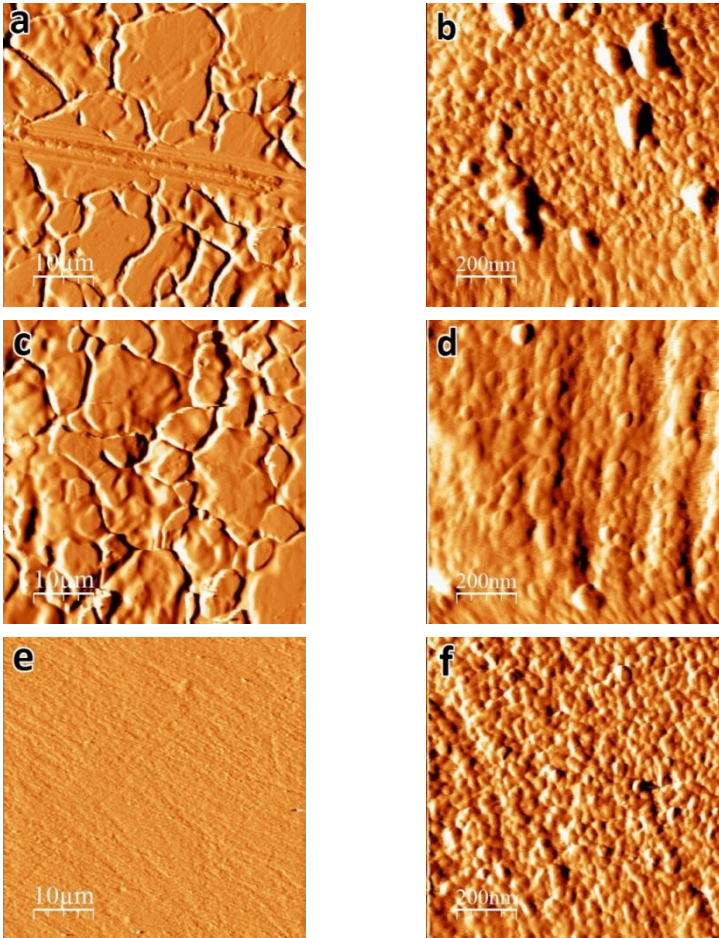
could have been formed by successive recurrence of type II and type IV dusting mechanisms. Further evidence for this hypothesis could be found in SEM micrographs. In the bare areas of samples like P1 (Fig. 1.4 (e)) sparse presence of particles with a size range of 50-100 nm is observed (pointed by arrows) implying surface break-up and particle removal. Some of these particles also show CNTs attached to them demonstrating their role in the catalysis of CNT growth. Furthermore, in samples with longer growth time (like Fig. 1.5 (b and d)) a blur view of an outspread granular layer can be distinguished beneath the thin CNT layer. This feature can be attributed to the graphite covering primarily broken-up particles removed from the surface as well as amorphous carbon. Longer exposure times to the carbonaceous atmosphere could have extended the surface break-up and particle removal period. Reminding the catalytic effect of these particles, the same feature can be the reason why increasing the growth time, decreases the uncovered area.

### 1.3.1.2 Effect of surface etching

In order to investigate the effect of etching on the CNT growth, topographic and compositional characterizations were performed on the etched samples. Fig. 1.8 shows the AFM images of the etched samples. In terms of morphology, the effect of etching can be realized as the formation of granular nano-features on the surface that tend to enlarge by increasing the etching time. Two by two comparisons of high resolution AFM images of AE-AES samples (Fig. 1.8 (b and d), respectively) or PE-PES samples (Fig. 1.8 (f and h), respectively) demonstrate the formation and size change of these nano-features.

Fig. 1.9 shows the distribution of nano-features lateral size for A, AE, AES, P, PE, and PES samples. Formation of nano-hills with an average diameter of 28 nm is observed for both as-received and polished samples after 5 min etching (samples AE and PE, respectively). However, by increasing the

etching time up to 10 min, nano-hills average diameters increased up to 35 and 57 nm for AES and PES samples, respectively.



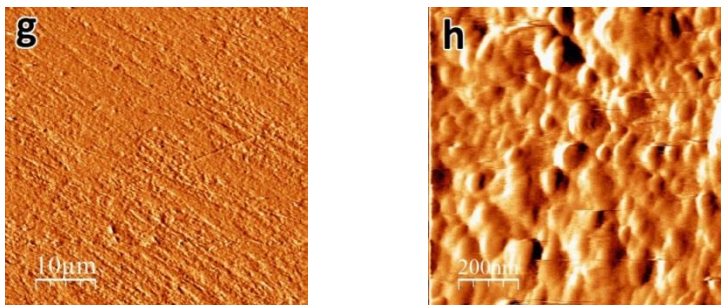


Fig. 1.8 AFM images of as-received and polished samples after different etching durations. AE (a, b) and PE (e, f) samples are etched in HCl for 5 min and AES (c, d) and PES (g, h) are etched in the same solution for 10 min (left column images are  $50 \times 50 \mu\text{m}$  low resolution scans and right column images are  $1 \times 1 \mu\text{m}$  high resolution scans).

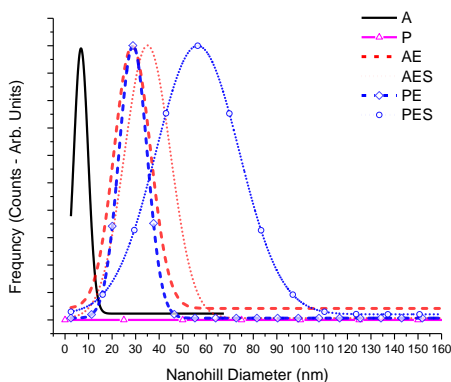
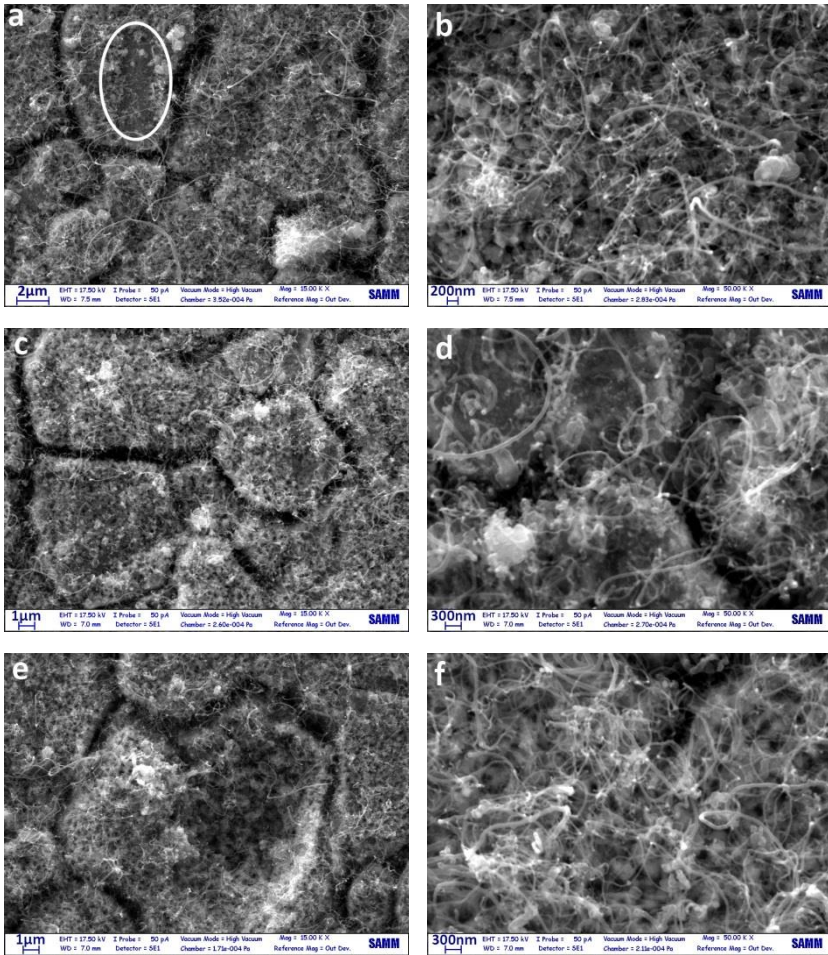


Fig. 1.9 Nano-hills diameter distribution for A, AE, AES, P, PE, and PES samples.

To investigate any chemical effect of etching on the surface composition and elemental distribution, EDX elemental mapping was performed on a 10 min etched sample. Apparently, no obvious change in the elements distribution occurred upon etching. In particular, iron remained homogeneously distributed on the surface without any localized concentration or depletion zones. Samples were then processed for CNT/CNF growth and subjected to SEM analysis for the assessment of the type of filamentous carbon.



**Fig. 1.10** SEM micrographs of samples AE1 (a, b), AE2 (c, d) and AES2 (e, f) in different magnifications.

Fig. 1.10 shows the SEM images of AE1 (a, b), AE2 (c, d) and AES2 (e, f) samples. As it can be seen in Fig. 1.10 (a) (the area encircled by the ellipse), some areas are not covered by CNTs and 5 min of etching has resulted in a

uniformity loss in the coverage compared to the A1 sample (Fig. 1.4 (a and b)). According to the SEM images of samples AE2 (10c, d), it is seen that although by increasing the growth time a decrease in the total area of uncovered regions occurred (compare Fig. 1.10 (c, d) (AE2) and Fig. 1.10 (a) (AE1)), they are still present. In contrast, higher etching time is likely to be a more effective way to decrease the uncovered areas as Fig. 1.10 (e and f) suggest.

Fig. 1.11 shows growth results on PE1(a, b), PE2 (c, d) and PES2 (e, f) samples. As Fig. 1.11 (a and b) suggest, the growth on PE1 is poor and the coverage in this sample is even worse than AE1. Growth is quite sparse and filaments are short. It is worth mentioning that according to Fig. 1.9, both these samples (AE1 and PE1) had an average nano-hill lateral size of 28 nm which should expectedly give rise to CNT growth.

The effect of increased etching time in polished samples is analogous to that of the as-received samples as can be seen in Fig. 1.11. While bare areas can still be seen for samples subjected to 5 min etching even after 20 min exposure to carbonaceous gas (Fig. 1.11 (c and d)), in the case of strong etching of polished samples (PES2) an almost full coverage of carbon filaments is achieved (Fig. 1.11 (e and f)).

In order to obtain a deeper understanding of the reasons behind such behavior, AFM measurements were performed on 5 and 10 min etched samples of group A after the reducing atmosphere heating step to explore any probable alteration of the surface topography caused by subsequent heat treatment. Results are shown in Fig. 1.12. It is seen that after the heating cycle surface nanostructure changed considerably and two different types of features with different sizes are observed. Some large grains with an average lateral size above 200 nm which contain smaller granular features with an average lateral size below 80 nm within them can be distinguished

in both AE and AES samples (Fig. 1.12 (b and d), respectively). Therefore, a bimodal size distribution can be recognized for samples treated by etching and subsequent controlled atmosphere heating.

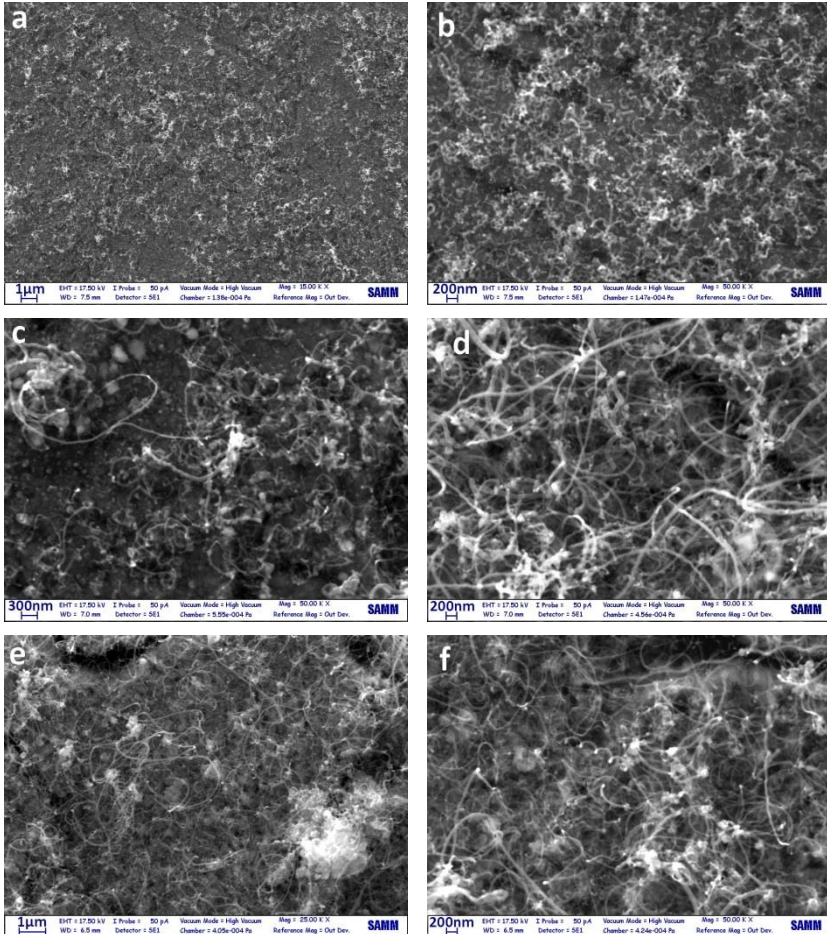


Fig. 1.11 SEM micrographs of the samples PE1 (a, b), PE2 (c, d) and PES2 (e, f) in different magnifications.

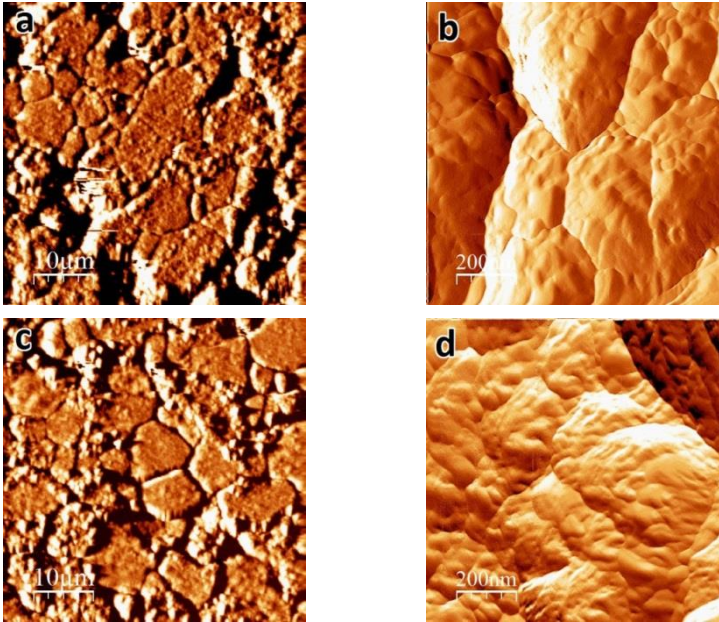


Fig. 1.12 Low ( $50 \times 50 \mu\text{m}$  scan, left column) and high ( $1 \times 1 \mu\text{m}$  scan, right column) resolution AFM images of the samples of groups AE and AES after the reducing atmosphere heating; (a, b) group AE samples after reducing atmosphere heating, (c, d) group AES samples after reducing atmosphere heating.

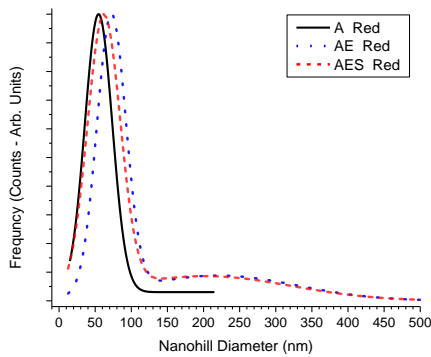


Fig. 1.13 Nano-hills diameter distribution for A, AE, AES samples after reducing atmosphere heating.

It is interesting to note that all these changes occur at the nanoscale and could not be observed just relying on the microstructural features as revealed by low resolution AFM (Fig. 1.12 (a and c)).

Fig. 1.13 shows the statistical analysis of lateral size distribution of nano-features for A, AE, AES samples after both etching and heating up. A bimodal distribution is confirmed for etched samples with a sharp peak at 72 and 62 nm (for AE and AES samples, respectively) and a wide peak at 220 and 200 nm (for AE and AES samples, respectively). These observations give some evidences for a restructuring hypothesis. It seems that the surface of catalytic substrate undergoes different extents of rearrangement depending on the type and intensity of the primarily applied treatment. This restructuring appears by the formation of nano-hills which tend to grow to a certain extent determined by the origin of the restructuring, e.g., chemical etching, reducing atmosphere or other factors. After a certain degree of growth, restructuring will recur and result in breaking of large grains and formation of finer grains at the expense of gradual vanishing of the overgrown ones. This should be considered as a dynamic and cumulative phenomenon in which the effect of different restructuring promoting factors, such as etching and reducing atmosphere treatment, can be superimposed to or pursued by the other. From this viewpoint, bimodal size distribution of etched samples after heating can be reread. Primarily formed nano-hills by etching will continue to grow under hydrogen atmosphere heating and after passing 200 nm border, tend to break into refined grains due to restructuring. In this regard, 10 min etched samples that have formed larger nano-hills compared to 5 min etching, would arrive to the stage of restructuring sooner under heating and symptoms of previous large grains would vanish faster relative to 5 min etched samples. This effect can be seen by lower average size of the larger grains in AES (second peak: 200 nm) compared to AE (second peak: 220 nm) after heating. Moreover, visual evidences of high resolution AFM also confirms the higher number of fine grains formed after restructuring in AES (Fig. 1.12 (d)) compared to AE (Fig. 1.12 (b)) and testify a longer restructuring period. It seems that the presence of features with a size over

200 nm is responsible for the naked areas in Fig. 1.10 and Fig. 1.11 and, by appearance of the restructured fine grains, those uncovered areas would minimize.

### **1.3.1.3 Effect of growth time**

Based on the result presented above, the effect of growth time can be evaluated by two comparison of SEM images of similar samples differing only in exposure time to ethylene (e.g., A1 vs. A2 (Fig. 1.4 (b) and Fig. 1.5 (b), respectively), AE1 vs. AE2 (Fig. 1.10 (b) and Fig. 1.10 (d), respectively), P1 vs. P2 (Fig. 1.4 (d) and Fig. 1.5 (d), respectively), and PE1 vs. PE2 (Fig. 1.11 (b) and Fig. 1.11 (d), respectively)). Accordingly, two main results would apply to all of these pairs caused by longer growth time and are summarized as follows:

- 1- Increasing the diameter of CNTs which can be translated either into the increase in the number of the walls or the formation of CNF rather than CNT.
- 2- Decreasing the percentage of bare areas on the surfaces not covered by CNTs in shorter growth durations due to the increased surface break-up at longer exposure times.

### **1.3.1.4 Effect of surface oxidation-reduction**

As another preparation method, oxidation-reduction pretreatment was performed on 316 SS followed by CNT growth cycle. Fig. 1.14 shows the AFM images of an unpolished sample which was subjected to oxidation and reduction pretreatments. Effect of oxidation can be seen as the formation of relatively large granular structure while, reduction step restructures the grains to smaller size. Fig. 1.15 shows the statistical analysis of lateral size distribution of nano-features for oxidized-reduced samples. It is seen that oxidation provides an average nano-hill lateral size of 137 nm and subsequent reduction step reduces this average size to 111 nm.

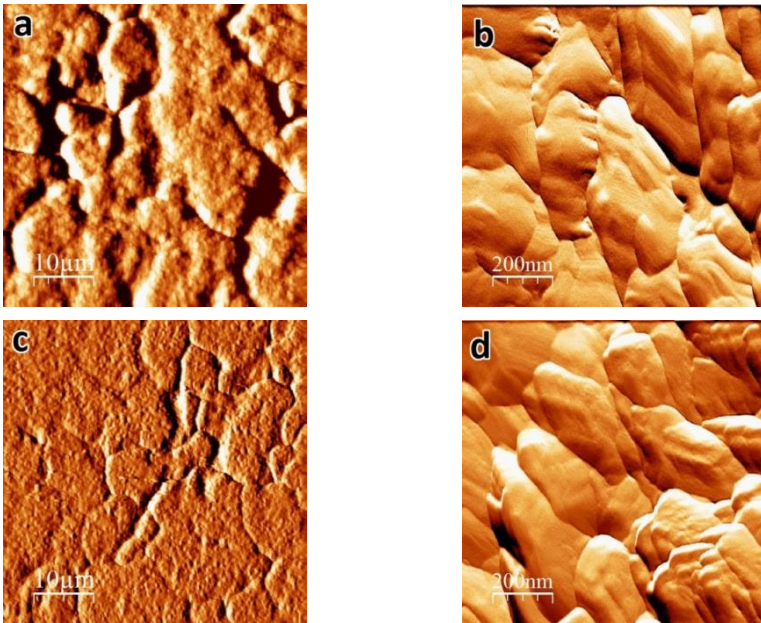


Fig. 1.14 Low ( $50 \times 50 \mu\text{m}$  scan, left column) and high ( $1 \times 1 \mu\text{m}$  scan, right column) resolution AFM images of the samples of groups OR; (a, b) after oxidation treatment step and (c, d) after reduction step followed by the primary oxidation.

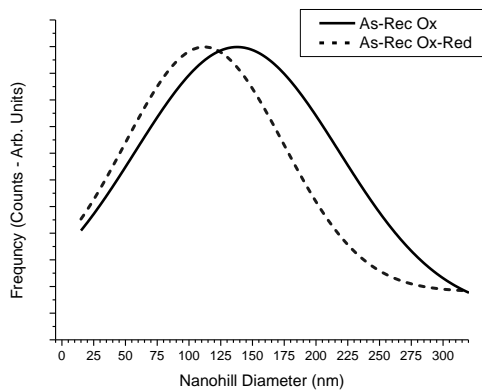


Fig. 1.15 Nano-hills diameter distribution for OR samples.

Nevertheless, even the size obtained after the restructuring effect of hydrogen reduction is higher than that required for CNT growth.

Fig. 1.16 shows the SEM images of OR group samples after synthesis step. Carbon filaments grown by this pretreatment should be characterized by two main features: 1- a full coverage with a thick layer of carbon filaments all over the surface, 2- formation of micrometer scale straw stack like carbon filaments (Fig. 1.16 (a)). Fig. 1.16 (b) shows the higher magnification of the plain area between the stacks and it can be clearly observed that carbon fibers formed thereon are of a wide range of diameter sizes from 100 nm up to 0.5  $\mu\text{m}$ . The thinnest ones, as Fig. 1.16 (e) shows more clearly, are not smaller than 80-100 nm in diameter. On the other side, higher magnification image of the stacks (Fig. 1.16 (c)) shows that they are intertwined bundles of CNFs. However, the “nano” prefix is not due for all of them since a considerable fraction is in the range of 200-500 nm. Higher magnification image of this part (Fig. 1.16 (d)) shows that in some cases a tree like morphology of carbon fibers can be distinguished with a stem in the diameter range of micrometers and branches in the order of hundreds of nanometers. More interestingly, at the end of the branches, formation of tiny CNT leaves can be realized. Similar morphological characteristics has been reported by Szakálos [110] to be a result of successive break of metal particles. Primarily detached large particle can catalyze synthesis of large fibers and subsequent breaks of the same one, would result in formation of thinner fibers and tubes. Almost in all areas of samples of group OR, the presence of catalyst particles on the tips of fibers and tubes is evident complying with the particle break-up activation mechanism.

Referring to AFM images (Fig. 1.14) revealing nano-features larger than 100 nm, formation of CNFs instead of CNTs seems reasonable. Nevertheless, pronounced presence of catalyst particles on the CNF tips elucidates another aspect of this pretreatment, namely, its potential to facilitate robust surface break-up and particle removal in subsequent steps

of synthesis and growth. Deeper understanding of this phenomenon requires further investigations.

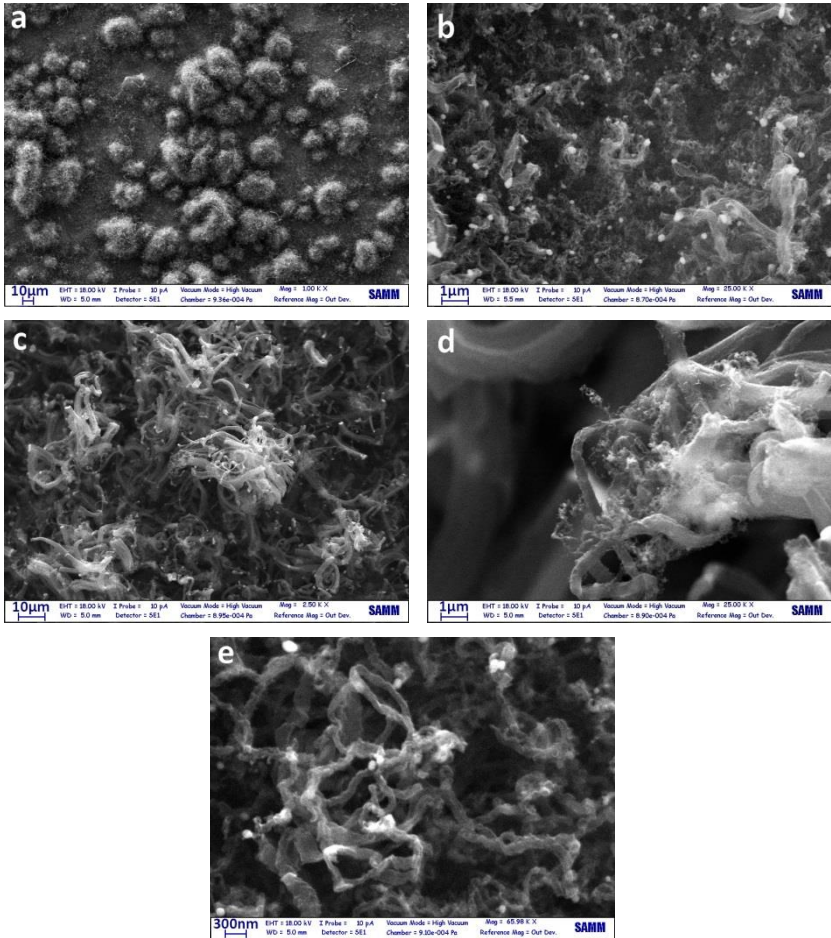


Fig. 1.16 SEM micrographs of sample OR in different magnifications.

### 1.3.2 Corrosion evaluation

#### 1.3.2.1 Microstructural characterization before corrosion

Fig. 1.17 (a and b) presents the SEM micrographs of CNT and CNF samples, respectively, directly grown on the stainless steel substrate, for a closer comparison purpose, regarding their subsequent corrosion behavior the will be discussed later. It is seen that CNTs are thin and their diameter size does not vary in a wide range. However, the presence of a small fraction of CNFs can be seen as individual filaments of larger diameter. Small catalyst particles can also be observed on the tips of CNTs as tiny bright spots. According to TEM studies, it is confirmed that the number of walls of CNTs is about 25 to 30, with inner diameter of  $10\pm 2$  nm and outer diameter of  $40\pm 10$  nm. CNFs, in contrast, show a range of diameter size, from 60 to hundreds of nanometers, and are characterized by the presence of a large number of catalyst particles at the tip of the filaments. The deposited carbon mass was measured to be  $0.5\text{ mg cm}^{-2}$  for CNTs and  $2\text{--}4\text{ mg cm}^{-2}$  for CNFs. The CNF carpet was quite thick ( $10\text{--}30\text{ }\mu\text{m}$ ) while the CNT one was much thinner ( $1\text{--}3\text{ }\mu\text{m}$ ). Although individual CNTs were as long as several micrometers, their entangled arrangement did not result in the formation of a thick layer.

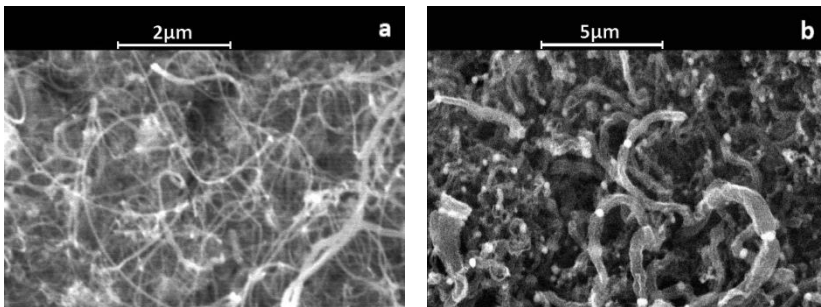


Fig. 1.17 SEM micrographs of as-grown samples showing (a) CNTs and (b) CNFs.

Fig. 1.18 shows the XRD patterns of CNT/CNF samples, similar to what presented in Fig. 1.6. However, some further patterns are included here

referring to stripped samples for the purpose of checking the structural changes taking place on the substrate material regardless of the CNT/CNF layer. It is seen that in addition to graphitic carbon peaks characteristic of both CNTs and CNFs, it can be inferred from the XRD patterns that the high temperature synthesis in the presence of ethylene resulted also in the formation of chromium and iron carbides – the latter more obvious for the case of CNF growth. In this respect, it may be inferred that the surface modifications caused by the oxidation-reduction pretreatment used for CNF synthesis resulted in an enhanced formation of iron carbide. Actually, at variance with CNT samples, XRD pattern of CNF samples showed relatively strong reflections of chromium and iron oxides.

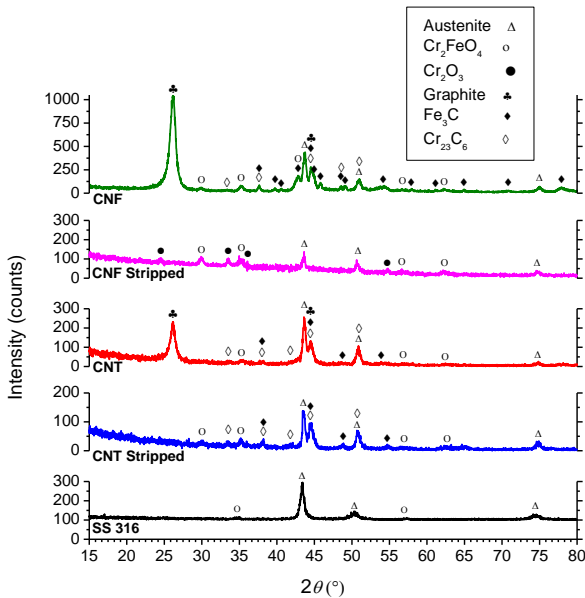


Fig. 1.18 XRD patterns of as-received and as-grown samples.

In the event that  $\text{Fe}_3\text{C}$  and possibly other carbides particles were trapped in the CNT/CNF layers, as it may be in view of their potential involvement in the mechanism of carbon nanotube and fiber growth [98,113,114,123–127], an attempt was made to separate the possible contribution of carbide

particles within the layer, e.g. at the tip of carbon filaments, from those due to substrate carburization. For this purpose, the carbon layer was removed by gently shaving the surface with a plastic blade, followed by mild cleaning of the stainless steel surface with a tissue. This procedure was used for both CNT and CNF samples in order to perform the XRD analysis on the stripped substrate after exposure to the CVD processing environment. The absence of graphite peaks in the patterns labeled “stripped” in Fig. 1.18 confirms that the carbon layer was effectively removed from the substrate, though, as revealed by SEM surface micrographs of the samples in Fig. 1.19, a small amount of filaments remained in the grooves, but apparently could not be detected by XRD.

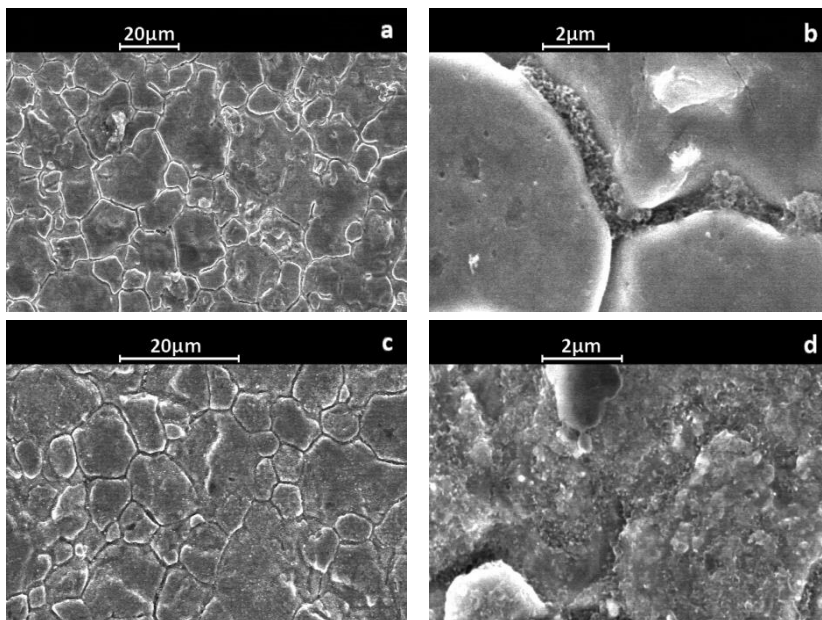


Fig. 1.19 SEM micrographs of 316 SS substrates stripped from (a, b) CNT and (c, d) CNF.

A further remark is that while chromium carbide was still detected after stripping of the CNT layer (see pattern “CNT Stripped” in Fig. 1.18), iron

and chromium carbides reflections disappeared from the XRD pattern of the CNF sample. Hence, notwithstanding the possibility of the presence of traces of carbide in the CNT Stripped sample –undetectable by XRD due to the low amount or the masking effect of a surface oxide–, it can be safely concluded that the  $\text{Fe}_3\text{C}$  formed during the synthesis of CNF was to a large extent incorporated within the carbon layer in the form of particles on the tip of filaments, which is in good agreement with the SEM observations (Fig. 1.17 (b)).

### 1.3.2.2 Electrochemical characterization

#### 1.3.2.2.1 Potentiodynamic tests

Fig. 1.20 shows potentiodynamic curves for the different samples in deaerated 1 M  $\text{H}_2\text{SO}_4$  + 2ppm HF electrolyte at 80°C. The potentiodynamic curves show obvious and marked differences. As a preliminary remark, it can be noticed that there were only relatively small changes in the free corrosion potential for coated samples, compared to the bare substrate ( $E = -0.328$  V vs. SCE for bare 316 SS,  $E = -0.325$  V vs. SCE for SS-NH,  $E = -0.314$  V vs. SCE for CNT on 316 SS sample and  $E = -0.280$  V vs. SCE for CNF on 316 SS sample). The observed corrosion potential is apparently the potential resulting from the coupling of the hydrogen reduction and iron oxidation reaction, irrespective of the presence of the filamentous carbon coatings and the surface modifications of the substrate during the growth process. This observation can be understood in the light of the porous nature of the layers. The slight higher value measured for the CNF sample is probably related to the oxidation of the surface, as revealed by XRD.

The Tafel extrapolation method [128] was used to calculate the corrosion current density (c.d.). The c.d. derived from this method is higher for both the CNT and CNF coated samples compared to that of the bare steel, namely: about  $15 \times 10^{-4}$ , and  $20 \times 10^{-4}$   $\text{A cm}^{-2}$ , compared to  $5 \times 10^{-4}$   $\text{A cm}^{-2}$ , respectively. Moreover, over almost all the anodic region above the free corrosion potential, coated samples show a much higher anodic c.d. which is indicative of high susceptibility to corrosion. In this regard, at both

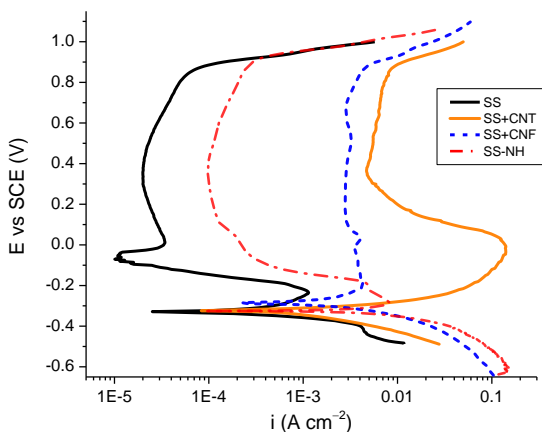


Fig. 1.20 Potentiodynamic curves of 316 SS, 316 SS+CNT, 316 SS+CNF and SS-NH samples in 1 M  $\text{H}_2\text{SO}_4$  + 2 ppm HF solution at 80°C.

potentials of  $-0.1$  V and  $0.6$  V vs. SCE, corresponding to the anodic and cathodic polarization of BPs, respectively, these materials will be liable to rapid attack.

Interestingly, the anodic c.d. of SS-NH in the passive region lies between that of the pristine 316 SS and those of CNT/CNF coated samples. This increase of the dissolution rate in the passive potential region obviously points to the susceptibility of SS to sensitization [129] upon exposure to the high temperature of CNT growth, independently of the presence of a carburizing environment. However, the increase of the c.d., though remarkable compared to bare 316 SS, is still far below the high anodic c.d. of CNT/CNF coated samples, suggesting that the carburizing atmosphere strongly aggravates the effects of heat treatment in CNT/CNF coated samples.

#### 1.3.2.2.2 Potentiostatic tests

The electrochemical behavior was further characterized by performing potentiostatic experiments, see Fig. 1.21, under conditions similar to those used to simulate anodic and cathodic environments in polymer electrolyte

fuel cells, i.e., in 1 M  $\text{H}_2\text{SO}_4 + 2$  ppm HF electrolyte, saturated with  $\text{H}_2$  or  $\text{O}_2$  and at  $-0.1$  V or  $0.6$  V vs. SCE, respectively, at  $80^\circ\text{C}$ . For the sake of brevity, these will be referred to in the following as anodic and cathodic conditions or environment.

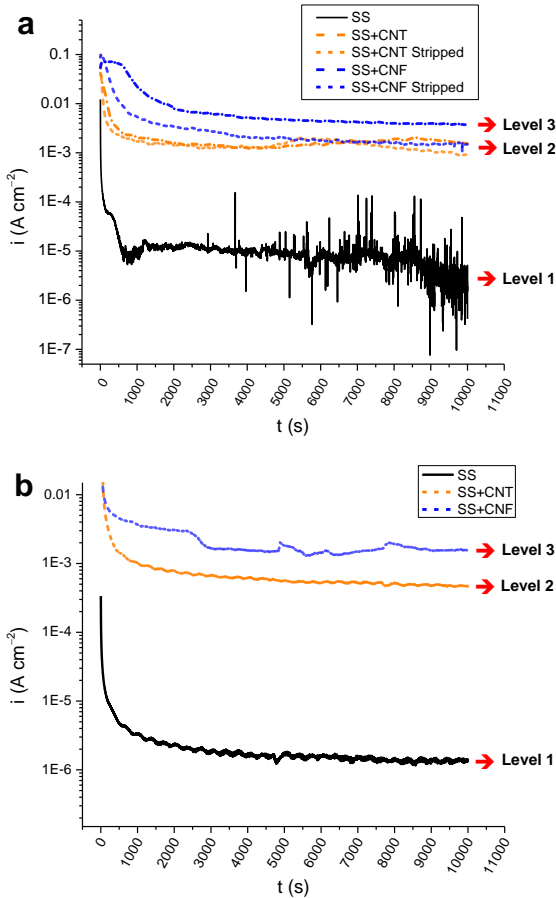


Fig. 1.21 Potentiostatic curves of 316 SS, 316 SS+CNT and 316 SS+CNF samples in 1 M  $\text{H}_2\text{SO}_4 + 2$  ppm HF solution at  $80^\circ\text{C}$ , (a) saturated with  $\text{H}_2$ , at  $-0.1$  V vs. SCE, and (b) saturated with  $\text{O}_2$ , at  $0.6$  V vs. SCE.

The results of the potentiostatic test under anodic conditions are presented in Fig. 1.21 (a), also for a stripped sample along with bare stainless steel, and CNT or CNF coated 316 SS samples. The anodic c.d. of the bare 316 SS decays rapidly at the beginning reaching a value in the range of  $10^{-5}$  A  $\text{cm}^{-2}$  after 1000 s. A steady state is then established, followed by a slow gradual decrease of the c.d. through an oscillating behavior and a faster reduction after about 10000 s, when the c.d. decreases down to about  $10^{-6}$  A  $\text{cm}^{-2}$  (level 1 in Fig. 1.21). CNT or CNF coated samples, as well as the corresponding so-called stripped samples, show c.d. almost three orders of magnitude higher, in the range of  $10^{-3}$  A  $\text{cm}^{-2}$ , with minor but significant differences. Namely, two different levels of dissolution c.d. can be observed: for the CNT coated and stripped samples (level 2 in Fig. 1.21); and for the CNF coated sample (level 3 in Fig. 1.21).

Fig. 1.21 (b) shows the results of potentiostatic tests for the cathodic environment. The general behavior of the samples is similar to that observed in the anodic environment, meaning that there are three different levels of c.d., the lowest referring to pristine 316 SS (in the range of  $10^{-6}$  A  $\text{cm}^{-2}$ ), and orders of magnitude higher values for both coated samples. The highest c.d., about  $2 \times 10^{-3}$  A  $\text{cm}^{-2}$ , is found for the CNF on 316 SS sample (level 3), while the CNT on 316 SS sample stands somewhat lower at about  $5 \times 10^{-4}$  A  $\text{cm}^{-2}$  (level 2). SS-NH samples subjected to potentiostatic tests (not shown here) confirmed the behavior revealed by the potentiodynamic polarization; namely, a steady dissolution c.d. of about  $1.5 \times 10^{-5}$  A  $\text{cm}^{-2}$  and  $8.0 \times 10^{-5}$  A  $\text{cm}^{-2}$ , respectively under the conditions simulating the cathodic and anodic environment, was observed for the SS-NH sample.

### 1.3.2.3 *Microstructural characterization after corrosion tests*

The effects of potentiostatic polarization tests were looked into by performing XRD and SEM characterization of the samples. XRD patterns of as-prepared and stripped CNT and CNF samples on 316 SS after testing under anodic conditions are collected in the graph of Fig. 1.22.

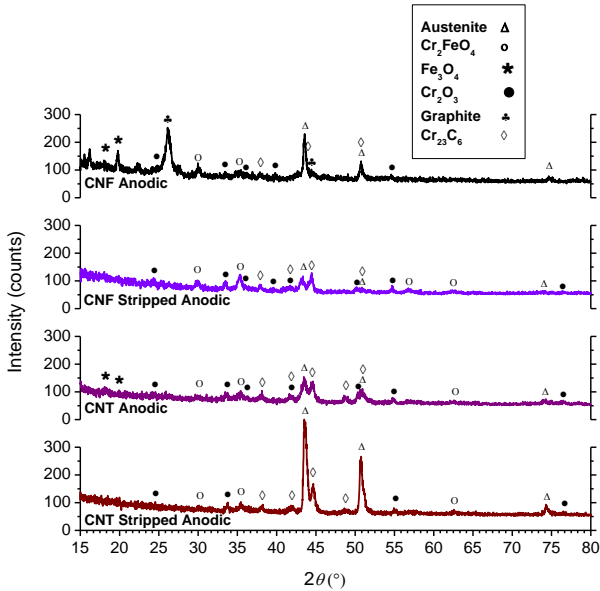


Fig. 1.22 XRD patterns of corroded samples.

CNF sample which had the maximum amount of filamentous carbon shows depressed peaks of graphite even after corrosion, which means that in some areas the CNF carpet still remains on the surface. The CNT sample, however, seems to have lost almost the entire CNT layer. Furthermore, XRD results indicate that oxides (typically  $\text{Cr}_2\text{O}_3$  and  $\text{Fe}_3\text{O}_4$ ) formed at the surface of all these samples. Apparently, the oxidation was stronger on the unstripped CNF corroded sample, particularly due to formation of  $\text{Fe}_3\text{O}_4$ . Significantly, the  $\text{Fe}_3\text{C}$  phase disappeared after anodic testing, suggesting the formation of iron oxide by dissociation of the carbide under the aggressive corrosion conditions [130]. In support of the latter view is the observation that only CNF samples showed clear evidence of the presence of  $\text{Fe}_3\text{C}$ . Besides, since the  $\text{Fe}_3\text{O}_4$  was found only on the surface of unstripped samples, the  $\text{Fe}_3\text{C}$  source responsible for its formation had to be already present in the CNF layer.

In the light of the XRD results of corroded samples, the behavior observed under potentiostatic polarization can be explained in more detail. The about three orders of magnitude increase of the c.d. (so called level 2) compared to pristine 316 SS (level 1) is mostly related to the effect of the carburization of the steel substrate on its corrosion resistance. Further evidence in this respect is given in the following section. A further increase in the dissolution c.d. (level 3) is mainly caused by the oxidation of the  $\text{Fe}_3\text{C}$  incorporated in the CNF layer over the 316 SS substrate. Though the presence of oxidizable particles in the CNT layer cannot be ruled out, it is reasonably assumed, according to SEM results (Fig. 1.17 (a)), that their overall mass, and consequently their contribution to the c.d. during potentiostatic tests, was negligible. Accordingly, the c.d. for CNT sample corrosion remains at level 2 and only CNF sample with a significant amount of iron carbide and possibly metal particles trapped in the layer (Fig. 1.17 (b)) will show higher c.d. (level 3).

SEM micrographs of 316 SS after potentiostatic test in simulated anodic environment are shown in Fig. 1.23. Although strong, the electrochemical attack was homogeneous and uniform all over the surface and local deep attacks could not be observed.

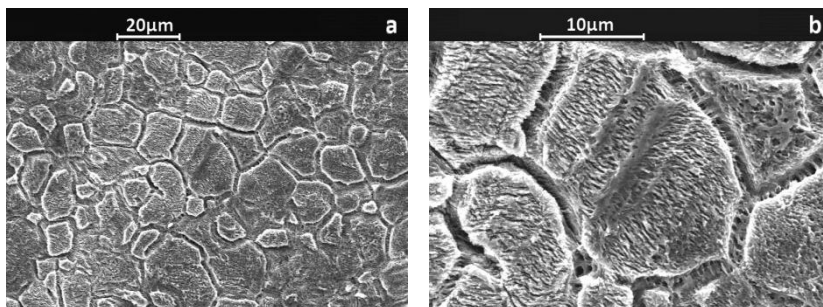
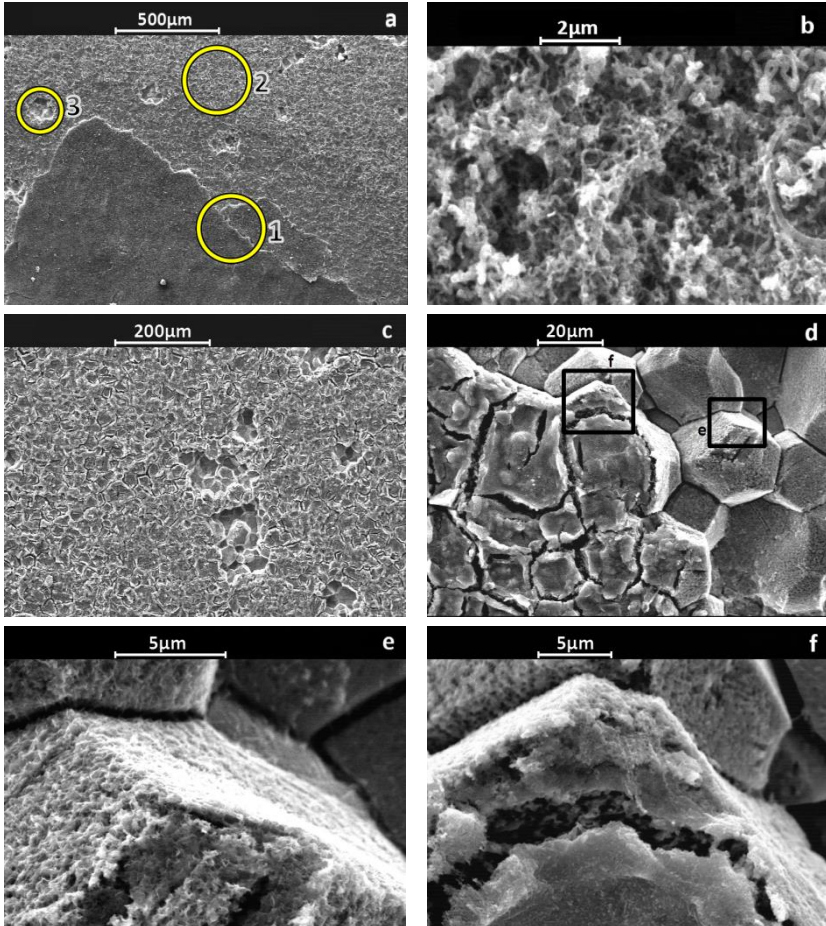


Fig. 1.23 (a) SEM micrograph of 316 SS after 10000 s potentiostatic test under anodic environment conditions, (b) higher magnification of (a).

Fig. 1.24 shows the SEM micrographs of CNT on 316 SS after 10000 s potentiostatic corrosion test under the anodic environment conditions.



**Fig. 1.24** SEM micrographs of “CNT on 316 SS” sample after 10000 s potentiostatic corrosion test under the anodic environment conditions showing three different zones and different magnifications of each zone.

Fig. 1.24 (a) shows a general view of the surface of the sample with three different areas highlighted: in area 1, the boundary between corroded and uncorroded regions; in area 2, the surface of the substrate beneath the CNT layer; in area 3, a severely damaged region with evidence of penetrating intergranular attack and grain removal from the substrate. From the

magnified view of area 1 in Fig. 1.24 (b), the accumulation of corrosion products within the CNT layer is apparent. The substrate beneath the CNT layer (area 2, shown in Fig. 1.24 (c)) exhibits obvious features due to preferential attack at grain boundary and in fact, locally, grain removal. A magnified view of area 3 is shown in Fig. 1.24 (d), with highlighted regions “e” and “f” presented in Fig. 1.24 (e) and (f), respectively. The presence of a layer of corrosion products can be noticed on the surface of the grains, within the area where grain removal has not occurred yet (like the one marked as “f” in Fig. 1.24 (d)). This is a porous and relatively thick layer apparently enveloping the grains, thus allowing for a comparatively faster intergranular attack and the ensuing grain removal. Besides, this film, which forms below the CNT layer, is likely responsible for the loss of adhesion of the CNT layer and its progressive detachment from the surface. The appearance of the grains in the damaged area (like the one marked as “e” in Fig. 1.24 (d)) can be understood as a result of the relatively slow formation of the surface layer following the detachment of grains.

Fig. 1.25 shows the SEM micrographs of a CNF sample after 10000 s potentiostatic corrosion test under the anodic environment conditions. As can be seen in Fig. 1.25 (a), the three regions characterizing the effects of corrosion on the CNT sample are present also in this sample. However, an extra layer marked as “0” is noticed here which did not form in the case of CNT coated sample. This layer, which appears rather thick and exhibits a kind of spongy morphology, is therefore a type of corrosion product only found over the CNF layer. Magnified view of this region (Fig. 1.25 (b)) shows individual grains obviously removed from the stainless steel substrate and trapped within the layer. Referring to the large number and size of the nanoparticles present in CNF and absent in CNT samples, it is quite likely that layer 0 is formed by oxidation of those particles. Fig. 1.25 (c) shows the CNF layer (layer 1) below the topmost corrosion products

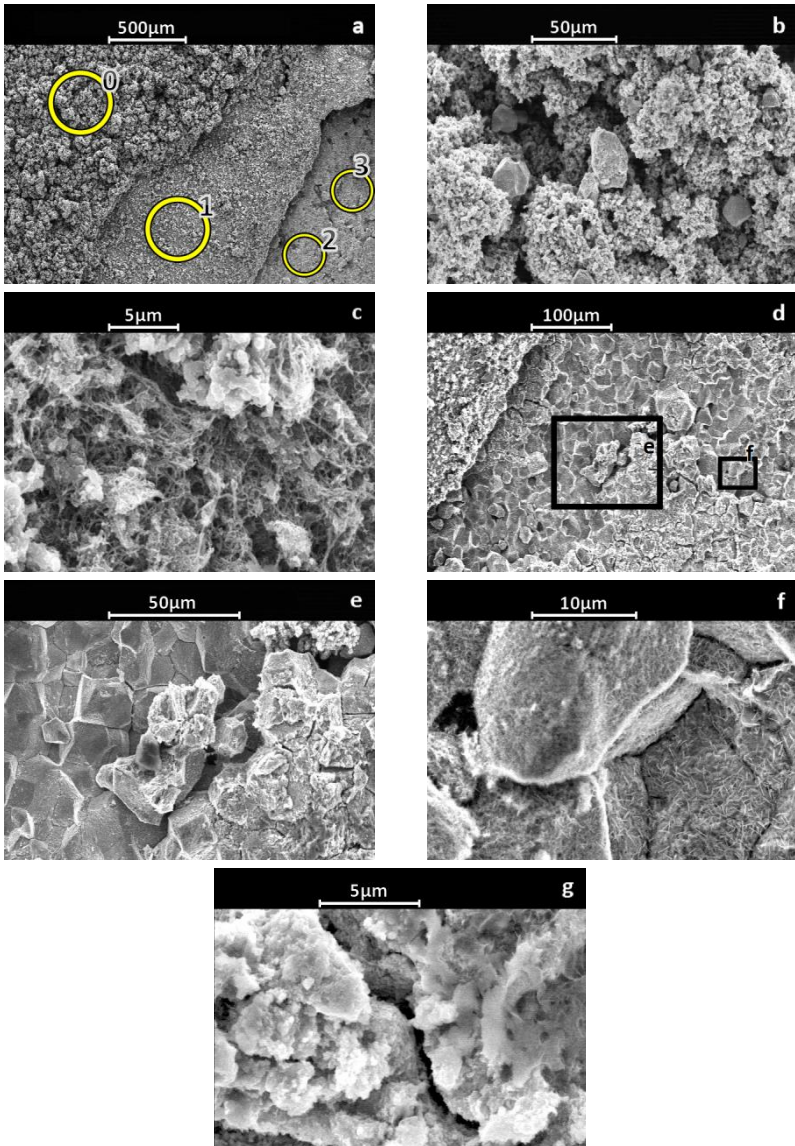
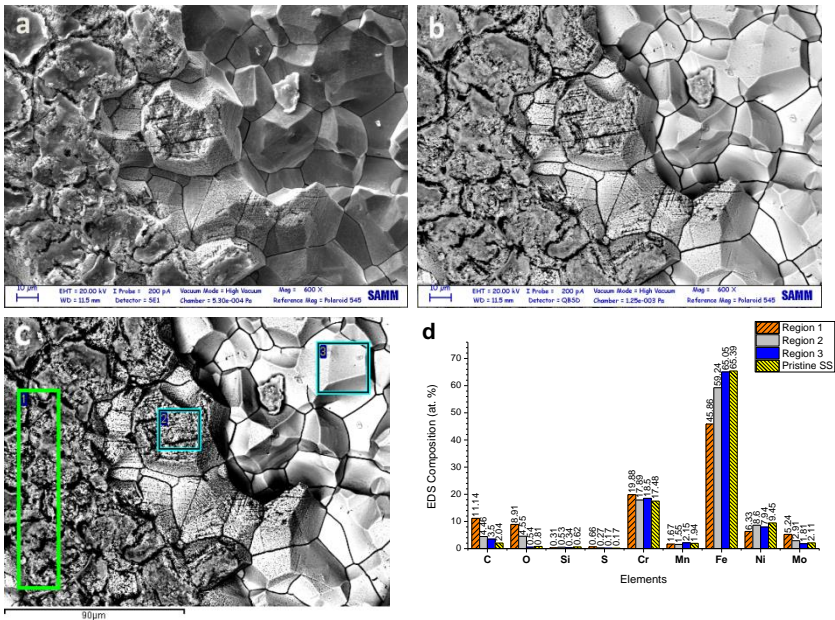


Fig. 1.25 SEM micrographs of “CNF on 316 SS” sample after 10000 s potentiostatic corrosion test under the anodic environment conditions showing four different zones and different magnifications of each zone.

(layer 0). The substrate beneath the CNF carpet is seen in Fig. 1.25 (d) in which grain removal and surface oxidation can be recognized. The area marked as “e” in this image shows an already detached group of grains which are magnified in Fig. 1.25 (e). The region marked as “f” in Fig. 1.25 (d) concentrates on a sub-layer beneath the removed grains (area 3) and, as can be seen in the magnified view (Fig. 1.25 (f)), it possesses a cleaner surface compared to the primary layer right below the CNF carpet. However, surface oxidation and formation of feather like oxides on this sub-layer is obvious. Finally, the corrosion products formed on the primary surface beneath the CNF carpet (Fig. 1.25 (g)) shows similar characteristics to the same area (i.e., area 2) of CNT sample.

In order to confirm the hypothesis pointed out above, a detailed microstructural analysis was also conducted on one of the stripped samples after potentiostatic test. Fig. 1.26 shows the SEM micrographs of a CNT sample, stripped and subjected to potentiostatic corrosion test during a duration of 10000 s, under the anodic environment conditions. Both images of secondary and back-scattered electrons (Fig. 1.26 (a and b), respectively) reveal the same features as observed in Fig. 1.24 and Fig. 1.25 for regular samples. Darker areas in Fig. 1.26 (b) suggest the formation of oxides. For a more precise evaluation of elements distribution, EDS analyses were conducted in three zones as indicated in Fig. 1.26 (c). Zone 1 is the top layer of corrosion products formed on the surface that was marked as area 2 in Fig. 1.24 and Fig. 1.25. Zone 2 indicates a region where the corrosion film of zone 1 was removed but not the grains. Zone 3 represents a region where the topmost layer of grains was removed and grains from the sub-surface layers are appearing (area 3 in Fig. 1.24 and Fig. 1.25). Fig. 1.26 (d) shows the EDS analysis results for elemental distribution of these three regions. As expected, region 1 shows the highest contents of chromium, carbon and oxygen and the lowest iron content. These results, accompanied by the

information provided from XRD patterns, suggest that this layer is mainly composed of iron and chromium oxides. Moreover, the relatively high carbon content detected by EDS in combination with the identification of  $\text{Cr}_{23}\text{C}_6$  peaks in XRD patterns, demonstrates the presence of chromium carbide in this region. Region 2 shows a much lower carbon content while the oxygen is still high, suggesting that oxidation is still considerable in this region. Region 3, which stands for the sub-layer beneath the removed grains, shows the lowest oxygen and highest iron content demonstrating the gradual decrease in oxidation intensity toward the depth of the sample. As a further remark, it is noted that the carbon content is not much decreased compared to region 2 as an indication of its penetration into the steel.



**Fig. 1.26** SEM micrographs of 316 SS+CNT stripped sample after 10000 s of potentiostatic corrosion test under the anodic environment conditions. (a) Secondary electron mode, (b) back scattered mode, (c) point analysis locations and (d) EDS results at three different zones, compared to pristine 316 SS.

To further assess the type and intensity of the corrosion attack, the stripped CNT sample was sectioned before and after anodic potentiostatic test,

mounted and etched with Nital 2% and subjected to SEM and EDS analysis. Since 316 SS cannot be etched with Nital 2% in normal condition, any probable etching would be a sign of carbide compounds formation. Fig. 1.27 (a) shows the cross section SEM micrograph of the uncorroded, Nital etched sample which reveals a grain boundary etching down to the depth of about 50  $\mu\text{m}$ . Fig. 1.27 (b) shows the sample after potentiostatic test without metallographic etching. It is seen that the characteristics of intergranular corrosion including boundaries dissolution and grain removal are all present.

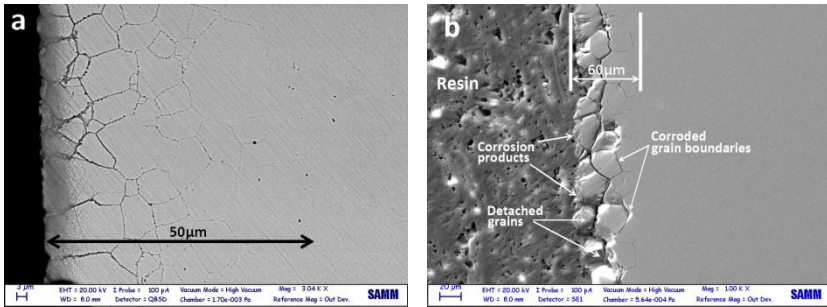


**Fig. 1.27 SEM micrographs of cross sectioned stripped 316 SS+CNT samples (a) etched with Nital 2% before corrosion test and (b) without etching after 10000 s of potentiostatic corrosion test under the anodic environment conditions.**

Fig. 1.28 shows the etched cross section of a stripped CNT sample before corrosion test. As it can be seen in Fig. 1.28 (a), a lamellar microstructure formed in the grain boundaries near the surface. To assess the elemental characteristics of this microstructure, a line scan was performed from point A to B intersecting the lamellar structure. The results are presented in Fig. 1.28 (b) showing a local modest increase in the chromium content and a decrease in the iron content with considerable and almost constant carbon content inside and outside the grain boundary. These observations reinforce the speculation that due to a sensitization like phenomenon, chromium carbide has been formed in the grain boundaries with a lamellar structure resulting in localized and accelerated corrosion.

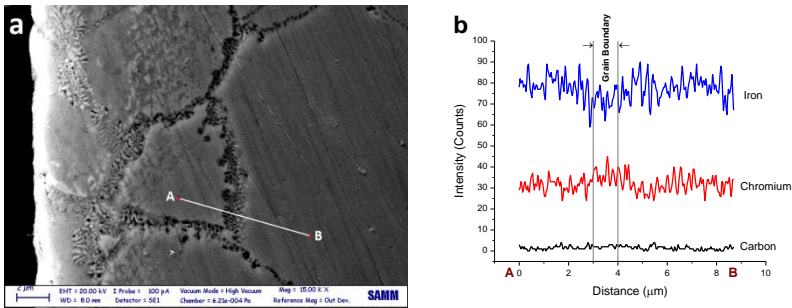


**Fig. 1.28** (a) SEM micrograph of an etched (Nital 2%) cross section of a stripped CNT sample before corrosion test and (b) EDS line scan results from point A to point B.

According to the results of the above discussed microstructural observations, it can be concluded that during the CNT/CNF synthesis process, the topmost surface layer of the stainless steel substrate undergoes carbon saturation and probably carbide formation leading to CNT/CNF growth on supersaturated sites [71,98]. However, carbon can diffuse quite deep in the bulk and, of course, this diffusion would be accelerated through shortcut paths, namely, grain boundaries. These high carbon content regions would encourage chromium carbide formation in specific areas such as grain boundaries during cooling down in a quite similar way to what happens during sensitization of austenitic stainless steels [129]. Consequently, the areas depleted from chromium due to carbide formation will lose their corrosion resistance and will undergo rapid attack. Grain boundaries as the most likely places for chromium carbide precipitation would experience the fastest corrosion rate resulting in intergranular corrosion and grain removal [131–134]. This kind of strong corrosion can be acknowledged as responsible for the large difference between dissolution c.d. of levels 1 and 2 in potentiostatic curves (Fig. 1.21). Since level 1 represents the corrosion rate of untreated 316 SS and level 2 represents the corrosion rate of carbon treated sample, the difference should be caused by “accelerated” intergranular corrosion. The dissolution c.d. of the sample heat treated in nitrogen, in the absence of carbonaceous gas, supposedly susceptible to normal sensitization of austenitic SS, lies well below so-

called level 2. Level 3 adds up the effects of both intergranular corrosion and oxidation of carbide and possibly metal particles trapped in the CNF layer.

## 1.4 Conclusion

Different types of filamentous carbon were grown directly on 316 SS without application of any external catalyst. Different pretreatment procedures were applied to the substrate surface and their effects on products were investigated. It was found that:

1- Type of filamentous carbon shows a direct relation to the size of surface nano-features formed as a result of each pretreatment. MWCNTs were the dominant products where the average size of nano-hills was below 60 nm. By increasing the average size above this level, the balance shifts in favor of CNFs. However, in any condition the final synthesized layer is a mixture of both and exclusive control over the type of the product is not trivial.

2- Since all of the samples experienced a reducing atmosphere heating step to arrive at the desired synthesis temperature and this heating step had certain effects on the arrangement of surface nano-features, the influence of any pretreatment should be assessed in conjunction with subsequent impact of heating. Polishing, as an instance, largely removed the nanoscale surface features, which should supposedly result in growth suspension. However, considering the next step of reducing atmosphere heating, the effect of polishing is likely that of enlarging the surface nano-features and forming local plateaus which can be translated into larger CNF fraction in final product and some uncovered areas. The investigation of the underlying mechanism controlling the surface restructuring phenomenon revealed in the present work, calls for a devoted and in depth study focusing on the effects of environmental parameters, composition and microstructure of the steel substrate on the morphology evolution and surface chemical modifications during the pre-growth period of CNT\CNF.

3- Two different growth mechanisms, namely base growth and tip growth modes, were observed. Base growth mode was originated from the catalysts

nano-hills formed on the surface due to pretreatment steps. A quasi-liquid or semi-crystalline state of catalyst was found to have been active in this case. Tip growth mode was inferred to be caused by surface break-up associated with type II dusting mechanism followed by filamentous carbon growth on catalytically active removed particles, i.e., type IV dusting mechanism, according to the classification of metal dusting mechanisms proposed by [110]. Increasing the growth time was found to increase the number of the walls of MWCNTs, to increase the CNF percentage, and to decrease the uncovered areas due to prolonged surface break-up.

4- Compositional changes made by etching pretreatment did not seem to have a negative effect on CNT/CNF synthesis since chemical attack did not degrade the main catalytic element of 316 SS, iron. Rather, main effect of etching followed by controlled heating should be considered as the formation of a bimodal distribution of lateral size of nano-hills on the surface resulting in degradation of filamentous carbon synthesis. Shorter etching times (5 min compared to 10 min) resulted in larger average sizes in both of the frequency peaks of the lateral size distribution and therefore, resulted in larger uncovered areas and larger CNF contributions. It is anticipated that applying different etching times or trying different etchant compositions followed by adequate heating cycle, proper nanostructured stainless steel surfaces can be created for controlled growth of CNT.

5- Oxidation-reduction pretreatment brought about surface nano-features with an average lateral size larger than 100 nm resulting in dominant CNF growth. Full coverage of carbon filaments accompanied by pronounced presence of relatively large particles on tips of CNFs reinforce the idea of strong surface break-up and tip growth mode. Therefore, the high potential of oxidation-reduction pretreatment for amplification of surface break-up should be concluded.

Furthermore, the corrosion behavior of the prepared materials was investigated under simulated anodic and cathodic working conditions of BPs of PEMFCs. Based on the electrochemical and microstructural results, general corrosion behavior of such materials can be summarized as follows:

1- Potentiodynamic results show similar free corrosion potential for 316 SS, 316 SS+CNT and 316 SS+CNF samples confirming that the porous carbon layers cannot provide a barrier type protection. The three samples, 316 SS, 316 SS+CNT and 316 SS+CNF, showed corrosion current density of about  $5.0 \times 10^{-4}$ ,  $15 \times 10^{-4}$  and  $20 \times 10^{-4}$  A cm<sup>-2</sup>, respectively.

2- Potentiostatic results showed three different levels of stabilized dissolution c.d., the lowest of which (level 1) was for pristine 316 SS. First increase in dissolution c.d. (to level 2) was related to the activation of intergranular corrosion; the final increase in the dissolution c.d. (level 3) observed only in 316 SS+CNF sample was related to the oxidation of large catalyst particles on the tips of CNFs.

3- Based on XRD, SEM and EDS results, corrosion products are mainly chromium and iron oxides. Iron carbide formed during CNF synthesis, and possibly also during CNT synthesis, though to a much minor extent, appears to undergo dissociation under strong acidic attack resulting in the oxidation of iron. On the other hand, chromium carbide formed during CNT/CNF synthesis seems to be stable, and can be observed in the XRD patterns after corrosion.

According to all above, it is concluded that the application of CNT or CNF coatings on sensitizable stainless steel by CVD direct growth method is not beneficial in terms of corrosion resistance. Since no evidence was observed suggesting the presence of a passive film, application of high temperature carbon coatings could be risky even for dense and non-porous layers especially for portable and transportation applications which are subject to mechanical shock and possible coating damage. Investigations on the growth of CNTs on heat resistant stainless steels such as high chromium content grade 310 and duplex stainless steels or stabilized grades 347 and 321 should be considered as a future research direction, to face the risk of severe damage of the base material due to carburization. Grade 310 or duplex stainless steel with high chromium content and consequently lower likelihood of grain boundary chromium depletion are supposed to provide better resistance against sensitization [135–137]. Moreover, stabilized grades 347 and 321 with strong carbide forming additives such as titanium,

niobium, or tantalum, could further reduce the risk of sensitization and intergranular corrosion [138].

## **2 Carbon nanostructures as catalyst support of fuel cells**

### **2.1 Introduction**

#### **2.1.1 Fuel cells and materials challenges**

Fuel cells, as alternative energy sources for traditional methods based on fossil fuels, are attracting progressive attention by the start of the 21<sup>st</sup> century, not only due to worrisome diminution of the energy resources along with the increasing energy demand worldwide [139], but also with regard to the environmental concerns reaching a warning limit based on the international reports on the greenhouse gases emission and concentration [140]. Although the initial reports on the operation of the hydrogen fuel cells date back to 175 years ago in the work of William Robert Grove [141], serious attention to the competence of this technology for the real world applications did not arouse until the second half of the 20<sup>th</sup> century when the world space programs relied on fuel cell power for the first manned spaceflights.

The basic principle of fuel cell operation is not complex. The chemical energy of a fuel, in particular hydrogen in varieties of hydrogen fuel cells, and an oxidant (oxygen), is electrochemically converted into electricity and heat along the water formation reaction. In practice however, accomplishment of this “simple” reaction is facing serious difficulties. The cost associated with the preparation of the catalyst that is mainly made of precious metals from one hand [142–146] and the durability of the entire electrochemical system from the other hand [147–149], put the main obstacles on the easy industrial use of this technology. As can be

understood by research communities of the field, establishment of pathways to address both problems are mainly associated with development of appropriate materials or manufacturing routes that would enable the cost of electricity to compete with the existing technology.

Concentrating on the “heart of the fuel cell” where the core electrochemical reactions take place and the electrocatalytic current is generated, namely, the catalyst, each of the mentioned problems has been tried to be addressed through a series of materials based strategies ranging from the catalyst species, state, size, morphology, distribution and amount to the catalyst environment including the support type and its interactions with the catalyst, humidity, temperature, working potential and many other parameters. Regarding the focus of this work, the importance and varieties of support materials will be discussed here.

In search for solutions to reduce the precious metal catalyst content of a fuel cell, one of the most obvious methods has conventionally been the increase of the specific surface area of the catalyst by spreading it over a conductive support in the form of fine particles. Supported catalysts not only possess a higher specific surface area, but also benefit from the “stabilization” provided by their attachment to the support. This way, access to a much larger number of catalytically active yet stable sites is provided compared to the corresponding bulk metal, even when the latter is ground to a fine powder [150].

Electrocatalysts for fuel cells are commonly supported on certain materials with special features. The critical requirements for the ideal support include but are not limited to: a) high electrical conductivity, b) large surface area, c) good electrochemical stability and corrosion resistance in the fuel cell environment and d) strong attachment to and interaction with the catalyst, e) ease of the recovery of the precious catalyst in the used support and f) water management capabilities to forbear flooding.

### **2.1.2 Support materials**

Regarding the requirements mentioned for the catalyst support, a wide range of candidates have been proposed and studied by the researchers.

Through various possible classifications for these materials, there is a good agreement on a division based on the presence of carbon family in the support [151,152]. On this basis, two broad groups are considered: a) carbonaceous supports and b) non-carbonaceous supports. This classification is mainly influenced by the evolution history of support materials and the great contribution of carbon family in that process.

### **2.1.2.1 Carbonaceous supports**

It can be said with confidence that carbon, as a material, plays the most pronounced role in different components of a fuel cell, from bipolar plates and gas diffusion layers to catalyst support, catalyst itself and even as a fuel [153]. Regarding the support materials, carbon has been used for many years as a support for industrial precious metal catalysts [150,154], and activated carbon, carbon black, graphite and graphitized materials have all been applied in various catalytic processes. Along the good electrical conductivity that is an obvious benefit, stability of carbon in both highly acidic and basic media is a great advantage over other frequently used supports such as metal oxides and carbides. Moreover, when the turn comes to recover the active precious metal, carbon can be burnt off without difficulty and with minimum environmental and ecological concerns [153].

#### **2.1.2.1.1 Carbon blacks and graphite materials**

Carbon black (also called furnace black if prepared by oil-furnace processes, like Vulcan XC-72, and acetylene black if prepared via acetylene processes, like Denka Black) is a material manufactured by the pyrolysis or incomplete combustion of hydrocarbons and petroleum products. In terms of crystallinity, this material is a paracrystalline carbon, meaning that it possesses a short or medium range ordering in its lattice but lacking long-range ordering. Compared to a graphite perfect single crystal with long range ordering, carbon black is in the form of turbostratic graphite. This form of carbon looks very similar to graphite except that, although there may be some degree of perfection within the planes, the adjacent planes are out of registry with one another and basal planes have slipped out of alignment. That is, in the hexagonal graphite structure, there is an atom in each adjacent plane that sits directly over the center of the hexagonal ring.

In turbostratic graphite, the adjacent planes are shifted with respect to one another and are out of registry. This results in an increase in the interlayer spacing, which can increase from 0.3354 nm (for perfect graphite) to more than 0.345 nm. Heating to temperatures in excess of 2800 K provides energy for mobility and can convert turbostratic graphite to single crystal graphite in a process called graphitization [155]. In Fig. 2.1, the typical near-spherical morphology of carbon black particles, usually <50nm in diameter, is shown. The source material and the process of its thermal decomposition largely determine the morphology and particle size distribution of carbon black. Accordingly, the surface area of this material can vary from 50 to 1500 m<sup>2</sup>g<sup>-1</sup> and can satisfy the requirements of the fuel cell catalyst support in this respect. The most popular support material is Vulcan XC-72 carbon black with a surface area of 250 m<sup>2</sup>g<sup>-1</sup> [151,152].

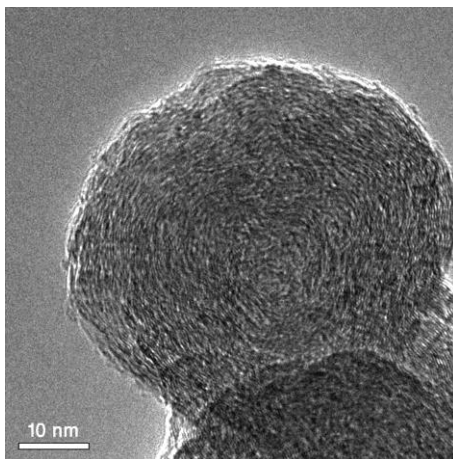


Fig. 2.1 Primary particle of carbon black. (Grivei, E., TIMCAL Belgium)

Due to its low cost and high availability carbon black has been widely used and studied as a cost effective catalyst support for the fuel cell [156–165]. Most of these works have been devoted to the effect of carbon black characteristics on the dispersion of supported metals and on their electrocatalytic activity. Depending on the synthesis method used to decorate the support with catalyst particles, either impregnation or colloidal

method, different support characteristics have influenced the morphology, distribution and electrocatalytic activity of the catalyst. By the former mechanism, uniformly impregnated catalysts are available because an equilibrium between adsorbed and free ions exists and diffusion into the core of each individual support particle can occur. The latter mechanism can give rise to egg-shell distribution. The colloid particles adsorb on the external surface of the support particles and in their macropores. Owing to the size of the colloid particles, the accessibility of the inner pores is very limited, leading to egg-shell distribution of the platinum [159]. In general, specific surface area, pore size distribution and surface properties of the carbon were recognized to play role on the mentioned properties of the catalyst. Platinum amount and distribution obtained by the impregnation method were found to be related to oxygen functional groups on the carbon surface, while in case of colloidal method, it depended on reaction conditions such as synthesis temperature, the surface-active agents used, and on the specific surface area of the carbon. In supports with low pore size, catalyst size and morphology showed the highest dependence on the preparation method (compared to low surface area ones) and above all, very low pore sizes ( $< 3$  nm) showed no effect on fuel cell performance. In fact, the ultimate effect of pore size and distribution was determined by a compromise between the accessibility of catalyst particles by the fuel through ionic conductive pathways, namely Nafion® ionomers, from one side and the availability of useful sites for diffusion and storage of the fuel from the other side. Since the size of Nafion® micelles ( $> 40$  nm) is larger than many recesses in the carbon black, metal nanoparticles (NPs) in pores with diameter lower than the micelle size are considered inaccessible to Nafion® and should show no contribution to the electrochemical activity. In contrast, those narrow pores (i.e., 3–8 nm which is in fact the lower band of the mesoporosity, i.e., 2–50 nm size) are useful for the fuel diffusion. The pores with size less than 3 nm no positive effect on fuel cell performance. This result indicates that, when the pore size is too small, supply of a fuel may not occur smoothly and the activity of the catalyst may be limited [159,166].

Another concern with the catalyst support, as mentioned earlier, is the electrical conductivity. When the conductivity becomes a critical issue,

conductivity shortage of carbon black can be addressed by moving towards higher degrees of graphitization of this material. Graphitized carbon black is another support material with high surface area that is obtained by recrystallization of the spherical carbon black particles at 2500–3000 °C. The partially recrystallized material possesses well-ordered domains. The degree of graphitization is determined by process temperature [166].

High surface area graphites (HSAG) that are prepared from graphitized materials by special mechanical modifications like grinding process, leading to less condensed graphite layers than usual and thus possession of higher surface area (around 100–300 m<sup>2</sup>g<sup>-1</sup>), are from the other graphitic materials of interest as catalyst support for fuel cells [167–171].

Finally, in spite of broad use of carbon black as catalyst–support, there are a number of problems with this material to be enumerated: a) self-agglomeration of the carbon particles that limits the approach of the fuel and oxidant to the active sites, and therefore the electrocatalyst efficiency of the fuel-cell electrode will be reduced, b) the presence of impurities such as organo-sulphur origination from the production method and precursor materials that can contaminate the fuel cell environment, c) large fraction of deep micropores (< 2 nm) trapping the catalyst NPs making them inaccessible to Nafion® ionomer and reactants and d) thermochemical instability of carbon black leading to accelerated corrosion of the support and consequently detachment of the catalyst particles.

Accordingly, serious need has been felt for new carbonaceous supports to cover the shortages of carbon black. Some of the results of these efforts will be following in the next sections.

#### 2.1.2.1.2 **Activated carbon**

Activated carbon (activated charcoal, activated coal, or carbo activatus) is a form of carbon that is processed in such a way to generate a large amount of small, low-volume pores in its structure and therefore, to increase the surface area available for adsorption or chemical reactions [172–174]. Two general methods are established for manufacturing activated carbon: chemical activation and physical activation [175]. Through these activation

processes, the primary imperfect pore structure of the precursor material is developed by controlled burn-off the tarry and non-graphitic part of carbon, leaving behind a porous network of highly disordered graphitic material bearing surface oxide groups. Fig. 2.2 shows a typical TEM micrograph of the activated carbon.

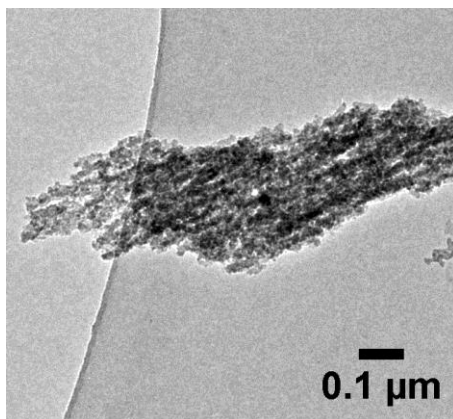


Fig. 2.2 Microstructure of activated carbon (Norit®)

Chemical activation is usually achieved by simultaneous carbonisation and activation of the raw material at 600–800 °C. The activating agent for this process, e.g.  $\text{H}_3\text{PO}_4$  or  $\text{ZnCl}_2$ , is incorporated into the raw material before heating starts. In this way, particularly wood-based activated carbons are made from sawdust. In contrast, Physically or so-called steam activated carbons are prepared from a precarbonised materials which are obtained by thermal decomposition of a carbonaceous precursor at 600–800 °C in the absence or under controlled admission of air. The activation step is usually performed in the presence of steam and/or  $\text{CO}_2$  at 800–1100 °C. Wood, coal, lignite, coconut shell and peat are the most important raw materials for the production of activated carbons, although other materials such as fruit pits, synthetic polymers or petroleum processing residues can also be used [150]. Finally, washing with pure water or acids may be carried out to remove the ash content and pore plugging materials. This becomes more important for applications like catalyst support where poisoning of the catalyst could be

critical, in addition to difficulties that a high ash content may bring about at the recovery stage of the catalyst from the used support.

Regarding the application of carbon materials as catalyst support in fuel cells, the most important feature or modification developed in activated carbon, is the introduction of surface functional groups to carbon. Although remarkable enhancement of the surface area and porosity is the main purpose of activation treatment, in the framework of catalyst support application, presence of functional groups could be considered even more important due to inclusion of a large fraction of the pores of activated carbon in the micro and lower band of meso size range.

In this respect, most of the works done on the activation of carbon, either starting from the original precursors (wood, peat, etc.) or doing the activation on carbon black or other preformed types of carbon, and whether using chemical [154,176–182] or physical [181,183,184] methods, are devoted to assessment of the effects of functional groups and surface chemistry of activated carbon. This aspect of the work will be reviewed in the section 2.1.3. Interactions between carbon support and catalyst.

### 2.1.2.1.3 *Mesoporous carbons*

Mesoporous carbon materials are defined as porous carbon materials whose pore size is in the range 2–50 nm. Mesoporous carbon materials can be classified into two categories according to their preparation methods and final structures as follows [185–189]: a) Ordered mesoporous carbon (OMC) and b) disordered mesoporous carbon (DOMC).

OMCs are synthesized by casting ordered mesoporous silica (OMS) templates or by direct templating triblock copolymer structures. The resulting mesopores are uniform and arranged periodically. Fig. 2.3 shows a typical microstructure of OMC.

DOMCs with irregular pore structure can be prepared through any of the following methods: thermal activation at high burn-off temperatures, catalytic activation using several metals or metal oxides and carbonization of mesoporous organic aerogels or polymer blends.

The general procedure for synthesis of these materials can be summarized as follows: a template with appropriate pore size and architecture is infiltrated with a carbon precursor (furfuryl alcohol, sucrose, acenaphthene and mesophase pitch, etc.), after which, the carbonization of the precursor is conducted followed by the template removal/dissolution. Obviously, if the primary template exhibits ordered three-dimensional pore structure, the resultant carbon will have ordered mesoporosity, otherwise disordered micro/mesoporous carbon will be formed.

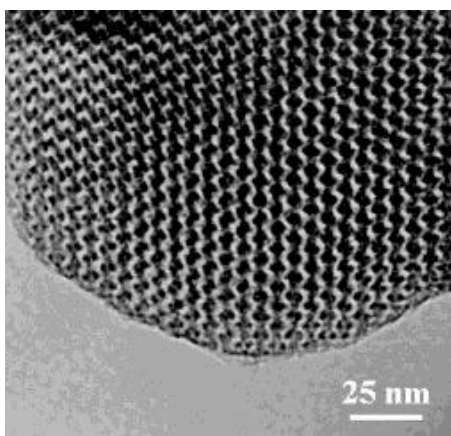


Fig. 2.3 Microstructure of ordered mesoporous carbon [187].

Generally, all OMC supported metals present higher metal dispersion and higher catalytic activity, both for oxygen reduction and methanol oxidation, than carbon black supported metals [190–195]. This has been attributed to the high surface area and uniform mesopore networks of OMC with lower amount or absence of micropores. In a mesoporous carbon supported catalyst, the metal catalyst particles are distributed and supported on the surface or in pores of the mesoporous carbon. A large mesopore surface area, particularly with pore size  $>20$  nm, gives rise to a high dispersion of Pt particles, which results in a large effective surface area of Pt with a high catalytic activity. The schematic shown in Fig. 2.4 represents the ideal pore size for easy access of the reactants to the catalyst while keeping the surface

area as high as possible [196]. Therefore, ordered 3-d pores of mesoporous carbons have been shown to improve the mass transport of reactants and products during fuel cell operation [193,196–198]. Possibility of synthesis of bi-metallic catalyst systems on OMC has also been demonstrated without problem [191,199–202].

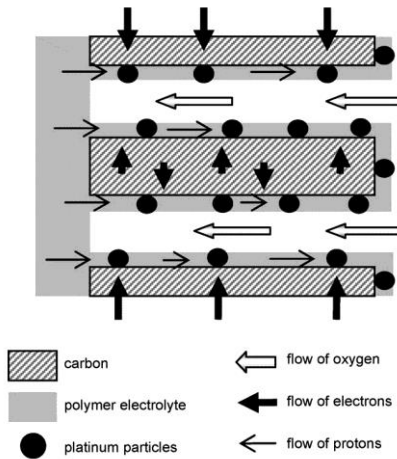


Fig. 2.4 The ideal pore size of OMC for easy access of the reactants to the catalyst [196].

Along with the advantages and positive points noted about OMC catalyst support, there are a number drawbacks mentioned in the literature, including its limited electrical conductivity due to the poor contribution of carbon connections among the rope-like particles [203]. Some researchers found out that this problem can be partially addressed by preparing a more graphitizable carbon at higher carbonization temperatures [203,204]. Another point worth mentioning is the low content of oxygen surface groups in this material, making the anchoring of the catalyst particles difficult. While functionalization can probably, introduce appropriate amount functional groups, the risk of disintegration of the ordered 3-d network of mesopores can be considered as a challenge [166].

#### 2.1.2.1.4 *Carbon fibers and nanofibers*

Carbon nanofibers and carbon nanotubes have been introduced properly in chapter 1 of this thesis. Accordingly, in this section we suffice to review the history and examples of application of these types of carbon as catalyst support for fuel cells.

Carbon fibers, either in micro or nano size and either as prepared or activated and functionalized, have been widely studied as support for metals in different applications [205,206].

Carbon fibers (CFs) that are distinguished from carbon nanofibers (CNFs) based on their diameter size, ranging from hundreds of nanometers to few micrometers, have relatively low surface area and hence, have rarely been studied as the catalyst support for fuel cells, where possession of a high surface area is a prerequisite. However, attention has been paid to the potential of this material after activation treatments. In this respect, CFs either in the form bundles of individual filaments or in the form woven cloths and felts, have undergone activation treatment for introduction of porosity, excess surface area and surface functional groups, making them alternative candidates for traditional catalyst supports of fuel cells. The earliest attempts to study the possibility of deposition of Pt particles on activated carbon fibers (ACFs) dates back to mid-ninety's and high reduction-adsorption capacity of ACF for Pt(IV) was concluded [207]. First studies on the application of such ACF as support for Pt in catalytic reactions appeared few year later [208,209]. Nevertheless, application of ACF as catalyst support for fuel cells did not happen before 21<sup>st</sup> century [210,211]. In general, good capacity for reduction of the metal ions and formation of strong bonding to catalyst particles, the flexibility of electrode and low resistance to flow of liquid and gases through a bundle of fibers in macro-scale are of the advantages mentioned for ACFs. However, the large fraction of micropores that is the characteristic of all activated carbons makes the mass transport issue and accessibility of the catalyst particles a challenge.

In contrast to CFs and AFCs, CNFs have received more attention as catalyst supports for fuel cells. One of the early attempts to use CNFs as a catalyst

support can be seen in the work of Rodriguez et al., where the catalytic activity of Fe-Cu particles supported on CNFs was studied with respect to hydrogenation of ethylene [212]. The degree of crystallinity of the support compared to traditional active carbon or alumina supports in addition to the possibility of strong interaction of metal crystallites with the crystalline support that might induce preferred crystallographic orientation of the particles was realized as the possible explanations for the superior activity of this catalyst-support system. Hoogenraad et al. also explored the viability of application of CNFs for liquid phase catalysis, hydrogenation of nitrobenzene [213,214]. In a series of works, Baker et al. studied the deposition of nickel onto the modified CNF for hydrogenation of light alkenes [215–217]. It was found that not only the activity but also the selectivity of nickel crystallites could be dramatically altered on CNFs compared to conventional supports. It was suggested that differences in the behavioral patterns of the catalyst systems are related to the modifications in metal particle morphological characteristics induced by the chemical and structural properties of the support materials.

The first reports of application of CNFs as catalyst supports for fuel cells was in 2001 [218,219]. In Bessel's work electrodes consisting of 5 wt % Pt supported on graphite nanofibers, which expose mainly edge sites to the reactants, were found to exhibit activities comparable to that displayed by about 25 wt% platinum on Vulcan carbon, with significantly less susceptibility to CO poisoning [218]. Steigerwalt et al. did the first studies on deposition of Pt-Ru bimetallic catalyst on CNFs for fuel cells [219,220]. Precursor composition and support structure were tuned in their work and it was concluded that a Pt-Ru/narrow tubular herringbone graphitic CNF nanocomposite shows the highest electrocatalytic performance. Comparative testing of their nanocomposite and an unsupported Pt-Ru colloid of similar surface area and catalyst particle size as anode catalysts in a working direct-methanol fuel cell (DMFC) revealed a 50% increase in performance for the Pt-Ru/GCNF nanocomposite.

Zhang et al. [221] prepared Pt/CNF catalyst through in situ polymerization acrylonitrile in a porous anodic aluminium oxide (AAO) template in presence of 1 wt%Pt(II) acetylacetonate [Pt(acac)<sub>2</sub>]. After removal of the

AAO template, the deposited Pt NPs had a reasonably low average size and a good dispersion showing a superior catalytic activity compared to that of Pt/C catalyst.

And from then, continuous work on different aspects of this material such as microstructural effects [222–224], functionalization effects [225,226] and many other parameters [227–230] on the catalyst activity and fuel cell performance have been carried out.

In general, CNFs proved advantages such good electrical conductivity and low mass transfer resistance. Microstructural features like availability of dangling bonds on the surface of CNFs, facilitates the anchoring of the catalyst particles and thus, a good dispersion. Moreover, the fact that the catalyst particles adopt specific crystallographic orientations when dispersed on the highly tailored graphitic nanofiber structures, allows for exposure of preferred catalyst orientation to the fuel cell environment by selecting the right CNF microstructure. However, drawbacks such as low surface area of CNFs can be considered as limits on this type of carbon support.

#### **2.1.2.1.5 Carbon nanotubes**

The earliest reports on application of CNTs as a catalyst support dates back to 1994 [231], just a few year after their discovery in 1991 [232]. In that work, Ru was supported on CNTs and was used as catalyst for liquid-phase cinnamaldehyde hydrogenation. Reports on possibility of using CNT as support for metallic catalyst continued to come out in the next years [233–235]. Nevertheless, the first report on the application of CNTs as catalyst support for fuel cells, was not published before 1998, in the work of Martin et al. [236], where an ensembles of aligned and monodisperse CNTs was prepared by a templating method that involved the chemical-vapour deposition of carbon within the pores of alumina membranes. The CNT array was then coated with NPs of electrocatalytic metals such as Pt and Pt/Ru alloys and used to electrocatalyse O<sub>2</sub> reduction and methanol oxidation. In 1999, an improved charge transfer at CNT based electrodes for fuel cells was demonstrated [237]. Then, a massive interest was attracted towards CNTs as support for catalyst by the start of 21<sup>st</sup> century as the few

following example reference can represent [162,230,238–248]. Currently, there are a couple of comprehensive reviews of the developments in CNT-supported catalysts for fuel cells including the various catalyst deposition techniques, electrocatalytic activity, functionalization and catalyst support interactions [151,152,166,206,242,249,250].

In most of the comparative studies of CNTs and carbon black as support for catalyst in fuel cells, a better activity of CNT support has been reported [210,238,239,243,251–260]. A number of reasons can be named for this among various reports in the literature that can in the meanwhile, be considered as the advantages of this support:

a) high conductivity of CNTs, due mainly to their crystalline nature [240], though, this good conductivity has a reverse relation with the degree of functionalization of CNTs [261].

b) efficient pore size and wide internal hollow channel facilitating the access of gasses and reactants to the support and catalyst [262].

c) a decreased hydrogen adsorption energy for Pt on the surface of CNT due to flat disposition of Pt crystallite caused by structural and chemical differences of CNTs with conventional carbon supports. This decreased hydrogen adsorption energy can be justified by a lowered d band center induced by the reduction of the Pt lattice constant, or by the charge transfer improvement from the anchoring sites of Pt to the support [258].

d) availability of specific sites (edge sites) on CNTs, due to their tubular architecture, on which, Pt crystallites will nucleate and anchor to the support. These sites are believed to be more active than the conventional equi-potential sites of carbon blacks [263].

e) the likelihood of presence preferred crystallographic orientations for anchoring of Pt to CNT and thus, presence of preferred crystallographic orientations to be exposed to the electrochemical environment that are more active, in particular, Pt (110) [254].

f) corrosion resistance of carbon nanotubes. Multilayer tubular structure of CNTs, with each layer being like a rolled up sheet of graphene with minimum number of dangling bonds and defects, makes the attack of

different oxidizing agents to this structure difficult [264,265]. Moreover, when attacked in corrosive environments, the damaged will be mainly limited to the external tubes in direct contact with the oxidants. Therefore, a primary relatively rapid attack can be expected on the outside shell especially onto the structural defects and available “edges”. However, any further advance of the corrosion front will be banned by the intact interior walls, that is difficult [266]. Furthermore, this electrochemical stability can be increased even more if a graphitization pretreatment has been done on CNTs [267].

Apart from these points that encourage the application of CNTs as the catalyst support, there are some concerns that impose cautions on the purely positive adjudication of CNTs. Some of these concerns will be discussed here.

The current technology of large scale synthesis of CNTs is not economic yet compared to conventional carbon blacks. Notwithstanding the remarkable costs reduction of mass production of CNTs in the recent years, development of more cost-effective methods is still a demand.

In addition, although various catalyst synthesis methods like impregnation and precipitation [240,268–270], polyol and microwave-assisted polyol process [230,271–281], sputter deposition [282,283], colloidal [269,284,285], ion-exchange [286] and electrochemical deposition [242,287,288] have been used to deposit the electrocatalyst NPs on CNTs for fuel cell applications, there is agreement on the intrinsic inertness of pristine CNTs that makes the anchoring of the catalyst to support difficult. Therefore, successful deposition of catalyst on CNTs is consistently believed to depend upon a functionalization treatment to introduce surface groups to support that serve as nucleation and anchoring sites for catalyst NPs. Regardless of the complexities that the functionalization treatment can add to entire procedure, it will necessarily result in the introduction of defects to the atomic structure of CNTs and consequently, will decrease the electrical conductivity of the CNTs, that was one the benefits of its application.

### 2.1.2.1.6 Carbon nanohorns, nano onions and nanocoils

Along with conventional carbon blacks and newer carbon family members such as CNTs, CNFs and graphene that have been extensively studied for application as catalyst support of fuel cells, there are other members that have yet to be explored more. Carbon nanohorns (CNHs) [289], carbon nanocoils (CNCs) [290], carbon nano-onions (CNOs) [291] are some examples of this latter group.

Carbon onions consist of spherical closed carbon shells and owe their name to the concentric layered structure resembling that of an onion. Carbon onions are sometimes called carbon nano-onions (CNOs) or onion-like carbon (OLC) [291]. One can also consider CNOs as multi-shell fullerenes [292]. Fig. 2.5 shows a real and a simulated nanostructure of CNOs.

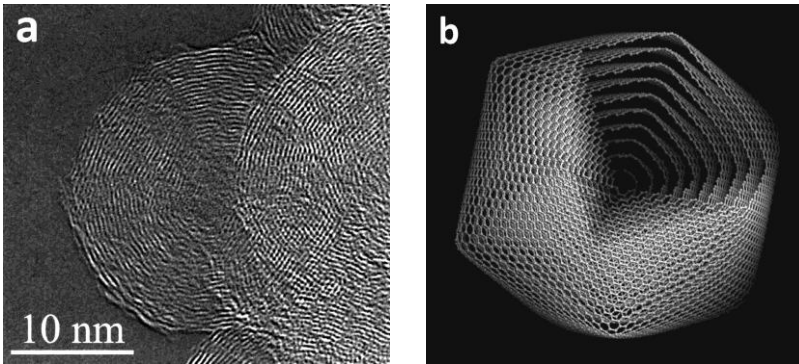
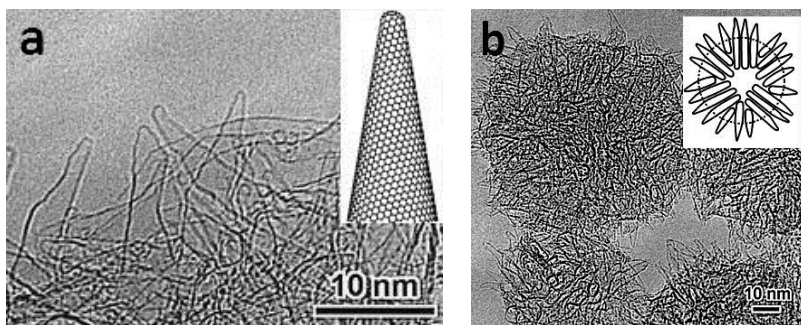


Fig. 2.5 (a) HRTEM images of CNOs produced by the arc discharge in water [293], (b) The icosahedral-quasicrystal-like model of an onion carbon particle constructed with the classical molecular dynamics technique [294].

The term carbon nanohorn was coined by Iijima and colleagues in 1999 to horn-shaped sheath aggregate of graphene sheets [295]. However, similar structures had been observed in 1994 by other researchers [296]. Carbon atom monolayers not only are stable as isolated objects (graphene), curved cylindrical geometries (nanotubes) or quasispherical geometries (fullerenes), but also there are intermediate states between a sheet and a fullerene, i.e., the carbon nanocone, wherein a single pentagonal ring or assembly of nearby pentagonal rings defines a conical apex, which is then

extended by a pure-hexagon graphenic network into a larger conical structure [289]. Fig. 2.6 shows the TEM micrographs of aggregated CNHs forming flower-like morphologies.



**Fig. 2.6** (a) A magnified TEM micrograph of CNOs with inset representing a simulated single CNH and (b) lower magnification of the same, showing an aggregate of CNHs making a “Duhlia”. Inset schematically showing the same [295].

The structure of a carbon nanocoil is similar to that of MWCNTs, except helical shape. It can be therefore said that a carbon nanocoil is a helical MWCNT. CNCs can be either in the form of fibers or tubes. Preparation of coiled carbon fibers was first reported by Motojima in 1991 by catalytic pyrolysis of acetylene [297]. The existence of helically coiled carbon nanotubes was first predicted by Ihara et al. and Dunlap in 1993 [298–300] and a few years later a Belgian research group reported their experimental observation [301]. Fig. 2.7 shows the TEM micrograph of a CNC with multi-walled tubular structure.

The studies on applicability of these materials as catalyst support for fuel cells is scattered and just few works are available about CNCs [302,303], CNHs [304,305] and CNOs [306–309] in this context. Although based on these few works, a good catalytic activity of the catalyst on these supports has been reported, it is better to avoid early affirmation on general superiority of these materials over conventional supports.

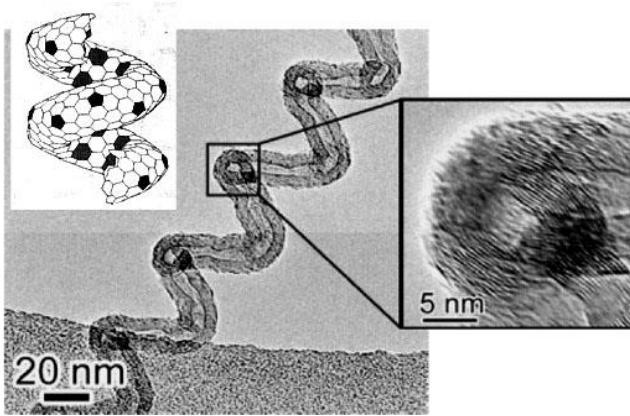


Fig. 2.7 TEM micrograph of a CNC with inset on right showing the multi-walled structure of the coil (from [310]) and the inset on left, showing a simulated model of the coil [298].

#### 2.1.2.1.7 Nanodiamonds and doped diamonds

The first production of nanoscale diamond particles took place by detonation in the USSR in the 1960s [311], but serious research work on them did not continue until the end of the 1980s [312,313]. A number of promising achievements starting from late 1990s however, put this material under the spotlight again. Preparation of colloidal suspensions of nanosized diamonds, application of fluorescent nanodiamonds for biomedical imaging, development of nanoscale magnetic sensors, discovery of the chemical reactivity of the surface of nanodiamonds were parts of these achievements [313].

Diamond, with  $sp^3$  hybridization of carbon atoms and a diamond cubic crystal structure, can also be formed in nanoscale. The term nanodiamond is referred to a broad range of diamonds consisting of facets less than 100 nm in size. However, a second term “ultrananocrystalline diamond” has been introduced to make the range narrower just referring to diamonds with grain sizes less than 10 nm. The morphological differences basically originate in the growth process. A wide range of synthesis methods have also been proved for nanodiamonds, including: detonation technique, laser ablation,

high-energy ball milling of high-pressure high-temperature (HPHT) diamond microcrystals, plasma-assisted chemical vapour deposition (CVD), autoclave synthesis from supercritical fluids, chlorination of carbides, ion irradiation of graphite, electron irradiation of carbon onions and ultrasound cavitation, with the first three of these methods being used commercially [313]. Fig. 2.8 (a) shows the TEM image of formation of a nanodiamond encapsulated within the shell of a CNO [314]. In Fig. 2.8 (b), the crystalline nature of the nanodiamond is shown in a HRTEM image.

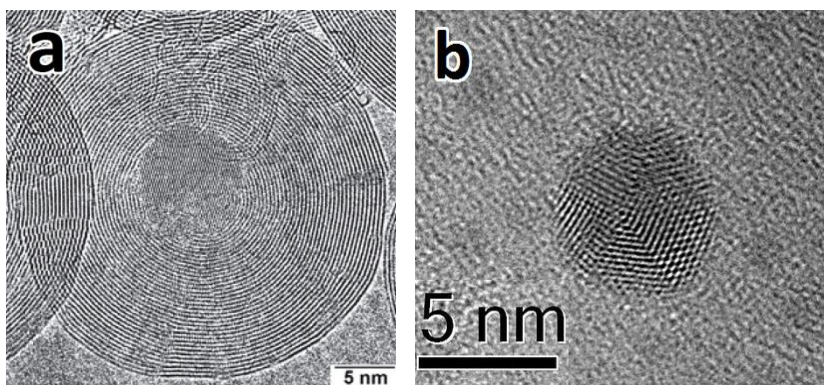


**Fig. 2.8 (a)** The conversion of a “carbon onion” (multi-walled concentric fullerene-like balls) into a diamond using particle beams. A growing diamond is seen inside concentric graphitic layers [314], **(b)** a nanodiamond crystal.

The  $sp^3$  hybridization present in bonding of carbon atoms of diamond, make it an electrical insulator incapable of being used in catalyst support of fuel cells, where the electrical conductivity is a necessity. However, different degrees of electrical conductivity can be given to diamond when doped with appropriate dopants. The common dopants include boron (for p-type) and phosphorous or nitrogen (for n-type). Intensive studies on electrochemical properties of boron-doped diamond (BDD) thin-film electrodes had started in 1990s [315,316]. By late 1990s and beginning of 21<sup>st</sup> century, fuel cell directed works started to appear based on nanodiamond catalyst supports [317–322]. Through those works as well as the more recent ones [323–332], a number of advantages of BDD catalyst support can be concluded. BDD

has a high electrochemical stability and corrosion resistance under acidic and alkaline conditions, good thermal stability, a wide electrochemical window in aqueous as well as non-aqueous media and finally, low and stable voltammetric and amperometric background currents.

Nonetheless, this support has also its own drawbacks without thinking about solutions for which, wide application of BDDs in fuel cells will remain unlikely. The most important concern is the electrical conductivity of this support. Although doping improves the conductivity of the diamonds, this will be at the expense of its stability. In fact, electrochemical stability that is the biggest advantage of BDDs, will deteriorate upon excessive doping with the intention of improving the conductivity. The other concern, is the strength of adhesion of the catalyst particle to the crystalline facets of the diamond. Actually, this can be translated to weak stability of the catalyst-support interaction, in contrast to high electrochemical stability of the support. Current researches have shown however, that this effect can be solved to some extent by reducing the size of support NPs.

#### **2.1.2.1.8 Graphene and reduced graphene oxide**

Graphene is the enabling material of the 21st century and there are high expectations for its potential applications. In just 10 years from its discovery [333,334], graphene has become a lodestar for researchers all over the world [335]. Moreover, the interest in two-dimensional, sheet-like or flake-like carbon forms has expanded beyond monolayer graphene to include related materials with significant variations in layer number, lateral dimension, rotational faulting, and chemical modification [336]. This interest has been so intense and the mass of the research carried out has been so remarkable that even a precise nomenclature in reference to different members of the family of “graphene materials” has become a concern. Accordingly, it is tried here to start this section with a precise definition and classification of this material, according to which, the rest of this work will be built up. All the definitions in this part are adopted from an editorial proposed nomenclature for two-dimensional carbon materials [336].

Graphene – a single-atom-thick sheet of hexagonally arranged,  $sp^2$ -bonded carbon atoms that is not an integral part of a carbon material, but is freely suspended or adhered on a foreign substrate. The lateral dimensions of graphene can vary from several nanometers to the macroscale. With this definition, other members of graphene family of 2D materials cannot be simply called “graphene” but must be named using a unique multi-word term that distinguishes them from the isolated monolayer.

Graphene layer – a single-atom-thick sheet of hexagonally arranged,  $sp^2$ -bonded carbon atoms occurring within a carbon material structure, regardless of whether that material structure has 3D order (graphitic) or not (turbostratic or rotationally faulted). The “graphene layer” is a conceptual structural unit that has been used for many years to describe the structure and texture of 3D carbon materials with primary  $sp^2$ -hybridized bonding.

Multi-layer graphene (MLG) – a 2D (sheet-like) material, either as a free-standing flake or substrate-bound coating, consisting of a small number (between 2 and about 10) of well-defined, countable, stacked graphene layers of extended lateral dimension.

Graphite nanoplates; graphite nanosheets; graphite nanoflakes – 2D graphite materials with ABA or ABCA stacking, and having a thickness and/or lateral dimension less than 100 nm. The use of nanoscale terminology here can be used to help distinguish these new ultrathin forms from conventional finely milled graphite powders, whose thickness is typically  $>100$  nm.

Graphene oxide (GO) – chemically modified graphene prepared by oxidation and exfoliation that is accompanied by extensive oxidative modification of the basal plane. Graphene oxide is a monolayer material with a high oxygen content, typically characterized by C/O atomic ratios less than 3.0 and typically closer to 2.0.

Graphite oxide – a bulk solid made by oxidation of graphite through processes that functionalize the basal planes and increase the interlayer spacing. Graphite oxide can be exfoliated in solution to form (monolayer) graphene oxide or partially exfoliated to form few-layer graphene oxide.

Reduced graphene oxide (RGO) – graphene oxide (as above) that has been reductively processed by chemical, thermal, microwave, photo-chemical, photo-thermal or microbial/bacterial methods to reduce its oxygen content.

Based on such attempts to define rational morphological descriptors for graphene family, structural characteristics of this family have also been classified by other scholars as shown briefly in Fig. 2.9 [335].

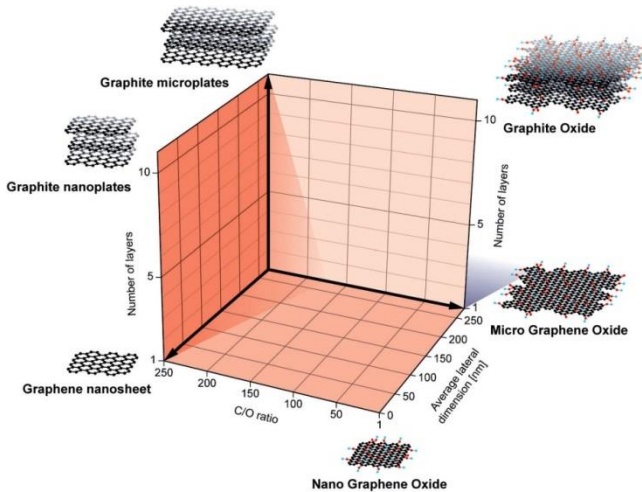


**Fig. 2.9** Classification grid for the categorization of different graphene types according to three fundamental properties: number of graphene layers, average lateral dimension, and atomic carbon/oxygen ratio [335].

In general, characteristics such as high conductivity, very fast electron transfer capabilities and large surface area propose graphene family as ideal materials for catalyst support of fuel cells. Appearance of the graphene family in the context of catalyst support materials for fuel cells started four years after its discovery in the works of Si [337] and Xu [338]. Interestingly, both these works have used the RGO and not graphene. This implies along with other things the potential difficulties of large scale production of high quality defect free graphene that is necessity for any industrial application. So far, various methods have been proposed for synthesis of graphene including exfoliation and cleavage (mechanical

[333,334,339], shear induced liquid phase [340], sonication induced liquid phase [341], wet ball milling [342] and porphyrin exfoliation [343]), CVD synthesis [344], arc discharge [345,346], epitaxial growth on electrically insulating surfaces such as SiC [347], un-zipping CNTs [348] and reduction of graphene oxide [349]. Although methods such as shear induced liquid phase exfoliation or arc discharge are claimed to be able to scale up the production of graphene, the majority of the literature of graphene family exploitation in fuel cell catalyst support is based on reduction of GO [337,338,350–354,354–363,363] along with a less intense interest on CVD method [364–367]. In contrast to defect free graphene synthesis methods, reduction of GO gives rise to a defective structure of graphene which behaves in a quite different way from the ideal graphene. Obviously, the scaled up production of graphene via reduction of GO is at the expense of perfectness of the atomic structure and crystallinity, that in turn, can be translated to a remarkably decreased electrical conductivity.

Overall, although graphene is still a relatively new material, the impact it has made in the fuel cell support materials is significant. The general output of exploitation of this material as the fuel cell support has been promising and has shown superiority in many aspects over other supports. Enhanced electrocatalytic activity toward oxygen reduction reaction (ORR) [353] and methanol oxidation reaction (MOR) [368], enhanced electrochemical active surface area (ECSA), higher CO poisoning tolerance [369], Enhanced durability [353,370], tunability of surface chemistry and functional groups through a variety of functionalization processes [371] and the possibility to be used as a metal-free fuel cell catalyst upon proper doping [364,372] are just some of the positive feedbacks found in the literature. Characteristics such as what comes in the following have been mentioned to be responsible for such improvements in their behavior:

- a) high surface area (theoretical specific surface area of  $2630 \text{ m}^2\text{g}^{-1}$ ) and the lack of micro-pores and deep cracks where the catalyst would be isolated from the ionomer phase and thus unable to form electrochemically active triple-phase boundaries (TPBs),
- b) availability of both the edge planes and basal planes to interact with the catalyst NPs due to the 2-D planar structure of the carbon sheet,

c) the fast electron transport mechanism and high conductivity (in case of defect free graphene),

d) strong interactions of the support and the catalyst especially in the case of RGO or functionalized graphene where anchoring sites for the catalyst NPs are provided by the surface functional groups.

Notwithstanding the benefits enumerated for the graphene support and its impact on the fuel cell technology, there are a number of cautions to be considered when thinking about this material as a catalyst support of fuel cells.

First of all, the majority of literature on this topic, have used RGO instead of defect free graphene either due to its ease and scalability or due to conceivability of the catalyst synthesis on RGO. In any case, at least one of the biggest advantages of graphene support, that is high electrical conductivity and electron transport rate, is sacrificed in such choice of synthesis method. In this respect, a deep shortage is felt about synthesis, characterization and electrochemical performance of defect free graphene as the catalyst support of fuel cells.

Properties and behavior of graphene depends fundamentally on its synthesis method and therefore, a certain behavior observed in a given report (like CO poisoning tolerance observed on RGO toward MOR) cannot be simply generalized to all graphene preparation methods.

Another illusory point about graphene that should be looked at with care is the concept of specific surface area. Although for graphene, the theoretical specific surface area of graphene is more than  $2600 \text{ m}^2\text{g}^{-1}$ , but the specific area of multilayer graphene decreases. The limiting case is graphite, having a specific surface area of only  $10 \text{ m}^2\text{g}^{-1}$ . Therefore a wide range of surface area is conceivable and only if the re-stacking problem of graphene sheets is addressed through a sophisticated engineering of the nanostructure, the high surface area of graphene can be expected.

Finally, further work is required to develop the most suitable methods for preparing either pure graphene or modified graphenes for fuel cell applications. The development of cost effective and high quality processes

for synthesis, doping, layer number control, defect optimization, and surface functionality modification of graphene will be the key factors in future research. Also, systematic studies for a fundamental understanding of the chemical and physical mechanisms that govern the electrochemical properties of graphene-based catalysts are essential. This will require a diverse contribution from many research fields including chemistry, physics, electronics, mechanics, and material science.

#### **2.1.2.2 Composite carbonaceous supports**

One of the strategies to overcome the limitations of individual carbonaceous materials conventionally used as the catalyst support of fuel cells, is the opportunity of using different materials together. Composite materials, made from two or more constituent materials with different physical or chemical properties, that when combined, produce a material with characteristics different from the individual components, can be potential alternatives to benefit the positive points of different supports in the same time. Moreover, the weaknesses of each constituent can be covered relying on the other one. Although for a composite support any two or more kinds of materials (carbonaceous, metal oxides, conducting polymers, etc.) can be combined, considering only all-carbonaceous constituents, just few attempts have been reported so far with a narrow variety of constituents. Regarding their superior behavior and impact in the research community, CNTs and graphene have been studied slightly more as components of a composite support [373–383]. Although promising results have been reported through these works, further investigations are still required to discover more precisely different corners of this field and to recognize the potentials of this strategy for development of modern catalyst supports.

#### **2.1.2.3 Non-carbonaceous supports**

Notwithstanding the great impact of nanostructured carbon on the performance of the catalyst supports used in fuel cells, there are still challenges to be addressed for their carefree application in fuel cell. Most important concern, is the corrosion of carbon that in spite of promising advances in improving its stability under fuel cell working conditions, can

still take place anyways. Corrosion of the support inherently leads to further issues like loss of catalyst, which drastically affects the overall performance of the fuel cell.

Basically, this very concern, has been the motivation of a wide and robust research on corrosion resistant materials for catalyst support applications. Obviously, a candidate fulfilling all the requirements can hardly be found, and the absence of a group of desirable characteristics of carbon in such alternatives should be taken for granted. In any condition, the requirement of more corrosion resistant support materials has raised interest on inert supports such as metal oxides and carbides [384] and conducting polymers [385]. Since a detailed review of all attempts in these fields is out of the scope of this work, only a brief mention of the examples of each category will be followed here. Most studied metal oxides and carbide supports include titanium oxides [386], titanium nitride [387], titanium diboride [388], aluminum oxide [389], tin oxide [390], indium tin oxide (ITO) [391], silicon dioxide [392,393], tungsten and tungsten oxides [394–396], tungsten carbide [397,398], sulfated zirconium oxide [399,400] and cerium oxide [401]. On the other hand, most studied conducting polymers for this application include polyaniline (PANI) [402], polypyrrole (PPy) [403], Polythiophene (PTh) [404,405], poly(3,4-ethylenedioxythiophene) or PEDOT [406] and composites such as poly(3,4-ethylenedioxythiophene)–poly(styrene sulfonic acid) or PEDOT-PSS [407], poly(N-vinyl carbazole) and poly(9-(4-vinylphenyl) carbazole) [408], poly(diallyldimethylammonium chloride) or PDDA [409].

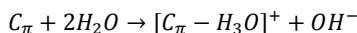
### **2.1.3 Interactions between carbon support and catalyst**

The role of carbon in a carbon-supported catalyst system is more than merely an inert ground for the catalyst to sit on. Many crucial parameters such as shape, size and dispersion of the catalyst NPs, stability or the degree of mobility of the catalyst particles as well as the strength of their bonding to the support, the Galvani potential of the catalyst system, its electronic density and Fermi level, and therefore, the electron conduction of the system are all strongly influenced or even dictated by the characteristics of the support [162,410–413]. Most importantly, the surface chemistry of the

support including the degree of inertness, or rather, the extent of oxygen surface groups or any other functional groups introduced to the surface, in addition to the surface area and porosity of the support, are the parameters that determine how the catalyst, in a broad sense, will be interacting with the support, or in narrower senses, how strongly it is attached to the support, how finely and homogeneously it is dispersed on the support, how stable/unstable and how sessile/mobile it is on the support, how fast it can exchange the electrons with the support and how active it is for electrocatalytic reactions.

Although carbon is considered to be an inert material, and its surface is, generally, assumed to be amphoteric in nature with acidic and basic centers coexisting thereon, in the context of support-catalyst interactions, different chemical characters have been attributed to different regions of graphitic carbon crystal.

Defect free basal planes of graphite that are energetically uniform and homogeneous, are considered to possess a basic nature [414]. The type of sites responsible for the basic properties of carbon surfaces has been the subject to many debates and different models have been proposed to explain it. However, the most widely agreed model tries to justify the carbon basicity based on the following equation:



(2-1)

where  $C_{\pi}$  is defined as a graphitized carbon surface platelet (i.e., basal plane) [415]. Further works also confirm the potential of basal planes to act as Lewis base centers [415–418]. Therefore, when for instance a high surface area carbon black is subjected to an inert atmosphere heat treatment in at elevated temperatures, due to graphitization, a decrease in surface area, an increase in crystalline ordering and crystallite size and consequently, an increase in the basicity of the carbon will be observed which cannot be explained by basic surface functional groups.

On the other hand, graphitic carbon surfaces have also regions where the continuity of crystalline structure is interrupted. Such regions are mainly

constituted by unsaturated valences at the edges (dangling bonds) and defects of the graphitic hexagonal crystallites. Moreover, treatments on the surface that are accompanied by the introduction of heteroatoms (mainly oxygen, hydrogen and nitrogen) are other sources of defect generation in the crystalline structure. There is general agreement in attributing acidic nature to crystalline defects of graphite including the edges, steps, defects and functional groups. Obviously, increasing the porosity and surface area of the carbon source that translates to more edge sites available, along with the functionalization treatments will increase the proportion of these acidic sites.

Considering the synthesis and subsequently, catalytic behavior of the catalyst on carbon support, the role of acidic and basic carbon surface sites becomes more obvious. Based on the amount of the edge and defective sites as well as the extent and types of functional groups on different regions of carbon surface, both negatively and positively charged surface sites exist in the synthesis medium, depending on the pH. Then, a certain pH can be considered (the isoelectric point,  $\text{pH}_{\text{IEP}}$ ) at which the net overall surface charge will be zero; at  $\text{pH} > \text{pH}_{\text{IEP}}$  the carbon surface, covered by negative charges, will attract cations from solution; at  $\text{pH} < \text{pH}_{\text{IEP}}$  it will attract anions [419]. This is schematically indicated by Fig. 2.10. Accordingly, the intensity and type of negative and positive sites of carbon surface can determine the  $\text{pH}_{\text{IEP}}$  and consequently, can dictate the synthesis condition (pH in this case) at which the desired form of catalyst precursor (anions or

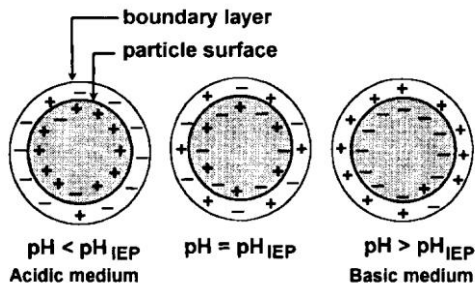
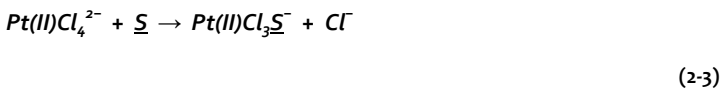
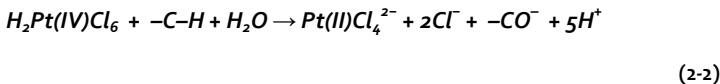


Fig. 2.10 Illustration of the amphoteric character of carbon materials [419].

cations of preference) can be selected for deposition on the surface. This is just a simple example to show how the knowledge of the probable interactions of the support and the catalyst can be used to tune the chemical accessibility of the support and thus, the catalyst dispersion. For instance, the electrostatic repulsion forces between anionic catalyst precursor species in solution and a negatively charged surface may be stronger than the nonspecific dispersion forces of attraction, resulting in inhomogeneous and unpredictable dispersion of the catalyst, regardless of the extent of the specific surface area of the support. In general, the “maximum catalyst dispersion is favored when the entire carbon surface is chemically accessible, i.e., when there is electrostatic attraction between the positively charged surface (below  $\text{pH}_{\text{IEP}}$ ) and the catalyst precursor anions or between the negatively charged surface (above  $\text{pH}_{\text{IEP}}$ ) and the catalyst precursor cations” [416].

Apart from the electrostatic models for explanation of the support–catalyst (carbon–Pt) interactions, the adsorption process of platinum onto carbon has been tried to be explained through other mechanisms, especially in cases where a simple electrostatic mechanism cannot give a sufficient explanation. For instance, the evidenced Pt reduction in the impregnation catalyst synthesis method [180,181], implies a redox process in the interaction of hexachloroplatinic acid ( $\text{H}_2\text{PtCl}_6$ ) with the carbon in which the metal complex is stabilized as  $\text{Pt}^{2+}$  on the carbon surface [420].

The proposed model to explain these observations is based on a primary reduction of Pt(IV) complex to a Pt(II) complex by carbon, which is then coordinatively bound to the carrier, as:



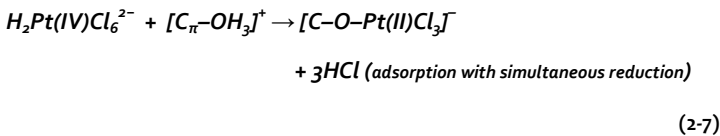
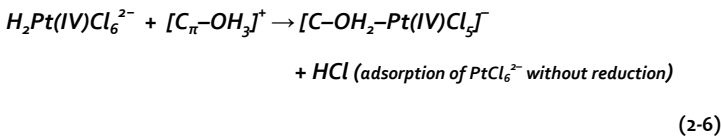
where the ligand site S is assumed to be either a  $\pi$ -complex structure or an oxygen surface group. A model for an oxidized carbon surface would be

based on independent acid and basic groups, which ionize according to the following equilibria:



where A and B represent sites of the carbon solid matrix or surface oxygen groups. Accordingly, the combination of the model proposed in Eq. (2-2) and (2-3) with the model for the ionization of the carbon surface based on independent acid and basic groups (Eq. (2-4) and (2-5)), results in the conclusion that the acid oxygen surface groups are behaving like weak anchoring sites. On the other hand, basic sites of carbon surface act as strong anchoring sites for the hexachloroplatinic anion bonding on carbon.

Alternatively, an explanation based on Lewis type character of basic sites of carbon surface which are associated with  $\pi$ -electron rich regions within the basal planes, has been proposed for the strong adsorption of  $PtCl_6^-$ , using the mechanism of inner-sphere adsorption [421]. In this model, an electron-donor-acceptor complex made of protonation of oxygen-free basic carbon sites, namely,  $[C_\pi-OH_3]^+$  (see Eq. (2-1)), plays a major role in adsorption of  $PtCl_6^-$ , as described in the following:



In this model, surface groups would replace some of the original ligands ( $\text{Cl}^-$ ) of the transition metal (catalyst) in solution. In Eq. (2-6) a water ligand is inserted and in Eq. (2-7) a C–O–Pt linkage is formed.

After the brief introduction about the catalyst-support interactions and the role of surface chemistry of the support in those interactions, a summary of the modification methods of the surface affecting its chemistry and crystallinity and therefore, influencing the interactions, can be helpful. As explained before, the carbon support can be characterized as a mixture of basal and edge planes. While a surface built up of only basal planes is considered as a homogeneous surface, a mixture of the edge and basal planes is considered as a heterogeneous surface and a wide range of investigations confirm that a heterogeneous surface would serve better for the stability and dispersion of the catalyst on support [183,422].

The choice of the type and extent of the defects/edge sites available on the support surface can be made upon a number of factors such as the type of the support [210,246,258,423], functionalization (acidic/basic and oxidative [162,168,177–179,181–183,410,420,424,425], nitrogen doping [262,354,426–430], sulfur-modification [431,432], sulfonation and phosphonation treatments [433–439] and so on) and heat treatment [181,184,440–442].

#### **2.1.4 Objective**

In summary of what reviewed so far, a wide range of carbonaceous materials for the catalyst support of fuel cells have been used and investigated. Traditional carbon blacks with benefits such as high availability and low cost, have been tried to be modified for improved support-catalyst interactions to promote metal loading and dispersion via chemical activation. Nevertheless, intrinsic problems of activated carbon such as majority of micropores reducing the accessibility of the reactants to catalyst along with low thermal and electrochemical stability, are inevitable. Therefore, the search for new materials has been continued leading to development of supports such as OMCs, CNFs, CNHs, CNOs, CNCs,

CNTs, doped diamonds and graphene family. Although any of them has its own virtues and liabilities, they have opened new horizons over the fuel cell technology as a more efficient and cost effective alternative for the world energy demands.

In particular, discovery and exploitation of CNTs and graphene as catalyst supports, has revolutionized the entire field and added a vast volume of information to the present literature making our understanding and knowledge of the carbon support clearer and more comprehensive.

Accordingly, it is intended through this work, with focus on these two premier carbon materials, to conduct a systematic and comparative study on the behavior of each species as the Pt catalyst support for ORR in the cathode of PEMFCs. A thoroughly laboratory based program has been designed and followed for preparation of the support materials, synthesis of the catalyst and microstructural and electrochemical characterizations. CNTs were prepared through fluidized bed CVD method and the graphene type used was prepared by reduction of graphene oxide, both being the most likely candidate methods for scaled production of the corresponding materials. CNTs are known to have high electrical conductivity, high degree of crystallinity, efficient pore size distribution and good corrosion resistance. In the meanwhile, drawbacks such as intrinsic inertness of pristine CNTs and the necessity of introduction of catalyst anchoring sites by some degree of functionalization along with relatively low surface area are the concerns of CNTs carefree application in this field. In contrast, RGO, features high specific surface area and abundance of catalyst anchoring sites caused by robust oxidative preparation method. On the other hand, relatively reduced electrical conductivity of RGO originating from the structural defects and also the risk of restacking of graphene sheets and loss of surface area, are the main issues of wide application of RGO in the industry. As seen, the pros and cons of each candidate are exactly the opposite sides of a coin. Therefore, such comparative study can help understanding the degree of importance of each parameter and the extent to which, each parameter is benefiting or suffering from the presence or absence of a key feature, respectively.

Furthermore, such combination of strengths and weaknesses in CNT and RGO, is inciting a big temptation for thinking about a composite support made of these two. In theory, the composite of CNT and RGO should benefit from the pros of both and should recover from the cons of each relying on the pros of the other. Therefore, along with CNT and RGO as individual electrodes, composite CNT-RGO electrode was prepared and underwent all the required characterization.

The synthesis of the Pt catalyst NPs on the supports was carried out by microwave assisted polyol process that along with environmentally friendly characteristic, benefits from short duration and easy operational features. Moreover, in the case of RGO and CNT-RGO supports, the reduction of graphene oxide is simultaneously taking place with the synthesis of Pt NPs. Accordingly, there is no need for separate reduction of the GO that is a further advantage of this method.

Finally, in the interpretation of the electrochemical performance of the catalyst-support systems toward ORR, a variety of characterization methods have been used to elucidate the role different supports and their physical and chemical characteristics in the overall behavior of the system and thereby, to cast light on potentials and limitations of each as a practically feasible candidate for real world exploitation compared to the commercial carbon supported Pt electrocatalysts (Vulcan XC72–30wt%Pt).

## 2.2 Experimental

### 2.2.1 Carbon supports preparation

#### 2.2.1.1 CNTs synthesis

The experimental set-up for CVD synthesis of CNTs was as based on the established procedure explained in previous works [443,444]. A metallic iron-based catalyst supported on neutral  $\gamma$ -alumina (Sigma-Aldrich) was prepared with a quantity of metallic Fe amounting to 9.5% of the weight of the  $\text{Al}_2\text{O}_3$ . The alumina obtained from the retailer was characterized using the B.E.T. method and found to have a surface area of  $155 \text{ m}^2/\text{g}$ ; this

alumina was subjected to a pre-calcination treatment in air at 750 °C for two hours. A second B.E.T. measurement was obtained on a part of the resulting alumina powder, from which it emerged that, after the treatment, the alumina had a surface area of 130 m<sup>2</sup>g<sup>-1</sup>. The average particle size of the alumina after the heat treatment was measured to be 110 μm. 20 g of alumina thus selected were immersed in 7.5 ml of ethanol and mixed to facilitate impregnation. The first impregnation generates heat, so the system was left to cool before a further 7.5 ml of ethanol were added. A solution of an iron precursor salt was separately prepared by dissolving 16.07 g of Fe(NO<sub>3</sub>)<sub>3</sub>·9H<sub>2</sub>O in 9.4 ml of ethanol, and stirring. The iron salt solution was poured into a balloon flask in a rotary evaporator, then the solvent containing the alumina was added to the solution. The alumina was left to become impregnated with the iron salt for one hour at 30 °C, stirring the system by rotation at 30 rpm. Then, the solvent was removed from the alumina, operating under a partial vacuum of 30 mbar at 30 °C for one hour and continuing to turn the rotary evaporator at 30 rpm. The nearly dry product recovered was then completely dried in a quartz tubular reactor positioned horizontally in a tubular furnace, operating under a flow of nitrogen of 100 sccm at 78 °C for one hour.

The dried product was then calcined in a quartz tubular reactor (2 cm in diameter and 75 cm in length), positioned horizontally in a tubular furnace. The heat treatment took place in a dynamic environment, in the presence of a flow of air, in the following working conditions: temperature gradient of 10 °C min<sup>-1</sup> from room temperature up to 700 °C, isotherm of one hour at 700 °C, continuous air flow of 100 sccm all the treatment time.

For each synthesis batch, 3 g of catalyst materials were loaded onto the porous distributor plate of a vertical reactor forming a fixed bed of 0.8 cm in height. The reactor was a quartz tube (ISO 4793-1980, inner diameter 2.28 cm, length 100 cm with a 40 cm hot zone) heated in a temperature controlled electrical furnace (Carbolite, mod. Endotherm VST 24-16). The tube was coupled to a gas flow control system (flow meter, Brooks Instrument BV, Model 5878). The arrangement of the tube in the furnace was vertical so as to provide the conditions of fluidized bed set-up. The 40 cm hot zone was divided into two parts by a distribution plate: a preheating

zone of 10 cm and a second fluidization zone of 30 cm. The reactor is heated at a rate of  $10\text{ }^{\circ}\text{C min}^{-1}$  from room temperature up to  $650\text{ }^{\circ}\text{C}$  under an atmosphere consisting of 200 sccm of hydrogen ( $\text{H}_2$ ) and 200 sccm of nitrogen ( $\text{N}_2$ ) to establish the fluidized bed conditions. Upon arrival to  $650\text{ }^{\circ}\text{C}$ , an isothermal phase of 45 minutes is followed at the same atmospheric conditions. In this step, the calcined iron catalyst supported on alumina is activated by hydrogen reduction. Subsequently, a flow of 50 sccm of ethylene ( $\text{C}_2\text{H}_4$ ) is added to the said mixture for 60 min. the total gas flowing into the reactor is thus, 450 sccm ( $\text{N}_2$ :  $\text{H}_2$ :  $\text{C}_2\text{H}_4 = 4: 4: 1$ ). These conditions correspond to growth of CNTs on the activated iron catalyst. After the 60 min growth time, the reactor is cooled down to ambient temperature under a flow of  $\text{N}_2$ .

#### 2.2.1.2 CNTs purification

In a typical purification treatment, 5 g of synthesized CNTs were suspended in 250 ml of an acid mixture consisting of sulfuric and nitric acids ( $\text{H}_2\text{SO}_4$ : 4 M and  $\text{HNO}_3$ : 1 M). The suspension was then refluxed at  $110\text{ }^{\circ}\text{C}$  for 5 h. during this step, dissolution of alumina support, iron catalyst particles and amorphous carbon phases takes place resulting in purification of CNTs. Moreover, CNTs undergo a degree of functionalization mainly due to the presence of  $\text{HNO}_3$ . By the end of 5 h high temperature treatment, the suspension was quenched in a room temperature water bath followed by dilution of the suspension with distilled water up to a volume of 2 L. The diluted suspension was stirred for 1 h and sonicated in an ultrasonic bath (Ultrasonic Bath Falc Starsonic 35) for 30 min followed by filtration. The filtered products were again immersed in distilled water and stirred and sonicated under the same conditions. The washing treatment was continued until the pH 7 arrived, after which the final filtration was carried out. The products were then dried overnight in an oven at  $100\text{ }^{\circ}\text{C}$ .

#### 2.2.1.3 GO synthesis

GO was prepared from natural graphite powder by using a modified Hummer's oxidation process [445]. 10 g of natural graphite (Sigma-Aldrich) and 7.5 g of  $\text{NaNO}_3$  (Sigma-Aldrich, purity 99%) were placed in a

flask and were added 350 ml of concentrated  $\text{H}_2\text{SO}_4$  (purity 96%). The mixture was stirred under cooling in an ice water bath for 30 min and then, 45 g of  $\text{KMnO}_4$  (Sigma-Aldrich, purity 99%) was gradually added over about 1 h, while the system was kept under the cooling conditions. In 2 h the cooling was completed and the mixture was then allowed to stand under stirring for five days (120 h) at room temperature. Gradually, a highly viscous liquid was formed. By completion of 120 h stirring, the liquid obtained was added to 1000 ml of 5 wt%  $\text{H}_2\text{SO}_4$  aqueous solution over about 1 h with stirring to avoid severe effervescence and uncontrollable temperature rise. The resultant mixture was further stirred for 2 h. Then, 25 ml of  $\text{H}_2\text{O}_2$  (30 wt% aqueous solution) was added slowly (dropwise) to the above liquid and the mixture was stirred for another 2 h. In order to purify the oxidized graphite from oxidizing agent especially manganese ions, the following washing procedure was repeated 10 times: centrifugation, removal of the supernatant liquid, addition of 1000 ml mixed aqueous solution of 3 wt%  $\text{H}_2\text{SO}_4$ /0.5 wt%  $\text{H}_2\text{O}_2$ , 30 min stirring and 30 min sonication. This purification procedure was similarly repeated a further 10 times except that the liquid to be added was replaced with water. The resultant mixture was then used as the reservoir of GO. For each experiment, the required amount of suspension was vacuum filtered and the product was dried at 40 °C before being used.

### 2.2.2 Catalyst synthesis

Catalyst synthesis was based on microwave-assisted polyol process (MWAPP) proposed by Sharma et al. [369]. For the synthesis of the catalyst on each class of support, i.e., CNT, GO and CNT-GO, 40 mg of the support was suspended in 20 ml of ethylene glycol (EG) and ultrasonicated for 60 min. In case of the composite support, CNT-GO, a weight ratio of 1:1 was considered between the constituents (20 mg each). The appropriate amount of aqueous solution of potassium hexachloroplatinate ( $\text{K}_2\text{PtCl}_6$ , 0.05  $M_{\text{Pt}}$ , e.g., 29.9 mg  $\text{K}_2\text{PtCl}_6$  dissolved in 1.23 ml water) was added to the suspension, based on stoichiometric ratios so as to have a final 30 wt% of Pt present in the catalyst-support (Pt+C) system, and the solution was stirred. Then, the pH of the mixture was adjusted to 8 by dropwise addition of a

0.4M KOH aqueous solution. After another 60 min ultrasonication, the yellow/brown suspension was moved to a domestic microwave oven for MWAPP to synthesize the Pt particles on the support. The mixture was heated for 50 s inside the microwave oven at the maximum power (700 W) and then cooled down to ambient temperature under the fume hood.

The black precipitate obtained was washed three times by ultrasonication in acetone for 5 min followed by centrifugation at 3000 rpm for 15 min to decant the acetone and replace it with a fresh one. The cleaned powders were collected after drying at 50 °C overnight in vacuum.

A commercially available Pt reference catalyst (30 wt% Pt on Vulcan XC-72 carbon black from Alfa Aesar, called hereafter as Pt/C) was used as the control sample for the purpose of comparison.

### **2.2.3 Microstructural characterization**

Catalyst-support systems were characterized for phase analysis by X-ray diffraction (XRD) technique using an 1830 PW Philips X-ray generator equipped with a PW 3020 Philips goniometer and a PW 3710 Philips control unit. The radiation used was Cu K $\alpha$  ( $\lambda = 1.540 \text{ \AA}$ ), with scan step time of 1.00 s and step size ( $2\theta$ ) of  $0.02^\circ$  having the sample in the Bragg–Brentano configuration.

Nanostructure of supports before and after the catalyst synthesis were characterized with a transmission electron microscope (TEM, Philips CM200 FEG) equipped with a field emission gun with Schottky emitter operated at 200 kV.

Thermo gravimetric analysis (TGA) was performed in Oxygen by using PerkinElmer Simultaneous Thermal Analyzer (STA 6000) at a heating rate of  $10 \text{ }^\circ\text{C min}^{-1}$  up to  $900 \text{ }^\circ\text{C}$ .

X-ray photoelectron spectroscopy (XPS) was carried out by using an AXIS Nova (Kratos Analytical) equipped with monochromatic Al K $\alpha$  ( $h\nu=1486.69 \text{ eV}$ ) X-ray source. The Kratos charge neutralizer system was used for all analyses. Sample preparation for XPS studies consisted of drop-drying of the support–catalyst ink (ink preparation is described in the

Electrode preparation section) before addition of Nafion, onto a silicon wafer and subsequent drying under an infrared lamp. XPS analyses were performed on samples in thin-film configuration.

XPS low resolution spectra (narrow scans) were acquired through 3 sweeps with pass energy of 160 eV and acquisition time of 362 s. Scan steps were adjusted to 1000.0 meV and step dwell time to 100 ms.

XPS high resolution spectra (surveys) were acquired through 10 sweeps with pass energy of 20 eV and acquisition time of 666 s. Scan steps were adjusted to 100.0 meV and step dwell time to 332 ms.

#### **2.2.4 Electrode preparation**

In order to evaluate the electrocatalytic activity of different support-catalyst systems, proper electrodes for rotating disk electrode (RDE) based cyclic voltammetry (CV) were prepared based on the standard practice proposed by Garsany et al. [446].

The general procedure for evaluating a catalyst's electrocatalytic activity by the RDE methodology involves the casting of a catalyst thin-film of known concentration on the surface of a glassy carbon electrode (GCE) substrate. The GCE used had a glassy carbon disk with a diameter of 5 mm and geometric area of 0.196 cm<sup>2</sup> embedded in a Teflon cylinder (Pine Instruments).

Before casting each catalyst thin-film, the GCEs were polished with three different alumina particle suspensions (1, 0.3 and 0.05 μm in size, respectively) on moistened polishing cloth (Buehler, Micro-Cloth) to obtain a mirror finish. The polished electrode were then rinsed well with deionized water and sonicated for 5 min in deionized water, followed by a final deionized water and ethanol rinsing and room temperature drying. Based on the intended catalysts concentration (30 wt% Pt over the entire carbon support+catalyst), a Pt loading of 17.5 μg<sub>Pt</sub> cm<sup>-2</sup> was selected to be cast on GCEs (in the standard range of 7-30 μg<sub>Pt</sub> cm<sup>-2</sup> for such Pt concentrations).

A typical catalyst ink was consisting of 1.7 mg support-catalyst (carbon+Pt) and 2 ml of a solvent composed of 24.7 vol% isopropyl alcohol (IPA, 0.494

ml), 74.8 vol% H<sub>2</sub>O (water, 1.469 ml) and 0.5 vol% of a Nafion ionomer solution (0.01 ml, Nafion solution of 5 wt%). For the supports containing CNTs, due to hydrophobicity of CNTs, formation of a homogeneous suspension was not possible with a water based electrolyte. Therefore, some ethanol was added to such inks and their composition was modified as follows: 1.7 mg support-catalyst (carbon+Pt) immersed in 2 ml of a solvent composed of 12.35 vol% isopropyl alcohol (IPA, 0.247 ml), 37.4 vol% H<sub>2</sub>O (water, 0.748 ml), 49.75 vol% ethyl alcohol (ethanol, 0.995 ml) and 0.5 vol% of a Nafion solution (0.01 ml). The detailed instruction on the calculations for planned and obtained Pt concentrations and loadings on different samples can be found in Appendix A.

After having the support-catalysts immersed in the right composition of the solvent, a sonication step of 15 min was followed for homogenization of the ink, after which a well dispersed suspension was formed.

Based on the planned concentration of Pt (30 wt% Pt over the entire carbon support+catalyst), and the desired Pt loading on GCEs (17.5  $\mu\text{g}_{\text{Pt}} \text{cm}^{-2}$ ), 13.45  $\mu\text{l}$  of the ink was cast on the 0.196  $\text{cm}^2$  area of the clean, polished GCE using a micro pipette such that it completely covered the GCE disc but did not cover any of the Teflon. The ink was then dried under an infrared lamp.

### 2.2.5 Electrochemical characterization

Once the thin-films of support-catalyst were prepared on the GCE, the catalyst electrocatalytic activity was evaluated in a standard three-electrode electrochemical cell with catalyst coated GCE as the working, a Pt mesh as the counter, and a reversible hydrogen electrode (RHE, consisting of a high surface area Pt mesh platinized with Pt black, immersed in H<sub>2</sub>-saturated 0.1 M HClO<sub>4</sub> electrolyte) as the reference electrode to obtain CVs in a de-aerated electrolyte and ORR polarization curves in an O<sub>2</sub>-saturated electrolyte [446]. For the working electrolyte, the standard electrolyte that simulates a perfluoro-sulfonic acid ionomer (low anion adsorption of bound sulfonic acid groups) in RDE measurements, i.e., 0.1 M HClO<sub>4</sub> was used.

Electrochemical measurements were carried out using a PGSTAT302N potentiostat/galvanostat (Metrohm Autolab). The electrochemical cell was a Pine RDE Cell (150 mL, with water jacket), and was linked to a thermostatically controlled bath. The cell was placed in a Faraday cage to avoid any electrical interference from surrounding equipment. A C10-P5 Thermo Scientific circulating water bath was used to maintain the temperature of the cell at 25 °C.

The working electrode was always electrochemically cleaned via potential cycling prior to measuring the CVs for electrochemical surface area (ECSA) determination and the ORR. For this, the working electrode was cycled between 0.05 and 1.20 V versus the RHE for 500 cycles at 250 mVs<sup>-1</sup>.

The CV measurements for ECSA determination of the catalyst were carried out by cycling 4 times at 20 mVs<sup>-1</sup> between 0.05 V and 1.20 V in the electrolyte (0.1 M HClO<sub>4</sub>) de-aerated with nitrogen bubbling for 30 min.

After completion of the ECSA measurements, the saturation gas was changed, and the electrolyte was saturated for 30 min with O<sub>2</sub>. Then, ORR measurements were carried out at different rotation rates including 400, 800, 1200, 1600 and 2000 rpm in order to have both the standard rotation rate for ORR measurement (1600 rpm) and to have the required data for Levich-Koutecky curves. ORR measurements were carried out by linear sweep voltammetry (LSV) at a scan rate of 20 mVs<sup>-1</sup> in the potential window of 0.05 to 1.10 V. The background current was measured by running the ORR sweep profile in the same scan rate and potential window in the same electrolyte purged for 30 min with N<sub>2</sub> before the ORR measurements to account for the capacitive current contributions to be subtracted from the electrocatalytic current measured during ORR.

## 2.3 Results and discussion

### 2.3.1 Supports preparation

Fig. 2.11 shows the TEM micrographs of the synthesized CNTs by CVD method after the purification treatment. It is seen in Fig. 2.11 (a) that CNTs

possess a homogeneous diameter size distribution in the range of 10-15 nm and the purification has successfully removed the Fe based catalyst particles from the tips or inside the channels of nanotubes. From the HRTEM image (Fig. 2.11 (b)) it is realized that CNTs are multi-walled type with 10-20 walls and interplanar spacing of 3.4 Å that is characteristic of hexagonal graphite.

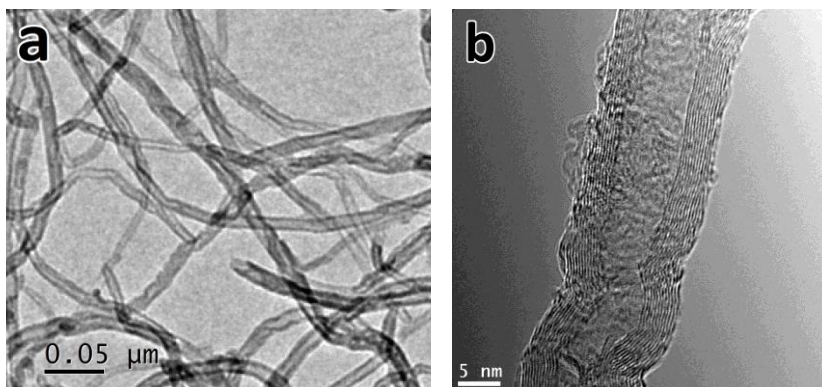


**Fig. 2.11 (a) high magnification and (b) high resolution TEM images of CNTs synthesized by CVD method after purification.**

Fig. 2.12 shows the TGA of CNTs before and after the acid purification. It is clear that before purification, a high concentration of impurities consisting of amorphous carbon and catalyst Fe based particles along with their alumina support is present in the CNTs forming 42.6 wt% of the total mass. However, after the purification, the impurity level has decreased to almost 5 wt%, the constituents that have not burnt under the air heating conditions of the TGA. Although the purity level of CNTs can be considered appropriate for the next steps, the remaining content of impurities will be taken into account when measurements of catalyst concentration on the support will be carried out.

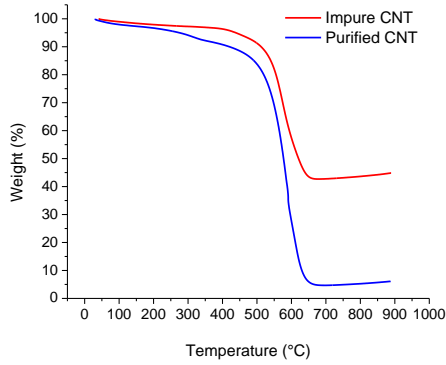


Fig. 2.12 TGA of as synthesized and purified CNTs.

Fig. 2.13 shows the TEM micrograph of the synthesized GO. A sheet composed of few layers of GO is shown in part (a) of the image with indications of local damage of layer (white arrows) probably due to strong oxidative treatment and also some folding of the layer (black arrow). In Fig. 2.13 (b), HRTEM of a wrinkle on GO is resolved and shows two times of the GO layers available in this sheet (real number of layers, 3). Irregular spacing of the layers can be realized in this image.

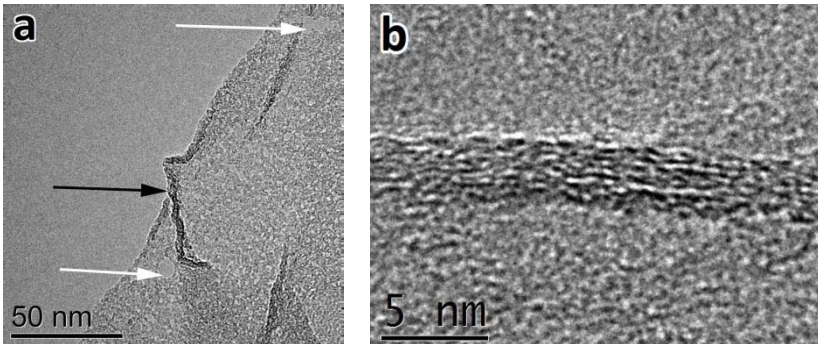


Fig. 2.13 TEM micrograph of a few layered GO sheet.

### 2.3.2 Catalyst synthesis on supports

In this work, synthesis of Pt NPs on different supports, was done via one-pot MWAPP as outlined in Fig. 2.14.

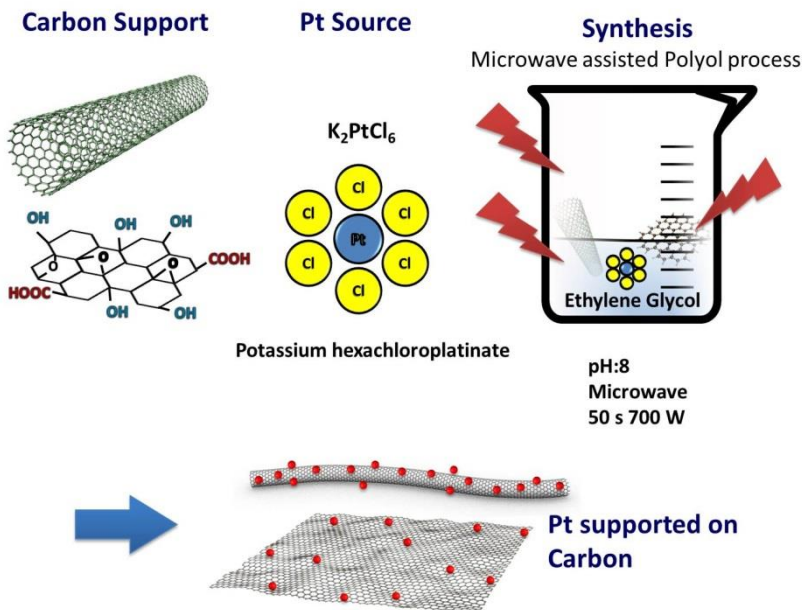


Fig. 2.14 schematic representation of Pt synthesis on different supports using MWAPP.

The mixture of the carbon support and  $\text{K}_2\text{PtCl}_6$  in EG, forms the polyol solution that is then heated rapidly in the microwave oven leading to formation of reducing species from EG that simultaneously reduce the Pt ions in the solution. The produced fine metal particles find the nucleation centers at the support material suspended in the solution, thus resulting in the synthesis of metallic NPs supported on the support. In the meanwhile, for supports such as GO, the same reducing species will be responsible for reduction of the support as well, resulting in the formation of RGO. Regardless of the starting support material, the result of the MWAPP is a

black suspension consisting of the support material decorated with Pt NPs. It will be shown later that how and to which extent the simultaneous reduction oxide supports such as GO is achieved with MWAPP.

### 2.3.2.1 TEM studies

Fig. 2.15 shows the TEM micrographs of the CNT supported Pt catalyst with indications of homogeneity and crystallinity of both support and catalyst. Fig. 2.15 (a) shows the distribution of Pt NPs on CNTs and demonstrates homogeneous size of NPs and lack of agglomeration. However, some CNTs (indicated with white arrows) show less Pt

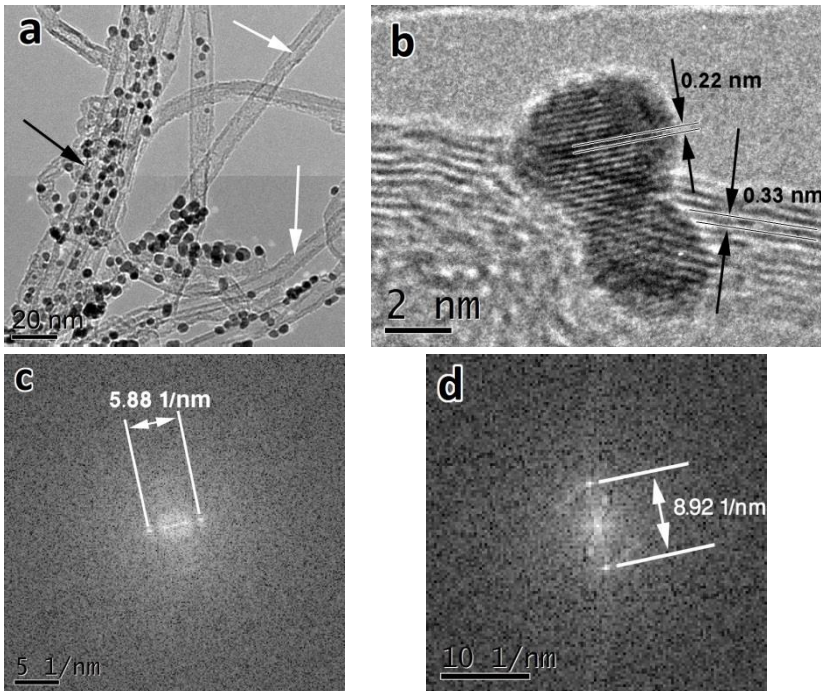


Fig. 2.15 TEM micrographs of the CNT supported Pt catalysts (a) high magnification TEM of the the distribution of Pt NPs on the CNTs, (b) HRTEM of Pt and CNT, (c and d) FFTs of CNT and Pt, respectively.

deposition. That is probably due to intrinsic inertness of CNTs that the purification/functionalization treatment in acid solutions has adequately solved it. In contrast, some other CNTs that do not suffer from this problem and have obtained enough anchoring sites (indicated with black arrow) show a good distribution of Pt particles with appropriate spacing which is necessary for maximized ECSA and electrocatalytic activity of the catalyst. In Fig. 2.15 (b) HRTEM image of both catalyst and support is shown. An interplanar spacing of 2.2 Å that is characteristic of (111) planes of face centered cubic (FCC) Pt is measured in this image along with an interplanar spacing of 3.3 Å that is characteristic of (002) planes of hexagonal graphite. Therefore, it is confirmed that the Pt synthesis has been successful and a reasonable degree of crystallinity has been achieved. Furthermore, the crystallinity of CNT support has not been damaged in the course of catalyst synthesis. As a further evidence, fast Fourier transform (FFT) of the high resolution images of CNT and Pt crystals were prepared as shown in Fig. 2.15 (c) and (d), respectively. Crystallinity of both structures is revealed by the presence of the spots in the reciprocal lattices and the spacing of the spots (5.88 and 8.92 nm<sup>-1</sup> for CNT and Pt, respectively) demonstrates an interplanar spacing (3.40 and 2.24 Å for CNT and Pt, respectively) identical to those measured from the HRTEM images. Similar studies were carried out for GO and CNT-RGO supports as well, both showing similar characteristics.

As a complementary step, average Pt particle size synthesized on different supports was evaluated based statistical analysis on TEM results as shown in Fig. 2.16. Based on the Gaussian fitting to size distributing of Pt particles, center of the normal distribution fitted to different support-catalyst systems was as follows: 3.04 ± 0.01 nm (FWHM: 0.97 ± 0.03 nm) for RGO-Pt, 3.62 ± 0.05 nm (FWHM: 1.76 ± 0.16 nm) for CNT-Pt and 3.51 ± 0.02 (FWHM: 1.08 ± 0.05 nm) for CNT-RGO-Pt. It is seen that the finest particle size and the narrowest distribution belongs to RGO-Pt and largest particle size and widest distribution to CNT-Pt. This can be justified by the abundance of the anchoring sites available for the nucleation of the catalyst. CNT support with inert surface and partial functionalization, provides less

anchoring sites for the nucleation of the catalyst and therefore, lower number of catalyst particles with larger size will deposit on it. In contrast, RGO with vast structural defects and functional groups, provides the

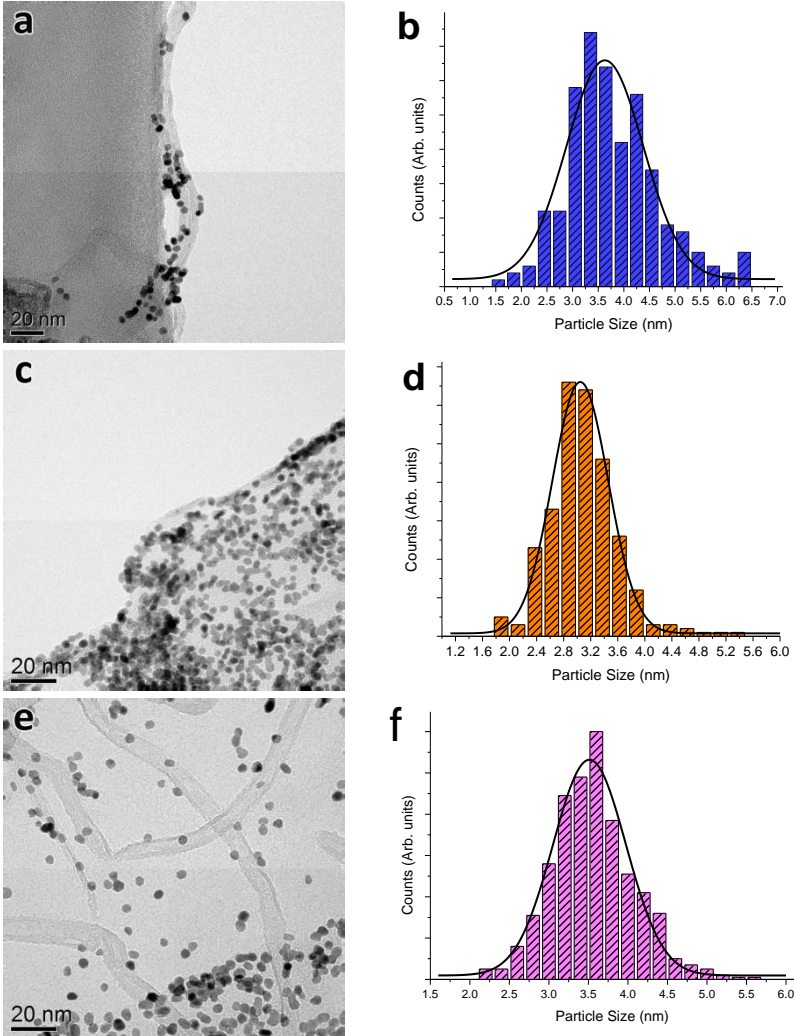


Fig. 2.16 Morphology and corresponding particle size distribution of (a and b) CNT-Pt, (c and d) RGO-Pt and (e and f) CNT-RGO-Pt systems.

highest number of anchoring sites for catalyst deposition. Reasonably, the composite support has a mixture of both characteristics and its particle size distribution is between the other two.

Another interesting feature found in the RGO–Pt sample is its denser catalyst arrangement compared to the others (Fig. 2.16 (c)). Obviously, this is also accompanied by less spacing of the Pt NPs and in many cases, contacting particles and even agglomeration. Notwithstanding the aforementioned reason for this, namely, abundance of catalyst anchoring sites, it seems that overall concentration of the catalyst is higher on this sample. Validity of such perception was explored via TGA studies as will be discussed in the following section.

Finally, the composite support (Fig. 2.16 (c)) shows some interesting features including, coexistence of CNTs and RGOs both deposited by Pt NPs, lack of agglomeration of carbon supports, appropriate spacing between the Pt NPs and minimized particle contact. This suggests a good behavior in terms of availability of ECSA for electrocatalytic activity. This behavior will be discussed in details in the electrochemical characterization section.

### 2.3.2.2 TGA studies

Fig. 2.17 shows the TGA of different catalyst support systems carried out in air at a heating rate of  $10\text{ }^{\circ}\text{C min}^{-1}$  up to  $900\text{ }^{\circ}\text{C}$ . TGA analysis is a reliable method of measurement of catalyst concentration since it is carried out on a bulk of the support–powder and no special sample preparation is required for that. Furthermore, along with the catalyst concentration, information about the functional groups of the support species are also deducible from TGA results.

Fig. 2.17 (a) shows the TGA of CNT–Pt system. An initial weight loss of almost 3.5% is observed below  $200\text{ }^{\circ}\text{C}$  centered at  $151.33\text{ }^{\circ}\text{C}$  that is due to the evaporation of absorbed water molecules from CNTs. After this, only a single weight loss peak is observed centered at  $592.12\text{ }^{\circ}\text{C}$  that refers to the burning of CNTs. According to this test, the absence or insignificant

presence of functional groups can be inferred since there is no obvious weight loss between that of the water evaporation and the one for carbon burning. Also in the derivative plot of the weight minor indication of loss between those two can be observed. By the end of the analysis at 900°C, a residue of 28.39 % is remaining that refers to Pt. Moreover, as discussed in the CNT synthesis and purification section, a residue of 5 % in CNTs refers to the remained impurities not removed by purification. Therefore, the concentration of Pt is 23.39 %. This value, although not exactly, but with some degree of deviation is close to desired concentration of Pt to be deposited on CNTs based on the stoichiometric ratios mentioned in the experimental part (i.e., 30%). Most probably, inadequate anchoring sites for Pt deposition has a big responsibility in this shortage.

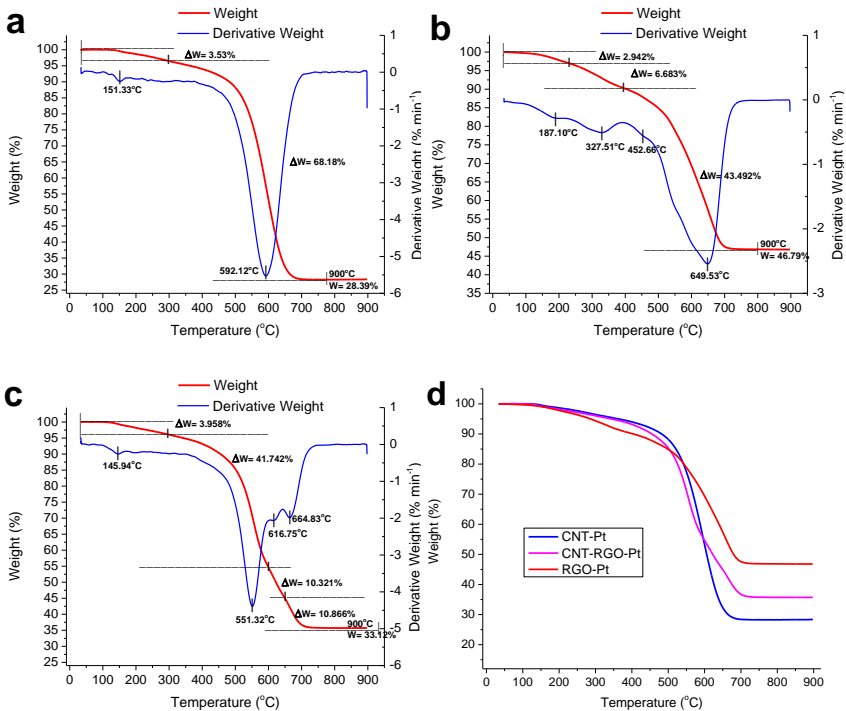


Fig. 2.17 TGA studies on (a) CNT-Pt, (b) RGO-Pt, (c) CNT-RGO-Pt and (d) overlay of the three systems.

In contrast to CNT–Pt, the TGA of RGO–Pt system (Fig. 2.17 (b)) shows multiple weight loss peaks before the RGO combustion. An initial weight loss of approximately 2.94% is observed below 200 °C related to water evaporation centered at 187.10 °C, followed by a further 6.68% loss between 250–350 °C that is believed to be due to removal of unstable oxygen functional groups such as carboxyl groups. After 400 °C the main weight loss related to combustion of RGO initiates centered at 649.53 °C. However, presence of a little groove in the initial part of this valley (in particular the dent indicated on weight derivative curve at 452.66 °C), implies the removal of more stable oxygen functional groups such as carbonyl groups. Finally, a residue of 46.79% remained unburnt that is the Pt deposited on the support. This value is considerably higher than the intended 30%. A part of the explanation of this over-concentration can be found in the abundant structural defects, edge sites and functional groups that serve as catalyst nucleation sites and making the Pt deposition on the support maximized. However, the original explanation of this can be found in the fact that in this case, the starting material upon which the stoichiometric calculations were based, has been GO, that has a remarkable mass fraction related to oxygen groups. During the catalyst synthesis, not only the Pt is reduced and deposited on the support, but also GO is being reduced losing a major part of its mass belonging to oxygen groups. Therefore, remaining RGO mass is considerably lower than the initial GO and consequently, the Pt/RGO weight ratio will be more than 30%. As seen in the TGA plot, the GO weight loss before 400 °C has been approximately 10% due to water evaporation and carboxyl groups removal. Adding the contribution of the more stable carbonyl groups removed around 450 °C, raises the unforeseen mass loss up to 15%, that balances well with the difference of the final Pt concentration (46.79%) with the desired one (30%).

In Fig. 2.17 (c) the TGA result of the composite CNT–RGO–Pt system is shown. In this sample, similar to CNT–Pt and RGO–Pt, the initial weight loss related to water evaporation is seen at relatively low temperatures, namely, 145.94°C, corresponding to 3.95% weight loss. The behavior in the medium temperatures between 200 to 400 °C is more similar to CNTs.

Since the starting support material in this sample has been a mixture CNTs and RGO, the removal of the functional groups and their supposed mass loss has been overshadowed by the presence of CNTs and only a fade indication can be realized in the TGA curve. By the start of the carbon combustion, two different rates of burning can be observed in TGA plot confirmed with two different peaks in the derivative curve. These two rates reasonably refer to burning of the two different species, namely, CNT and RGO. The region which continues until 600 °C and is centered at 551.32 °C reveals the combustion of CNTs with sharp and rapid loss. It is seen the CNTs account for about 35-40% of the initial mass, depending on the contribution of the functional groups that cannot be determined here precisely. Above 600 °C, most of the CNTs are burnt and the remaining carbon is combusted with an slower rate, characteristic of RGO, centered at about 660 °C, similar to RGO–Pt sample. This region accounts for almost 20% mass loss related to RGO contribution that is again less than the expected value due to similar reasons discussed for RGO–Pt. Finally, a residue of 33.12% remained after complete combustion that is mainly Pt and a minor contribution. Based on the CNT/GO ratio in this sample and also the issue of mass loss of GO during reduction to RGO, the contribution of CNT impurities was calculated to be approximately 3% and therefore, a concentration of 30% Pt was obtained. In fact, the inertness of CNTs and its under-concentration Pt when combined with defective structure of GO and its reduction induced mass loss and Pt over-concentration, has resulted in an overall balance of Pt concentration on the composite support. In Fig. 2.17 (d) an overlay of all the three samples is shown for comparison.

### 2.3.2.3 XRD studies

Fig. 2.18 shows the XRD patterns of CNT and GO starting materials before MWAPP. Purified CNTs show the two characteristic reflections of hexagonal graphite at 26.31° for (002) and 43.91° for (101) planes with interplanar spacings of 3.38 and 2.10 Å, respectively. In case of GO, the oxidative treatment in acids has completely changed the crystalline structure and due to intensive introduction of functional groups and O-moieties between graphene layers, the interplanar spacing has increased resulting in

shift of the peaks to lower  $2\theta$ s. Accordingly, the peak of  $26.31^\circ$  for graphite has moved to  $10.4^\circ$  for GO and the peak of  $43.91^\circ$  to  $42.50^\circ$ , corresponding to interplanar spacings of 8.50 and 2.12 Å, respectively.

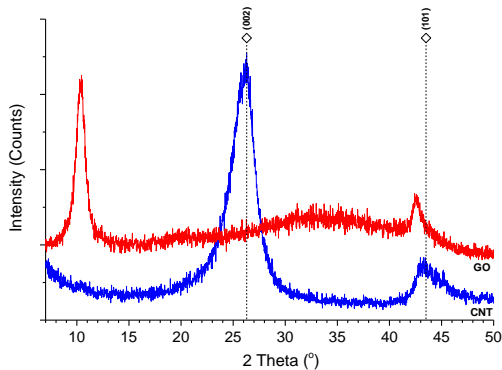


Fig. 2.18 XRD patterns of CNT and GO as the starting support materials before Pt synthesis.

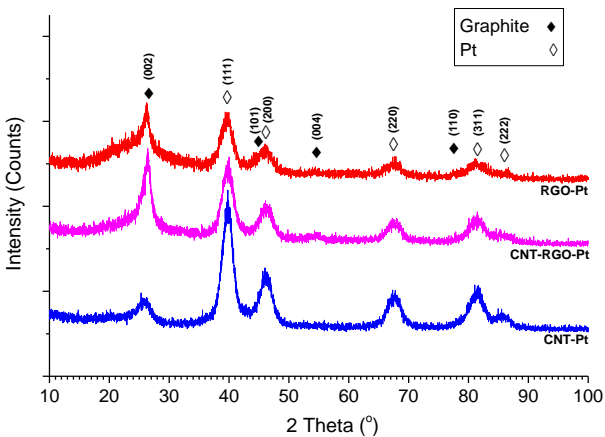


Fig. 2.19 XRD patterns of the three support-catalyst systems.

Fig. 2.19 shows the XRD patterns of the three support-catalyst systems after MWAPP synthesis of Pt. As seen, the formation of crystalline Pt is

confirmed with characteristic reflections at  $39.76^\circ$  for (111) planes,  $46.24^\circ$  for (200) planes,  $67.45^\circ$  for (220) planes,  $81.28^\circ$  for (311) planes and  $85.71^\circ$  for (222) planes. Another observation is that (111) peaks of graphite become sharper and more intense by decreasing the RGO content. One explanation for this can be based on the particle size measurements as discussed in TEM studies. It is known that peak broadening is a phenomenon that happens as the crystallite size becomes finer. Therefore, RGO–Pt with smallest particle size shows the broadest and least intense peak. In contrast, CNT–Pt with the largest particle size shows the sharpest Pt (111) peak.

Furthermore, in all supports, just standard peaks of graphite, namely,  $26.31^\circ$  for (002) and a little hump at  $43.91^\circ$  for (101) planes as a shoulder on the Pt (200) are observed. Although for CNT it might seem normal, in GO containing samples, appearance of the peaks of graphite and complete suppression of those of GO demonstrate the reduction of GO and formation of RGO.

#### **2.3.2.4 XPS studies**

XPS spectra of the samples were acquired in both wide (survey) and narrow scans as described in the experimental section. Elaboration and interpretation of the XPS results were carried out using CasaXPS software (product version 2.3.12.8).

##### **2.3.2.4.1 Survey scans**

Survey scans were useful for general understanding of the elements present in each sample as well as the overall composition of each sample. Furthermore, a necessary calibration step for all narrow scans should be carried out based on the surveys. In the following, it is tried to describe the general procedure used for elaboration of the surveys and subsequent quantification.

1- Calibration of the spectra based on the C 1s photoelectron line. The standard binding energy for C 1s is at 284.8 eV [447]. Obviously, changing the position of C 1s line to 284.8 eV is accompanied by similar shift in entire survey.

- 2- Generalizing the calibration of the survey to all narrow scans to be processed later.
- 3- Qualitative analysis and identification of the peaks based on the standard binding energies of the elements (XPS Handbooks).
- 4- Selection of a “Background type” and “Average width” parameters. The background type used was Shirley that is one of the most commonly used types of background. The use of an appropriate Av. width is for the level of noise in the data and it specifies the number of data channels on either side of the data channel corresponding to the start energy or the end energy over which an average intensity is determined for the background at the limits. An Av. Width of one or two (mainly one) was used for the Shirley background.
- 5- Quantification and generating quantification reports for elemental composition from survey spectra.
- 6- Evaluation of the error margins and standard deviation of the calculated concentrations.

Fig. 2.20 shows the typical XPS surveys of the three support–catalyst systems. Photoelectron peaks of the elements present in the studied are assigned in this plot, confirming the presence of carbon, platinum and oxygen as the main elements in all samples. Furthermore, traces of nitrogen and fluorine were found in some samples and were considered as contamination introduced to the samples during the XPS sample preparation through the drop-drying method or during the introduction of the samples into the XPS analyzer chamber. Therefore, these contaminations were ignored in the quantification of the XPS spectra.

The quantification results of the survey spectra are presented in Table 2-1.

The mass concentrations reported in this table are plotted in Fig. 2.21 (a) for better comparison. It is clearly seen that CNT–Pt sample has the lowest content of oxygen. Expectably, CNTs have minute amount of oxygen that has been introduced during the purification acid treatment. For samples

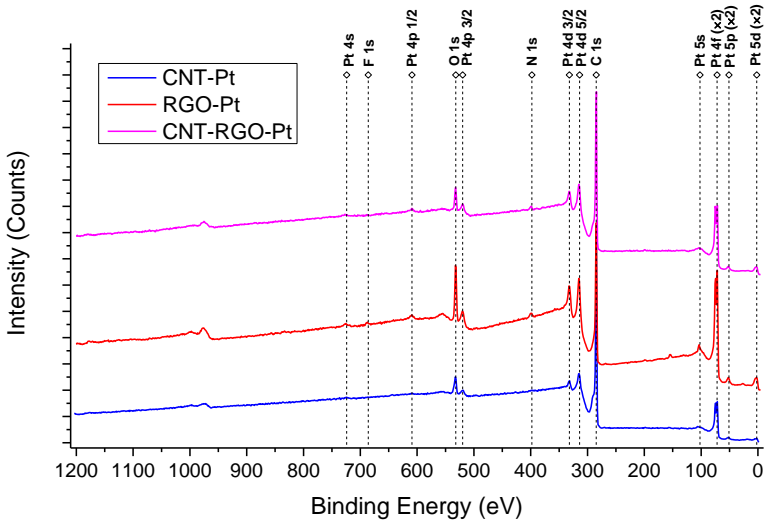


Fig. 2.20 XPS surveys of the three support–catalyst systems.

containing GO in the starting support precursor, the XPS spectra confirms the XRD results about the reduction of GO by showing the oxygen contents of 5.26 atm% (4.89 wt%) and 11.67 atm% (9.79 wt%) for CNT–RGO–Pt and RGO–Pt samples, respectively. In previous our works it has been shown that GO prepared through the same method has an oxygen content of 32.46 atm% (38.58 wt%) [369]. Such reduction in oxygen content clearly demonstrates the viability of simultaneous reduction of GO during MWAPP.

As an indication of the degree of oxidation of carbon, C to O atomic ratio can be calculated from XPS analysis or alternative methods. The higher this ratio the lower the oxygen content including all different functional groups possible. For the GO prepared via different methods, C/O atomic ratios ranging from 4:1 to 2:1 have been reported [448–451]. After the reduction of GO, this ratio increases and the higher it goes, the more successful the reduction procedure has been. Wide range of C/O ratios have also been reported for RGO ranging from 2.5:1 [369] to 246:1 [452]. In our work,

Table 2-1 Quantification results (averaged) of the XPS survey spectra of different support–catalyst systems.

Elements / samples	% Atomic (Mass) Conc. from XPS			%Mass Conc. from TGA
	C	O	Pt	Pt
CNT–Pt	93.59 (70.84)	4.39 (4.42)	2.02 (24.73)	(23.38)
CNT–RGO–Pt	92.02 (64.24)	5.26 (4.89)	2.72 (30.87)	(30.73)
RGO–Pt	84.7 (53.23)	11.67 (9.79)	3.62 (36.98)	(46.80)
GO	67.54 (61.42)	32.46 (38.58)	NA	NA

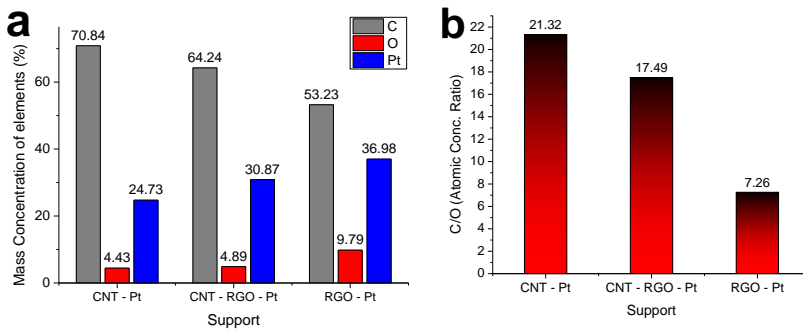


Fig. 2.21 (a) Mass concentration of the elements present in different supports based on quantification results (averaged) of the XPS survey and (b) C/O ratio calculated from the same.

the highest C/O ratio measured for RGO–Pt (7.26) is remarkably higher than the initial ratio for GO (2.08), demonstrating once more the successful reduction of GO (C/O ratios are summarized in Fig. 2.21 (b)). The composite CNT–RGO–Pt has a C/O ratio (17.49) approximately equal to the average of RGO–Pt (7.26) and CNT–Pt (21.32), that reveals the conceivability of the GO reduction even in presence of other species such as CNTs.

In the two last columns of Table 2-1, the mass concentration of Pt is reported based on the XPS and TGA results, respectively. Although a very

good consistency is observed in the results of the two methods for CNT–Pt and CNT–RGO–Pt, some deviation is realized in case of RGO–Pt. It should be noted that TGA is a thermal analysis and gives the bulk composition while XPS is a surface analysis technique. Moreover, XPS analysis was performed on samples in thin-film configuration (prepared by drop-drying on Si wafers), and therefore, the film thickness and uniformity (surface topography) may vary from sample to sample. For this reason, the priority in precision of the mass concentration of Pt and its subsequent use for electrochemical measurements was given to TGA results.

#### 2.3.2.4.2 *Narrow scans*

Interpretation of the narrow scan XPS spectra and close approximation of the chemical states of the elements under study, requires a sophisticated elaboration of the data based on a deep knowledge of the physics behind the photoelectric behavior of materials as well as mathematical skills for meaningful and sound curve fitting. Therefore, before going through the discussion of the results, it is tried to review briefly the procedure used for elaboration of the XPS narrow scan spectra in CasaXPS software.

- 1- Having the calibration carried out on surveys generalized to all narrow scans, precise selection of the borders of regions of interest.
- 2- Selection of a “Background type” and “Average width” parameters similar to survey scans. The background type used was Shirley and an Av. Width of one or two (mainly one) was used for the Shirley background.
- 3- Selection of the proper line shape based on the symmetry and geometry of the peak. The most commonly used synthetic lineshapes were:
  - Product Gaussian-Lorentzian  $GL(m)$  for symmetric peaks,
  - The line-shape  $LF(\alpha, \beta, w, m)$  with asymmetric line-shapes based on the Lorentzian functional form convoluted with a Gaussian for asymmetric peaks.
- 4- Creating components, where each component stands for a certain shift in binding energy representing a different chemical state.

5- Adjusting the synthetic model composed of all the created components with putting a minimum number of constrains on peaks position, peaks area and FWHM. Use of the constraints should be conducted with absolute care and with the purpose of giving a physical meaning to the numerical calculations done by the software for the fulfillment of the least squares criterion for the curve fitting.

6- Fitting a line to the components.

7- Checking the fitted components for any controversy.

8- Generating quantification based on the best fit obtained.

#### 2.3.2.4.2.1 Carbon narrow scans

For carbon narrow scans, GL(30) lineshape was used to model the components since there was no problem of the asymmetry of the peak. Moreover, since there was not a spin-orbit splitting for C 1s singlet, there was no need to consider any constraint as a ratio between the areas of the peaks. The only constraint considered was for the position of the peaks as energy intervals for given chemical states according to the frequently reported values in the literature. It was tried to expand those interval to the smallest min and the largest max found in the literature. These energy intervals were as follows in Table 2-2.

Table 2-2 Position constraints used for deconvolution of C 1s components.

C1s chemical states	Energy interval as a constraint on the peak position (eV)
sp <sup>2</sup>	284 – 286
C-OH (Hydroxyl)	285.2 – 286
C-O-C (epoxy, ether)	286.4 – 287
>C=O (carbonyl, ketone)	287.4 – 288
HO-C=O (carboxylic)	288.2 – 289.5
π- π*	291.3 – 291.8

Fig. 2.22 shows the high resolution XPS spectra of C 1s for different support–catalyst systems. Correspondingly, the peak assignments and the relative contributions, estimated from the curve fitting of the spectra, are displayed in Table 2-3 (a detailed table including the deconvolution results of the high resolution XPS spectra (peak positions and percentage contributions) of both C 1s and Pt 4f is also presented in Table 2-5 for all the support–catalyst systems). The deconvolution of C 1s, revealed five components for all the samples, related either to intact  $sp^2$  hybridization of carbon or to different chemical states of carbon such as C-OH (Hydroxyl), C-O-C (epoxy, ether),  $>C=O$  (carbonyl, ketone), HO-C=O (carboxylic) groups and finally  $\pi$ - $\pi^*$  (HOMO-LUMO) transition. The exact peak position of for each component, consistent with constraints mentioned in Table 2-2, is presented in Table 2-5.

As a first consideration, XPS analysis confirms once more the reduction of GO during the MWAPP (Fig. 2.22 (b) and (c) for RGO–Pt and CNT–RGO–Pt, respectively). Typically, C 1s spectra of GO is characterized by a double peak due to intensive presence of oxygen groups increasing remarkably the intensity of aforementioned components such as hydroxyl, carbonyl and carboxylic groups. Fig. 2.22 (b) however, shows the significant loss of those oxygen moieties evidenced by the absence of such the double peak. It should be noted that GO reduction through MWAPP does not result in complete removal of oxygen groups and residues of these groups and their contributions were estimated based on peak fittings as shown in Table 2-3 and Table 2-5.

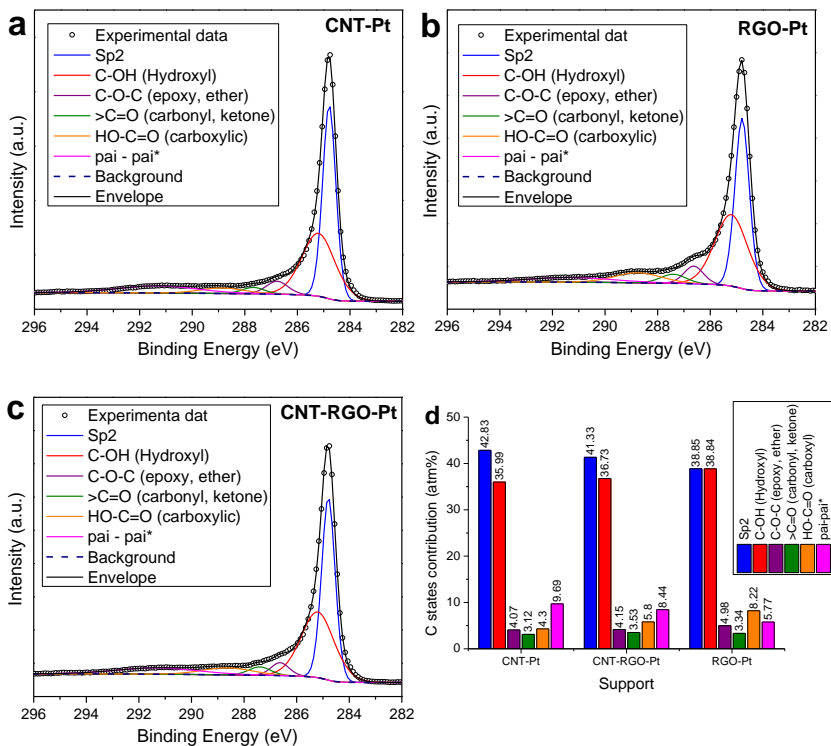


Fig. 2.22 High-resolution deconvoluted XPS spectra of C 1s for (a) CNT-Pt, (b) RGO-Pt (c) CNT-RGO-Pt and (d) comparison plot of chemical states of Pt in different supports.

Table 2-3 Quantification results (averaged) of high-resolution deconvoluted XPS spectra of C 1s of different support-catalyst systems.

Chemical state / samples	Conc. %atm					
	sp <sup>2</sup>	C-OH (Hydroxyl)	C-O-C (epoxy, ether)	>C=O (carbonyl, ketone)	HO-C=O (carboxyl)	π-π*
CNT-Pt	42.83	35.99	4.07	3.12	4.30	9.69
CNT-RGO-Pt	41.33	36.73	4.15	3.53	5.80	8.44
RGO-Pt	38.85	38.84	4.98	3.34	8.22	5.77

The other noteworthy point is the content of  $sp^2$  carbon in different samples. Since  $sp^2$  contribution represents the type of orbital hybridization present in intact aromatic rings (C=C/C-C) that is responsible for conductivity of carbon, the content of this component can imply the degree of conductivity or rather, the amount of deviation from the ideal graphitic carbon. CNTs with 42.83%  $sp^2$  contribution are supposed to have the lowest deflection and RGO, with 38.85%  $sp^2$  contribution, has the largest deviation from purely graphitic and conductive carbon. CNT-RGO composite with 41.33%  $sp^2$  contribution, is more similar to CNTs rather than RGO and in this respect, it seems that a good conductivity behavior can be expected from this support. Although the C/O ratio of this sample was approximately the average of the individual constituents, the  $sp^2$  contribution or conductivity, seems to be more influenced by CNTs. This effect can also be confirmed by the  $\pi-\pi^*$  (HOMO-LUMO transition) contribution. The  $\pi-\pi^*$  transition is a characteristic shake-up line (satellite peak) for carbon in aromatic compounds coming from the ring excited by the exiting photoelectrons [447,453]. CNT-Pt and CNT-RGO-Pt are showing a higher contribution of this transition (9.69% and 8.44%, respectively) compared to RGO-Pt (5.77%) and therefore, possess higher amount of  $\pi$ -conjugate delocalized electrons which can be considered another evidence for better conductivity. Probably, the high contribution of  $\pi-\pi^*$  transition in the composite is due to the presence of CNTs and is not a sign of higher quality of reduction of RGO in this sample.

Hydroxyl groups (C-OH) are the most abundant type of surface groups on all samples. Even CNT-Pt is showing a relatively high amount (35.99%) of these surface groups that is most likely caused by the acid treatment of CNTs. Again, the composite support proves a C-OH content between that of CNT and RGO. The same fact applies to C-O-C and HO-C=O groups as well. Consequently, a higher content of almost all oxygen containing groups on RGO is concluded compared to CNT whereas on CNT-RGO composite, medium content of these groups is observed.

As the last noteworthy point, while the content of almost all oxygen functional groups are moderately higher on RGO-Pt compared to CNT-Pt, the biggest jump in the content of a certain group from CNT to RGO is

realized for HO–C=O (carboxyl) groups. The contribution of this species in RGO is almost two times as high as the case of CNTs. Therefore, the main difference between RGO–Pt and CNT–Pt regarding the mechanism of the support–catalyst interactions, if assumed to exist any, would be most likely caused by their HO–C=O group content.

#### 2.3.2.4.2.2 *Platinum narrow scans*

Since the narrow scan analysis of Pt involves Pt doublet (4f 7/2 and 5/2), a physically meaningful solution for constraining the synthetic model to be fitted to experimental data involves ensuring the ratio of the peak areas based on the spin-orbit splitting concept. Doublet peaks resulting from the emission of a f-orbital appear with intensities in the ratio 2(5/2)+1:2(7/2)+1 or 3:4. Therefore, in Pt 4f doublet,  $\frac{\text{Area of 4f } 5/2}{\text{Area of 4f } 7/2} = 0.75$ . This applies not only to the Pt<sup>0</sup>, but also to oxidized chemical states such as Pt<sup>2+</sup> and Pt<sup>4+</sup>.

The other characteristic of Pt 4f doublet, similar to many other doublets, is the asymmetry of the peak appearing as a tale on the higher energy side of the spectra. Obviously, using symmetric lineshapes to build components to be fitted to such peaks, results in assignment of larger contributions to the components located at the higher energy side of the spectra, without having a physically meaningful explanation for that. Using asymmetric line shapes (such as Lorentzian Asymmetric Lineshapes Convolved with a Gaussian) with carefully selected line characteristics can help to avoid this issue.

After extensive trials on a proper method of fitting a physically meaningful lineshape to Pt 4f doublet, a Lorentzian Asymmetric Lineshape Convolved with a Gaussian and with an asymmetric tail damping parameter, named as LF ( $\alpha$ ,  $\beta$ ,  $w$ ,  $m$ ) in CasaXPS, was selected for this purpose. The implementation of the asymmetric Lorentzian lineshape in CasaXPS includes a parameter specifying the width of Gaussian used to convolute the Lorentzian curve, where  $m$  is an integer defining the width of the Gaussian. On the other hand, in such function,  $\alpha$  and  $\beta$  are parameters by increase of which, a reduction in the spread of the tail for the Lorentzian curve takes place, resulting in steeper edges to the lineshape. The use of these two parameters enables the spread of the Lorentzian tail to be different either

side of the peak maximum and therefore an asymmetric profile is made possible. Finally,  $w$  is the damping parameter to force the tail to reduce towards the limits of the integration limits [454,455].

Results of high-resolution deconvoluted XPS spectra of Pt 4f fitted using LF ( $\alpha$ ,  $\beta$ ,  $w$ ,  $m$ ) lineshape, is shown in Fig. 2.23 for the three support-catalyst systems. Also the contributions of each Pt state are presented in Table 2-4. The methodology used in the deconvolution of the Pt 4f (the doublet for Pt 4f7/2 and Pt 4f5/2) spectra, resulted in the acknowledgement of Pt<sup>0</sup>, Pt<sup>2+</sup>, and Pt<sup>4+</sup> oxidation states for all samples. Obviously, other types

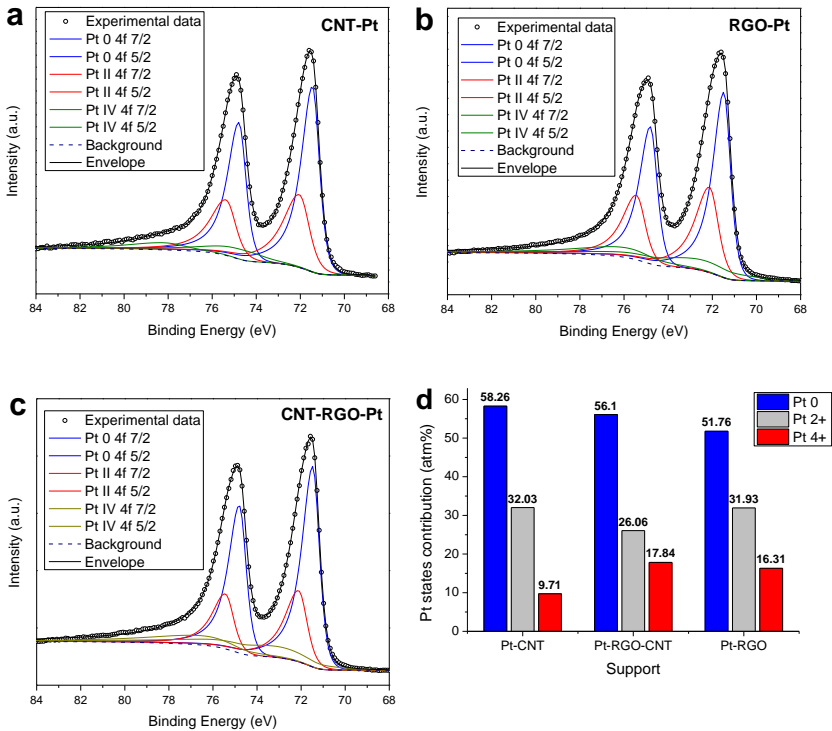


**Fig. 2.23** High-resolution deconvoluted XPS spectra of Pt 4f for (a) CNT-Pt, (b) RGO-Pt (c) CNT-RGO-Pt and (d) comparison plot of chemical states of Pt in different supports.

Table 2-4 Quantification results (averaged) of high-resolution deconvoluted XPS spectra of Pt 4f of different support–catalyst systems.

Chemical state / samples	Conc. %atm		
	Pt <sup>0</sup>	Pt <sup>2+</sup>	Pt <sup>4+</sup>
CNT–Pt	58.26	32.03	9.71
CNT–RGO–Pt	56.10	26.06	17.84
RGO–Pt	51.76	31.93	16.31

Table 2-5 Detailed table showing peak positions and percentage contributions obtained from deconvolution of the high resolution XPS spectra of all the support–catalyst systems studied.

Sample s / Element	Peak Assignment	CNT–Pt		RGO–Pt		CNT–RGO–Pt		GO	
		Position	atm %	Position	atm %	Position	atm %	Position	atm %
Pt	Pt 0 4f 7/2	71.44	33.28	71.47	29.57	71.46	32.04	NA	NA
	Pt 0 4f 5/2	74.78	24.98	74.8	22.19	74.79	24.05	NA	NA
	Pt II 4f 7/2	72.03	18.3	72.12	18.24	72.1	14.89	NA	NA
	Pt II 4f 5/2	75.37	13.73	75.43	13.69	75.43	11.17	NA	NA
	Pt IV 4f 7/2	74.64	5.55	72.46	9.32	73.27	10.20	NA	NA
	Pt IV 4f 5/2	78.18	4.16	75.81	6.99	76.38	7.65	NA	NA
C	sp <sup>2</sup>	284.79	42.83	284.79	38.85	284.79	41.33	284.5	39.67
	C–OH (Hydroxyl)	285.2	35.99	285.2	38.84	285.2	36.73	285.86	10.4
	C–O–C (epoxy, ether)	286.77	4.07	286.63	4.98	286.63	4.15	286.55	14.73
	>C=O (carbonyl, ketone)	287.67	3.12	287.4	3.34	287.4	3.53	287.52	20.4
	HO–C=O (carboxylic)	288.87	4.30	288.75	8.22	288.64	5.80	288.95	14.8
	π - π*	291.3	9.69	291.3	5.77	291.3	8.44	NA	NA

of fitting could allow for different deconvolutions. As an instance, a large number of works do not consider any  $Pt^{4+}$  in the final product [209,456–460] whereas some others, discuss the presence of all oxidation states of Pt [273,276,369,461–463]. Based on one of the works [462] best describing the nucleation and growth of Pt NPs on GO and also explaining the co-reduction of GO, the following mechanism has been proposed to be responsible for the Pt synthesis in such method:



(2-8)

According to this mechanism,  $Pt^{4+}$  ions in the precursor solution are first partially reduced to  $Pt^{2+}$  by nucleation on GO. Then, this species plays a key role in the reduction of GO, and thereby gets oxidized to  $Pt^{4+}$ . We believe that in this stage, the bonding of carbon to surface functional groups is replaced by that of Pt to surface functional groups leading to reduction of GO and a higher oxidation state of Pt. Further continuation of MWAPP can result in disbanding of surface functional groups from Pt and formation of metallic  $Pt^0$ . It should not be forgotten however, that abundance of oxygen surface groups on GO, translate to availability of  $Pt^{2+}$  and  $Pt^{4+}$  species in the products as long as the precursor solution is not completely depleted from the Pt ions.

According to above, there is good consistency between the  $Pt^{4+}$  in a given sample and the presence of GO in starting support material. RGO–Pt and CNT–RGO–Pt are showing considerable amount of  $Pt^{4+}$  (16.31 and 17.84%, respectively) whereas less amount of this species is found on CNT–Pt (9.71%). On the other hand, the highest content of metallic Pt ( $Pt^0$ ) is found in CNT–Pt (58.26%). The composite CNT–RGO–Pt sample is more similar to CNT–Pt in this case (56.10%) than RGO–Pt (51.76%). Finally, there is a good amount of  $Pt^{2+}$  in all samples confirming the key intermediate role of this species in the Pt synthesis through the above mentioned mechanism.

### 2.3.3 Electrochemical characterization

#### 2.3.3.1 Electrochemical surface area (ECSA)

Fig. 2.24 shows the CVs of different support–catalyst systems along with that of the commercial Pt/C (30 wt% Pt on Vulcan XC-72) carried out at 20  $\text{mVs}^{-1}$  within the 0.05–1.20 V potential window in de-aerated 0.1 M  $\text{HClO}_4$ . The CVs are normalized by the mass of the catalyst placed on GCE. It should be noted that since the electrode preparation was based on the initial stoichiometric ratios between the carbon and Pt precursors (30 wt% Pt over the entire carbon support+catalyst) and relied on the assumption that the those ratios would be maintained during the MWAPP synthesis, similar weights of different support–catalyst systems (13.45  $\mu\text{l}$  of the ink composed of 1.7 mg support–catalyst (carbon+Pt) and 2 ml of a solvent ) were cast on 0.196  $\text{cm}^2$  GCEs to result in a supposedly 17.5  $\mu\text{g}_{\text{Pt}} \text{cm}^{-2}$  loading. However, after the TGA analysis, it was realized that different Pt concentrations has been obtained on different samples. Therefore, based on the TGA results and the weight of support+catalyst cast on GCEs for each sample, the real Pt loading was recalculated for different samples as shown in the legend of the CVs for ECSA determination. Obviously, RGO–Pt with a positive deviation from the desired 30 wt% Pt (due mainly to GO mass loss during reduction), has achieved a higher Pt loading on GCE and CNT–Pt with a negative deviation (due to inertness of CNTs) has reached a lower Pt loading.

The ECSA of the Pt in the working electrode was calculated using the following equation from the hydrogen desorption charge ( $Q_{\text{H-desorption}}$ ) in the positive-going potential scan in the so-called  $H_{\text{upd}}$  (region of the CVs (in our case, 0.05–0.4 V, as shown typically for RGO–Pt sample with red dashes) shown in Fig. 2.24 after correction for double-layer charging (the yellow dashed region shown typically for RGO–Pt sample) by subtracting the current at 0.40 V from the total current.

$$ECSA_{Pt, cat} (m^2 g_{Pt}^{-1}) = \left[ \frac{Q_{H-desorption}(C)}{210 \mu C cm_{Pt}^{-2} L_{Pt}(mg_{Pt} cm^{-2}) A_g(cm^2)} \right] 10^5 \quad (2-9)$$

The charge of full coverage for clean polycrystalline Pt is  $Q_H = 210 \mu C cm^{-2}$  and is used as the conversion factor [446,464].  $L_{Pt}$  is the working electrode Pt loading ( $mg_{Pt} cm^{-2}$ ) and  $A_g (cm^2)$  is the geometric surface area of the glassy carbon electrode ( $0.196 cm^2$ ).

The results of ECSA determination along with the Pt loading on different samples are quantitatively shown in Fig. 2.25 and with some more details about the electrochemical performance in Table 2-6. The measured ECSA in the liquid electrolyte from CVs measures all of the catalyst that is in contact electronically to the carbon and the electrode while simultaneously in contact with protons from the acid electrolyte and catalytically active for an electrochemical reaction. The chemical adsorption and desorption peaks of hydrogen on different low-index planes of Pt are delineated to a reasonable extent for almost all the samples and show a direct relation with the magnitude of the charge.

The ECSAs of CNT–Pt, RGO–Pt and CNT–RGO–Pt electrodes were determined to be 25.62, 14.70 and 41.03, respectively, compared to 53.39 for Vulcan XC-72 30%Pt and follow the trend Vulcan–Pt > CNT–RGO–Pt > CNT–Pt > RGO–Pt. One of the influential parameters on ECSA is the catalyst particle size as smaller particles increase the surface area of identical masses of the catalyst and therefore, increase the catalytic site for electrochemical reactions. In this respect, based on particle size analysis carried out on TEM results (RGO–Pt: 3.04, CNT–RGO–Pt: 3.51 and CNT–Pt: 3.62 nm), a trend such as RGO–Pt > CNT–RGO–Pt > CNT–Pt was expected. Although this trend is observed for CNT–Pt and CNT–RGO–Pt, the ECSA of RGO–Pt is the lowest value in contrast to our expectations. As mentioned before, ECSA accounts for both electronic contact of the catalyst with support and its active surface in contact with the electrochemical medium. Therefore, we assume that the main reason for depressed ECSA of RGO–Pt support is the deficient electrical conductivity compared to other

samples. Although the reduction of GO has been achieved through the MWAPP as demonstrated through XRD and XPS results, the degree of

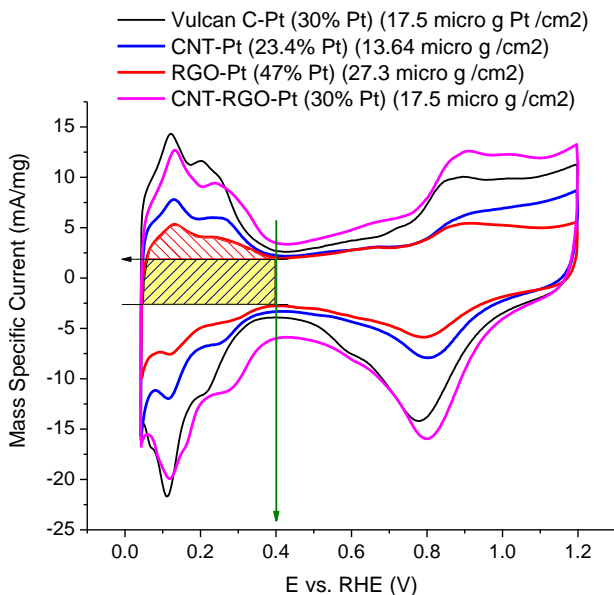


Fig. 2.24 Cyclic voltammograms of different support-catalyst systems for ECSA determination carried out at 20 mVs<sup>-1</sup> in de-aerated 0.1 M HClO<sub>4</sub>.

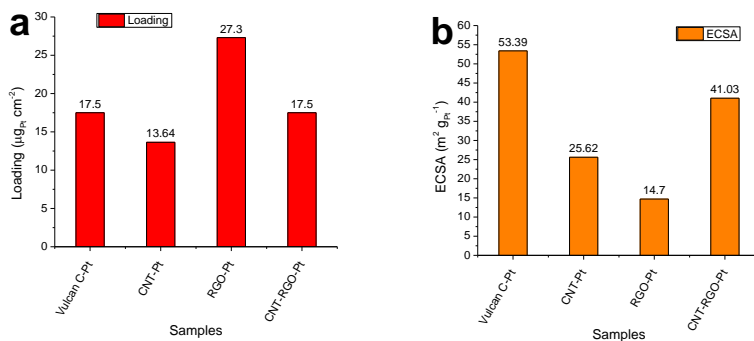


Fig. 2.25 Bar charts of (a) Pt loading and (b) ECSA of different support-catalyst systems.

reduction and in particular C/O ratio (7.26, see Fig. 2.21 (b)) of this sample is still lower than those of other samples. Interestingly, the CNT–RGO–Pt which benefitted from the conductivity of CNTs and possessed a good C/O ratio (17.49) and  $sp^2$  carbon content (41.33%, see Table 2-3), has apparently overcome the conductivity problem and is showing the best ECSA. Along particle size, the homogeneity of catalyst distribution and the degree of agglomeration are other factors affecting the ECSA. As seen in TEM studies (Fig. 2.16), RGO–Pt is heavily loaded with Pt NPs and this has resulted in a very low inter-particle spacing and in many cases, lateral contact of the NPs and even some degree of agglomeration. Therefore, a decrease in ECSA due to this effect can be expected. On the other hand, CNT–Pt catalyst, in addition to its slightly larger particle size, was showing a degree of inhomogeneity of the catalyst distribution (Fig. 2.15). These facts, along with the lower specific surface area of CNTs compared to RGO, can have resulted in the relatively high difference of ECSAs of CNT–Pt and the composite support. In fact, CNT–RGO–Pt has benefitted from the effectiveness of a 2D support such as RGO in dispersing Pt NPs with lower size and at the same time, from the good conductivity of CNTs.

The other parameter that has been considered by some researchers as to be influential on the electrocatalytic activity of Pt, is the concentration of Pt in metallic state ( $Pt^0$ ) on the electrode [369,458]. Although the idea that the electrocatalytic activity of the catalyst and in particular, Pt, is mainly dictated by the metallic state of Pt ( $Pt^0$ ) is logically reasonable, there are controversies regarding the stability of oxidized states of Pt, namely,  $Pt^{2+}$  and  $Pt^{4+}$ , in the electrochemical medium of ECSA, ORR and MOR testing. The main criticism is in other words, that the concentration of different oxidation states of Pt measured by XPS, are basically indicative of the characteristics of the catalyst prepared through a certain synthesis method and thus, during the electrochemical testing, all the varieties of Pt are converted to  $Pt^0$  as soon as they are placed in the electrolyte since the Pt oxides are thermodynamically unstable in the common electrolytes. In any case, as a further step towards the understanding of the behavior of the

samples,  $\text{Pt}^0$  loading of the electrodes were calculated by combining the information of Table 2-4 and Fig. 2.25 (b) as presented in Fig. 2.26. Although  $\text{Pt}^0$  loading for CNT-Pt and CNT-RGO-Pt is in good agreement with the ECSA results, the RGO-Pt sample with the highest  $\text{Pt}^0$  loading remains unjustified due to reasons discussed earlier.

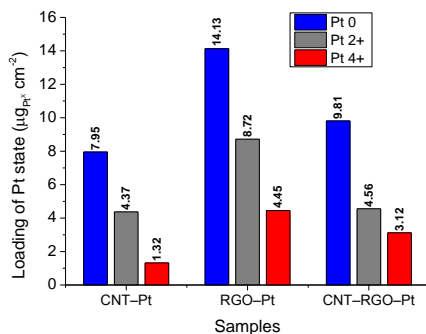


Fig. 2.26 loading of different oxidation states of Pt, ( $\text{Pt}^0$ ,  $\text{Pt}^{2+}$  and  $\text{Pt}^{4+}$ ), on the electrodes tested for ECSA and ORR determination.

Finally, the lower ECSA of the lab-made electrodes compared to commercial Vulcan XC-72, can be explained by the quality of thin film cast on the GCE for RDE testing. In particular, CNTs are intrinsically superhydrophobic and although underwent some degree of functionalization during the purification process, they could still be hardly suspended in water and that was why a different ink composition with high ethanol concentration had been used for them. Apparently, a lower degree of film homogeneity is in any case inevitable for CNT containing samples unless a proper functionalization treatment is improvised. This fact can not only affect the quality of thin film cast on GCE, but also electrochemical accessibility of the support-catalyst system in the aqueous electrolyte environment. RGO-Pt, although is supposed to benefit from good wettability due to sufficient oxygen content, is suffering from conductivity issues and reduced exposed area due to high loading and agglomeration. Addition of RGO to CNTs in composited support has improved the

wettability, further efforts are however required for an optimum film quality.

### 2.3.3.2 Oxygen reduction reaction (ORR)

Fig. 2.27 shows a typical anodic sweep (0.05 V  $\rightarrow$  1.03 V<sub>RHE</sub>) of the ORR polarization curve carried out similarly for all the samples. As seen, the raw data includes current measurement by the potential sweep. Two distinct current behaviors are observed in ORR plots, namely, diffusion control and kinetic control regions.

In diffusion control region (lower potentials or actually large overpotentials from the reversible electrode potential), the ORR current is controlled by the diffusion of oxygen to the catalyst layer, and therefore, remains almost constant over a potential range, forming a current plateau. The higher the diffusion rate, the higher the ORR current plateau. Using different rotation speeds in RDE test is to assess the effect of mass transport limitations on the electrocatalytic oxygen reduction current. It is clear that by increasing the rotation speed, due to the formation of a vortex underneath the electrode

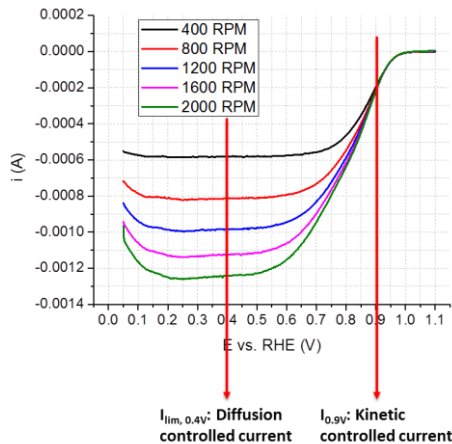
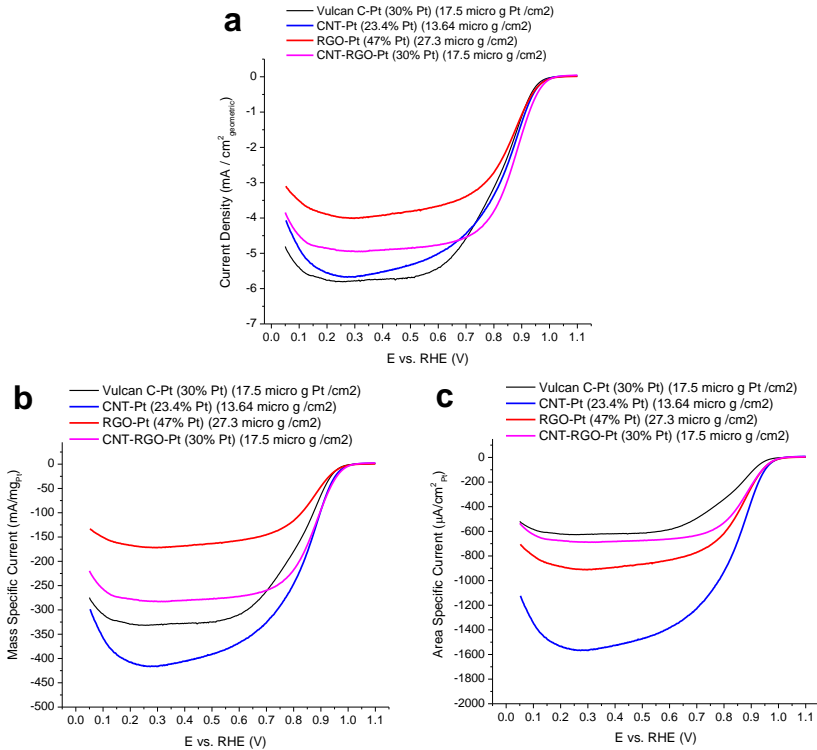


Fig. 2.27 A typical anodic sweep of the ORR polarization curve carried out at different rotation rates. Measurement of the diffusion and kinetic controlled currents is shown schematically at  $E = 0.40$  V<sub>RHE</sub> and  $E = 0.90$  V<sub>RHE</sub>, respectively.

which pulls the electrolyte upwards (a forced convection to the electrode), the thickness of the diffusion controlled region in the electrolyte decreases and the ORR current increases. From these data, the current at infinite speed is extrapolatable from a Koutecky-Levich plot. However, it is also possible to consider the 1600 rpm as a standard rotation speed for calculation of the activity parameters [446]. The standard potential for measuring the diffusion controlled current, is in the center of diffusion region plateau, namely,  $E = 0.40 \text{ V}_{\text{RHE}}$  (see Fig. 2.27), having the ORR polarization curves corrected by subtracting background current measured under identical conditions under  $\text{N}_2$  atmosphere without rotation.

At low overpotentials where the rate of the ORR decreases and mass transport is not a limiting factor for the current anymore, the ORR current is a function of the kinetics of the oxygen reduction reaction on the catalyst. The transition between the diffusion and kinetics controlled regions is characterized by a descending current magnitude wave in the anodic sweep,  $0.05 \rightarrow 1.10 \text{ V}_{\text{RHE}}$  (or an ascending current magnitude wave in the cathodic sweep,  $1.10 \rightarrow 0.05 \text{ V}_{\text{RHE}}$ ), where the current is controlled by both mass transport and kinetics of the reaction. This region is called the mixed kinetic–diffusion controlled region.

Fig. 2.28 compares the anodic sweep ( $0.05 \rightarrow 1.03 \text{ V}_{\text{RHE}}$ ) of the ORR polarization curves of different samples. Fig. 2.28 (a) shows the raw experimental current density measured for each sample during the potential sweep (like the typical plot shown in Fig. 2.27, at 1600 rpm rotation speed) whereas Fig. 2.28 (b) and (c) show the normalization of the same plot by the Pt loading of the electrode and the Pt electrochemical surface area, respectively. The diffusion controlled current densities for the lab-made samples show some degree of deviation from the theoretical value of  $j_{\text{lim}} = 5.8 \text{ mA cm}^{-2}$  at 333 K. While the commercial catalyst with a supposedly low surface area and reasonable film quality was almost in the range of theoretical value, a decrease in the diffusion limited current density of the experimental samples was observed apparently proportional to their surface



**Fig. 2.28** ORR polarization curves recorded during the anodic sweep (0.05V to 1.1 V<sub>RHE</sub>) at 20 mV s<sup>-1</sup>. Electrode rotation rate.

area and conductivity. The effect of the capacitive behavior of the carbon support on the diffusion limited current density has been reported before [465], and here, the support with the highest surface area, namely, RGO, is showing the largest deviation from the theoretical value of  $j_{lim}$  at the applied scan rate of 20 mV/s. Furthermore, this support, based on our XPS studies is supposed to have the lowest electrical conductivity and this can account for a part of the deviation as well. Another characteristic of RGO that might be in charge partially for the lower  $j_{lim}$ , can be the net shape morphology of the 2D graphene sheets that can work as traps for the transport of the reactants. CNTs with the highest conductivity and lowest surface area and 1D morphology are showing the lowest deviation from the theoretical  $j_{lim}$ ,

however, the diffusion region plateau is not very even and well-developed for this sample. In general, the quality of the catalyst thin film and the wettability of the support have also important roles in the development and flatness of the diffusion control region and in this regard, the hydrophobicity of CNTs can be a reason of the deviation from such behavior. Finally, the diffusion plateau of composite CNT–RGO–Pt benefits from the higher  $j_{lim}$  of CNTs and the flatness of RGO. Obviously, the conductivity of this sample is improved due to presence of CNTs and its surface area and wettability is modified by the RGO. Moreover, any probable negative effect of the 2D morphology of RGO on diffusion of the reactants is moderated with 1D CNTs. In fact, CNTs can be considered as not only electronic interconnects, but also as shortcuts for ionic charge and electrochemical species. This sample is also showing a single, steep reduction wave with a mixed kinetic-diffusion control region that is a promising feature for ORR catalyst–support materials. Since different samples came out to have different loadings and catalyst particle size, a comparison based on just raw ORR current densities is not so adequately helpful. Therefore, the  $mass_{Pt}$ -normalized and  $area_{Pt}$ -normalized ORR plots are presented in Fig. 2.28 (b) and (c), respectively, for giving a better insight to the behavior of different samples. Based on the normalized plots, it is seen that initiation of the reduction wave takes place at higher potentials (lower overpotentials) for the lab-made samples compared to the commercial catalyst, that is a good indication of the catalytic activity of these samples. In the mass specific current plot (Fig. 2.28 (b)), the CNT–Pt sample shows the highest electrocatalytic current and the commercial sample competes with the lab-made samples. CNT–RGO–Pt stays in the middle of CNT and RGO supports with a still a better behavior compared to the commercial sample in the mixed kinetic-diffusion control region  $0.75\text{ V} < E < 1.00\text{ V}$ . In the area specific current plot (Fig. 2.28 (c)), all the samples are showing a higher current compared to the commercial sample in all the regions. Along with the promising area specific behavior of the lab-made supports, it should be noted that since the effect of loading is neglected in

this plot, the appropriateness of the samples with high loading (such as RGO–Pt) and low ECSA, is overestimated.

### 2.3.3.2.1 Electrocatalytic activity

Regarding the complexities in the comparison of different samples summarized in the discussion of Fig. 2.28, including the different loadings, different hydrophobic properties, different conductivity and possibly, different real electrocatalytic activities, a proper way of differentiating between the samples is to evaluate the activity of the catalyst on different supports in a more precise way.

The goal in the evaluation of the catalyst activity, is to obtain a value of activity that is as much as possible unaffected from the mass-transport effects. This translates to focusing on the current measurements in a regime where ORR kinetics dominate and any residual mass-transport present can be calculated and used to make corrections to obtain a purely kinetic current. Formulation of such mass-transport correction has been developed for thin-film RDEs as presented in the following equation [466]:

$$i_k(A) = \frac{i_{lim,0.4V(A)} \times i(A)}{(i_{lim,0.4V} - i)} \quad (2-10)$$

where  $i_k$  is the “purely” kinetic current (A),  $i_{lim}$  is the measured limiting current (A) at  $E = 0.40 \text{ V}_{RHE}$  and  $I$  is the experimentally measured raw current (A). Subsequently, the Pt mass-specific activities ( $i_m(A \text{ mg}_{Pt}^{-1})$ ) are assessable by normalizing the  $i_k$  to the Pt loading of the RDE as shown in the following equation:

$$i_m(A \text{ mg}_{Pt}^{-1}) = \frac{I_k(A)}{L_{Pt}(mg_{Pt})} \quad (2-11)$$

Furthermore, Pt area-specific activities ( $i_s(\mu\text{Acm}_{Pt}^{-2})$ ) can be estimated via normalizing the  $i_k$  to the Pt electrochemical surface area as shown in the following equation:

$$i_s(\mu A cm_{Pt}^{-2}) = \frac{I_k(A)}{(Q_{H-desorption}(C)/210\mu C cm_{Pt}^{-2})} \quad (2-12)$$

Applying the diffusion correction for calculation of the kinetic current and normalizing it by either mass or active surface area of the catalyst, provides the opportunity of comparative studies on mass and area specific activities of the catalyst as shown in Fig. 2.29. The Tafel plots were prepared by logarithmic presentation of the mass specific (Eq. (2-11) and Fig. 2.29 (a)) and area specific (Eq. (2-12) and Fig. 2.29 (b)) currents versus the potential in the kinetic controlled region.

Regarding the mass specific activity, it is seen that RGO–Pt sample, in spite of its low  $i_{lim}$  observed in Fig. 2.28 is showing an activity almost close to that of commercial sample in the kinetic region. By increasing the overpotential and an increase in the mass transport limitations on the current, this sample shows slightly lower activity to the commercial one. However, samples containing CNTs show an obvious superiority in the mass activity over the entire kinetic region. Surprisingly, the composite CNT–RGO–Pt support is behaving even better than pure CNT support, implying the value added by the wettability and surface area factors from RGO to CNT. Furthermore, quantitative comparison of the catalyst electrocatalytic activity towards the ORR is also performed at  $E = 0.90 V_{RHE}$  because interferences from mass-transport losses cannot be completely excluded at the higher current densities observed below  $E = 0.90 V_{RHE}$  [466], and are presented as bar charts in Fig. 2.29 (c and d) and Table 2-6 for mass and area specific activities, respectively. Fig. 2.29 (c) as well as Table 2-6 demonstrate a lower mass activity of RGO–Pt than the commercial support at  $E = 0.90 V_{RHE}$ , whereas CNT–Pt and CNT–RGO–Pt are showing 58% and 80% improvements, respectively.

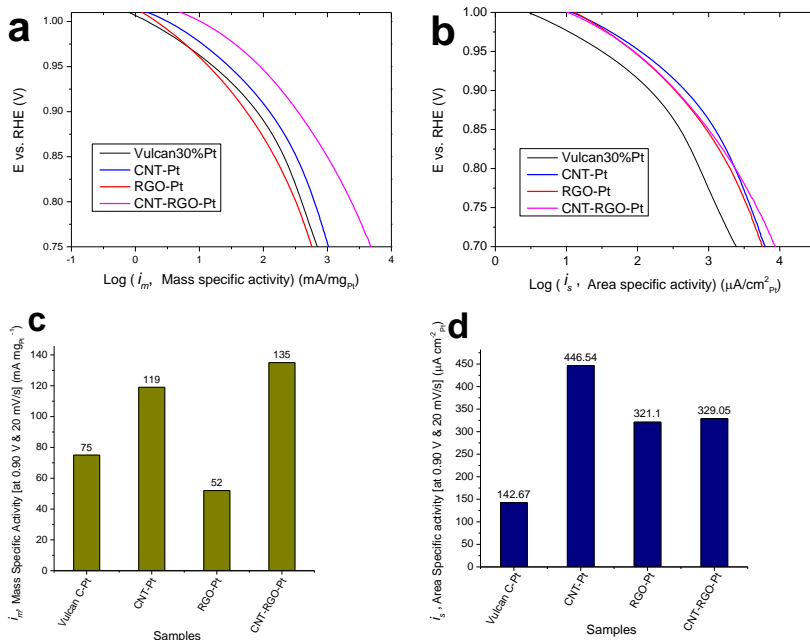


**Fig. 2.29** activity plots of different support–catalyst systems (a and b) Tafel plots of mass and area specific activities, respectively, and (c and d) the values of mass and area specific activities at  $E = 0.9 \text{ V}_{\text{RHE}}$ .

**Table 2-6** Comparison of the mass-specific ( $i_m$ ) and area-specific activities ( $i_s$ ) of different support–catalyst systems for the ORR at  $E = 0.90 \text{ V}$  versus RHE determined from the anodic sweep ( $0.05 \text{ V}$  to  $1.10 \text{ V}$ ) at  $20 \text{ mV s}^{-1}$ .

Parameters / Samples	$m_{\text{Pt}}$ on GCE ( $\mu\text{g}$ )	$L_{\text{Pt}}$ ( $\mu\text{g}_{\text{Pt}} \text{ cm}^{-2}$ )	ECSA ( $\text{m}^2 \text{ g}^{-1} \text{ Pt}$ )	$i_m$ (0.90 V), 20 mV/s ( $\text{mA mg}^{-1} \text{ Pt}$ )	$i_s$ (0.90 V), 20 mV/s ( $\mu\text{A cm}^{-2} \text{ Pt}$ )
Vulcan XC-72 30%Pt	3.43	17.5	53.39	75	142.67
CNT-Pt	2.67	13.64	25.62	119	446.54
RGO-Pt	5.35	27.3	14.70	52	321.10
CNT-RGO-Pt	3.43	17.5	41.03	135	329.05

Regarding the area specific activities, all the lab-made samples are quite clearly performing better than the commercial sample over the entire kinetic

region. Furthermore, the differences between the lab-made samples are less pronounced in Fig. 2.29 (b). This implies firstly, that the surface quality of the Pt NPs synthesized by MWAPP is to a good extent similar and appropriate for ORR. Secondly, the specific activities of RGO–Pt, CNT–RGO–Pt and CNT–Pt samples at  $E = 0.90 V_{\text{RHE}}$ , are 2.25, 2.3 and 3.13 times higher than the commercial sample (Fig. 2.29 (d) and Table 2-6), respectively. One should note that in area specific activity, since normalization by the electrochemically active surface area is carried out, deficiencies of the support electrical conductivity are not well considered. In other words, the effect of electronic charge transfer of the support emerges in both  $i_k$  and ECSA and thus, is neutralized in the calculated  $i_s$ . For instance, the relatively low kinetic current of RGO–Pt sample is normalized by its low electrochemically active surface area and thus, the value of  $i_s$  is as high as RGO–CNT–Pt. Therefore, this measure is good for judgment of the crystallinity, chemistry and other features of the catalyst responsible for ORR. In this respect, the XPS studies on the oxidation states of Pt synthesized by MWAPP (see Fig. 2.23, Fig. 2.26, and Table 2-4) can be re-checked to see if there exists any consistency between these factors. It is seen that the trend in the content of metallic Pt is similar to the trend of area specific activity. This observation can support, though not very strongly, the idea of dependence of the catalytic activity of Pt on its as synthesized oxidation states even within the environments where the oxides are thermodynamically unstable.

In contrast,  $i_m$  is a more general feature that not only reflects the gain/cost factor of a support-catalyst system that is of major importance in the development of economical catalysts, but simultaneously represents the quality of the catalyst, support and their interactions as well. In this respect, the distinct superiority of the mass specific activity of the composite supported catalyst in particular at  $E = 0.90 V_{\text{RHE}}$  ( $135 \text{ mA mg}^{-1}_{\text{Pt}}$ ) over either the commercial catalyst ( $75 \text{ mA mg}^{-1}_{\text{Pt}}$ ) or both its parents, RGO ( $52 \text{ mA mg}^{-1}_{\text{Pt}}$ ) and CNT ( $119 \text{ mA mg}^{-1}_{\text{Pt}}$ ) supported catalyst is a figure of merit for this sample.

As a further evidence for the catalytic activity, assessment of some potential based indicators is also a common method in this field. These indicators usually include the ORR onset potential ( $E_{\text{onset}}$ ) and half-wave potential ( $E_{1/2}$ ).  $E_{\text{onset}}$  is the potential at which a given (small) current density is reached, and that current density is usually chosen to roughly correspond the lowest value readily distinguished from zero by visual check. The comparison of onset potentials on this basis is however somewhat arbitrary and imprecise. Therefore, in our work a minimum kinetic current density (i.e., after the mass transport correction on the geometric current density) such as  $10 \mu\text{A cm}^{-2}$  was selected as the reference for  $E_{\text{onset}}$  determination.

**Table 2-7 Potential based activity indicators of different samples**

Parameters / Samples	OCP after 30 min O <sub>2</sub> purge (V)	E <sub>ORR→OER</sub> in anodic sweep (V)	E <sub>onset</sub> (E at $j_k = 1\text{E-}5 \text{ A/cm}^2_{\text{Geo}}$ ) (V)	E <sub>1/2</sub> (V)
Vulcan XC-72 30%Pt	1.008	1.020	1.014	0.817
CNT-Pt	1.038	1.026	1.017	0.837
CNT-RGO-Pt	1.032	1.026	1.020	0.871
RGO-Pt	1.058	1.043	1.029	0.853

On the other hand,  $E_{1/2}$  is the potential corresponding to a current (or current density) point half-way between zero current and the diffusion limited current (or current density) plateau (i or j at  $E = 0.4 V_{\text{RHE}}$ ). In our work, we also added some more potential indicators to above, including the open circuit potential (OCP<sub>ORR</sub>) of the electrode after 30 min purging in O<sub>2</sub> before the start of ORR measurements as well as the inversion potential during the anodic sweep (E<sub>ORR→OER</sub>), where the sign of current is inversed or actually, a ORR to OER shift is taking place. These two parameters are helpful for understanding the differences in intrinsic practical overpotential of different support–catalyst systems and obviously, the higher those potentials (or the lower the overpotentials), the better the activity of the catalyst in the corresponding system. Summary of these potentials is presented in Table 2-7. Interestingly, it is seen that OCP<sub>ORR</sub> and E<sub>ORR→OER</sub> are the highest for

RGO–Pt sample. This positive catalytic feature on RGO support is possibly due to the specific interaction of the different crystal faces of Pt with the typical functional groups of the support serving as anchoring sites for catalyst deposition. It also implies that the depressed diffusion limited current of this sample is not due to poor catalytic activity, but other factors like what mentioned in the discussion of Fig. 2.28.

While  $OC_{\text{ORR}}$  and  $E_{\text{ORR} \rightarrow \text{OER}}$  of the Vulcan–Pt are in all cases lower than the lab made samples, these parameters for CNT–RGO–Pt sample are very similar to those of CNT–Pt, i.e., higher than the commercial and lower than the RGO–Pt samples. Considering the possibility of specific interaction of the different crystal faces of Pt with the typical functional groups of the support, two hypotheses can be assumed for the observed similarities in  $OC_{\text{ORR}}$  and  $E_{\text{ORR} \rightarrow \text{OER}}$  of CNT–Pt and CNT–RGO–Pt systems.

Firstly, CNTs could have affected the mechanism of Pt synthesis on the RGO content of the composite support. It is known that the reduction of Pt ions on carbon supports requires in some point, the electron transfer from the support to the ion. Therefore, the electronic charge transport properties of the support can affect the rate and thus, the mechanism of synthesis. CNTs which are working like highly conductive interconnects between less conductive GO/RGO sheets, can affect the rate and mechanism of Pt synthesis on RGO therefore. Consequently, the Pt catalyst on composite support would have characteristic more similar to those on CNTs and behave similar to CNT–Pt towards ORR.

Secondly, during the Pt synthesis, functional groups of RGO and any specific interaction between them and Pt, should act similarly regardless of the presence or absence of nanotubes. Therefore, the reason they do not show their effect during the ORR can be justified by the dominance of the Pt features present mainly on CNT–Pt over the ORR of the composite support at near equilibrium potentials. This can include both specific functional groups of CNTs interacting in a particular way with different crystal faces of Pt or the electron transfer rate through CNTs.

Based on the other two potential indicators, i.e.,  $E_{\text{onset}}$  and  $E_{1/2}$ , the lowest activity of the commercial catalyst is confirmed again and the general trend

in the activity of other systems is retained. Only at high enough current densities, corresponding to  $E_{1/2}$ , it is seen that RGO–Pt loses its first rank and is overpassed by the composite sample. All these potential based indicators imply the thermodynamic superiority of RGO support for ORR. However, when kinetic parameters are considered and the magnitude of current becomes larger and larger, the composite support fulfills better the requirements and outperforms both CNT and RGO supports.

## 2.4 Conclusion

In this work, fabrication of Pt NPs electrocatalysts supported on different carbon materials, namely, CNT, RGO and composite CNT–RGO was successfully demonstrated using a rapid and simple microwave-assisted approach (MWAPP). Pt NPs anchoring and dispersion on different supports became possible due to the presence of surface functional groups, mainly oxygen containing, of the support. In case of CNTs the functional groups were introduced through the purification/functionalization procedure obtained via acid treatment, whereas in RGO, abundance of surface functional groups was already provided due to robust oxidative treatment of graphite in Hummer's synthesis method.

The availability of multitudinous anchoring sites on RGO, provided more homogeneous dispersion of Pt NPs compared to intrinsically inert CNTs. However, the reduction induced mass loss of the primary GO during the MWAPP reduction to RGO, resulted in a higher concentration of Pt on this support, lower spacing of the Pt NPs and in some cases, attachment and slight agglomeration. TEM and XRD studies confirmed high quality and crystallinity of Pt NPs and a dependence of Pt NPs size on the type of the support was observed in the following trend: RGO–Pt < CNT–RGO–Pt < CNT–Pt. The difference in type and number of oxygen functional groups of different support were considered to be responsible for the observed particle size distribution of the supports.

XPS studies, demonstrated the highest content of oxygen on RGO–Pt and the lowest on CNT–Pt while the composite support had an intermediate oxygen content, resulting in a C/O ratio trend of the supports in the

following order: RGO–Pt (7.26) < CNT–RGO–Pt (17.49) < CNT–Pt (21.32). These observations supported the assumption of the higher conductivity of CNT support than the RGO.

Moreover, high resolution XPS narrow scans of C 1s spectra revealed the highest content of  $sp^2$  and  $\pi-\pi^*$  components on CNT compared to others, reinforcing the assumption of better electrical conductivity of the support. Interestingly, contributions of  $sp^2$  and  $\pi-\pi^*$  components in CNT–RGO composite support were more similar to those of CNTs than RGO, suggesting a successful transfer of electrical properties of CNTs to the composite support. While the content of almost all oxygen functional groups were moderately higher on RGO–Pt compared to CNT–Pt based on HR–XPS results, the biggest jump in the content of a certain functional group from CNT to RGO was realized for HO–C=O (carboxyl) groups. The contribution of this species in RGO was almost two times as high as the case of CNTs. Therefore, the main difference between RGO–Pt and CNT–Pt regarding the mechanism of the support–catalyst interactions either in the synthesis step or during the electrocatalytic activity, was assumed to be caused by their HO–C=O group content.

HR–XPS results of Pt 4f spectra enlightened the chemical characteristics such as oxidation states of the catalyst on different supports quantitatively. It was seen that the content of oxidized states of Pt changes in line with the oxygen content of the support and therefore the highest and lowest metallic Pt ( $Pt^0$ ) content were observed on CNT–Pt and RGO–Pt, respectively. Interestingly, the content of  $Pt^0$  of the composite support was more influenced by CNT (thus more similar to CNT–Pt) whereas its content of heavily oxidized Pt ( $Pt^{4+}$ ) was more influenced by RGO (thus more similar to RGO–Pt).

The prepared supported catalysts were tested for oxygen electroreduction via RDE method and showed promising results compared to a commercially available Vulcan XC72–30%Pt catalyst. Activity evaluation of the samples toward ORR was carried out based on both mass and area specific kinetic currents as well as several potential based indicators such as OCP of the electrode after 30 min  $O_2$  purge ( $OCP_{ORR}$ ), the inversion potential during the

anodic sweep ( $E_{\text{ORR} \rightarrow \text{OER}}$ ), onset potential of ORR based on the anodic sweep ( $E_{\text{onset}}$ ) measured at  $j_k = 1\text{E-}5 \text{ A/cm}^2_{\text{Geo}}$  and  $E_{1/2}$ .

Regarding the area specific activities, all the lab-made samples were quite clearly performing better than the commercial sample over the entire kinetic region confirming the high surface quality and crystallinity of the PT NPs synthesized by MWAPP. In particular, the specific activities of RGO–Pt, CNT–RGO–Pt and CNT–Pt samples at  $E = 0.90 \text{ V}_{\text{RHE}}$ , are 2.25, 2.3 and 3.13 times higher than the commercial sample, respectively. It is seen that the trend of area specific activity is similar to the trend of content of the metallic Pt on the as synthesized support–catalyst systems. Although there are criticisms on the existence of any relationship between the oxidation states of as synthesized Pt catalyst before the ORR and its electrocatalytic activity due to thermodynamic instability of Pt oxides in the acidic environment, our results can moderately support such relationship.

Regarding the mass specific activity, RGO–Pt sample showed a poorer behavior compared to other lab-made samples, though still in the range of the commercial catalyst. In contrast, samples containing CNTs showed an obvious superiority in the mass activity over the entire kinetic region, reinforcing the assumption of important role of electrical conductivity of the support on mass specific activity of the catalyst. Particularly, CNT–RGO–Pt support showed a mass specific activity even better than pure CNT support, implying the value added by the wettability and surface area factors from RGO to CNT. The mass specific activities calculations at  $E = 0.90 \text{ V}_{\text{RHE}}$ , revealed a lower activity of RGO–Pt than the commercial catalyst, whereas CNT–Pt and CNT–RGO–Pt showed 58% and 80% improvements, respectively. Regarding the significance of mass specific activity from economical viewpoints, not only the importance of the support conductivity is highlighted, but also the strategy of hybridization of different supports with dissimilar properties seems to be an effective way of reducing the cost of commercially reasonable products.

Comparison based on the potential based indicators of catalyst suitability for ORR, showed a lower  $\text{OCP}_{\text{ORR}}$  and  $E_{\text{ORR} \rightarrow \text{OER}}$  of the Vulcan–Pt compared to all lab-made samples, implying the lower practical overpotential of the our support–catalyst systems compared to the

commercial catalyst. Interestingly, the highest  $OCP_{ORR}$  and  $E_{ORR \rightarrow OER}$  were observed for RGO–Pt sample. This was explained based on the specific interaction of the different crystal faces of Pt with the characteristic functional groups of the RGO which distinguished this support from the others, namely the relative abundance of HO–C=O (carboxyl) groups. Such effect could be further evidenced with the similarity of  $OCP_{ORR}$  and  $E_{ORR \rightarrow OER}$  for CNT–Pt and CNT–RGO–Pt, where the HO–C=O content of CNT–RGO–Pt was more similar to CNT–Pt rather than RGO–Pt.  $E_{onset}$  and  $E_{1/2}$ , confirmed once more the lowest activity of the commercial catalyst and the general trend in the activity of other systems.

Finally, issues such as shortage of electrical conductivity and probably some morphological concerns like trapping effect of the net shaped 2D RGO layers, were considered to be cons of RGO support especially in the diffusion controlled region and high over potentials. In contrast, specific interactions of HO–C=O (carboxyl) groups of RGO with crystalline faces of Pt resulting in a lower overpotentials achievable for RGO supported catalyst towards ORR, along with its good wettability and high surface area are the advantages to be enumerated for this support. On the other hand, CNTs benefitted from high electrical conductivity and provided better conditions for the formation of metallic states of Pt. However, it was suffering from hydrophobicity and difficulties associated with the preparation of a thin and homogenous film along with its relatively low surface area. The composite support, demonstrated the capability to successfully combine the main advantages of both parent supports and present exemplary kinetic activities at low and high overpotentials for oxygen electrocatalytic reduction.

## 3 *Carbon nanostructures as active materials of supercapacitors*

### 3.1 Introduction

Electrochemical capacitors (ECs), often referred to as supercapacitors or ultracapacitors and formerly electric double-layer capacitor (EDLC), store charge physically just as other types of capacitors do. But ECs differ in that they store tremendously greater amounts of charge, owing to the use of very high-surface-area electrodes with electric double-layer charge storage on that surface [467]. This enables them to combine a previously unattainable capacitance density. They provide higher energy density than dielectric capacitors, while demonstrating higher power density than batteries [468,469]. The operational voltage per cell, limited only by the breakdown potential of the electrolyte, is usually  $<1$  or  $<3$  volts per cell for aqueous or organic electrolytes respectively. In supercapacitors, physical charge storage does not rely on chemical reaction rates, as with batteries, which often limit power performance. Because of this, ECs, compared to other electrochemical devices such as batteries, benefit from high cycle life and very high-power capability on both charge and discharge. They also deliver exceptionally low-temperature performance, even at  $-40$  °C. As a result, electric double-layer capacitors are often used to complement batteries in applications with rapidly varying power requirements, electric and hybrid-electric vehicles, tramways, buses, cranes, forklifts, wind turbines and in opening emergency doors of airplanes being prominent cases in point [470,471]. Fig. 3.1 shows the plot of power against energy density, also called a Ragone plot, for the most important energy storage systems.

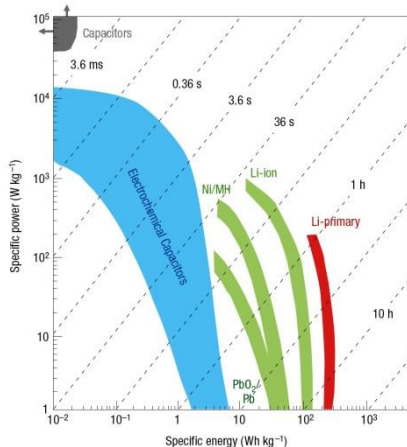


**Fig. 3.1** Specific power against specific energy, also called a Ragone plot, for various electrical energy storage devices. If a supercapacitor is used in an electric vehicle, the specific power shows how fast one can go, and the specific energy shows how far one can go on a single charge. Times shown are the time constants of the devices, obtained by dividing the energy density by the power [468].

In the early 1950s, General Electric engineers began experimenting with components using porous carbon electrodes for fuel cells and rechargeable batteries, the investigations results of which were first patented in 1957 by Howard I. Becker as a “Low voltage electrolytic capacitor with porous carbon electrodes”[472], but never commercialized. Becker did, however, appreciate the large capacitance values subsequently achieved by Robert A. Rightmire, a chemist at the Standard Oil Company of Ohio (SOHIO), to whom can be attributed the invention of the device in the format now commonly used. His patent, filed in 1962 and awarded in late November 1966 [473], and a follow-on patent by fellow SOHIO researcher Donald L. Boos in 1970 [474], form the basis for the many hundreds of subsequent patents and journal articles covering all aspects of EC technology [475].

Carbon is an element almost uniquely suited for fabrication of electrochemical capacitors of the double-layer type. It exists in several, well-known allotropic forms—diamond, the fullerenes, and graphite; the latter and glassy carbon can be generated in the form of high-area fibers or felts. Amorphous carbons and carbon black are available as high specific-

area powders. The fiber or felt materials are particularly convenient for formation of electrode structures having good mechanical integrity, while the high-area powders are more difficult to handle. However, glassy carbon, graphite, and carbon black materials are convenient for forming high-area electrode structures, often on a support matrix. From an electrochemical point of view, carbon is relatively, though not entirely, unreactive and thus has a potential voltage range of almost ideal polarizability, approaching 1.0 V in aqueous solution and possibly up to 3.5 V in nonaqueous media [467].

The range of possible carbon materials to be used for supercapacitors, as mentioned above is very wide and basically, all the species introduced in the introduction of chapter 2 of this work as candidate support materials for the catalyst in fuel cell applications can also be used as active materials for supercapacitors. Accordingly, we suffice here to the introduction of the species given in previous chapter, and here, we just provide a summary of the works carried out on different examples, with special focus on CNTs and graphene family or their hybrids as the objective of this work demands.

### **3.1.1 Carbon-based electrode materials**

#### **3.1.1.1 Activated carbons (A.C.s)**

A.C.s are the mostly widely used electrode materials due to their large surface area, relatively good electrical properties and moderate cost. A.C.s are generally produced from physical (thermal) and/or chemical activation of various types of carbonaceous materials (e.g. wood, coal, nutshell, etc.). Physical activation usually refers to the treatment of carbon precursors at high temperature (from 700 to 1200 °C) in the presence of oxidizing gases such as steam, CO<sub>2</sub> and air. Chemical activation is usually carried out at lower temperatures (from 400 to 700 °C) with activating agents like phosphoric acid, potassium hydroxide, sodium hydroxide and zinc chloride. Depending on the activation methods as well as the carbon precursors used, ACs possessing various physicochemical properties with well-developed surface areas as high as 3000 m<sup>2</sup>g<sup>-1</sup> have been produced and their electrochemical properties have been studied [476–481]. It is well known that the porous structure of ACs produced by activation processes have a

broad pore size distribution consisting of micropores (< 2 nm), mesopores (2–50 nm) and macropores (> 50 nm). Several researchers have pointed out the discrepancy between the capacitance of the ACs and their specific surface area.

With a high surface area up to  $3000 \text{ m}^2\text{g}^{-1}$ , only a relatively small specific capacitance  $< 10 \text{ }\mu\text{Fcm}^{-2}$  was obtained, much smaller than the theoretical EDL capacitance ( $15\text{--}25 \text{ }\mu\text{Fcm}^{-2}$ ) [467], indicating that not all pores are effective in charge accumulation [479]. Therefore, although the specific surface area is an important parameter for the performance of EDLC, some other aspects of the carbon materials such as pore size distribution, pore shape and structure, electrical conductivity and surface functionality can also influence their electrochemical performance to a great extent. Furthermore, excessive activation will lead to large pore volume, which results in the drawbacks of low material density and conductivity. These would in turn cause a low volumetric energy density and loss of power capability. In addition, high active surface areas may increase the risk of decomposition of the electrolyte at the dangling bond positions [482]. The presence of the acidic functionalities and moisture on the surface of ACs is responsible for the aging of the supercapacitor electrodes in organic electrolytes [483]. Efforts have been made to search for the relationship between the nanoporous structure of ACs and their capacitance performance in different electrolytes. In general, the capacitance of ACs is higher in aqueous electrolytes (ranging from  $100 \text{ F g}^{-1}$  to  $300 \text{ F g}^{-1}$ ) than in organic electrolytes (less than  $150 \text{ F g}^{-1}$ ). One reason for this is believed to be the larger effective size of the electrolyte ions in organic solutions when compared with those in water. Organic electrolytes increase the number of pores that are smaller than the ions, and therefore increase the number not contributing to the charge storage. The wettability of the carbon surface by the organic electrolyte, which is determined by the chemical affinity between the two may be another reason. Salitra and co-workers have concluded that a pore size above 0.4 nm can be active in EDL charging in aqueous solution [477]. The studies by the Beguin group also concluded that the optimal pore size for EDL capacitance is 0.7 nm in aqueous media and 0.8 nm in organic electrolytes [481]. All these findings have shown the essential role of micropores that are electrochemically accessible by the

electrolyte ions on the capacitance performance. More recent studies by Largeot et al. have clearly demonstrated the relationship between ion size and pore size for an EDLC using carbide-derived-carbons (CDCs) and concluded that the maximum EDL capacitance is achieved when the pore size matches with the ion size [484].

Besides the porous structure of ACs, the surface functionalities also play important roles on the carbon electrode performance, as they will affect the wettability of the carbon surface by the electrolyte ions and give additional pseudo-capacitance [482,485,486]. An activated carbon containing a high concentration of oxygen-functional groups with low porosity (BET specific surface area =  $270 \text{ m}^2\text{g}^{-1}$ ) has been prepared by one-step carbonization of an oxygen-rich carbon precursor [482]. The material showed a good electrochemical performance with a high energy density of  $10 \text{ Wh kg}^{-1}$  even at high power densities close to  $10 \text{ kW kg}^{-1}$  in acidic electrolyte. Moreover, good capacitance values were still retained after 10000 cycles, indicating few catalytically active sites on the carbon surface, probably due to the comparatively low surface area. However, most commercial supercapacitors use organic electrolytes because of the higher operating voltages, which offer a higher energy density. Pandolfo and Hollenkamp have given an overview of ACs with various types of functional groups and pointed out that the presence of some active surface oxides and a trace amount of water result in instability of the electrode, an increase of series resistance and the decomposition of the organic electrolyte [485]. Some other studies also showed the aging of AC electrodes in organic electrolytes due to the active surface of carbon [483,487]. Therefore, surface functionality and porosity of ACs should be optimized for improved long-term performance. Pure ACs without heteroatoms and water might be better for use in an organic electrolyte.

In short, ACs have been commercially used as supercapacitor electrode materials. However, their applications are still restricted to only certain niche markets due to the limited energy storage and rate capability. Although activated carbons provide a high surface area, the control of pore size distribution and pore structure is still challenging. Therefore, designing ACs to have narrow pore size distribution (accessible to the electrolyte ions)

with an interconnected pore structure and short pore length together with controlled surface chemistry would be beneficial for enhancing the energy density of supercapacitors, without deteriorating their high power density and cycle life.

### 3.1.1.2 CNTs

The discovery of CNTs has significantly advanced the science and engineering of carbon materials. As discussed previously, the major factor that determines the power density is the overall resistance of the components in a supercapacitor. Carbon nanotubes, due to their unique pore structure, superior electrical properties, and good mechanical and thermal stability, have attracted a great deal of attention for supercapacitor electrode applications [488–490]. CNTs can be categorized as single-walled carbon nanotubes (SWNTs) or multi-walled carbon nanotubes (MWNTs), both of which have been widely explored as energy storage electrode materials. CNTs are usually regarded as the choice of a high-power electrode material because of their good electrical conductivity and readily accessible surface area. Moreover, their high mechanical resilience and open tubular network make them a good support for active materials. The energy density is, however, a concern due to their relatively small specific surface area (generally  $< 500 \text{ m}^2\text{g}^{-1}$ ) as compared to ACs. Of greater importance is the difficulty in retaining the intrinsic properties of individual CNTs on a macroscopic scale [491] and the high purity and electrolyte-dependent capacitance performance [492].

Niu et al. have reported a MWNT-based supercapacitor electrode showing a high specific capacitance of  $102 \text{ Fg}^{-1}$  with surface area of  $430 \text{ m}^2\text{g}^{-1}$  and a power density of  $8 \text{ kW kg}^{-1}$  in an acidic electrolyte [493]. It should be taken into account that recent studies have shown that entangled CNTs are less efficient in facilitating fast ionic transportation when compared to aligned CNTs, due to the irregular pore structures and high entanglement of the CNT structure in the former [494]. Hence, the use of aligned CNT seems to be more advantageous in terms of power performance. Futaba and co-workers have presented a method to fabricate a densely packed aligned SWNT solid by using the zipping effect of liquids, which allowed the bulk

materials to retain the intrinsic properties of the SWNTs [491]. The energy density of the obtained SWNT solid was about  $35 \text{ Whkg}^{-1}$  (normalized to a cell consisting of two identical electrode materials) in organic electrolyte, and the rate capability was better than that of ACs. These studies showed the importance of the aligned tubular structures and preserved intrinsic CNT properties on the electrochemical performance of the electrode materials.

Research has been undertaken to improve the energy density of CNTs by increasing their specific surface area via chemical activation (KOH activation) [485]. However, a proper balance between the porosity and the conductivity must be achieved in order to have both high capacitance and good rate performance. Recently, an interesting CNT–aerogel composite material was synthesized by uniformly dispersing a carbon aerogel throughout the CNT host matrix without destroying the integrity or reducing the aspect ratio of the CNT [495]. A high specific surface area of  $1059 \text{ m}^2\text{g}^{-1}$  and extremely high specific capacitance of  $524 \text{ Fg}^{-1}$  were obtained, but at the expense of a tedious preparation pathway. Another way to enhance the specific capacitance is by modification of CNTs with active materials to realize pseudo-capacitance through faradic processes [496].

In spite of having excellent properties, the limited surface area of CNTs restricted their use as high energy performance EDLCs. In addition, the present difficulty in purification and high cost of production still hinder their practical applications.

### 3.1.1.3 Graphene and reduced graphene oxide

Graphene is considered to be an excellent electrode material for supercapacitors because of its high electrical conductivity, high surface area, great flexibility, excellent mechanical properties, and rich chemistry [497]. Chemically modified graphene (CMG) sheets can physically adjust themselves to be accessible to different types of electrolyte ions, free from the use of conductive fillers and binders. Besides, its flexibility facilitates an easy fabrication of supercapacitor devices [498]. Studies have shown that the specific capacitances of graphene can reach  $135 \text{ Fg}^{-1}$ ,  $99 \text{ Fg}^{-1}$  and  $75 \text{ Fg}^{-1}$  in aqueous, organic, and ionic liquid electrolytes, respectively [499,500]. Despite the intense interest and continuous report on

experimental observations, real applications of graphene have yet to be realized. This is mainly due to the difficulty in reliable production of high-quality graphene from a scalable approach [501]. While mechanical exfoliation produces graphene with the highest quality, the method is neither high throughput nor high yield. Zhao et al. [502] employed the chemical vapor deposition method to synthesize carbon nanosheets composed of graphene layers on conventional carbon fibers and carbon papers. It was found that such carbon nanosheets possess a capacitance value of  $0.076 \text{ Fcm}^{-2}$  (based on the geometric testing area) in a  $\text{H}_2\text{SO}_4$  solution. Hence, the total capacitance was estimated to be  $1.49 \times 10^4 \text{ F}$  based on a virtual supercapacitor device rolled in a sandwich pad with a given dimension.

The experimentally observed capacitances are mainly limited by the agglomeration of graphene sheets and do not reflect the intrinsic capacitance of an individual graphene sheet. Recently, an experimental determination of EDL capacitance ( $\sim 21 \mu\text{F cm}^{-2}$ ) and quantum capacitance of single layer and double-layer graphene were reported [503]. In order to harness the unique properties of graphene, graphene- and GO-based composite materials have been explored [504]. In this respect, graphene-conducting-polymer composites have received a great interest [505–507]. Cheng and co-workers [505] prepared a graphene/polyaniline composite paper (GPCP) by in situ anodic electropolymerization of aniline monomer as a PANI film on graphene paper. The obtained composite paper combines flexibility, conductivity and electrochemical activity and exhibited a gravimetric capacitance of  $233 \text{ Fg}^{-1}$  and a volumetric capacitance of  $135 \text{ Fcm}^{-3}$ . A graphene nanosheet/polyaniline (GNS/PANI) composite was also synthesized using the polymerization method [507]. Graphene (about 15 wt%) was homogeneously coated on the surface of PANI nanoparticles. A specific capacitance of  $1046 \text{ Fg}^{-1}$  was observed at a low scan rate. The energy density of the composite could reach  $39 \text{ Wh kg}^{-1}$  at a power density of  $70 \text{ kW kg}^{-1}$ . Although graphene nanosheets are excellent electrode materials, the use of highly toxic reducing agents, such as hydrazine and dimethylhydrazine, remains a serious issue for large-scale production. Murugan and co-workers [506] demonstrated a microwave-assisted solvothermal process to produce graphene nanosheets without the need for

highly toxic chemicals. The authors investigated the energy storage properties of these thus-prepared graphene nanosheets and associated PANI composites. The graphene/PANI composite with 50 wt% graphene displayed both EDL capacitance and pseudocapacitance with an overall specific capacitance of  $408 \text{ Fg}^{-1}$ . Zhang et al. prepared a series of CMG and PANI nanofiber composites using an in situ polymerization method [508]. PANI fibers were observed to adsorb on the graphene surface and/or filled between the graphene sheets. The composite displayed a specific capacitance as high as  $480 \text{ Fg}^{-1}$  at a current density of  $0.1 \text{ Ag}^{-1}$ . The results showed that good capacitive performance can be obtained by doping either graphene with a small amount of PANI or bulky PANI with a small amount of graphene.

Based on the brief summary presented on graphene-based materials for supercapacitors, it can be concluded that although most of the research has only been at a peak since 2008, graphene based materials are indeed very fascinating materials with great potential in the active field of supercapacitors. In theory, graphene has been considered to be the ideal supercapacitor electrode material due to its extremely large surface area, extraordinarily high electrical conductivity, and strong mechanical strength. In practice however, massive efforts are still needed to turn this promising material into a real practical material. The most essential problem lies in how to prepare large-scale and high-quality graphene-based materials in a cost-effective way. Until now, two methods –the chemical exfoliation of graphite into graphene oxide followed by controllable reduction to make reduced graphene materials or the in situ reaction (with transition metal oxides or conducting polymer precursor) to fabricate graphene-based composite materials– have been widely investigated and deemed as the most promising for producing supercapacitor electrodes. Another challenge is that graphene material is easy to re-stack, which causes the decline of its physical properties and processability. Some efficient methods, including the functionalization of graphene or the addition of spacers between the graphene layers, have been presented to solve this problem [509].

For the graphene-based EDLC applications, the conductivity and large specific surface area of graphene are two crucial factors for making high-

performance supercapacitors. A series of effective routes, such as low-temperature thermal exfoliation, solvothermal processing, microwave heating, introduction of spacer materials, and activation, have been utilized to reduce GO, to restore the conductivity and intrinsic specific surface area of graphene as much as possible, and to tune for the proper spacing size needed for the intercalating of ions. However, achieving a state with individual graphene layers and fully utilizing the specific surface area of perfect graphene is still a challenge, and thus future efforts are still needed for the development of more efficient fabrication techniques in order to reach enhanced performance [509].

#### **3.1.1.4 Templated ordered mesoporous carbons**

A templating method offers another effective way to produce nanostructured carbons with well controlled narrow pore size distributions, ordered pore structures, large specific surface areas and an interconnected pore network, making them promising candidates for supercapacitor electrode materials. There has been remarkable progress in the synthesis of ordered nanostructured carbons through templating techniques [510]. In general, the preparation procedure of templated carbons is infiltration of a carbon precursor into the pores of the template, followed by a carbonization treatment and finally the removal of the template to leave behind a porous carbon structure. Various carbon structures with well controlled micropores, mesopores and/or macropores produced from different types of template and carbon precursors have been studied for supercapacitor applications [511–516]. A functionalized microporous carbon material was obtained by using zeolite Y as a template and the resultant carbon material possessed a high gravimetric capacitance of about  $340 \text{ Fg}^{-1}$  in aqueous electrolyte with good cyclability (over 10000 cycles) [511]. Compared to ACs, whose micropores are essentially disordered and broad in pore-size distribution, the templated microporous carbons with a narrow pore size distribution, well adapted pore size to the electrolyte ions and the ordered straight pore channels are better for use as high-energy-density electrode materials. Moreover, the well-controlled porous structure facilitated an efficient use of pseudo-capacitance from the nitrogenated and oxygenated functionalities of the carbon materials.

It has been proposed that the presence of mesopores (usually 2–8 nm) can accelerate the kinetic process of the ion diffusion in the electrodes and improve the power performance at high current densities, whereas micropores that are accessible to the electrolyte ions are essential for high energy storage [513,517,518]. Wang and co-workers have reported a 3-dimensional (3D) hierarchical porous graphitic carbon (HPGC) material with macroporous cores, mesoporous walls and micropores for high rate supercapacitor applications [513]. In their designed hierarchical structure, macropores serve as ion-buffering reservoirs; the graphitic mesopore walls provide excellent electrical conductivity, capable of overcoming the primary kinetic limits of electrochemical process in porous electrodes. In addition, the presence of micropores can enhance the charge storage. Yamada's group have also synthesized ordered porous carbons containing meso/micro/macropores with large surface areas by a colloidal-crystal templating technique [519]. A high EDL capacitance of 200–350  $\text{Fg}^{-1}$  was achieved in an acidic electrolyte solution. Their investigation on pore-dependent capacitance properties have revealed that the micropores adjacent to the open mouths of pores are effective in charge storage, and larger pores that are interconnected are important for smooth electrolyte transportation. Hence, carbon materials having well controlled hierarchical porous structures would be favorable for designing high performance EDLC electrodes.

The templating method has been shown to be one of the most suitable techniques to control the preparation of porous materials, especially ordered porous solids. Through careful selection of the template materials as well as the carbon precursors, and with good control over the carbonization process, nanoporous templated carbons with desirable physical and chemical properties can be obtained. In view of their relatively high cost of production, development of a simple, economical and environmentally benign template route would be advantageous for their future application. Despite the cost, templated carbons are good materials to study, which provide valuable information about the effect of pore size, pore shape, channel structures and other parameters on the ion diffusion and charge storage in the nanoconfined system.

### 3.1.1.5 Other carbons

Other carbon structures such as activated carbon fibers (ACFs), carbon aerogels (CAGs) and carbon onions have also been studied for supercapacitor applications. The general rules for the selection of supercapacitor electrode materials are a high and accessible specific surface area with good electrical conductivity. ACFs typically have high specific surface areas, up to  $3000 \text{ m}^2\text{g}^{-1}$ , and a more or less controllable pore size distribution [520]. They are usually produced from the carbonization of pre-formed fibrous carbon precursors followed by activation processes. A high capacitance value of  $371 \text{ Fg}^{-1}$  in KOH electrolyte solution was reported recently. However, such a high specific surface area together with the presence of surface functional groups may cause a long term stability problem [468]. In addition, the cost of ACF production is generally higher than AC. CAGs are another interesting material suitable for use as a supercapacitor electrode. They are ultralight, highly porous materials, predominantly with mesopores, and have the possibility of usage without binding substances. CAGs are typically fabricated through a sol-gel process with subsequent pyrolysis of the organic aerogels. The special porosity of a CAG is based on the interconnection of colloidal-like carbon nanoparticles. In a report by Fang et al. [521] due to the dominance of mesopores (42 nm), the EDL capacitance was not so effective in CAG-based electrode materials. Hence, an additional activation process was employed to further increase the specific surface area by introducing microporosity. Despite a large increase in the total surface area (from 592 to  $2371 \text{ m}^2\text{g}^{-1}$ ), the improvement on the charge storage capacity was relatively small, especially at high discharge rates, which was assumed primarily to be due to the inaccessibility of the micropores produced during the activation and the relatively high internal resistance of the CAG matrix. Nevertheless, a new type of carbon nanotube aerogel electrode material gave promising capacitive properties, despite the difficulty in preparation [495].

### 3.1.2 Objective

As reviewed in the first part of the introduction, a wide range of carbon materials have been investigated so far for the supercapacitor applications.

Conventional A.C.s as the most widely used materials for supercapacitors, along with benefits such as high surface area and relatively low cost, still suffer from intrinsic problems such as majority of micropores reducing the accessibility of the ions as well as limited electrical conductivity. Therefore, the search for new materials has been continued leading to investigations on newer materials such as CNTs, graphene, OMCs, and other carbon species.

In particular, exploitation of CNTs and graphene in this field has caused a significant impact on the potentials and promises of the supercapacitors. Accordingly, it is intended through this work, with focus on CNTs and RGO, to conduct a systematic and comparative study on the behavior of each species as an active material for the supercapacitors. Furthermore, it is aimed to evaluate different performance characteristics of these materials as compared with the traditional A.C. material.

A thoroughly laboratory based program has been designed and followed for preparation of the active materials, preparation of the supercapacitor electrodes and microstructural and electrochemical characterizations. As explained in chapter 2, CNTs were prepared through fluidized bed CVD method and the graphene type used was prepared by reduction of GO.

Regarding the already known features of each of these materials, like high electrical conductivity, high degree of crystallinity, relatively low surface area and good corrosion resistance of CNTs along with high specific surface area and intermediate conductivity level of RGO, it was also tried to conduct a principled study on the composites made these materials and A.C., leading to formation of three classes of electrodes, namely, A.C.–CNT, A.C.–RGO and A.C.–CNT–RGO, within each, a compositional sweep was accompanied by a thorough electrochemical characterization.

It was believed that such comprehensive and comparative study is necessary for understanding the ways each material influences the supercapacitor's performance and the extent to which, the final behavior of the cell could be fine tuned as a function of electrode composition. Accordingly, for the electrochemical characterization of the electrodes, variety of techniques including charge–discharge, cyclic voltammetry and electrochemical impedance spectroscopy were used and parameters such as specific

capacitance, energy and power density, rate capability, internal resistance and max power at matched impedance condition, ideality of the performance, frequency response and relaxation time and finally durability of all electrodes were evaluated and compared.

## 3.2 Experimental

### 3.2.1 Carbon supports preparation

#### 3.2.1.1 CNTs synthesis and purification

Synthesis of CNTs and their purification was carried out the same way explained in details in sections 2.2.1.1 and 2.2.1.2, respectively. Briefly, the CNT synthesis consisted of catalytic growth of CNTs on a metallic iron-based catalyst supported on neutral  $\gamma$ -alumina in fluidized bed CVD reactor at 650 °C using  $C_2H_4$  as the carbon precursor. The purification consisted of refluxing the synthesized CNTs (at 110 °C for 5 h) in an acid mixture consisting of sulfuric and nitric acids ( $H_2SO_4$ : 4 M and  $HNO_3$ : 1 M), followed by multiple washing and drying.

#### 3.2.1.2 GO synthesis

Preparation of the GO, except in few points, was exactly similar to the procedure described in details in section 2.2.1.3. The main difference was in the reference method to be followed. In section 2.2.1.3, a modified Hummer's oxidation process [445] was followed. Basically, three original synthesis methods form the background of all variations in GO synthesis.

The first, well-known example came in 1859 by British chemist B. C. Brodie [522]. His method consisted of oxidation of graphite via addition of "potash of chlorate" (potassium chlorate;  $KClO_3$ ) to a slurry of graphite in fuming nitric acid ( $HNO_3$ ). Nearly 40 years later, L. Staudenmaier improved Brodie's  $KClO_3$ -fuming  $HNO_3$  preparation by the addition of concentrated sulfuric acid, to increase the acidity of the mixture, and in the meanwhile, adding the chlorate in multiple aliquots over the course of the

reaction [523]. And finally, 60 years after Staudenmaier, Hummers and Offeman developed an alternate oxidation method by reacting graphite with a mixture of potassium permanganate ( $\text{KMnO}_4$ ) and concentrated sulfuric acid ( $\text{H}_2\text{SO}_4$ ) [524]. Very recently, a modified version of Hummers method, based on the addition of concentrated phosphoric acid ( $\text{H}_3\text{PO}_4$ ) to concentrated sulfuric acid ( $\text{H}_2\text{SO}_4$ ) as the acid medium, has been introduced by Tour which has obtained popularity in the field [525].

In the current work, we used a combination of Staudenmaier and Hummers methods. More precisely, our acid medium was borrowed from the Staudenmaier's work by mixing the fuming  $\text{HNO}_3$  and concentrated sulfuric acid ( $\text{H}_2\text{SO}_4$ ) and our oxidizing agent was borrowed from Hummers work by making use of potassium permanganate ( $\text{KMnO}_4$ ).

Typically, 5 g of Highly Oriented Pyrolytic Graphite powder ( $<40\ \mu\text{m}$ , Sigma-Aldrich®) was added into 180 mL concentrated (96%)  $\text{H}_2\text{SO}_4$  and stirred for 1 h under a hood. Then 60 mL fuming (65%)  $\text{HNO}_3$  was slowly added to the mixture under ice-cooling and stirring. After cooling down, 25 g  $\text{KMnO}_4$  was slowly added under ice-cooling and stirring. The mixed slurry was stirred at room temperature in a hood for 120 h. 600 mL of deionized (DI) water was then slowly added into the reacted slurry and stirred for 2 h. During this process a temperature rise has been observed. Then, 30 mL (36%)  $\text{H}_2\text{O}_2$  was added in order to oxidize the remaining reagents and the slurry immediately turned into a bright yellow-green solution with bubbling. The resultant solution was stirred for 2 h and then allowed to deposit on the bottom of the beaker for 24 h. Afterwards, the supernatant was decanted. To remove the ions of oxidant and other inorganic impurities, the resultant yellow-green slurry was centrifuged (10000 rpm, 30 min) and then washed in 2 L DI water with 10 mL (37%)  $\text{HCl}$  and 6 mL (36%)  $\text{H}_2\text{O}_2$  added (5 cycles). Finally, the resultant slurry was purified by successive stirring and sonication in 2 L of pure DI water followed by centrifugation and supernatant decanting. This procedure was repeated until the pH of the suspension increased to almost neutral (e.g., more than 5, which took about 5–10 washing cycles). The remaining dark-yellow solid was dried using a vacuum evaporator (Rotavapor) at  $40\ ^\circ\text{C}$  for 48 h and the dried powder (10 g of GO) was collected. The choice of low

drying temperature was to avoid deoxygenation (partial reduction) of GO which initiates slowly above 60 to 80 °C.

### 3.2.1.3 GO reduction

GO reduction and preparation of RGO was carried out based on a thermal reduction procedure under controlled atmosphere. In particular, 1 g of GO was wrapped in an aluminum foil and placed in tubular furnace with quartz tube and heated up to 600 °C with a heating rate 10 °Cmin<sup>-1</sup>. The choice of the temperature was just based on the limitation of Al foil melting temperature. However, based on the reports in the literature, the higher the temperature of the thermal reduction, the better the degree of reduction. The reactor tube was purged with a flow of 100 sccm N<sub>2</sub> and 100 sccm H<sub>2</sub> since the beginning of heating. At the beginning of the heat-up step around 160–170 °C a robust exfoliation of GO takes place that if the proper safety measures are not considered, can be explosive and dangerous. For this reason, each reduction batch did not contain more than 2 g of GO (most often only 1 g) and the wrapping in Al foil was always loose and accompanied with introduction of a number punctures in the foil to allow the pressure build-up caused by the exfoliation to release. Also the exhaust of the tubular oven was immersed in water tank for bubbling and upon exfoliation, the gas wave could be easily discharged and leave the reactor. Upon arrival to the set temperature, 600 °C, a 20 sccm flow of ethylene (C<sub>2</sub>H<sub>4</sub>) was allowed since a carbon source is known to help the reconstruction of the damaged structure of GO during reduction. A reduction duration of 30 min was considered for each batch, after which, the ethylene flow was interrupted and the RGO was cooled down slowly under the flow of 100 sccm N<sub>2</sub> and 100 sccm H<sub>2</sub> to room temperature. The exfoliated and reduced black RGO powder was then collected and weight controlled. Typically, a yield of 20–25 wt% was obtained (i.e., 200–250 mg RGO out of 1 g GO).

### 3.2.2 Microstructural characterization

Active materials (different types of carbon) were characterized for phase analysis by X-ray diffraction (XRD) technique using an 1830 PW Philips

X-ray generator equipped with a PW 3020 Philips goniometer and a PW 3710 Philips control unit. The radiation used was Cu K $\alpha$  ( $\lambda = 1.540 \text{ \AA}$ ), with scan step time of 1.00 s and step size ( $2\theta$ ) of  $0.02^\circ$  having the sample in the Bragg–Brentano configuration.

Microstructural characterizations of the active materials and the prepared pastes were carried out using scanning electron microscope (SEM, using either a Zeiss EVO 50 EP equipped with energy dispersive X-ray (EDX) or a Stereoscan 360 Cambridge SEM instrument). Nanostructure of the the active materials was characterized with a transmission electron microscope (TEM, Philips CM200 FEG) equipped with a field emission gun with Schottky emitter operated at 200 kV.

Thermo gravimetric analysis (TGA) was performed in Oxygen by using PerkinElmer Simultaneous Thermal Analyzer (STA 6000) at a heating rate of  $10 \text{ }^\circ\text{C min}^{-1}$  up to  $900 \text{ }^\circ\text{C}$ .

### 3.2.3 Electrode preparation

Electrodes for supercapacitor testing were prepared based on a paste method. Each batch of paste preparation consisted of 82 wt% of the active materials and 18 wt% of the binder. As the binder, Poly(vinylidene fluoride) (PVDF, Aldrich) ground to powder form was use. Active materials included activated carbon (Activated Charcoal Norit<sup>®</sup>), lab-made CNTs and lab-made RGOs. The type of activated carbon (A.C.) used, was not a supercapacitor grade. Although Activated Charcoal Norit<sup>®</sup> did not possess a good electrical conductivity, no conductive type of carbon was added to the mixture in order to assess the effect of addition of supposedly well conductive lab-made CNTs and RGOs on the performance of the supercapacitor.

In a typical paste preparation procedure for preparation of 2 g of the final paste, 0.36 g PVDF was immersed in the appropriate amount of an organic solvent, namely, 1-Methyl-2-pyrrolidinone (NMP, Sigma-Aldrich) and heated at  $70 \text{ }^\circ\text{C}$  for complete dissolution. There was not specific restriction on the amount of NMP and it just depended on the type of active materials to be used in a given paste. For the pastes consisting of a major part of

heavy and low expandability powders like A.C., lower amount of NMP was used (15 ml), whereas for paste consisting of a reasonable amount of CNTs or RGOs, more NMP (40-50 ml) was used. In any condition, the NMP content is just important for controlling the viscosity and thickness of the paste upon casting after which, it should be completely evaporated.

Having the PVDF completely dissolved in NMP, the active materials (different fractions of A.C., CNT and RGO, kept in the oven at 100 °C overnight for complete drying) were added to the solution and stirred for 30 min. Then, a handheld ultrasonic homogenizer (UP200Ht Hielscher Ultrasonic Technology) was used to homogenize and disperse the soaked powders, for 2 min. A considerable volume expansion of the paste was observed in this step for the batches containing 10 wt% or more of CNT or RGO in the active materials, while no change was observed for the batches containing basically A.C. only. Then the suspension was left on the heating plate (80–90 °C) and under stirring until the appropriate viscosity and thickness was obtained by evaporation of the excess NMP. This could take 8–10 h depending on the primary content of NMP. Then, the paste was transferred to a mixer (ULTRA-TURRAX<sup>®</sup> Tube Drive control, IKA) and dispersed at 3000 rpm for 2 h (typically, 6 stainless steel balls were used for mixing 2 g of paste).

When the paste was ready, an appropriate amount was cast on a graphite sheet (Graphite foil, 1mm thick, 97% (metals basis impurities), Alfa Aesar) with spatula and was homogeneously spread with a thickness of 500 µm using doctor blade. The paste coated graphite sheet was then heated at 75 °C in the oven for 10 min to partially dry the paste (almost 50% drying should not be exceeded otherwise the punching step would result in cracking and detachment of the paste) and then circular electrodes (12 mm diameter) were punched out of the sheet. Fig. 3.2 shows schematically the steps of electrode preparation. The punched electrodes were then completely dried. Complete final drying conditions depend a lot on the type of active materials. Electrodes made of only A.C. or RGO could stand the heating

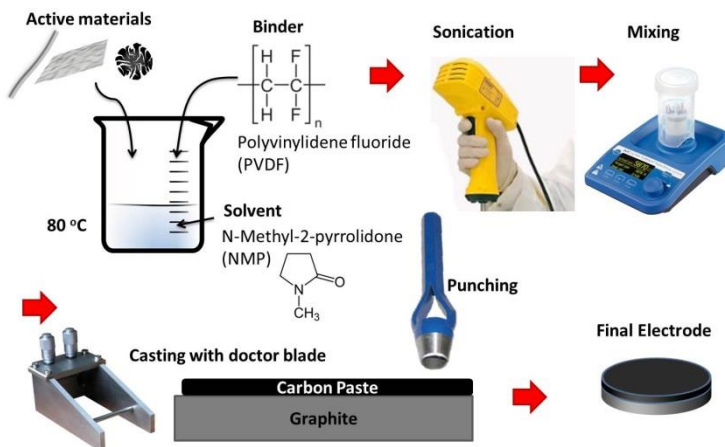


Fig. 3.2 Illustration of the preparation steps of supercapacitor electrodes.

without problem and therefore, were dried at 85 °C for 2 h. In contrast, electrodes containing even minimum content of CNT were vulnerable to cracking even in room temperature drying. Accordingly, CNT containing electrodes or other types susceptible to cracking were partially dried and before the initiation of any cracking were immersed in the proper electrolyte for supercapacitor testing. The final thickness of the active layer after complete drying was obviously different from the 500  $\mu\text{m}$  as cast condition and varied sample to sample depending on the type of the active materials.

Careful weight measurement of the electrodes was carried out after complete drying and weight of active material on each type of electrode was evaluated by statistical comparison of the weight of a population of each batch with weight of bare graphite sheets punched with the same size. For the batches where the active material was vulnerable to cracking, a larger number of electrodes were prepared and a part of them were soaked upon partial drying and before the start of cracking and the rest of electrodes were fully dried just for weight measurement purpose.

### 3.2.4 Electrodes classification

Based on the initial materials used, i.e., A.C., CNT and RGO, different classes of electrodes were prepared and studied. First of all, electrodes made of only pure initial materials were characterized as references. Then, composite electrodes of A.C.–CNT, A.C.–RGO, A.C.–CNT–RGO, and CNT–RGO were also prepared and characterized in order to form a systematic study based on the composition of the paste.

It is worth mentioning that usually, in the literature of the field, the specific values of the supercapacitor are reported on the basis of weight of the active materials only and the contribution of the binder is neglected. Although in the industrial point of view, the specific values should be reported with the consideration of the final weight of the product including not only the binder, but also the current collectors and packaging, in laboratory scale, the focus is limited to active materials. Nevertheless, in this work, we included also the weight of the binder in calculation of the specifications of the supercapacitor. In fact, the total weight of the dried paste on current collector has been considered as the active weight that although is a realistic and practical assumption, will result in reduced specific values being reported in this work.

Accordingly, the entire range of the electrodes prepared and studied is summarized in Table 3-1 with a comment on the naming protocol used for referring to different samples. That is, the contribution of the binder (18 wt%) should be considered for all the names reported in the Table 3-1, though it is not appearing for the sake of simplicity and brevity. For instance, the sample called “A.C. pure”, is the sample in carbon part of which, only A.C. has been used. However, the final dried paste of this electrode consists of A.C. 82 wt% + PVDF 18 wt%. As another example, the sample called A.C.– 25% CNT, is referring to a final dried paste consisting of A.C. 57 wt% + CNT 25 wt% + PVDF 18 wt%.

Table 3-1 Compositions of the supercapacitor electrodes prepared and characterized.

Samples	Weight percent (wt%)			
	A.C.	CNT	RGO	PVDF
A.C. pure	82	0	0	18
A.C. - 5%CNT	77	5	0	18
A.C. - 15%CNT	67	15	0	18
A.C. - 25%CNT	57	25	0	18
A.C. - 50%CNT	32	50	0	18
CNT pure	0	82	0	18
A.C. - 5%RGO	77	0	5	18
A.C. - 15%RGO	67	0	15	18
A.C. - 25%RGO	57	0	25	18
A.C. - 50%RGO	32	0	50	18
RGO pure	0	0	82	18
A.C. - 25%CNT - 5%RGO	52	25	5	18
A.C. - 25%CNT - 15%RGO	42	25	15	18
A.C. - 25%CNT - 25%RGO	32	25	25	18
RGO-25%CNT	0	25	57	18

### 3.2.5 Electrochemical characterization

Electrochemical characterizations were carried out in a two electrode configuration (packed cell) with equal active material loading on positive and negative electrodes (symmetric) using a flat cell consisting of two gold-coated copper current collectors and a PTFE body as schematically shown in Fig. 3.3. The electrodes prepared according to aforementioned procedure were soaked for 5 h in the electrolyte before testing.

As the electrolyte medium and also separator in the packed cell, cellulose-type papers (thickness 25  $\mu\text{m}$ ) were soaked in the same electrolyte as electrodes and were placed between the two facing electrodes. As the electrolyte, a 1 M  $\text{Na}_2\text{SO}_4$  solution was used.

All the electrochemical measurements were carried out using a ModuLab<sup>®</sup> XM ECS high-performance potentiostat / galvanostat system (Solartron

Analytical, XM PSTAT 1 MS/s) coupled with a frequency response analyzer (Solartron Analytical, XM FRA 1MHz) for AC measurements and of the electrochemical impedance spectroscopy. Three different electrochemical techniques were used to fully characterize the electrodes, namely, cyclic voltammetry (CV), galvanostatic charge-discharge (CD) and electrochemical impedance spectroscopy (EIS).

CV tests were carried out in a potential window of 0 – 1 V and at four different scan rates, including 5, 20, 50 and 100 mVs<sup>-1</sup>.

CD tests were carried out with specific currents ranging from 0.1 to 3 A g<sup>-1</sup> at seven different steps (with respect to the mass of active material on a single electrode) in a potential window of 0 – 1 V. Medium term cyclability (life cycle) of the samples was evaluated based on a course of 1000 CD cycles in a potential window of 0 – 1 V at a CD rate of 1 A g<sup>-1</sup>. Long term cyclability (life cycle) of the samples was evaluated based on a course of 10000 CD cycles in a potential window of 0 – 1 V at a CD rate of 1 A g<sup>-1</sup>.

EIS measurements were performed at open circuit potential (OCP) using a 10 mV excitation signal, in the frequency range from 100 kHz to 10 mHz, sampling 10 points per decade.

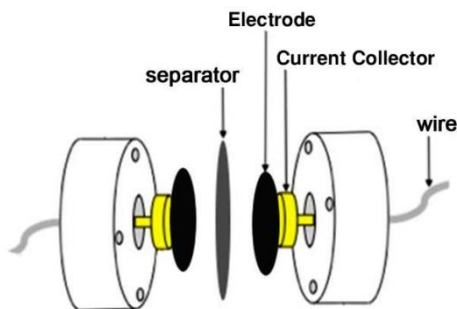


Fig. 3.3 Schematic presentation of the cell used for electrochemical measurements.

The order of different electrochemical measurements to be carried out on each sample was organized based on a comprehensive protocol to allow the

assessment of different aspects of the material's behavior. The diagram of Fig. 3.4 shows schematically the established electrochemical characterization protocol. As seen, complete characterization of each electrode has been achieved under three different categories of measurements. First, the general behavior of the electrode is characterized using CVs. Second, the comprehensive characterization is carried out based on CDs, by use of which, not only the specific capacitance is measured and checked with the CV results, but also the energy and power densities are

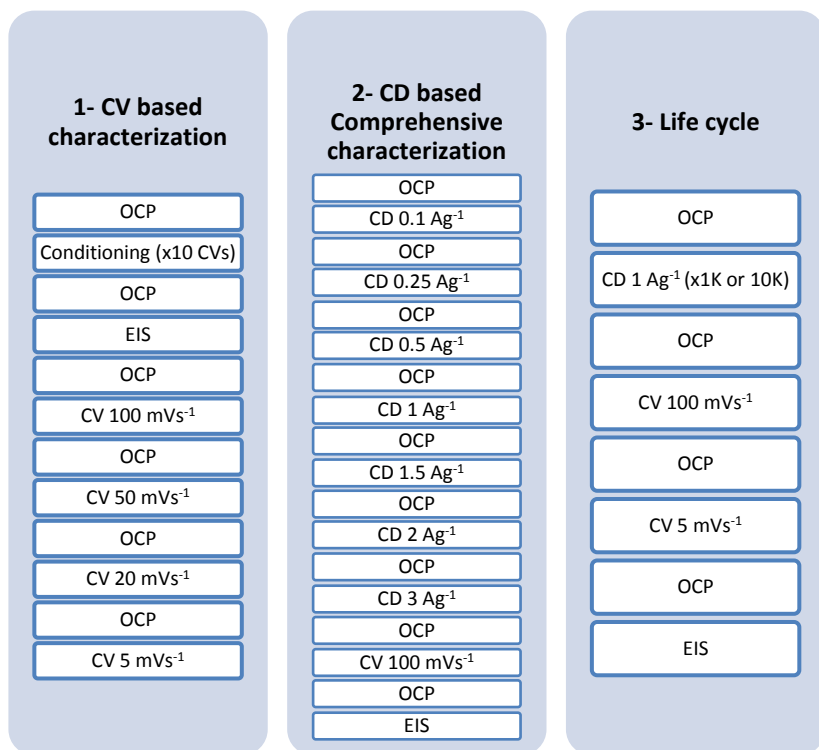


Fig. 3.4 Diagram of the protocol adopted for comprehensive electrochemical characterization of the electrodes.

measured and the Ragone plot is simulated. Internal resistance of the cell is also measured in this step and is used for calculation of the maximum

power possible for the supercapacitor (matched impedance power). At the beginning of the first and at the end of the second stage, EIS measurements are carried out and compared to each other. They are also used as the third criterion for specific capacitance measurement. Moreover, relaxation time of the supercapacitor is also evaluable based on the EIS results. Provision of a OCP step between each two successive characterization is just a simple tool to give a short relaxation to the cell before the next step starts. Finally, at the third stage, life behavior of the electrode is characterized (either medium or long term cycling, as desired). Also the end of the third stage, control CV and EIS measurements have been adopted to be checked to primary results. Obviously, depending on the sample's behavior and the desired information, appropriate modifications in the general protocol have been exploited where required.

### 3.2.6 Conductivity measurement

Electrical conductivity measurements were carried out using a home-made cell designed based on the proposal of Ref. [526,527] for the conductivity measurement of powder materials. The home-made cell consists of a thick isolating PTFE die (inner diameter 6.1 mm), vertically fixed on a heavy circular copper support containing a stationary piston (with a diameter of 6.1 mm, screwed in the PTFE cylinder) that closes the bottom of the cylinder. A close-fitting copper plunger (6 mm diameter), which is allowed to move down in the cylinder, closes the compression chamber. After filling the chamber with an accurately weighed amount of powder, the load applied on the piston was controlled by standard weighing masses, varying from 2 to 150 N (including the weight of the upper piston), which resulted in a pressure range from 72 kPa to 5.27 MPa (regarding the  $2.83\text{E-}05\text{ m}^2$  area of the piston/cylinder). Fig. 3.5 shows schematically the cell used for conductivity measurements. The dc electrical resistance of the compressed powders was measured using a potentiostat by the linear potential sweep method. The slope of the E-I curve was considered as the resistance of the powders due to ohm's law. The measurement was carried out at different load/pressures in the aforementioned range and each time the change in the

height of the powder ( $h$ ) and the resistance were recorded. The conductivity at each pressure was then calculated using the following equation:

$$\sigma = \frac{l}{A.R}$$

(3-1)

where  $l$  represents the powder column height, obtained by the displacement of the piston,  $A$  is the cross-section area of the piston and the measured resistance. Finally, the conductivity was plotted as a function of the applied pressure for each sample.

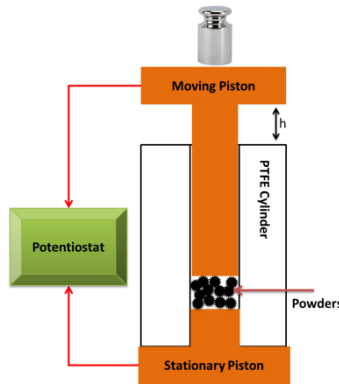


Fig. 3.5 Schematic of the conductivity measurement cell.

The electrical resistance of the cell itself (copper pistons in contact with each other plus cable contacts tightly connected to the pistons) was measured ( $55 \text{ m}\Omega$ ) and subtracted from the measured resistance of the powders.

### 3.3 Results and discussion

#### 3.3.1 Microstructural characterization of the active materials

##### 3.3.1.1 TEM studies

In order to have a clear understanding of the microstructural features of different carbon materials, TEM characterizations were carried out as shown in Fig. 3.6. As described in chapter 2 of this work, CNTs possess the same characteristics as discussed in Fig. 2.11. It is seen in Fig. 3.6 (a) that CNTs possess a homogeneous diameter size distribution in the range of 10-15 nm and the purification has successfully removed the Fe based catalyst particles from the tips or inside the channels of nanotubes. From the HRTEM image (Fig. 3.6 (b)) it is realized that CNTs are multi-walled type with 10-20 walls and interplanar spacing of 3.4 Å that is characteristic of hexagonal graphite.

Fig. 3.6 (c and d) shows the nanostructure of the GO after thermal reduction at 600 °C under mixed atmosphere of nitrogen, hydrogen and ethylene. Similar wrinkled 2D characteristics of GO (see Fig. 2.13) can be seen for RGO as well. However, local damages observed in GO (white arrows in Fig. 2.13 (a)) are not present in RGO. This can imply partial reconstruction of the atomic layers of graphene due to presence of a carbon source, e.g., ethylene, in the thermal reduction atmosphere. HRTEM image (Fig. 3.6 (d)) shows a folded sheet composed of few layers of RGO.

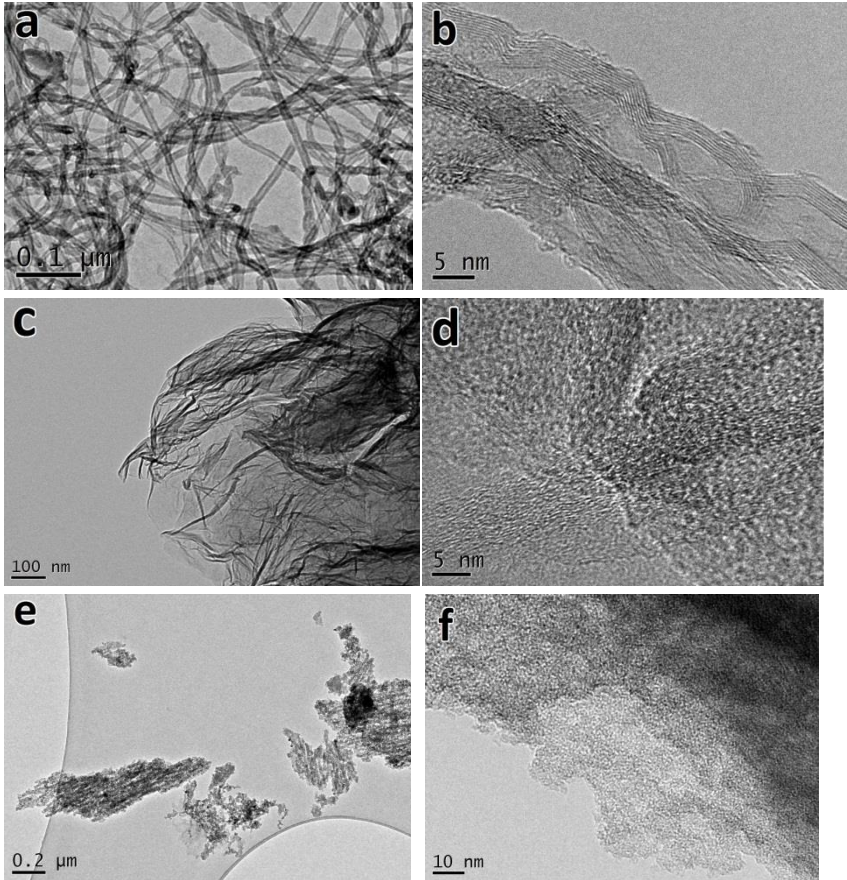


**Fig. 3.6** HRTEM and HRTEM micrographs of (a and b) CNT, (c and d) RGO and (e and f) A.C.

Finally, nanostructure of A.C. is shown in Fig. 3.6 (e and f). Large porous particles with size distribution ranging from several hundreds of nanometers to several micrometers could be observed (e.g., small particle shown in Fig. 3.6 (e)). HRTEM image of A.C. (Fig. 3.6 (f)) can hardly show any crystallinity and at best, such structure can be considered as a turbostratic

graphite. Pores of A.C. could be realized in the HRTEM image as brighter regions with various sizes.

### 3.3.1.2 XRD studies

For a better understanding of successfulness of the reduction treatment on RGO, XRD studies were carried out and are compared in Fig. 3.7. Similar to the discussion presented in Fig. 2.18, CNTs show the two characteristic reflections of hexagonal graphite at  $26.31^\circ$  for (002) and  $43.91^\circ$  for (101) planes with interplanar spacings of 3.38 and 2.10 Å, respectively, whereas, GO, shows deviation from reflections due to intensive introduction of functional groups and increased interplanar spacing. It is seen that thermal reduction has successfully removed a major part of the functional groups and thus, the characteristic deviated peaks of GO have been removed, regardless of the type of reducing atmosphere. However, thermal reduction of GO is accompanied by robust exfoliation taking place at around  $170^\circ\text{C}$

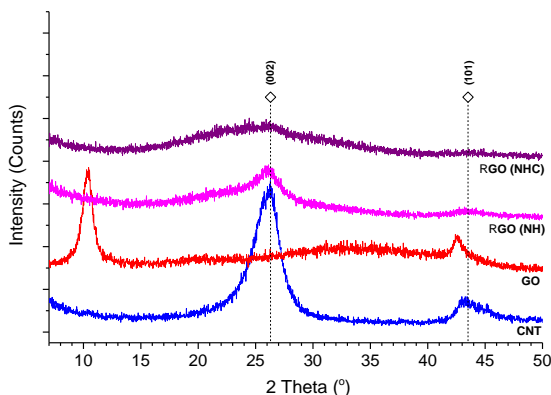


Fig. 3.7 XRD patterns of purified CNTs, GO, and RGO prepared via thermal reduction under  $\text{N}_2+\text{H}_2$  (RGO(NH)) or  $\text{N}_2+\text{H}_2+\text{C}_2\text{H}_4$  (RGO(NHC)) atmosphere.

leading to detachment and dispersion of the stacked GO powder. Therefore, in an ideal reduction, where the oxygen functional groups are removed and graphene layers are exfoliated completely, neither the reflections of GO nor

those of graphite should be observed. XRD patterns of RGO prepared under  $N_2+H_2$  atmosphere (RGO (NH)) show successful removal of GO peaks. However, presence of a little peak at the characteristic region of (002) planes of graphite suggests either a degree of restacking of the RGO layers or presence of some graphitic residues. Finally, the XRD patterns of RGO prepared under  $N_2+H_2+C_2H_4$ , (RGO (NHC)), not only show the removal of GO peaks, but also present a minimum intensity around the region of (002) planes of graphite implying the best reduction and exfoliation conditions. Accordingly, the subsequent steps of electrode preparation and electrochemical characterization were conducted based on this method of reduction and hereafter, any reference to RGO, would stand for RGO (NHC), unless otherwise stated.

### 3.3.1.3 TGA studies

Fig. 3.8 show the TGA results of the synthesized CNTs after purification as well as that of the RGO. The purification process of CNTs shows an acceptable degree of the impurities removal so as a residue of only 0.8 wt%

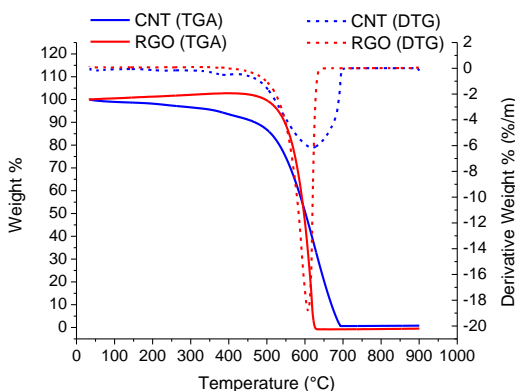


Fig. 3.8 TGA results of the purified CNTs and RGO.

is remaining after the treatment. An initial weight loss observed in CNTs below 200 °C is due to the evaporation of absorbed water molecules from CNTs. A further little groove is also observed at 385 °C that is believed to

be due to removal of unstable oxygen functional groups such as carboxyl groups. After this, only a single weight loss peak is observed centered at 619 °C that refers to the combustion of CNTs. Interestingly, the TGA results of RGO, do not show any sign of weight loss before the sharp peak of the carbon combustion at 607 °C and therefore, the removal of a major part of the functional groups by reduction is confirmed. Furthermore, regarding the final stage of the experiment at 900 °C, absolutely no residue has remained, demonstrating that the washing and purification treatments carried out on GO after the termination of the graphite oxidation, has been successful to remove all the impurities and in particular, potassium and manganese (from the oxidizing agent used), from the prepared GO.

#### 3.3.1.4 SEM studies of the pastes

In order to have clearer understanding of the morphological properties of the active materials after mixing forming the paste followed by film casting and drying, SEM studies of the pastes were carried out and important features are selected through several samples and are presented here.

Fig. 3.9 shows the SEM micrographs of pure A.C. electrode. Large particles in the averages size range of 10  $\mu\text{m}$  are observed in Fig. 3.9 (a) forming a porous film with large pores between the particles as magnified in Fig. 3.9 (b). Also smaller A.C. particles are seen in the magnified view placed between the large particles and slightly reducing the empty space. Nevertheless, the general structure of the film is not so densely packed.

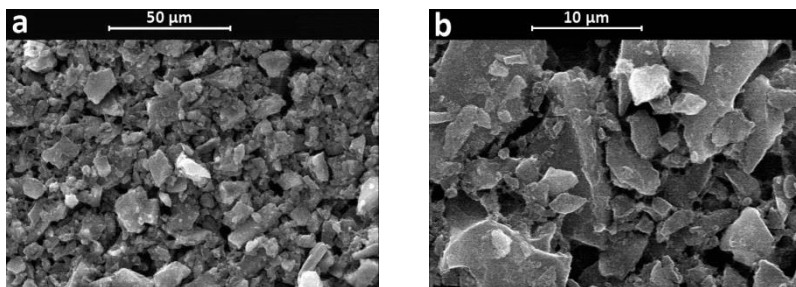


Fig. 3.9 SEM micrographs of pure A.C. electrode paste in two magnifications.

Fig. 3.10 shows the SEM micrographs of A.C.–5%CNT electrode paste and as part (a) suggests, the density of the film is not too better than the pure A.C. electrode. The large A.C. particles are easily seen all around (black arrows in Fig. 3.10 (b)) and the second phase (CNTs+binder) is partially filling the inter-particle spacings. The region indicated by a rectangle in Fig. 3.10 (b) is magnified in Fig. 3.10 (c) and reveals the free space between two A.C. particles (left and right sides of the image). It is seen that CNTs are sticking to the walls of the A.C. particle (white arrow), but are enough in content to fill completely the space. The magnified view of the region pointed by the white arrow is shown in Fig. 3.10 (d) confirming the CNT content of the paste.

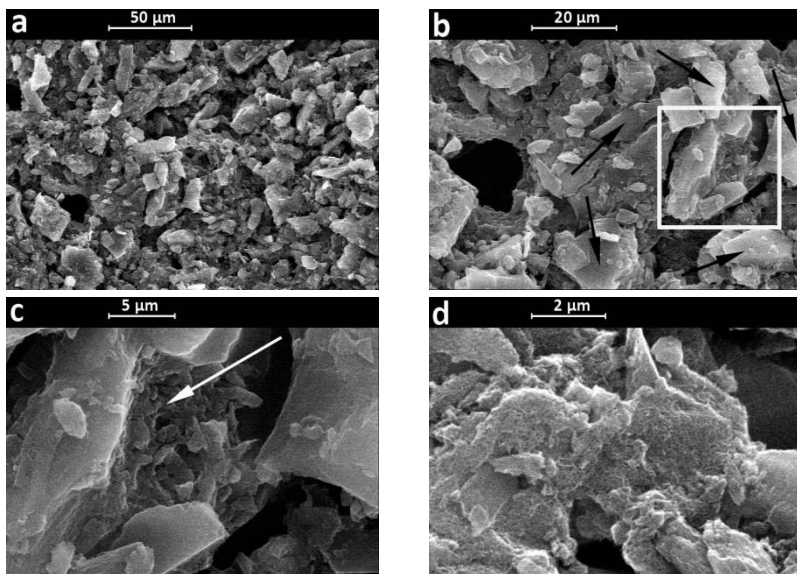


Fig. 3.10 SEM micrographs of A.C.–5%CNT electrode paste in different magnifications.

Fig. 3.11 shows the SEM micrographs of the A.C.–25%CNT electrode paste, demonstrating the capability of CNTs to fill almost completely the empty interparticle spacings given a sufficient content is available. Although A.C. particles can still be identified (black arrows in Fig. 3.11 (b)), the micrometer size empty spaces are filled completely (Fig. 3.11 (c)) and high magnification images (Fig. 3.11 (d)) confirm the presence of CNTs in those regions. It is worth mentioning that although CNTs are occupying the free interparticle spacings, this will not lead to surface area or degree of porosity in the context of supercapacitor electrodes. In fact, the micrometer size pores are far beyond the definition of beneficial pore size distribution for double layer capacitance. Micropores (<2nm) are the smallest pores most difficult to access to by the ions and thus, can affect the supercapacitor performance only at very low rates. Mesopores (2–50nm) are the most beneficial ones accommodating the majority of ions with different sizes and improving the charge storage of the supercapacitor in a wide range of rates. Finally, macropores (>50 nm) will contribute slightly in the electrochemically active surface area and thus, will not add to much value to the characteristics of the supercapacitors. The large empty spaces filled with CNTs in the above discussion, are mostly macropores and their filling with CNTs would not give rise to a decreased surface area. However, the main origin of the surface area change is the internal pores of A.C. and CNTs that are not observable in our SEM studies. The majority of pores of A.C. are in the micropores class and those of CNTs are in the mesopores class instead. Therefore, replacing the A.C. with CNTs would result in a decreased surface area.

Fig. 3.12 shows the SEM micrographs of a pure CNT electrode paste. low magnification image (Fig. 3.12(a and b)) shows a solid overview of the paste, whereas higher magnifications (Fig. 3.12(c and d)) confirm the porous spaghetti like microstructure of the CNTs.

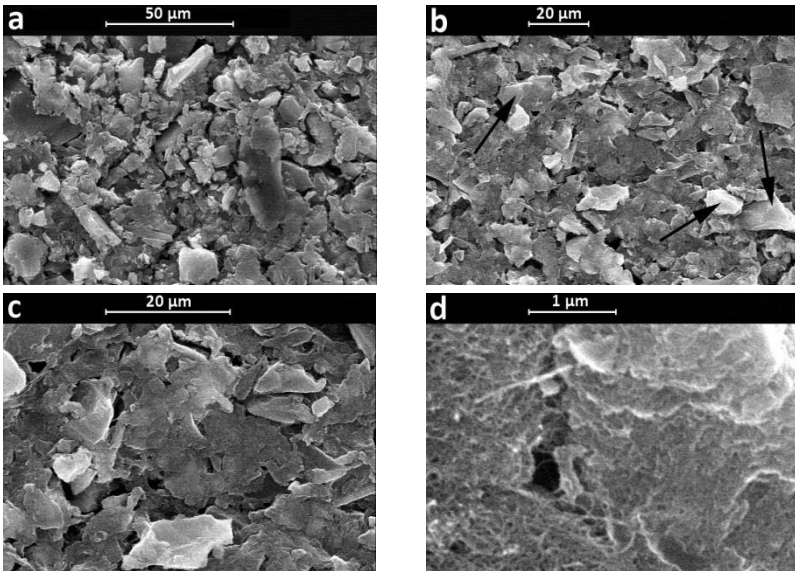


Fig. 3.11 SEM micrographs of A.C.-25%CNT electrode paste in different magnifications.

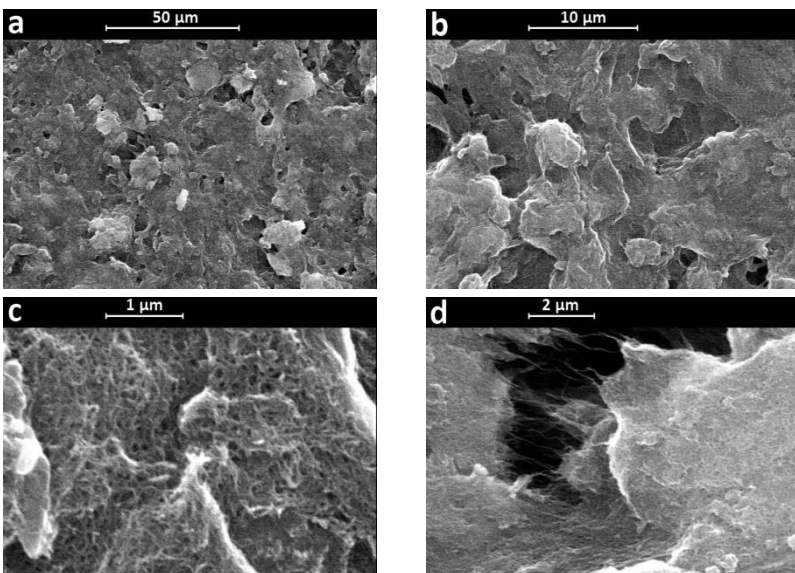


Fig. 3.12 SEM micrographs of pure CNT electrode paste in different magnifications.

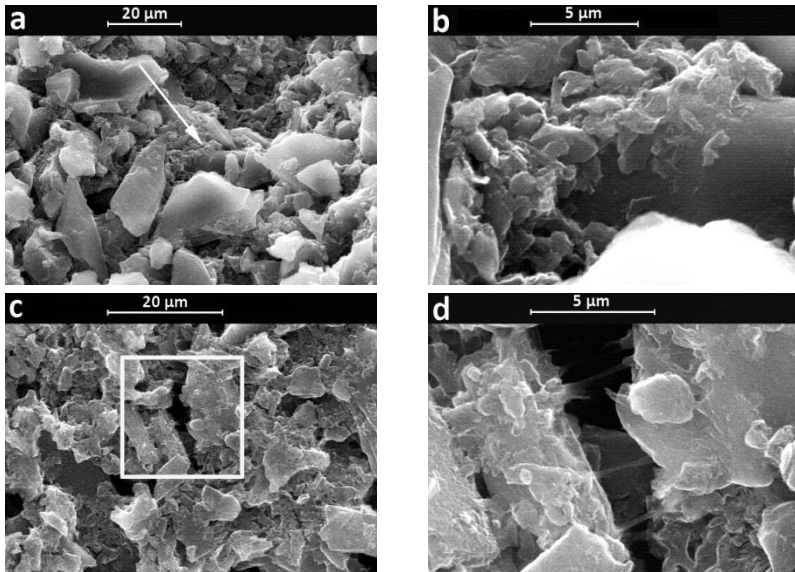


Fig. 3.13 SEM micrographs of A.C.-5% RGO electrode paste in different magnifications.

Similar morphological studies were carried out on RGO containing samples as comes in the following. Fig. 3.13 shows the SEM micrographs of A.C.-5% RGO electrode paste. Similar to A.C.-5% CNT electrode, voluminous empty spaces can be seen between A.C. particles with insufficient RGO sticking to A.C. particles (white arrow in Fig. 3.13 (a) and magnified in Fig. 3.13 (b)). Flake like RGO sheets mixed with the binder are demonstrated (the marked region in Fig. 3.13 (c) with higher magnification in Fig. 3.13 (d)) to be incapable of improving the integrity of the electrode.

By increasing the RGO content, a more homogenous structure is obtained with less macropores as shown in the SEM micrograph of A.C.-25% RGO electrode paste (Fig. 3.14 (a)). Large A.C. particles (black arrows in Fig. 3.14 (b)) are surrounded smaller spherical objects that higher magnifications (Fig. 3.14 (c and d)) confirm that they are crumpled paper ball like RGO

sheets. Paste preparation process consisting of hours of mixing and sonication of the starting materials has resulted in cumpling of the RGO sheets, though their thin and flake like nature is still distinguishable.

Fig. 3.15 shows the SEM micrographs of the pure RGO electrode paste. the overview of the paste is solid with minimum macropores (Fig. 3.15 (a and b)) and higher magnifications (Fig. 3.15 (c and d)) reveal the foldings and wrinklings of the RGO sheets. Along with the high specific surface area of graphene family including RGO due to their expanded and 2D geometry, these foldings and wrinkles can serve as a secondary means for accommodation of the ions with larger size and also to facilitates high rate processes that need a larger pore size.

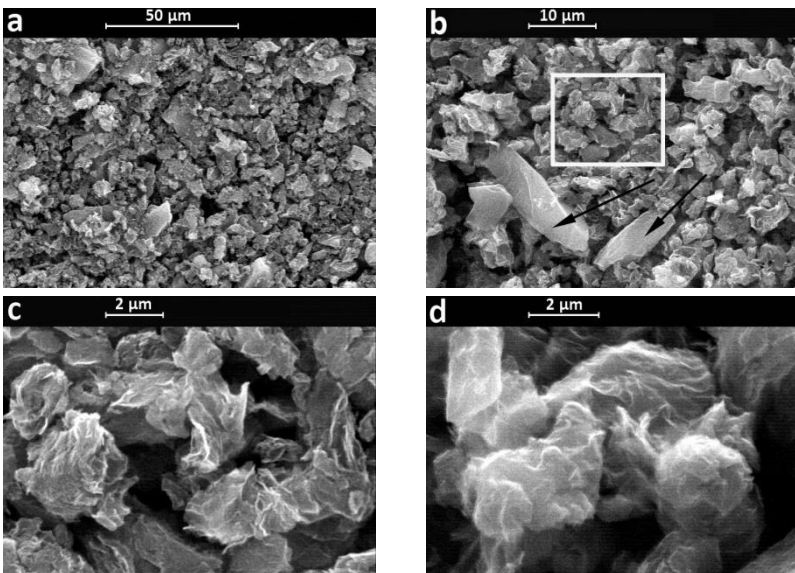


Fig. 3.14 SEM micrographs of A.C.-25% RGO electrode paste in different magnifications.

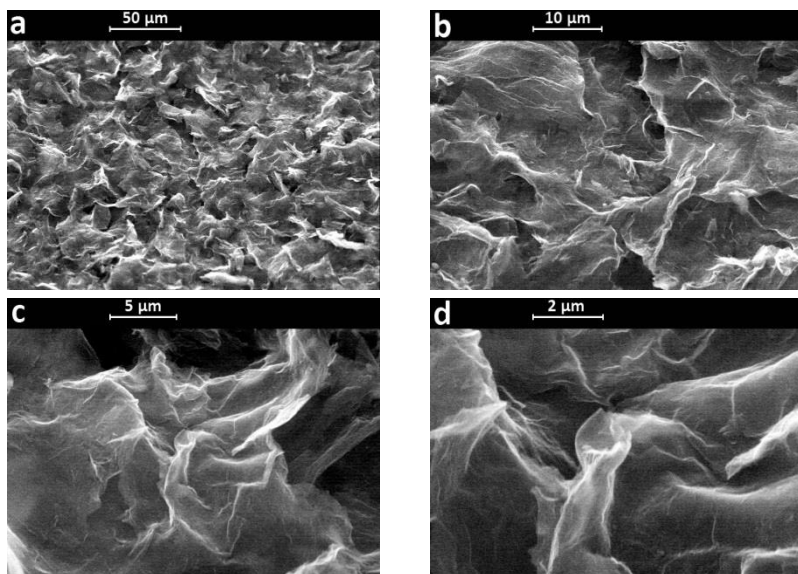
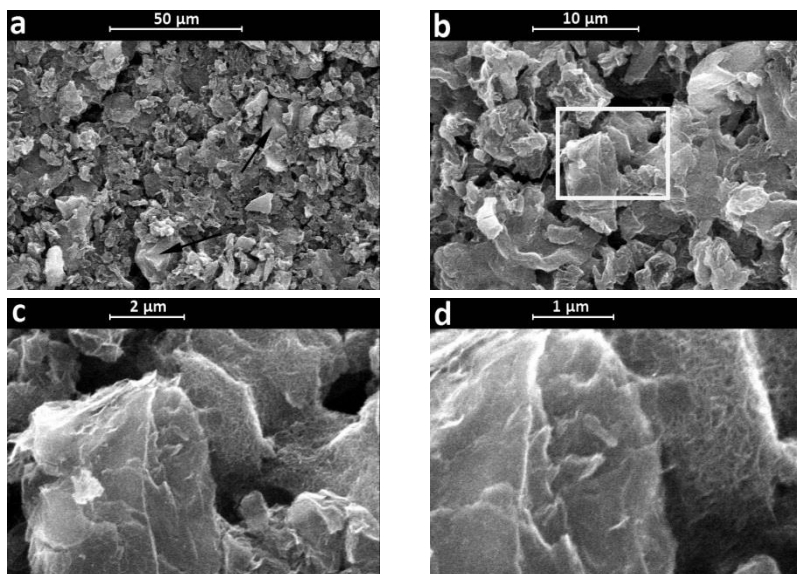


Fig. 3.15 SEM micrographs of pure RGO electrode paste in different magnifications.

Fig. 3.16 shows the SEM micrographs of A.C.–25%CNT–25%RGO that contains all the three active species at the same time. Since the content of CNT+RGO is high enough, the voluminous pores characteristic of high A.C. content pastes are rarely seen, and those A.C. particles present (black arrows in Fig. 3.16 (a)) are well enclosed by other species. Mixture of CNTs and RGO sheets has good homogeneity so that they are not easily distinguishable even at intermediate magnifications (Fig. 3.16 (b)). However, at higher magnifications, coexistence of both species is concluded as demonstrated by Fig. 3.16 (c and d) showing the marked region of Fig. 3.16 (b).



**Fig. 3.16** SEM micrographs of A.C.-25%CNT-25%RGO electrode paste in different magnifications.

Fig. 3.17 shows the SEM micrographs of RGO-25%CNT electrode paste, the upper extreme of the third class of electrodes, where the entire A.C. content is replaced by RGO. The general overview of the paste is rather porous (Fig. 3.17 (a)) compared to pure CNT and pure RGO electrode. This is probably an effect of the mixing of the components. The crumpled paper ball like morphology of the RGO is appearing again ((Fig. 3.17 (b)) that suggests such phenomenon is not induced only by A.C. particles (Fig. 3.14), but it is due to mixture of different components and geometrical modification of the RGO sheets during the paste preparation process. Magnified view of the marked region of Fig. 3.17 (b) shows the homogeneous mixture and coexistence of both components (Fig. 3.17 (c and d)).

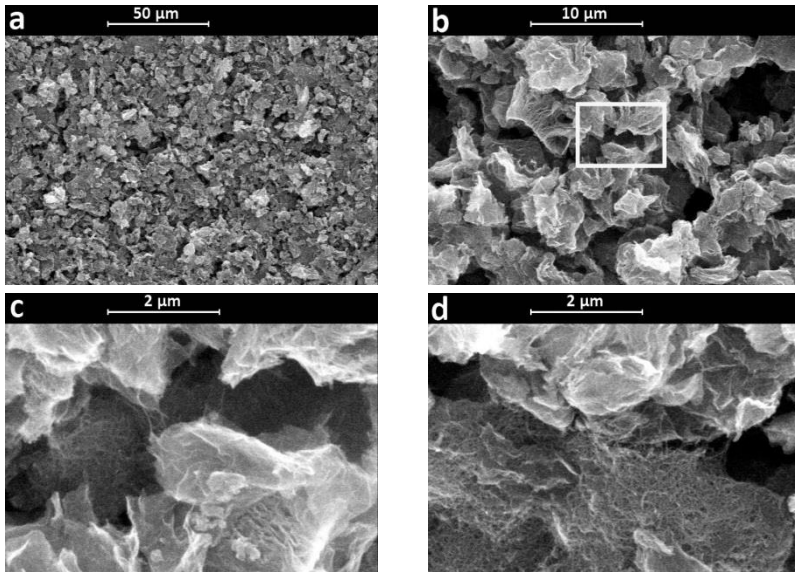
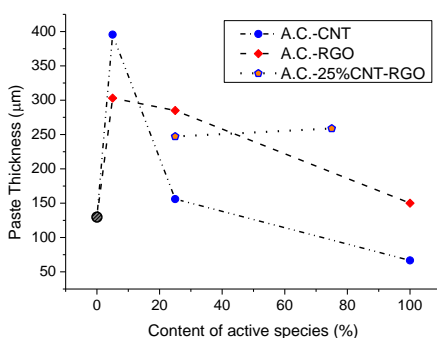


Fig. 3.17 SEM micrographs of RGO-25%CNT electrode paste in different magnifications.

SEM studies were also carried out on the scratched samples in tilted mode for paste thickness measurements. The results of thickness measurements are presented in Fig. 3.18. In this plot, the x axis represents the content of active components other than A.C., thus the point zero, shown with a different symbol, is the pure A.C. electrode. Moving along the x axis, the content of CNT/RGO increases. The plot of the three component electrode, A.C.-25%CNT-RGO, always contains 25%CNT along with indicated content of RGO and rest will be occupied by A.C.. As seen, both CNT and RGO containing electrode show a maximum dry thickness at 5% composition, while the as cast thickness of all electrodes has been 500  $\mu\text{m}$ . shrinkage of the paste by drying is an expectable phenomenon, the extent of this contraction however, depends on the composition.

The higher thickness of A.C.-5%CNT and A.C.-5%RGO electrodes can be justified according to some microstructural clues observed and discussed earlier in the SEM results. Both these samples had a large volume of macropores due to insufficient content of the second phase to fill the

interparticle spacings. Regarding the low density (or packing) and high surface area of CNT and RGO, a remarkable volume expansion of the corresponding pastes would take place that after drying will shrink. In the pastes with very low content of these species, like A.C.–5%CNT and A.C.–5%RGO, the available content of CNT and RGO induces a noticeable volume expansion during the paste preparation, forming a 3D foamy skeleton of A.C. particles suspending in the CNT/RGO matrix. However, during drying, the 3D skeleton of A.C. particles is retained and as soon as a minimum solvent is evaporated, they touch each other and do not settle further. Therefore, the foam of CNT/RGO will dry and stick to the walls of



**Fig. 3.18** Results of the dried paste thickness measurement via SEM as a function of the paste composition.

A.C. particles as shown in Fig. 3.10 (c) and Fig. 3.13 (d). By further increase of CNT/RGO content, this effect is decreased and the thickness decreases more by drying.

### 3.3.2 Electrical characterization

#### 3.3.2.1 Conductivity measurement

Fig. 3.19 shows the conductivity measurements of the raw initial materials. As a reference, the conductivity of pure natural graphite (Sigma-Aldrich) was also measured. This is the graphite from which the GO and

subsequently RGO were prepared. It is seen that by increasing the pressure the conductivity increases that is due to compression of the powder particles and a higher and better degree of inter-particle electrical contact. At increased pressures, the conductivity reaches a plateau like steady state where further increase of the pressure does not affect too much the conductivity since a near optimum particle contact has been obtained. For this reason, the last point in this plot corresponding to a pressure of 3.5 MPa has been labeled with the value of the measured electrical conductivity for the purpose of comparison. The initial graphite had a conductivity of almost  $400 \text{ Sm}^{-1}$ , higher than all other carbon species. Purified CNTs were quite close to graphite with a conductivity of  $332 \text{ Sm}^{-1}$ . A.C. showed the lowest conductivity in the order of  $10 \mu\text{Sm}^{-1}$ , that suggests a high degree of

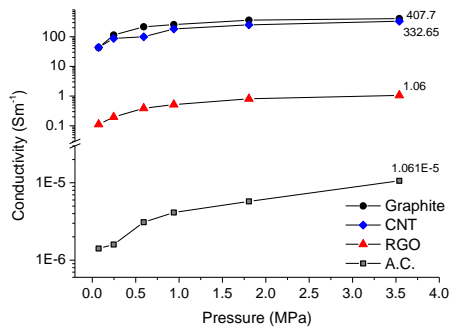


Fig. 3.19 Conductivity measurements of the raw initial materials.

structural damage during the activation procedure. Although turbostratic structure carbon blacks is characterized with low degree of graphitic nature and low conductivity, the activation treatment can degrade it even more resulting in the conductivity levels similar to what measured in this work. In this respect, RGO shows a promising conductivity in spite of the robust oxidation treatment carried out on graphite for preparation of GO. Considering the near-insulation nature of GO, the observed conductivity of RGO suggest a relatively successful reduction process leading to a conductivity five orders of magnitude higher than the pure A.C.

Nevertheless, this material is still far below the CNT in terms of electrical conductivity as revealed clearly by the plot.

Conductivity measurements were also carried out on the prepared pastes for controlling the effect of mixing of the constituents and also the binder. Since the performance of the supercapacitor is basically determined by the properties of the paste cast on the graphite substrate, conductivity of the pastes can be a better measure of the performance of the supercapacitor.

Fig. 3.20 shows the conductivity measurements of different pastes. In Fig.

3.20 (a) the effect of addition of CNTs to A.C. is shown and gradual increase in the conductivity is confirmed. Furthermore, it is interesting that the conductivity of pure A.C. electrode composed of A.C. powder and PVDF binder is two orders of magnitude higher than the conductivity of pristine A.C. powder. This can be justified by a better inter-particle connection of the large A.C. powders due to paste preparation procedure and also due to the PVDF binder filling the free space between particles. Since PVDF is also known to have a degree of electrical conductivity [528–530], it is inferred that it has partially contributed in the observed conductivity improvement. 50% of CNT addition to the paste has resulted in four orders of magnitude improvement and the pure CNT electrode is still three times more conductive than the A.C.–50%CNT. It is worth mentioning that in case of highly conductive electrode materials, the effect of PVDF is the opposite of what observed for poorly conductive A.C., and the conductivity of the paste of pure CNT is lower than the pristine CNTs. Similar gradual improvement of the conductivity of the paste is confirmed with increase of the RGO content in A.C.–RGO electrodes as shown in Fig. 3.20 (b). Interestingly, also the conductivity of RGO has improved in the paste (compare pure RGO electrode in Fig. 3.20 (b) and RGO powder in Fig. 3.19). Finally, electrodes containing both CNT and RGO along with A.C. are shown in Fig. 3.20 (c) and compared to pastes of pure elements. It is seen that the conductivity of these pastes is in the same range, higher than

pure RGO and lower than pure CNT, and it is inferred that the CNT content is the determining factor in the overall conductivity of such pastes.

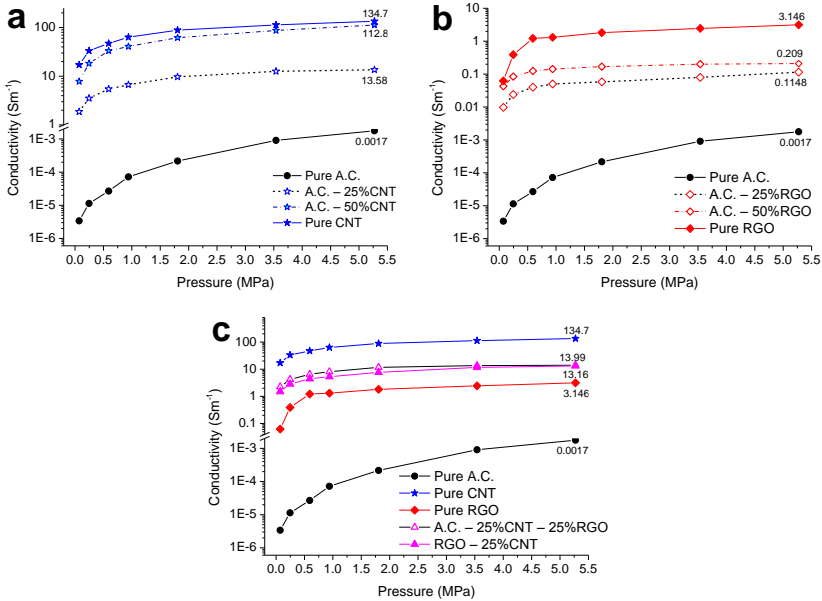


Fig. 3.20 Conductivity measurements of the paste electrodes of supercapacitors.

### 3.3.3 Electrochemical characterization

Electrochemical characterization of the electrodes for evaluation of the supercapacitor performance was carried out based on a wide range of techniques. In most cases, the results of different techniques confirm each other and in some cases, each technique clarifies some specific corners. In this regards, in the section, depending on the potentials of different techniques and their correlation, results of a single or multiple techniques will be presented the assessment of the supercapacitor behavior.

#### 3.3.3.1 Specific capacitance and energy density

Specific capacitance of a supercapacitor is the very first indicator of its properties. All the aforementioned techniques, CV, CD and EIS, are capable

of being used for the calculation of the specific capacitance after proper elaboration. Fig. 3.21 shows the conformity of CV and CD results on evaluation of a typical supercapacitor's specific capacitance. However, it is not so easy to make a straightforward correlation between the rate criteria in both techniques, namely, scan rate of CV and CD current. In any case, due to stronger correspondence of the CD technique to the supercapacitors real

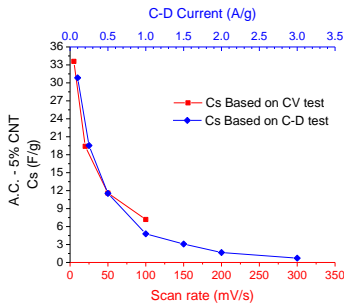


**Fig. 3.21** Specific capacitance of a typical electrode calculated via CV at different scan rates and CD at different currents.

working condition, it was decided to establish the comparative assessments on the basis of the CD results. The methodology used to calculate the specific capacitance from the CD tests, was based on a direct calculation of the specific energy using the following equation:

$$E_s = \frac{E_{cell}}{m_{total}} = \frac{V_{disch}Q}{t} = \frac{i_{disch} \int V(t)_{disch} dt}{m_{total}} \quad (3-2)$$

where  $E_s$  is the specific energy,  $Q$  is the withdrawable charge during the discharge cycle,  $V_{disch}$  is the effective discharge potential (potential after the ohmic drop),  $V(t)_{disch}$  is the discharge potential as a function of the time,  $i_{disch}$  is the discharge current,  $m_{total}$  is the total weight of active materials on both electrodes and the term  $\int V(t)_{disch} \times i_{disch} dt$  represents the total energy withdrawable from the cell,  $E_{cell}$ .

Since the specific energy and specific capacitance are correlated through the square of the effective working potential (after the ohmic drop), the specific capacitance,  $C_s$ , can be obtained easily as the following equation suggest:

$$E_s = \frac{C_{cell} V_{disch}^2}{2 \times m_{total}} = \frac{1}{2} \times \frac{C_s \times m_{total} \times V_{disch}^2}{4 \times m_{total}} = \frac{1}{8} C_s V_{disch}^2 \quad (3-3)$$

Fig. 3.22 shows a typical CD plot of a supercapacitor with area under the real discharge line (in blue) in the dashed form. In addition, the straight black line shows the discharge path if the same capacitor was performing ideally. The area of the dashed region, that is in fact the integral of the real discharge line (blue), if multiplied by the constant discharge current, gives the total energy of the cell,  $E_{cell}$  and can easily be converted to  $E_s$  via normalization over the total active mass of the cell. The aforementioned method of calculation of the specific capacitance benefits from the satisfaction of the definitive concept of capacitance by direct and precise measurement of the stored energy and translating it to an equivalent capacitance through the Eq. (3-3).

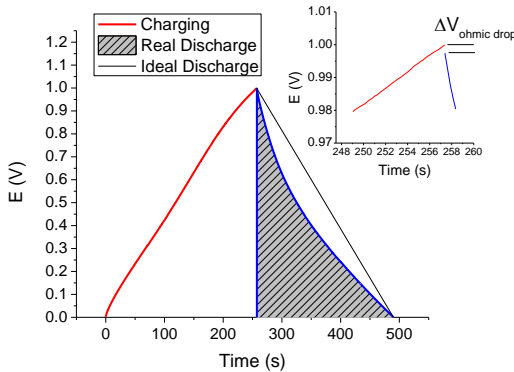


Fig. 3.22 Demonstration of the methodology used for specific capacitance and energy calculation based on the CD technique.

In contrast to this method, the usual way of calculation of the capacitance in the literature using the CD method is based on the following equation:

$$C_{cell} = \frac{I}{\frac{dV}{dt}} \quad (3-4)$$

where  $\frac{dV}{dt}$  is the “dominant” slop of the discharge curve and  $C_{cell}$  will be the packed cell (two-electrode) capacitance. Therefore, the specific capacitance ( $C_s$ ) could be calculated by a mass normalization:

$$C_s = 2 \times \frac{C_{cell}}{m_{sing}} \quad (3-5)$$

where  $m_{sing}$  is the weight per electrode of the active material.

This method suffers from the lack of precision in determination of the point where the  $\frac{dV}{dt}$  should be measured. Most often, it is seen that a direct connection of the initiation point of the discharge curve to its termination point is used and in fact,  $\frac{dV}{dt}$  is replaced by  $\frac{\Delta V}{\Delta t}$  over the entire discharge region. However, that would be the wrong assumption of the ideal behavior of the supercapacitor and thus, results in a remarkable overestimation of the capacitance of the cell, as can realized from the difference in the area under the real and ideal discharge curves in Fig. 3.22.

Another point to be noted is the direct relation of the specific energy and capacitance as revealed in Eq. (3-3). Therefore, the trend of the change in specific energy will be the same as that of the specific capacitance. This fact will be confirmed through the following discussions and plots of different samples.

For the comparative studies, the 15 electrodes of Table 3-1, were classified in three general groups (see section 3.2.4 Electrodes classification)

including A.C.–CNT, A.C.–RGO, A.C.–CNT–RGO, and will be discussed in the same order.

### 3.3.3.1.1 A.C. – CNT electrodes

Fig. 3.23 shows the specific capacitance (a, c, and d) and specific energy (b) of A.C.–CNT electrodes. As seen, an identical trend in of specific capacitance and energy change with CD current is observed (compare Fig. 3.23 (a and b)) in relevance to Eq. (3-3). In order to have a better understanding of the capacitance dependence on the composition of active materials, 3D plots of specific capacitance are also presented. In Fig. 3.23 (c) the effect of CD current on the capacitance of different compositions is highlighted, whereas in Fig. 3.23 (d) the effect of composition on the capacitance is highlighted at different CD currents.

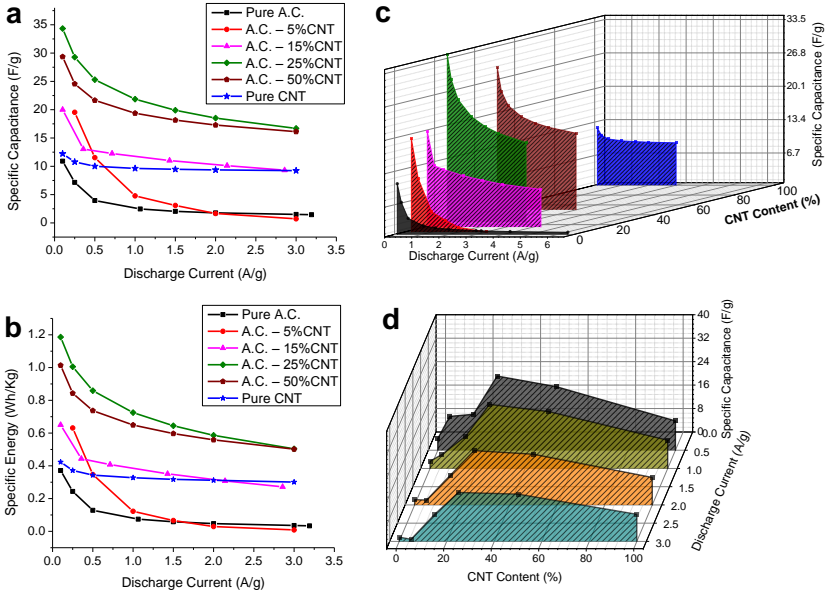


Fig. 3.23 Specific capacitance (a, c, and d) and specific energy (b) of A.C.–CNT electrodes.

As expected, at higher CD rates,  $C_s$  drops due to insufficient time for the activity of micropores and sites with difficult accessibility for ions. On the other hand, the extent of this drop as well as its minimum and maximum values, show strong dependence on the composition. It is necessary to note that the relatively poor capacitive behavior of the pure A.C. electrode compared to the reported values in the literature [470,531–533] is due to the type of this material used in our work, namely, Norit<sup>®</sup> activated charcoal, that is not a supercapacitor type A.C. and the capacitance obtainable with this materials is limited. Furthermore, the electrical conductivity of all types of A.C., including the current one (see Fig. 3.19), is poor and in usual electrode preparation procedures a fraction of conductive carbon species is added. However, in this work, the main objective was to study the effect of other constituents such as CNT and RGO, on the behavior of the composite electrode and since these materials are supposed to have a better electrical conductivity than A.C. as confirmed by the electrical conductivity measurements (see Fig. 3.19 and Fig. 3.20), no other conductive elements were added, neither to pure A.C. electrode nor to the others, to provide the opportunity of studying the materials of interest and avoid any interference from other ingredients. Therefore, the observed capacitance of the pure A.C. electrode is the consequence of both mentioned factors. By gradual addition of CNTs,  $C_s$  increases initially that is mainly due to conductivity enhancement provided by CNTs. This increase reaches a maximum between 25–50% CNTs, after which  $C_s$  drops again. Since the conductivity of the composite reaches to sufficiently high values above certain amounts of CNT content, further increase of CNTs will just result in the reduction of the active surface area of the electrode and thus, the specific capacitance drops. Similar drop has been reported for A.C.–CNT electrodes in organic binders [534]. Finally, the pure CNT electrode, shows a stable specific capacitance of 10–15  $\text{Fg}^{-1}$  at various CD rates.

The other noteworthy point is the exclusion of A.C.–5%CNT electrode from the initial increasing trend of the  $C_s$  by composition, at high scan rates. Referring to SEM studies, this observation can be justified by the typical microstructure of this electrode, and the influences it can have on the

porosity distribution, layer thickness and electrical conductivity of the paste. As discussed earlier (Fig. 3.10, Fig. 3.18 and related discussions), low content of CNTs has resulted in an extraordinarily thick paste with weak interconnection of the particles. Therefore, it is assumed that this content of CNTs couldn't have played an active role in the conductivity of the paste since it has been mostly sticking to the walls of A.C. particles without forming an interconnected matrix or network. Furthermore, higher thickness of the layer could have slightly hampered the ionic accessibility of the depth of the paste. At lower CD currents, this effect has been disappeared.

### 3.3.3.1.2 A.C. – RGO electrodes

Fig. 3.24 shows the specific capacitance (a, c, and d) and specific energy (b) of A.C.–RGO electrodes. Similar to A.C.–CNT class, the 3D plots of  $C_s$  as function of CD current (Fig. 3.24 (c)) and composition (Fig. 3.24 (d)) are also presented. There is no need to discuss again the reverse relation of  $C_s$  and CD current. The main point of difference between this group of samples and A.C.–CNT class is trend of  $C_s$  change by composition. In contrast to CNTs, addition of RGO has continuously increased the  $C_s$  and the maximum value for  $C_s$  has been obtained at pure RGO electrode. The high surface area of RGO compared to CNT can explain the different behavior [497]. Actually, given the theoretical value for the graphene's surface area ( $2630 \text{ m}^2\text{g}^{-1}$  [535]) is available, a huge  $C_s$  should be obtained. However, as observed in the SEM studies of RGO conaing samples (Fig. 3.13, Fig. 3.14, Fig. 3.15, Fig. 3.16 and Fig. 3.17), RGO sheets are folded and crumpled and most probably, a certain level of stacking of the sheets is quite likely. In any case, the surface area of RGO in the current work, is definitely in a higher level than CNTs so as leads to continuous increase of the  $C_s$ . This fact becomes clearer when considering the conductivity of this sample that was shown to be orders of magnitude lower than CNTs in both pristine or paste mode. Therefore, the active surface area has been large enough to compensate the conductivity shortages and store a charge similar to best CNT containing samples (A.C.–25% CNT).

It is interesting that also in A.C.–RGO class, the low contents of RGO (mainly 5%, and also 15%) do not follow the general increasing trend of  $C_s$

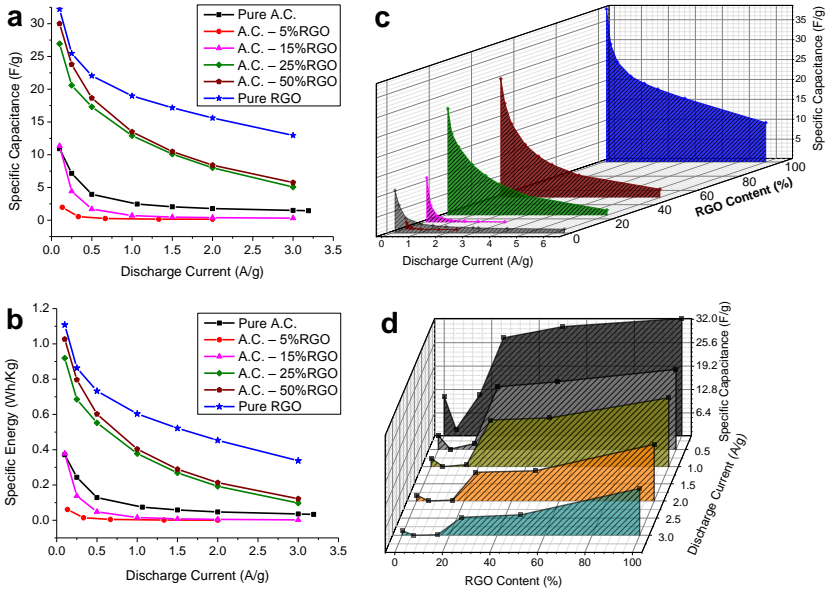


Fig. 3.24 Specific capacitance (a, c, and d) and specific energy (b) of A.C.–RGO electrodes.

by RGO content. This has also been observed in A.C.–5%CNT electrode and has been explained by the special microstructure of this sample. Similar features have been observed in SEM studies of A.C.–5%RGO (Fig. 3.13 and Fig. 3.18) and subsequently, a similar electrochemical behavior was obtained, implying the similar origin of the issue in both samples.

### 3.3.3.1.3 A.C. – CNT – RGO electrodes

Fig. 3.25 shows the specific capacitance (a, c, and d) and specific energy (b) of A.C.–CNT–RGO electrodes. A 25% content of CNTs has been fixed in all samples and the RGO content has been increased gradually. Therefore, the zero content RGO sample, would be A.C.–25%CNT electrode, that in the meanwhile, had shown the best  $C_s$  among the A.C.–CNT class and for

this reason, had been selected as the constant CNT content of interest. The maximum content of RGO in this class has been obtained by complete removal of A.C. and its replacement by RGO, named as RGO–25%CNT. The negative effect of the low content of RGO is observed also here, in spite of the availability of 25%CNT. Therefore, it is confirmed that as long as the electrode preparation is going to be carried out by the paste casting method, a lack of integration of the low content constituent in the paste matrix is quite likely (specially the low density and high surface area species) leading to faulty architecture of the electrode's microstructure and deficient performance.

At higher RGO contents however, a minimum dependence of  $C_s$  of this class on the composition was observed, in particular at high CD rates. In fact, the A.C. content, coupled with conductive elements such as CNTs and RGO, is responsible for a considerable part of the capacitance especially at low CD rates. That is why at zero or low RGO contents and typically low CD rates, a good capacitive behavior was observed. By gradual replacement of this constituent with RGO, the conductivity remains almost constant (due to presence of constant amount of high conductivity CNTs, see Fig. 3.20) and the surface area does not increase (high surface area A.C. is replaced by relatively high surface area RGO) and therefore, the capacitance does not change too much. In fact, due to high fraction of micropores of A.C., at low RGO contents and low CD rates, the capacitive behavior is even slightly better than the high RGO content side of the composition plot. Therefore, the similarity of the capacitive behavior at two ends of the composition plot is more clearly observed at high CD rates where the contribution of the micropores of A.C. becomes minimal.

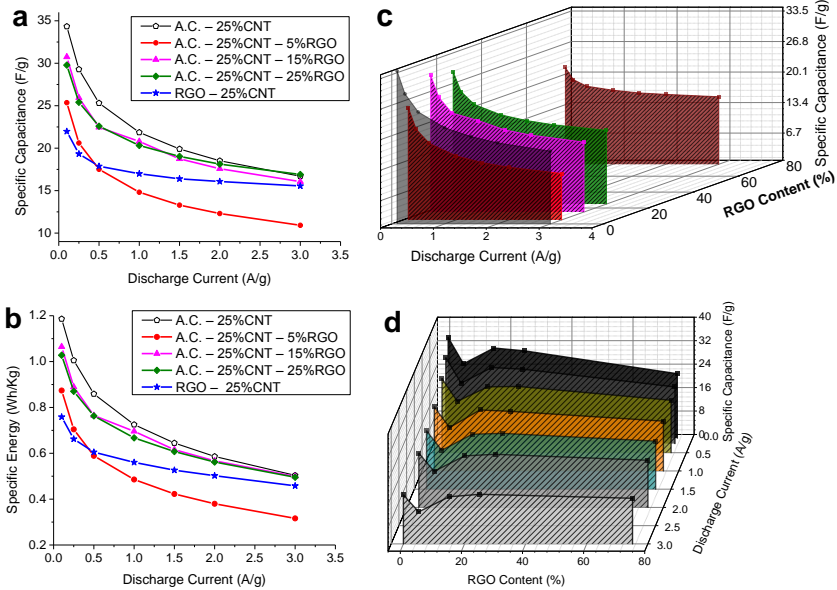


Fig. 3.25 Specific capacitance (a, c, and d) and specific energy (b) of A.C.-CNT-RGO electrodes.

### 3.3.3.2 Rate capability

The rate capability of a supercapacitor is defined as the dependence of its specific capacitance on the rate at which it is charged/discharged. The lower this dependence, the better the rate capability of the supercapacitor is considered [536]. That is, since the capacitance of the electrical double layer capacitors comes from the electrostatic storage of charge at the electrode surface that is a very fast process, charging/discharging of the cell should be very fast as well, unless the microstructure and porosity of the electrodes puts limitations on the ionic accessibility of the surface of the electrode and in particular the pores. The lower the pore size, the more difficult and timely the access of ions to all pores and thus, a higher dependence of the specific capacitance on the rate of charge/discharge. Obviously, pseudocapacitors with a faradic nature of the charge storage and the requirement of electron transfer across the electrode–electrolyte

interface for charge build-up, are remarkably lower rate capable compared to electrical double layer capacitors.

Several methods can be used to evaluate the rate capability of a supercapacitor. One way is to use the so-called “Peukert” plot that expresses the capacity of a cell in terms of the rate at which it is discharged. Although this method has been presented by the German scientist W. Peukert in 1897, for evaluation of the performance of batteries, it is also applicable to supercapacitors. In fact, what presented in the previous section as the  $C_s$  vs. CD rate, were a Peukert type plot and will be referred to in the discussion here as an indication of the rate capability.

The other method is based on the comparison CV curves of a given supercapacitor at different scan rates. If the current axis of the CV plot is normalized by the scan rate and the active materials mass, it will be converted to capacitance ( $Fg^{-1}$ ) and an ideal rate capability would appear as coincidence of all the voltammograms recorded at the different scan rates. For this purpose, CVs of a number of samples (selected in a way to be representative of the effect of the composition change on CVs) are normalized by mass and scan rate (5, 20, 50 and 100  $mVs^{-1}$ ) and are presented in Fig. 3.26 and Fig. 3.27.

As seen in Fig. 3.26, the pure A.C. electrode shows the highest degree of the  $C_s$  dependence on the scan rate. This can be understood from the small and narrow CV “boxes” at high and large and ones at low scan rates, confirming the strong influence of the scan rate on the capacitive behavior of this sample. Not only the size and width of the voltammogram is of importance, but also its shape can imply many facts. The CV of an ideal supercapacitor should be like a rectangle or box. The deviation from this shape indicates the non-ideality of the supercapacitor due to factors such as

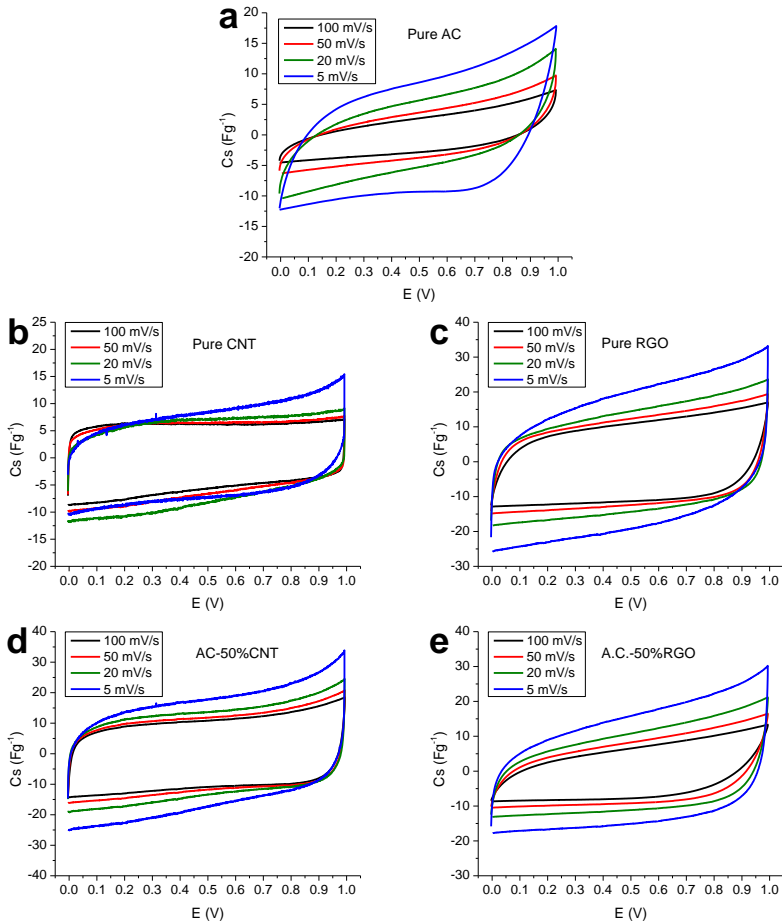


**Fig. 3.26** CVs of (a) pure A.C., (b) pure CNT, (c) pure RGO, (d) A.C.–50%CNT and (e) A.C.–50%RGO electrodes normalized by scan rate and electrode mass for rate capability studies.

irreversible faradic reactions on the electrode surface due to presence of heteroatoms and functional groups reacting with the electrolyte in the charge–discharge cycle or even due to corrosion of the active material.

Furthermore, internal resistance of the electrode is another factor causing deviation of the CVs from the rectangular shape. This effect is also

observed clearly in pure A.C. electrode with banana like CVs at high and semi-rectangular CVs at high scan rate. As a further evidence, Peukert type plots of Fig. 3.23, confirm a strong rate dependence of  $C_s$  for the pure A.C. electrode highlighting the contribution of micropores of A.C. in the charge storage process and its consequent rate sensitivity.

In contrast to pure A.C., pure CNT electrode (Fig. 3.26 (b)) shows the lowest dependence of the shape and the size of the box on the scan rate. In fact, at 100, 50 and 20  $\text{mVs}^{-1}$  scan rates, CVs are almost superimposing and only at the lowest scan rate, 5  $\text{mVs}^{-1}$ , an enlargement of the CV is observed. Moreover, the shape of the CVs are the most similar ones to a rectangle in this electrode, all implying a good rate capability of this electrode. This fact can further supported by the Peukert type plots of Fig. 3.23, where the  $C_s$  of pure CNT electrode was almost constant at all CD currents and just increased slightly at lowest CD rates. Such superior rate capability of CNTs can be explained by their pore size distribution that is believed to be in the micro range (2-50 nm) facilitating the ionic movement in the pores and easy access to the entire available surface [488,489]. That is why this component has been widely used in composite electrodes as a constituent to improve the rate capability and power performance modifier of pseudocapacitors [537–541].

The A.C.–50%CNT electrode (Fig. 3.26 (d)) with almost similar contents of CNT and A.C., shows a remarkable improvement compared to pure A.C. electrode and is behaving more similar to pure CNT in the sense that at scan rates equal or higher than 20  $\text{mVs}^{-1}$ , CVs are showing slight change and only at 5  $\text{mVs}^{-1}$  the change becomes obvious. Therefore, the CNT can be considered as a stronger variable than A.C., to influence the rate capability. Also referring to Peukert type plots of Fig. 3.23, it is seen that in general the initial addition of CNTs to A.C. just causes the capacitance improvement due to conductivity reasons and without considerable effect on the rate capability. However, at compositions with higher than 25%CNTs, the  $C_s$  starts to drop and instead, the rate capability improves.

Pure RGO electrode (Fig. 3.26 (c)) is showing a clear rate dependence of the CVs. Although this dependence is less pronounced compared to pure A.C. and a slighter change of the CVs by the scan rate can be realized, it is still incomparable with CNTs especially at high scan rates. The shapes of the CV boxes are more similar to an ideal supercapacitor in this sample compared to A.C. that is another indication of the superiority of this electrode. Comparison of this sample with A.C.–50%RGO (Fig. 3.26 (e)) also confirms the continuous improvement of the rate capability by increase of the RGO content. However, in contrast to A.C.–CNT class, increasing the RGO content is always accompanied by the increase of  $C_s$ . Peukert type plots (Fig. 3.24) further support this idea by showing first, an improvement in  $C_s$  at intermediate and low CD rates by the initial addition of RGO (due to conductivity reasons) and then, additional  $C_s$  improvements at high CD rates at high contents of RGO. Moreover, it demonstrates that the capacitance difference of the low and high ends of the CD rate, decrease progressively by increase of the RGO content.

Fig. 3.27 shows the voltammograms of the A.C.–25%CNT–RGO class at different scan rates. As long as there is some fraction of A.C., the rate dependence of  $C_s$  is obvious (Fig. 3.27 (a, b and c)). However, at A.C.–25%CNT–25%RGO (the lowest A.C. content in three–components sample) it is less pronounced than A.C.–25%CNT–5%RGO and A.C.–25%CNT–15%RGO. Due to presence of 25%CNT, the conductivity is always kept at a reasonable level and due to constant overall content of high surface area components (A.C.+RGO) the  $C_s$  level at low scan rates does not vary too much in the three–components sample. By the complete removal of A.C. (Fig. 3.27 (d)),  $C_s$  drops slightly, but the rate capability increases significantly, so that RGO–25%CNT is comparable to pure CNT sample (Fig. 3.26 (b)). The excellent rate capability of RGO–25%CNT sample can also be confirmed through Peukert type plots of Fig. 3.25, where the lowest degree of  $C_s$  change from the highest to the lowest CD rate was observed.

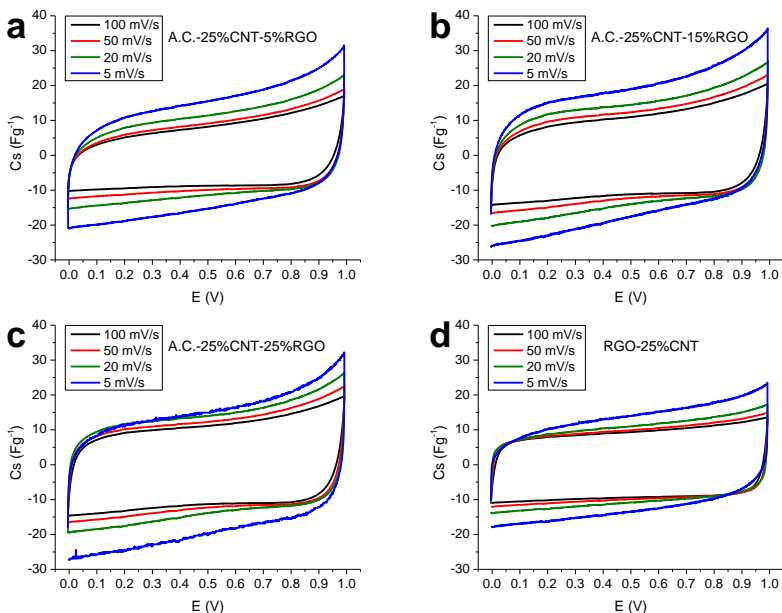


**Fig. 3.27** CVs of (a) A.C.-25%CNT-5%RGO, (b) A.C.-25%CNT-15%RGO, (c) A.C.-25%CNT-25%RGO and (d) RGO-25%CNT electrodes normalized by scan rate and electrode mass for rate capability studies.

The positive point of RGO-25%CNT compared to pure CNT is that along with a good rate capability, the  $C_s$  is also kept in reasonably high values. On the other hand, the positive point of RGO-25%CNT compared to pure RGO, is the superior rate capability, though accompanied by some capacitance loss.

### 3.3.3.3 Ideality of the performance

Since the performance of a real supercapacitor is always accompanied by some degree of deviation from an ideal capacitor due to irreversibility lossess, faradic reactions, internal resistances and so on, development of an indicator of the degree of ideality of a supercapacitor can be of great importance and interest. Unfortunately, such criterion has not been paid enough attention so far and to the best of our knowledge, it has not been reported in the literature. Therefore, it was tried in this work to define a

simple parameter based on the basic concepts of charge/energy storage in the cell to be compared with the ideal counterpart of the same capacitor and thus, give a measure of the ideality of the cell.

As discussed on Fig. 3.22 about the calculation of energy density or specific capacitance of supercapacitor via the CD technique, an ideal supercapacitor would discharge according to the straight black line after the initial ohmic drop, whereas the real supercapacitor will suffer from some losses and deficiencies due to which, it deviates from the ideal discharge line. Therefore, the area under the real discharge line (dashed region under the blue line), which is directly related to the withdrawable energy from the cell, can be compared to the area under the ideal discharge line, which is directly related to the withdrawable energy from the ideal counterpart of the same supercapacitor, and its deviation from ideality can be determined. On this basis, the *Ideality Factor*,  $IF$ , was determined as follows:

$$IF = \frac{E_{real}}{E_{ideal}} = \frac{i_{disch} \int V(t)_{disch} dt}{\frac{V_{disch} \times \Delta t_{disch}}{2}} \quad (3-6)$$

where  $V(t)_{disch}$  is the discharge potential as a function of the time,  $V_{disch}$  is effective discharge potential (after the ohmic drop),  $i_{disch}$  is the constant discharge current and  $\Delta t_{disch}$  is the total discharge time. Obviously, the region under the ideal supercapacitor discharge line in CD technique resembles a geometrically perfect triangle with an area higher than that under the real discharge line, leading to the principle that  $IF \leq 1$ . Therefore, the closer the performance of the real supercapacitor to the ideal one, the closer the IF to unity.

Accordingly, this factor was calculated for all the electrodes at all CD currents discussed in section 3.3.3.1 and is presented in Fig. 3.28. The A.C.–CNT class electrodes are compared in Fig. 3.28 (a) and direct relation of the IF with the CNT content can be observed. By the initial addition of CNTs, the IF drops to values even smaller than pure A.C. that reminds us

the SEM observation of the low content A.C.–CNT electrode and the resultant extraordinary thickness (Fig. 3.10, Fig. 3.18 and related discussions), as well as the corresponding weak capacitive behavior (Fig. 3.23). by increase of the CNT content, the IF becomes less rate dependant and increases in value. Only at high enough contents ( $\geq 50\%$ CNT), the ideality surpasses the pure A.C. and becomes almost rate independent. The pure CNT electrode reaches IF values about 0.9 that is in close proximity to an ideal discharge. A reasonable IF is also achieved by A.C.–50%CNT (0.85) that sounds even more interesting when remembering its almost twofold  $C_s$  compared to pure CNT electrode. It is concluded that in the A.C.–CNT class, a better performance is expected only at high enough contents of CNTs ( $\geq 50\%$ CNT).

The A.C.–RGO class electrodes are compared in Fig. 3.28 (b) and their

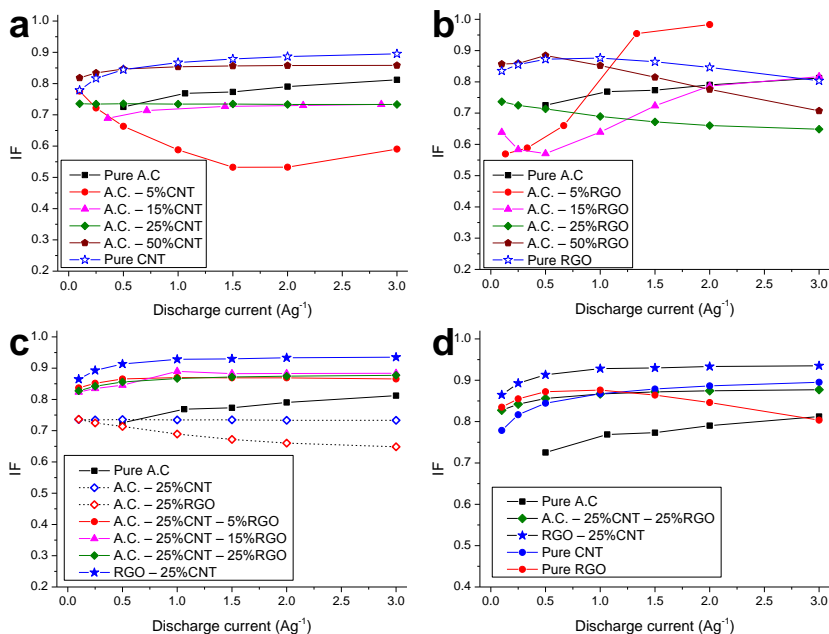


Fig. 3.28 Ideality factor (IF) of different electrodes as a function of CD current.

ideality at low RGO contents, is even worse than the A.C.–CNT class. One major point of difference between the A.C.–RGO and A.C.–CNT in terms of ideality, can be found in the rate dependence of this factor. While for A.C.–CNT class this dependence was minimal, A.C.–RGO class shows a reverse relation with the rate and loses the ideality at high CD rates. This can be explained based on the higher surface area and supposedly smaller pore size of RGO, as discussed in the rate capability section too. In any case, the ideality level at low and intermediate CD rates is reasonable for high RGO content electrodes (almost 0.88 for both A.C.–50%RGO and pure RGO). In this respect, this class can be considered as a rate complement for A.C.–CNT class.

The ideality factor A.C.–CNT–RGO class electrodes is presented in Fig. 3.28 (c) and compared to corresponding values for intermediate contents of A.C.–CNT and A.C.–RGO classes. Interestingly, electrodes of this class show extraordinarily high and steady IF values over the entire CD rates range. According to what observed and discussed for A.C.–CNT and A.C.–RGO classes, it is inferred that the combination of appropriate ideality of A.C.–CNT at high rates with the good ideality of A.C.–RGO at low and intermediate rates, has provided an acceptable and rate independent ideality for A.C.–CNT–RGO class. By the complete replacement of A.C. content with RGO in RGO–25%CNT electrode, an almost always  $IF \geq 0.9$  condition is established, giving rise to IF values as high as 0.93. Furthermore, since a minimum CNT content of 25% is always available, the problem related to low contents of second phase constituents is never seen in this class and all the compositions behave significantly more ideal than intermediate compositions of both A.C.–CNT and A.C.–RGO classes (like A.C.–25%CNT and A.C.–25%RGO both shown in the same plot).

For a more comprehensive comparison, electrodes of A.C.–CNT–RGO class are also compared to single component electrodes (Fig. 3.28 (d)). It is seen that pure CNT and pure RGO samples are making a cross over the CD rate range, pure CNT increasing by rate and pure RGO decreasing by rate. As a consequence, the RGO–25%CNT steadily stays above both at IF

values more than 0.9. Also A.C.–25%CNT–25%RGO is comparable at low rates with pure RGO and at high rates with pure CNT.

#### 3.3.3.4 Durability

Another important parameter to be studied in characterization of supercapacitors, is the trend of change of behavior over time. In fact, long and repetitive service cycle wears the electrode materials gradually, increasing the irreversibility losses and capacitance drop. For this reason, characterization of the properties change over a relatively long testing time under iterative charge–discharge cycling is of great importance. Fig. 3.29 shows the life cycling results of different classes of the electrodes. As a general observation, it is seen that almost all the electrodes of all classes experience a capacitance decrease overtime, that is expectable. Pure A.C. electrode however, shows a slight increase by time, implying the gradual development of ionic pathways to small pores of this material. It should be noted that since these plots the capacitance retention has been reported as percent of the initial capacitance, the magnitude of the capacitance is not presented and for pure A.C. electrode, that initial value has not been large. Then, due to repeated charge–discharge cycles and frequent movement of the ions into and out of the pores, some initially inaccessible pores and pathways of this material have been opened and thus, the capacitance has slightly increased. For the other electrodes with higher initial capacitance however, the degradation of the electrode due to irreversible electrode reaction and partial corrosion of the active material has dropped. This drop has been more considerable in A.C.–CNT class (Fig. 3.29 (a)) and since pure CNT shows one of the best retentions in the entire range of electrodes, it can be concluded that remarkable capacitance drop of A.C.–CNT class electrodes is not due to corrosion or degradation of the CNT constituent, but rather, probably due to loss of effective interactions of individual constituents. In other words, it seems that the high electrical conductivity network of CNTs between the A.C. particles has lost a part of its connection with the particles and thus, the capacitance drop is mainly caused by the conductivity degradation.

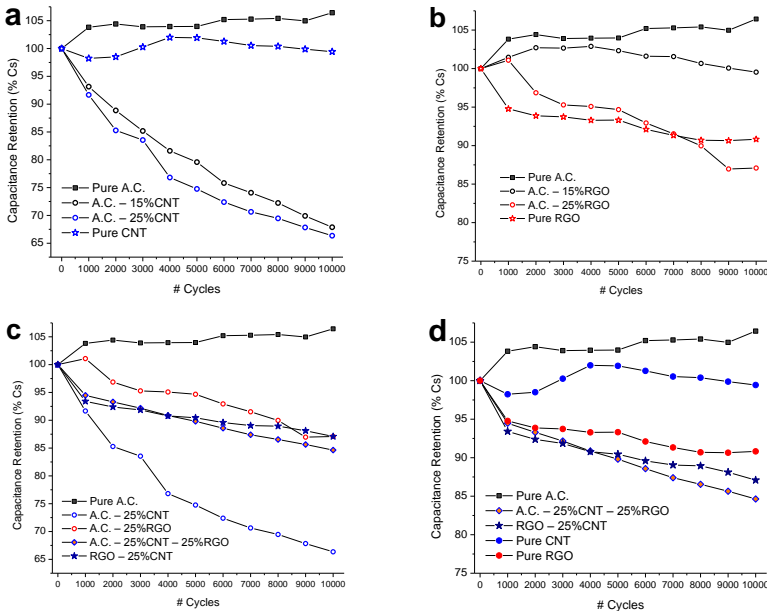


Fig. 3.29 Specific capacitance change over a 10000 CD life cycle testing.

In A.C.-RGO class (Fig. 3.29 (b)) a gradual decrease of the cyclability is observed by RGO content, that reaches a stable level at maximum content of RGO, namely, pure RGO electrode. Therefore, a lower degree of corrosion resistance for RGO can be concluded. Since RGO preparation has been accompanied a primary robust oxidation of graphite, a dramatic structural damage has been introduced to this material accompanied by attachment of oxygen functional groups to the surface. Although in the reduction step the functional groups have been acceptably removed, the initial structural damage caused by oxidation has not recovered completely and therefore, this material is inherently more susceptible to undergo degradation under corrosive working conditions. It is interesting however to note, that notwithstanding the occurrence of partial degradation in this material, this damage is not significantly influence the capacitance and after the 10000 cycles, a 90% of the primary capacitance is retained in pure RGO electrode, that is better than many reports in the literature.

Fig. 3.29 (c) presents the durability of A.C.–CNT–RGO class. It is seen that class also presents a continuous decrease of the capacitance and by the end of the cycling, they reach values in the same range as the A.C.–RGO class and considerably better than A.C.–CNT class. This means that in presence of RGO, the aforementioned issue of the conductivity loss of A.C.–CNT class has been remarkably addressed and the inherent degradation of RGO would dictate the degradation rate of performance of A.C.–CNT–RGO class. By complete replacement of A.C. particles by RGO (RGO–25%CNT electrode), the durability of the electrode becomes even better, confirming once more the role of A.C.–CNT interactions in the durability of the supercapacitor. Finally, Fig. 3.29 (d) compares the A.C.–CNT–RGO class with the one components electrodes, highlighting the concerns associated with the durability of composite electrodes. Therefore, in the energy improvements obtainable by the composite materials strategy, durability concerns should also be considered carefully.

### 3.3.3.5 Frequency response and relaxation time based on EIS

EIS is a widely used technique to investigate electrochemical systems, including supercapacitors. One advantage of EIS is that it is generally non-destructive and thus, can be carried out at different stages of the supercapacitor characterization to monitor the trend of possible changes in the properties of the electrode [542]. EIS is also a very common method for measuring the inherent resistance of the cell, called as equivalent series resistance (ESR) when measured through the EIS. The resistance values measured via EIS are usually smaller than those calculated via the CD test based on the ohmic drop at the initiation of the discharge cycle and its correlation with the internal resistance of the cell through the ohm's law. In our work, the basis for evaluation of the resistive properties of the supercapacitor was put on the CD test since it is more similar to real working condition of a supercapacitor.

In EIS, a sinusoidal AC excitation signal is applied to the investigated system and the AC response is measured. The frequency of the input signal is varied during the measurement. Finally, the impedance  $Z$  of the system is

calculated, expressed in terms of magnitude  $|Z|$  in ohms ( $\Omega$ ) and phase shift  $\phi$  in degree ( $^\circ$ ). This way of presentation of the results is called Bode plot. Since impedance  $Z$  is a complex number, it is possible to present the EIS results as the real ( $Z'$ ) and imaginary ( $Z''$ ) parts of the impedance in different frequencies [542]:

$$Z(\omega) = Z'(\omega) + jZ''(\omega) \quad (3-7)$$

where  $\omega$  is the angular frequency which equals  $2\pi f$  and  $f$  is the frequency. This way of presentation of the results is called Nyquist plot as shown for a typical electrode in Fig. 3.30 (a).

The relationship of impedance  $Z(\omega)$  with the capacitance  $C(\omega)$  can be written as [543]:

$$Z(\omega) = \frac{1}{j\omega C(\omega)} \quad (3-8)$$

and therefore, it is possible use the EIS data to evaluate the capacitive properties of the supercapacitor as a function of the frequency by combination of Eq. (3-7) and Eq. (3-8) through the following equation [534]:

$$C(\omega) = \frac{1}{\omega(jZ'(\omega) - Z''(\omega))} \quad (3-9)$$

It is then possible to define:

$$C(\omega) = C'(\omega) - jC''(\omega) \quad (3-10)$$

leading to [534]:

$$C'(\omega) = \frac{-Z''(\omega)}{\omega|Z(\omega)|^2} \quad (3-11)$$

$$C''(\omega) = \frac{Z'(\omega)}{\omega|Z(\omega)|^2} \quad (3-12)$$

where,

- $C'(\omega)$  is the real part of the capacitance  $C(\omega)$ ; the low frequency value of  $C'(\omega)$  corresponds to the capacitance of the cell that is measured during constant current discharge, for example.
- $C''(\omega)$  is the imaginary part of the capacitance  $C(\omega)$ ; corresponding to an energy dissipation by some kind of irreversible processes that can take place and lead to a hysteresis, such as an example the dielectric losses in water occurring during the rotation or the movement of the molecules.

Finally, it is possible to present the EIS results in the form of real and imaginary parts of the capacitance as functions of the frequency. Fig. 3.30

(b) shows such was of presentation for a typical electrode.

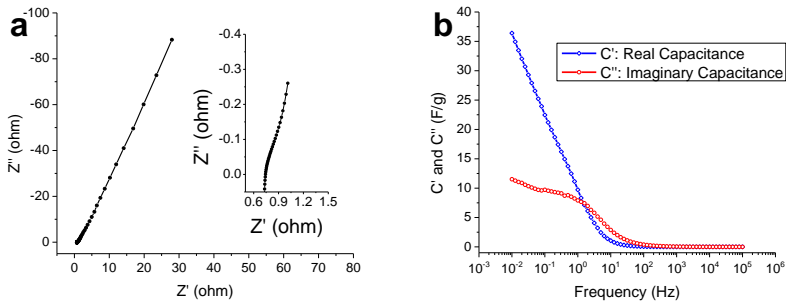


**Fig. 3.30** The EIS results of a typical supercapacitor, (a) Nyquist presentation with inset magnifying the high frequency region, (b) real and imaginary capacitance obtained by elaboration of the raw EIS data, as a function of the frequency.

As seen, in the plot of  $C''(\omega)$  vs.  $f$ , a peak appears at a particular frequency, known as the relaxation frequency ( $f_0$ ) at which the behavior of the supercapacitor transits from resistive to capacitive. Regarding some electronic basics of resistor–capacitor circuits (RC circuits) containing a charged capacitor and a resistor, the voltage decays exponentially:

$$V(t) = V_0 e^{-\frac{t}{RC}} \quad (3-13)$$

therefore, a time constant  $\tau_0$  can be defined as:

$$\tau_0 = RC \quad (3-14)$$

at which the potential of the capacitor  $V(t)$  drops by factor of  $e$  (Euler's number = 2.718) compared to its initial fully charged state potential  $V_0$ :

$$\frac{V(t)}{V_0} = \frac{1}{e} = 0.368 \quad \text{at } t = \tau_0 \quad (3-15)$$

and correspondingly, the energy stored in capacitor, drops (is delivered to the resistor in fact) by a factor of  $e^2$  compared to its initial fully charged state energy  $E_0 = E_{max}$ :

$$\frac{E(t)}{E_0} = \frac{1}{e^2} = 0.135 \quad \text{at } t = \tau_0 \quad (3-16)$$

therefore, after a time equal to time constant  $\tau_0$  a capacitor has released 86.5% of the total energy stored in it. This time constant  $\tau_0$ , according to its definition,  $\tau_0 = RC$ , represents the time by which a resistive to capacitive transition in the behavior the circuit takes place.

Accordingly, in the context of supercapacitors, such time constant  $\tau_0$ , can be defined as the frontier between the capacitive and and the resistive behaviors, corresponding to the reciprocal of relaxation frequency,  $f_0$ ,

introduced before. Obviously, the higher the relaxation frequency  $f_0$  and the lower the relaxation time  $\tau_0$ , the higher the power delivery of the supercapacitor.

### 3.3.3.5.1 A.C. – CNT electrodes

Fig. 3.31 shows the mass normalized real and imaginary capacitance components of the A.C.–CNT class electrodes as functions of frequency based on the EIS results. From Fig. 3.31 (a), similar trend of specific capacitance change by the CNT composition can be observed as the one obtained by the CD technique (compare to Fig. 3.23 (a)). In Fig. 3.31 (b), a maximum can be observed in the  $C''(\omega)$  plot of all CNT containing samples, corresponding to relaxation frequency as discussed earlier. The corresponding relaxation time  $\tau_0$  has been calculated for each electrode as shown in Fig. 3.34, demonstrating a faster frequency response at increased contents of CNTs. In case of pure A.C. electrode, the frequency response has been so poor (low relaxation frequency and high relaxation time) that no peak appeared in the  $C''(\omega)$  plot in the investigated frequency window (100 kHz to 10 mHz, corresponding to relaxation time window of 0.00001 s to 100 s, respectively). It is inferred that this electrode has such slow frequency response that in the entire frequency range of this experiment has

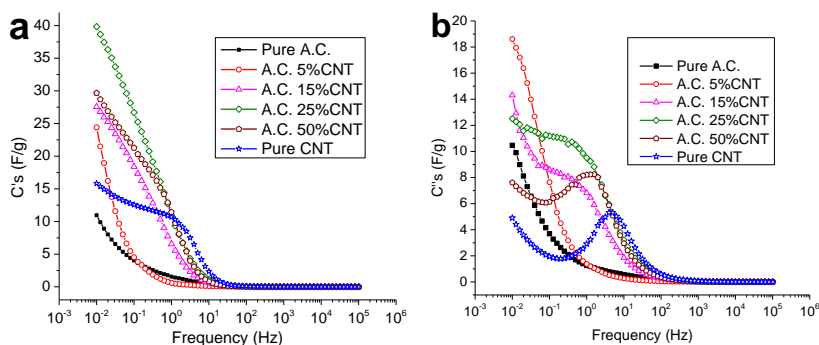


**Fig. 3.31** EIS results of A.C.–CNT class electrodes presented in the form of (a) real and (b) imaginary capacitances as functions of frequency.

shown a dominant resistive characteristic and any probable transition to capacitive behavior would have happened only at much lower frequencies. The excellent frequency response of CNTs is well known and is attributed to homogeneous pore size distribution of this material in the mesopore range and open and straightforward ionic paths towards the pores due to cylindrical morphology of CNTs [534,544–546]. Therefore, the improved frequency response by CNT content is not strange. Even at low CNT contents (A.C.–5%CNT) the relaxation frequency has appeared, though is still low.

### 3.3.3.5.2 A.C. – RGO electrodes

Fig. 3.32 shows the mass normalized real and imaginary capacitance components of the A.C.–RGO class electrodes as functions of frequency based on the EIS results. Also in this class a good agreement between the EIS and CD results can be seen in the trend of change of the specific capacitance with the composition (compare Fig. 3.32 (a) and Fig. 3.24 (b)).

RGO shows a positive influence on the frequency response of the A.C. based supercapacitor. However, it is not as effective as CNTs in this respect. Only at high enough RGO contents ( $\geq 25\%$ ) the relaxation frequency appears in the plot and the pure RGO sample shows a relaxation time 33 times longer than pure CNT (see Fig. 3.34). This, in general implies

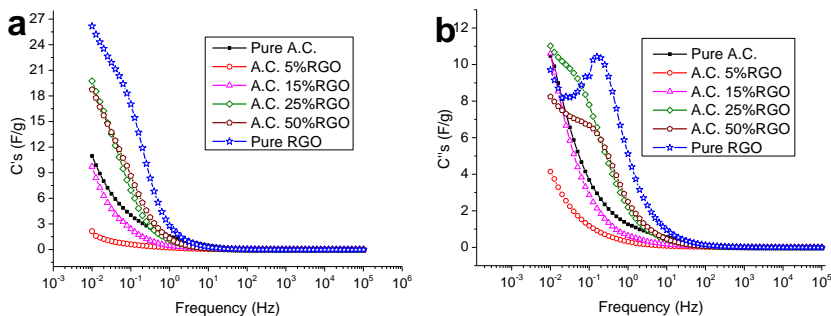


Fig. 3.32 EIS results of A.C.–RGO class electrodes presented in the form of (a) real and (b) imaginary capacitances as functions of frequency.

the higher surface area of RGO along with its smaller pore size. However, it seems to have more homogeneous distribution of pore size and closer to the mesopore range, compared to A.C., according to its positive contribution to the frequency response of pure A.C. electrode. Moreover, the effect of electrical conductivity should not be forgotten as it will directly affect the internal resistance of the cell. According to conductivity measurements (see Fig. 3.19 and Fig. 3.20), RGO possessed a conductivity between CNT and A.C., that would also contribute in the overall frequency response and relaxation time of this class of electrodes.

### 3.3.3.5.3 A.C. – CNT – RGO electrodes

Fig. 3.33 shows the mass normalized real and imaginary capacitance components of the A.C.–CNT–RGO class electrodes as functions of frequency based on the EIS results. All the samples of this class show an acceptable frequency response and the constant 25% CNT content guarantees a short a relaxation time. It is seen that primarily, by the increase of the RGO content in presence of A.C., the relaxation time increases slightly, due to accumulative high syrface area and low pore size effect of A.C. and RGO. However, by complete replacement of A.C. with RGO, the time constant decreases again to values close to 1 s.

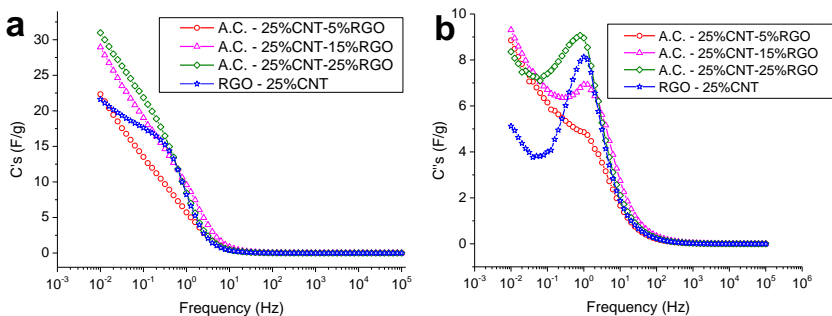


Fig. 3.33 EIS results of A.C.–CNT–RGO class electrodes presented in the form of (a) real and (b) imaginary capacitances as functions of frequency.

By a quick summary of the EIS results and frequency response of all the electrodes in terms of relaxation time in Fig. 3.34, it can be concluded that A.C.–CNT–RGO class electrodes show the most stable yet fast frequency response among the others and in this respect, the strategy of hybridizing the electrode materials seems to be reasonable and promising.

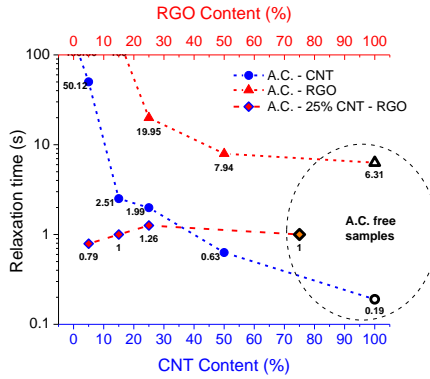


Fig. 3.34 Relaxation time  $\tau_0$  of different classes of electrodes as a function of the composition.

### 3.3.3.6 Power performance

#### 3.3.3.6.1 Power density

In definition, the electrical power  $P$  delivered to a component is given by:

$$P = \frac{E}{t} = \frac{VQ}{t} = V \cdot I$$

(3-17)

and given  $V = I \cdot R$  by ohm's law;

$$P = I^2 \cdot R = \frac{V^2}{R}$$

(3-18)

Where,  $E$  is the energy released in a time  $t$ ,  $Q$  is electric charge moved through an electric potential of  $V$ , causing a current of  $I$  to flow.

Therefore, in case of supercapacitors, the electrical power can be evaluated based on the energy density calculated for it through any of CV, CD or EIS techniques. In our work, as explained before, the results of CD technique were used for this purpose and since this technique could provide the opportunity of direct calculation of the specific energy according to Eq. (3-2), the specific power or power density could be easily calculated by:

$$P_s = \frac{E_s}{t_{disch}} \quad (3-19)$$

where  $E_s$  is the specific energy and  $t_{disch}$  is the corresponding discharge time in hour.

It should be noted that for evaluation of the power density of supercapacitors, the delivered power corresponds to a certain rate of discharge into some load resistance at a particular arbitrary current density, and being defined (as expressed in Eq. (3-17)) as

power = current (I) . voltage (V)

obviously depends on the discharge current  $I$  applied. Therefore, we tried to calculate the power density at all the different discharge currents discussed in section 3.3.3.1 and present it as  $P_s$  vs.  $I_s$  plots, shown in Fig. 3.35.

Fig. 3.35 (a) shows the specific power plots for A.C.-CNT class electrodes at different discharge specific currents and as seen, straightening and steeping of the curves take place by increasing the CNT content. The pure A.C. electrode inclines at currents above  $1 \text{ Ag}^{-1}$  showing its poor capability for fast energy delivery. As understood from Eq. (3-19), both the discharge time and the stored energy that in turn depends on the ohmic drop, can

affect the power density. Hence, the inclination of the  $P_s$  vs.  $I_s$  plots shown in Fig. 3.35 says that at increased currents, either the ohmic drop becomes so significant the limits the energy storage and withdrawal or the dominant charge storage processes on the electrode become inactive due to the fast CD. In this sense, pure A.C. electrode is performing even poorer than low CNT content electrodes such as A.C.–5% CNT. At CNT contents higher than 15% no inclination is observed in the discharge current window investigated here, i.e., 0.1 to 3 Ag<sup>-1</sup>. At 3 Ag<sup>-1</sup> the A.C.–50% CNT and pur CNT electrodes could reach power densities close to 700 Wkg<sup>-1</sup> that seems to be still far below the max power density obtainable with these electrodes (due to still straight appearance of the plots and absence of any slope change).

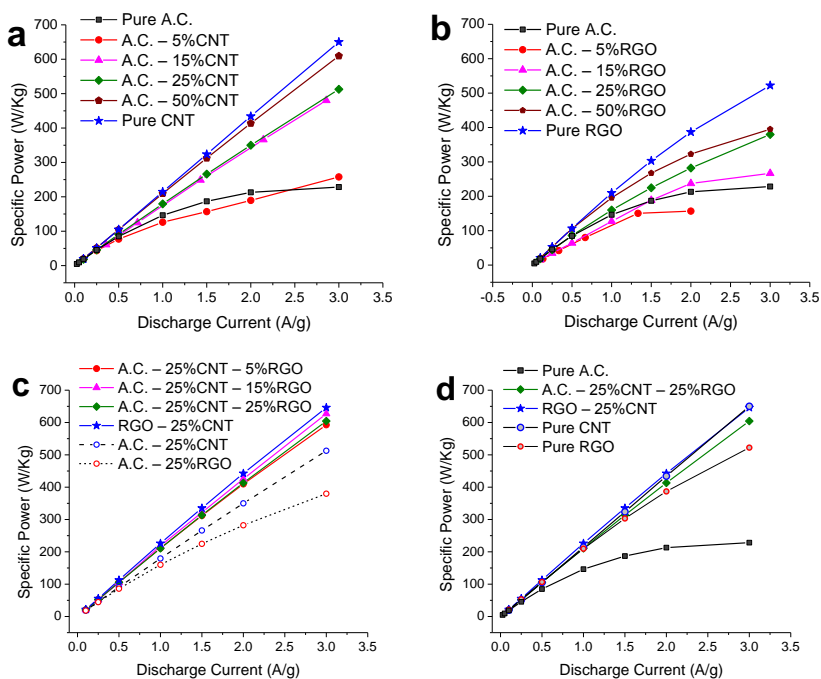


**Fig. 3.35** Power performance of different classes of supercapacitor electrodes as a function of discharge specific current.

Fig. 3.35 (b) shows the the specific power plots for A.C.–RGO class electrodes at different discharge specific currents. The shape of the plots has changes compared to A.C.–CNT class and almost all of them show a slope change and initial inclination, implying lower power performance with respect to CNT containing electrodes. This fact was observed in the EIS results as well in the from of higher relaxation times for this class (see Fig. 3.32 (b)). However, also this group of electrodes show a better performance than the pure A.C. electrode by increasing the RGO content as reveald by the corresponding upward (higher power) shifting of the plots. Fig. 3.35 (c) shows the effect of coexistence of CNT and RGO in A.C.–CNT–RGO class in the form an excellent improvement in power performance and the lack of any slope change in all the electrodes along with higher power densities than than either A.C.–25% CNT or A.C.–25% RGO at all discharge currents. In particular, RGO–25% CNT which is completely depleted from A.C., shows a power density in the order of pure CNT electrode (as presented in Fig. 3.35 (d) and compared with other single component electrodes), outperforming all the A.C.–CNT–RGO class electrodes. This confirms another time the promising potential of the composite material strategy for developing high power performance supercapacitors.

### 3.3.3.6.2 Internal resistance and matched impedance power ( $P_{max}$ )

In electrical engineering, the maximum power transfer theorem states that, to obtain maximum external power from a source with a finite internal resistance, the resistance of the load must equal the resistance of the source as viewed from its output terminals. Moritz Hermann von Jacobi published the maximum power (transfer) theorem around 1840; it is also referred to as “Jacobi's law” [547]. Therefore, from the maximum energy stored in a capacitor with capacitance  $C$ ,  $E_{max} = \frac{1}{2}CV^2$ , a part of it will be ready to be transferred to an external load ( $E_{Load}$  or  $E_L$ ) and part of it will dissipate inside the capacitor itself due to its internal resistance ( $E_{Series Resistance}$  or  $E_s$  or  $R_{internal}$ ), generating heat. Thus:

$$E_{max} = E_L + E_s$$

(3-20)

It can be demonstrated through Eq. (3-20) in combination with Eq. (3-17) and Eq. (3-18) that:

$$P_{total} = P_L + P_s = V_L I + V_s I = \frac{V_L^2}{R_L} + \frac{V_s^2}{R_s}$$

(3-21)

where  $P_{total}$  is the total power available due to release of the maximum energy stored in the capacitor and  $R_L$  and  $R_s$  are the load resistance and the internal resistance, respectively, connected in series as shown schematically in Fig. 3.36.  $V_c$  in the illustration is a theoretical value of the internal voltage on the capacitance, which is inaccessible for measurement,  $V_L$  is the voltage at the physical terminals of the storage device after the potential drop  $V_s$  due to the internal resistance of the capacitor (thus  $V_s$  is voltage at the equivalent series resistance  $R_s$ ). Regarding the power available for transfer to the external load regardless of the fraction of the energy that is dissipated in the

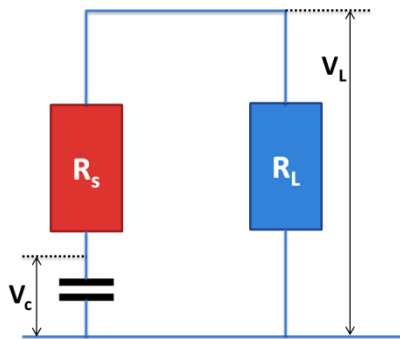


Fig. 3.36 Supercapacitor electrical equivalent circuit adopted from [548].

internal resistance of the cell,  $V_L$  should be considered as the potential of the load and thus:

$$P_L = \frac{V_L^2}{R_L}$$

(3-22)

In a particular case called *impedance matching*, i.e., when  $R_S = R_L$ , the power available for the external load  $P_L$  and the power dissipated in the internal resistance  $P_S$  are equal since in this condition, the voltage on the “pure” capacitance  $V_C$ , is double that of the voltage at the capacitor terminal  $V_L$ . In this condition, the power available for transfer to external load can be written as:

$$P_{\text{matched impedance}} = \frac{(V_C/2)^2}{R_L=R_S} = \frac{V_{max}^2}{4R_S}$$

(3-23)

When the resistance of the external load is very large (i.e., very larger than the internal resistance of the supercapacitor), a very small current will be flowing and a small potential drop due to internal resistance of the supercapacitor will happen. Therefore, the power transferred to the load is low (due to low current flow) and the efficiency is high (due to low dissipation inside the supercapacitor). By gradual decrease of the resistance of the external load compared to the internal resistance of the supercapacitor, a larger current will flow and the transferred power to the load increases, but at the expense of increased power dissipation due to larger ohmic potential drops inside the supercapacitor. At matched impedance condition, these two become equal and the efficiency reaches to 50%. When the resistance of the external load is smaller than the internal resistance of the supercapacitor, most of the stored energy is burnt in the internal resistance of the storage component, with the consequence of fast heating. Therefore, the available power for the load reaches a maximum at match impedance conditions after which, the dissipation becomes dominant and the available power for transfer to the external load decreases again. In this respect, the Eq. (3-23) can be rewritten in this form:

$$P_{s,max} = \frac{V^2}{4 \times R_s \times m_{total}}$$

(3-24)

where  $P_{s,max}$  is the maximum available specific power for the load,  $V$  is full potential window of the supercapacitor without consideration of any drop,  $R_s$  is the internal resistance of the cell and  $m_{total}$  is total weight of the active materials in the device.

Accordingly, internal resistances ( $R_s$  or  $R_i$ ) of all the electrodes were calculated based on the CD test results and the observed ohmic drops of the potential at the initiation of the discharge cycle and as Fig. 3.37 (a) shows for a typical sample, stable and almost constant values were obtained for a given cell at different CD currents.

Finally, the average internal resistance over the entire CD current range was calculated for each electrode as shown in Fig. 3.37 (b), and the maximum power available for transfer to external load corresponding to the calculated internal resistances were calculated and averaged as indicated in Fig. 3.37 (c). The A.C.-CNT class shows a continuous reduction in the  $R_i$  by CNT content, except at A.C.-5% CNT where a sudden increase is observed. This exception can be justified based on the SEM observations and issues concerned with architecture of the low content CNT or RGO electrodes (see Fig. 3.10 and Fig. 3.13 and the related discussions). At maximum CNT content, i.e., pure CNT electrode, a  $R_i$  as low as  $0.8 \Omega$  and a  $P_{s,max}$  as high as almost  $22 \text{ kWkg}^{-1}$  were obtained, and proved the best power performance of this electrode compared to all others. A.C.-RGO electrodes also showed a decrease in  $R_i$  by RGO content (except A.C.-5% RGO), though to a certain level. Accordingly, their  $P_{s,max}$  did not exceed  $5.6 \text{ kWkg}^{-1}$  for the best performing sample, i.e., pure RGO. The A.C.-CNT-RGO class showed the minimum  $R_i$  fluctuations by composition, probably due to presence of a constant 25% content of CNTs supplying them with reasonable electrical conductivity. Therefore, their  $P_{s,max}$  was also steady in the range of  $10 \text{ kWkg}^{-1}$ .

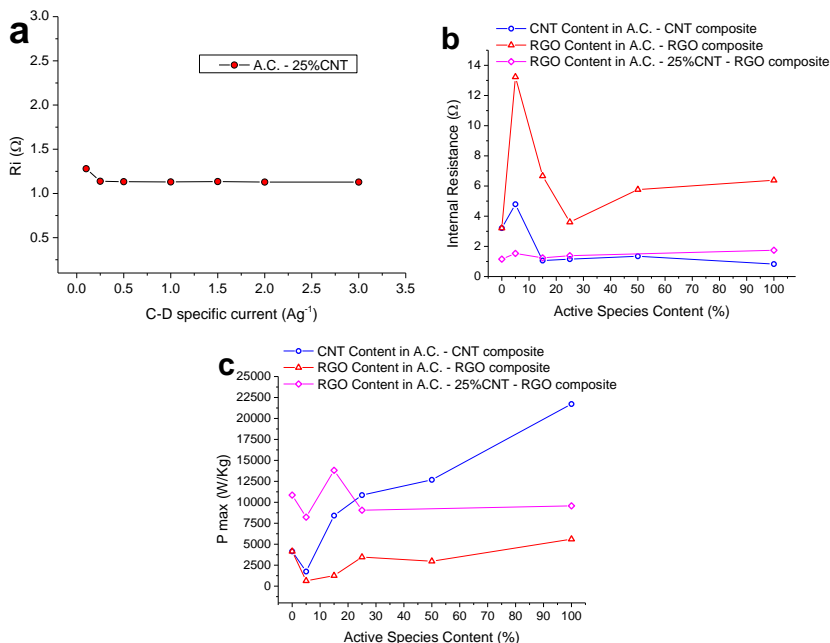


**Fig. 3.37** (a) internal resistance of a typical sample calculated at different CD currents, (b) average internal resistance of different electrodes as a function of the composition and (c) the power of matched impedance for different electrodes as a function of the composition.

### 3.3.3.7 Ragone plots

Ragone plots are used for comparison of the energy and power performance of various energy-storing devices. On such a chart the energy density (in  $\text{W}\cdot\text{h}/\text{kg}$ ) values are plotted versus power density (in  $\text{W}/\text{kg}$ ). Both axes are logarithmic, which allows comparing performance of very different devices. Since the calculations of energy and power density in our work were carried out based on the performance of a two electrode packed cell, it could be helpful to project the calculated power densities corresponding to an energy density measured in the same CD current and build up the Ragone plot of the supercapacitors. The results are shown in Fig. 3.38 for different classes of electrodes. Theoretically, at low CD currents where the slow electrode

processes can also contribute in the energy storage on one hand and the ohmic drop is low on the other hand, high energy densities and lower power densities are formed and at high CD currents where only fast electrode processes can contribute in the energy storage on one hand and the ohmic drop is large on the other hand, low energy densities and higher power densities are formed. However, depending on the type of electrode materials and the nature of charge storage, some maximum CD currents can be considered above which, the power density would not increase any more due to extremely large ohmic drops and exceeding the power at matched impedance criterion. In fact, large DC currents simulate a very small external load, corresponding to  $R_L \leq R_i$ , where most of the power will be dissipated in the internal resistance of the supercapacitor and at an extreme case,  $R_L \rightarrow 0$  and a short circuit takes place. Therefore, the high power end of different devices in Ragone plot will for a “hook” where a change in the slope of the plot appears and finally, no further increase in power density will be seen.

Fig. 3.38 (a) shows the Ragone chart of the A.C.–CNT class and a gradual move to the high energy end of the plot is realized by the initial increase of the CNT content along with an increased slope of the curve. This means that up to a limit (between 25–50%) increasing the CNT contents increases both energy and power densities. However, after this limit, the slope continuously further steepening, implying further improvement of the power performance, but the curves move to the low energy side demonstrating a decreased energy expectancy at high CNT contents. The hook has appeared for A.C.–5% CNT and A.C.–15% CNT, but not for higher CNT contents, suggesting further room for higher CD currents and thus, higher power densities.

Fig. 3.38 (b) shows the Ragone chart of the A.C.–RGO class and in contrast to A.C.–CNT class, the hook has appeared for all the samples in the investigated CD currents range, evidencing lower power expectancy from this class. Increase of the RGO content in this class has continuously increased both energy and power performance as proven by the up-right shift of the plots corresponding to higher RGO contents.

More interesting results were observed for the A.C.–CNT–RGO class where

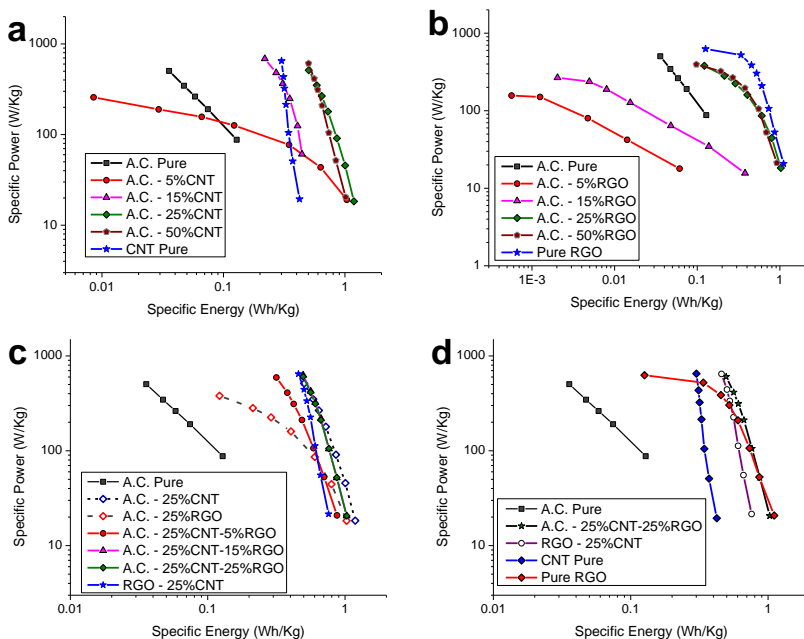


**Fig. 3.38** Ragone plots of different classes of electrodes as electrochemical energy storage devices.

positive features of different classes are combined (see Fig. 3.38 (c and d)).

For instance, in Fig. 3.38 (d) it is seen that A.C.–25% CNT–25% RGO is performing in the same energy level as pure RGO and keeping a similar slope as that of pure CNT electrode. By complete replacement of A.C. by RGO in RGO–25% CNT, the slope becomes even steeper. In brief, it can be concluded that the strategy of hybridizing the electrode materials such as CNT and RGO, provides a powerful tool for fine tuning the power and energy capabilities of the device.

### 3.4 Conclusion

In this work, a systematic study of different carbon nanostructures as active materials for supercapacitors was carried out. A.C. as the conventional

material for this application was characterized and compared with newer species like CNT and RGO, both synthesized in the laboratory. Furthermore, different combinations of these materials were investigated to have a clearer understanding of the potentials and risks of hybridization strategy for preparation of supercapacitor carbon based active materials. Microstructural characterizations showed that the CVD synthesis of CNT followed by proper purification and the thermal reduction of GO prepared by a combination of Staudenmaier and Hummers methods, have successfully resulted in 1D and 2D active materials for supercapacitors. Electrical conductivity measurements showed that CNT with a conductivity of  $332 \text{ Sm}^{-1}$  was the best electrically conductor species, whereas A.C. showed the lowest conductivity in the order of  $10 \mu\text{Sm}^{-1}$ . RGO with a conductivity in the range of  $1 \text{ Sm}^{-1}$  demonstrated a reasonable degree of reduction and conductivity recovery. However, further improvements of the electrical quality of the species is quite likely upon optimization of the reduction parameters such temperature and atmosphere.

Paste preparation and casting method was used for preparation of the supercapacitor electrodes in three main classes including A.C.–CNT, A.C.–RGO and A.C.–CNT–RGO, each class including a range of compositions. Electrochemical characterization of the electrodes was carried out using CV, CD and EIS techniques and most of the important specifications were evaluated based on the CD results.

Specific capacitance and energy density studies showed that a big contribution in the deficiency of A.C. electrodes was originating from the lack of electrical conductivity. Addition of more conductive species could address this problem. However, there were minimum required levels of the second phase (CNT or RGO) addition, below which, the composite material was performing poorly (like A.C.–5% CNT and A.C.–5% RGO) due to loose interconnection of the A.C. and the second phase particles and formation of a foamy architecture with extra ordinary thickness, voluminous macropores and low electrical conductivity. In A.C.–CNT class a maximum was observed in the specific capacitance and energy density in the intermediate compositions below which the composite suffered from low conductivity and above which, the lower specific surface area CNTs was

limiting the capacitance. In A.C.–RGO class however, a continuous increase of both specific capacitance and energy was observed by RGO content due to simultaneous improvement of conductivity and almost similar surface area. A.C.–CNT–RGO class showed the lowest dependence on the composition of the added constituents since a good conductivity was supplied by the constant 25% CNT content and an acceptable surface area was provided by the RGO.

Rate capability studies based on the Peukert type plots of CD test as well as CV measurements showed a superior behavior of pure CNT electrodes or those containing a high content of CNTs. RGO was behaving better than A.C. in this respect, but still more sensitive to the rate compared to CNTs. Composite three component electrodes of A.C.–CNT–RGO class benefitted from high accessibility and ionic conductivity of mesopore of CNTs along with the high surface area of RGO, and thus, presented high rate capability and energy density at the same time, so as the RGO–25%CNT was comparable to pure CNT sample in terms of rate capability.

Ideality of the performance of different electrodes were checked based on a novel criterion defined in this work as the ratio of the area under the real discharge curve to that under the ideal discharge curve and the proximity of the this ideality factor, IF, to unity, could describe the degree of ideality of the performance. This factor was showing a direct relation with the content of both CNT and RGO, so as the IF of both A.C.–CNT and A.C.–RGO classes increased at increased contents of the corresponding components. This factor also showed a direct relation with CD rate for A.C.–CNT and a reverse relation with CD rate for A.C.–RGO class. Interestingly, electrodes of A.C.–CNT–RGO class showed extraordinarily high and steady IF values over the entire CD rates range. By the complete replacement of A.C. content with RGO in RGO–25%CNT electrode, an almost always  $IF \geq 0.9$  condition was established, giving rise to IF values as high as 0.93.

Durability studies showed one of the few infirmities of the composite electrodes in this work. In general, single components electrodes especially pure CNT and pure A.C. had the best stability and capacitance retentions. Pure RGO showed a poorer stability due to inherent structural damages introduced to it during the robust oxidation process, making it more

susceptible to corrosion and degradation. The negative effect of hybridizing the electrode materials on their durability was considered to be originating from the integrity loss of the active film over time. This comprises the loss of mechanical and electrical interconnection of the constituents generating heterogeneity in electronic and ionic properties of the entire electrode. In this respect, the larger the morphological dissimilarities of the initial constituents, the higher the susceptibility to durability shortcomings. From another point of view, however, this can be looked at as a technical problem in the electrode preparation process that can be improved by optimization of the paste treatment and binder materials as well as possibly some stabilization post treatments.

EIS studies were carried out not only to confirm the capacitance behavior observed by the CD and CV techniques, but also to evaluate the frequency response and relaxation behavior of the electrodes. A faster frequency response and shorter relaxation time of CNT and RGO electrodes was confirmed compared to A.C., with distinct superiority of CNT. Almost all the observation of the rate capability studies were confirmed and direct relation between the relaxation frequency and CNT or RGO contents (in A.C.–CNT and A.C.–RGO classes, respectively) was demonstrated. The shortest relaxation time of A.C.–RGO class was 6.31 s for pure RGO electrode, whereas the pure CNT showed relaxation time of 0.19 s. Finally, the A.C.–CNT–RGO class electrodes showed the most stable yet fast frequency response (almost 1 s at all compositions) among the others and in this respect, the strategy of hybridizing the electrode materials seems to be reasonable and promising.

Internal resistance of the electrodes was also calculated based on the CD results and was used for the calculation of the maximum power availability for external load at matched impedance condition. Expectedly, a direct relation between electrode materials conductivity and the internal resistance was confirmed suggesting considerable power improvement of the CNT containing samples. The pure CNT sample was evaluated to have a  $P_{s,max}$  of 22 kWkg<sup>-1</sup>, whereas the best electrode of the A.C.–RGO class in this respect, pure RGO, showed a  $P_{s,max}$  of 5.6 kWkg<sup>-1</sup>. The A.C.–CNT–RGO class showed the minimum  $R_i$  fluctuations by composition, probably due to

presence of a constant 25% content of CNTs supplying them with reasonable electrical conductivity. Therefore, their  $P_{s,max}$  was also steady in the range of  $10 \text{ kWkg}^{-1}$ .

Eventually, the power densities of the electrodes were evaluated based on the CD results at different CD currents and was used along with the corresponding energy densities to establish the Ragone plot of the electrodes. It was concluded that the CNT constituent encourages the high power end shift of a given electrode's curve and postpones the appearance of the power limit hook to higher CD currents, whereas the RGO helps the energy capabilities. The Most promising results were therefore, observed for the A.C.–CNT–RGO class where positive features of different classes were combined. For instance, A.C.–25% CNT–25% RGO was performing in the same energy level as pure RGO and keeping a similar slope and power expectancy as that of pure CNT electrode. In brief, it can be concluded that the strategy of hybridizing the electrode materials such as CNT and RGO, provides a powerful tool for fine tuning the power and energy capabilities of the supercapacitor.

## References

- [1] Choy KL. Chemical vapour deposition of coatings. *Prog Mater Sci* 2003;48:57–170. doi:10.1016/S0079-6425(01)00009-3.
- [2] Zhou W, Han Z, Wang J, Zhang Y, Jin Z, Sun X, et al. Copper catalyzing growth of single-walled carbon nanotubes on substrates. *Nano Lett* 2006;6:2987–90. doi:10.1021/nl061871v.
- [3] Yoshihara N, Ago H, Tsuji M. Growth mechanism of carbon nanotubes over gold-supported catalysts. *Jpn J Appl Phys* 2008;47:1944–8. doi:10.1143/JJAP.47.1944.
- [4] Yuan D, Ding L, Chu H, Feng Y, McNicholas TP, Liu J. Horizontally aligned single-walled carbon nanotube on quartz from a large variety of metal catalysts. *Nano Lett* 2008;8:2576–9. doi:10.1021/nl801007r.
- [5] Takagi D, Homma Y, Hibino H, Suzuki S, Kobayashi Y. Single-walled carbon nanotube growth from highly activated metal nanoparticles. *Nano Lett* 2006;6:2642–5. doi:10.1021/nl061797g.
- [6] Lee S-Y, Yamada M, Miyake M. Synthesis of carbon nanotubes over gold nanoparticle supported catalysts. *Carbon* 2005;43:2654–63. doi:10.1016/j.carbon.2005.05.045.
- [7] Liu H, Takagi D, Ohno H, Chiashi S, Chokan T, Homma Y. Growth of single-walled carbon nanotubes from ceramic particles by alcohol chemical vapor deposition. *Appl Phys Express* 2008;1:014001–3. doi:10.1143/APEX.1.014001.
- [8] Steiner SA, Baumann TF, Bayer BC, Blume R, Worsley MA, MoberlyChan WJ, et al. Nanoscale Zirconia as a nonmetallic catalyst for graphitization of carbon and growth of single- and multiwall carbon nanotubes. *J Am Chem Soc* 2009;131:12144–54. doi:10.1021/ja902913r.
- [9] Takagi D, Hibino H, Suzuki S, Kobayashi Y, Homma Y. Carbon nanotube growth from semiconductor nanoparticles. *Nano Lett* 2007;7:2272–5. doi:10.1021/nl0708011.
- [10] Uchino T, Bourdakos KN, Ayre GN, de Groot CH, Ashburn P, Smith DC. CMOS compatible synthesis of carbon nanotubes. *MRS Online Proc Libr* 2008;1081:P01–9. doi:10.1557/PROC-1081-P01-09.
- [11] Uchino T, Ayre GN, Smith DC, Hutchison JL, Groot CH de, Ashburn P. Growth of single-walled carbon nanotubes using Germanium nanocrystals formed by implantation. *J Electrochem Soc* 2009;156:K144–8. doi:10.1149/1.3147248.
- [12] Uchino T, Bourdakos KN, de Groot CH, Ashburn P, Kiziroglou ME, Dilliwai GD, et al. Metal catalyst-free low-temperature carbon nanotube growth on SiGe islands. *Appl Phys Lett* 2005;86:N.233110: 1–3. doi:10.1063/1.1946191.
- [13] Charlier J-C, Iijima S. Growth mechanisms of carbon nanotubes. In: Dresselhaus MS, Dresselhaus G, Avouris P, editors. *Carbon Nanotub.*, Springer Berlin Heidelberg; 2001, p. 55–81.
- [14] G. N. Ayre, T. Uchino, B. Mazumder, A. L. Hector, D. C. Smith, P. Ashburn, et al. Chemical vapour deposition of CNTs using structural nanoparticle catalysts. In: Jose Mauricio Marulanda, editor. *Carbon Nanotub.*, InTech; 2010, p. 19–38.
- [15] Dupuis A-C. The catalyst in the CCVD of carbon nanotubes—a review. *Prog Mater Sci* 2005;50:929–61. doi:10.1016/j.pmatsci.2005.04.003.
- [16] Kaviani R, Vicenzo A, Bestetti M. Growth of carbon nanotubes on aluminium foil for supercapacitors electrodes. *J Mater Sci* 2011;46:1487–93. doi:10.1007/s10853-010-4950-1.
- [17] Sadeghi SN, Shafiekhani A, Vesaghi MA. Direct production of carbon nanotubes decorated with Cu<sub>2</sub>O by thermal chemical vapor deposition on Ni catalyst electroplated on a copper substrate. *J Nanoparticle Res* 2011;13:4681–9. doi:10.1007/s11051-011-0432-x.
- [18] García-Céspedes J, Thomasson S, Teo KBK, Kinloch IA, Milne WI, Pascual E, et al. Efficient diffusion barrier layers for the catalytic growth of carbon nanotubes on copper substrates. *Carbon* 2009;47:613–21. doi:10.1016/j.carbon.2008.10.045.

- [19] Yin X, Wang Q, Lou C, Zhang X, Lei W. Growth of multi-walled CNTs emitters on an oxygen-free copper substrate by chemical-vapor deposition. *Appl Surf Sci* 2008;254:6633–6. doi:10.1016/j.apsusc.2008.04.040.
- [20] Fiedler H, Hermann S, Schulz SE, Gessner T. Influence of copper on the catalytic carbon nanotube growth process. *Proc. Interconnect Technol. Conf. Mater. Adv. Met. IITCMMAM, IEEE International*; 2011, p. 1–3. doi:10.1109/IITC.2011.5940346.
- [21] Liu F, Zhang Y. In-situ growth of carbon nanotubes from Ni-based coatings and their wear properties. *Diam Relat Mater* 2012;25:144–54. doi:10.1016/j.diamond.2012.03.003.
- [22] Atthipalli G, Epur R, Kumta PN, Allen BL, Tang Y, Star A, et al. The effect of temperature on the growth of carbon nanotubes on copper foil using a nickel thin film as catalyst. *Thin Solid Films* 2011;519:5371–5. doi:10.1016/j.tsf.2011.02.046.
- [23] Song J, Sun M, Chen Q, Wang J, Zhang G, Xue Z. Field emission from carbon nanotube arrays fabricated by pyrolysis of iron phthalocyanine. *J Phys Appl Phys* 2004;37:5–9. doi:10.1088/0022-3727/37/1/002.
- [24] Bronikowski MJ, Manohara HM, Hunt BD. Growth of carbon nanotube bundle arrays on silicon surfaces. vol. 24, *Journal of Vacuum Science & Technology A*; 2006, p. 1318–22. doi:10.1116/1.2172943.
- [25] Handuja S, Srivastava P, Vankar V. On the growth and microstructure of carbon nanotubes grown by thermal chemical vapor deposition. *Nanoscale Res Lett* 2010;5:1211–6. doi:10.1007/s11671-010-9628-8.
- [26] Show Y, Fukuzumi N. Selective growth of CNT by using triode-type radio frequency plasma chemical vapor deposition method. *Diam Relat Mater* 2007;16:1106–9. doi:10.1016/j.diamond.2006.11.066.
- [27] Yang Q, Tang Y, Yang SL, Li YS, Hirose A. Simultaneous growth of diamond thin films and carbon nanotubes at temperatures  $\leq 550$  °C. *Carbon* 2008;46:589–95. doi:10.1016/j.carbon.2008.01.005.
- [28] Abu Qahouq JA, Carnahan DL. Spiral shape CNT on silicon substrate growth control method for on-chip electronic devices applications. *Electron Lett* 2012;48:639–41. doi:10.1049/el.2012.0899.
- [29] He D, Bai J. Acetylene-enhanced growth of carbon nanotubes on ceramic microparticles for multi-scale hybrid structures. *Chem Vap Depos* 2011;17:98–106. doi:10.1002/cvde.201006878.
- [30] Lin C-C, Yang C-L. Carbon nanotubes grown on nanoporous Alumina templates/Aluminum foil for electrodes of Aluminum electrolytic capacitors. *J Electrochem Soc* 2010;157:A237–41. doi:10.1149/1.3272640.
- [31] Dikonimos Makris T, Giorgi L, Giorgi R, Lisi N, Salernitano E. CNT growth on alumina supported nickel catalyst by thermal CVD. *Diam Relat Mater* 2005;14:815–9. doi:10.1016/j.diamond.2004.11.001.
- [32] Jung M, Kim H-G, Lee J-K, Joo O-S, Mho S. EDLC characteristics of CNTs grown on nanoporous alumina templates. *Electrochimica Acta* 2004;50:857–62. doi:10.1016/j.electacta.2004.02.057.
- [33] Suvacı E, Çelik Y, Weibel A, Peigney A, Flahaut E. Organized growth of carbon nanotubes on Fe-doped alumina ceramic substrates. *Carbon* 2012;50:3092–5. doi:10.1016/j.carbon.2012.02.034.
- [34] Lee TY, Han J-H, Choi SH, Yoo J-B, Park C-Y, Jung T, et al. Comparison of source gases and catalyst metals for growth of carbon nanotube. *Surf Coat Technol* 2003;169–170:348–52. doi:10.1016/S0257-8972(03)00108-7.
- [35] Cui H, Zhou Q, Stoner BR. Deposition of aligned bamboo-like carbon nanotubes via microwave plasma enhanced chemical vapor deposition. *J Appl Phys* 2000;88:6072–4. doi:10.1063/1.1320024.
- [36] Joon Yoon Y, Cheol Bae J, Koo Baik H, Cho S, Lee S-J, Moon Song K, et al. Growth control of single and multi-walled carbon nanotubes by thin film catalyst. *Chem Phys Lett* 2002;366:109–14. doi:10.1016/S0009-2614(02)01548-8.
- [37] Hsu CM, Lin CH, Chang HL, Kuo CT. Growth of the large area horizontally-aligned carbon nanotubes by ECR-CVD. *Thin Solid Films* 2002;420–421:225–9. doi:10.1016/S0040-6090(02)00799-X.
- [38] Yudasaka M, Kikuchi R, Matsui T, Ohki Y, Yoshimura S, Ota E. Specific conditions for Ni catalyzed carbon nanotube growth by chemical vapor deposition. *Appl Phys Lett* 1995;67:2477–9. doi:10.1063/1.114613.
- [39] Ren ZF, Huang ZP, Xu JW, Wang JH, Bush P, Siegal MP, et al. Synthesis of Large Arrays of Well-Aligned Carbon Nanotubes on Glass. *Science* 1998;282:1105–7. doi:10.1126/science.282.5391.1105.
- [40] Ermakova MA, Ermakov DY, Chuvilin AL, Kuvshinov GG. Decomposition of methane over Iron catalysts at the range of moderate temperatures: the influence of structure of the catalytic

- systems and the reaction conditions on the yield of carbon and morphology of carbon filaments. *J Catal* 2001;201:183–97. doi:10.1006/jcat.2001.3243.
- [41] Pan Z., Xie S., Chang B., Sun L., Zhou W., Wang G. Direct growth of aligned open carbon nanotubes by chemical vapor deposition. *Chem Phys Lett* 1999;299:97–102. doi:10.1016/S0009-2614(98)01240-8.
- [42] Chen P, Zhang H-B, Lin G-D, Hong Q, Tsai KR. Growth of carbon nanotubes by catalytic decomposition of CH<sub>4</sub> or CO on a Ni-MgO catalyst. *Carbon* 1997;35:1495–501. doi:10.1016/S0008-6223(97)00100-0.
- [43] Bacsa RR, Laurent C, Peigney A, Bacsa WS, Vaugien T, Rousset A. High specific surface area carbon nanotubes from catalytic chemical vapor deposition process. *Chem Phys Lett* 2000;323:566–71. doi:10.1016/S0009-2614(00)00558-3.
- [44] Venegoni D, Serp P, Feurer R, Kihn Y, Vahlas C, Kalck P. Parametric study for the growth of carbon nanotubes by catalytic chemical vapor deposition in a fluidized bed reactor. *Carbon* 2002;40:1799–807. doi:10.1016/S0008-6223(02)00057-X.
- [45] Ivanov V, Nagy JB, Lambin P, Lucas A, Zhang XB, Zhang XF, et al. The study of carbon nanotubules produced by catalytic method. *Chem Phys Lett* 1994;223:329–35. doi:10.1016/0009-2614(94)00467-6.
- [46] Li Y, Kim W, Zhang Y, Rolandi M, Wang D, Dai H. Growth of single-walled carbon nanotubes from discrete catalytic nanoparticles of various sizes. *J Phys Chem B* 2001;105:11424–31. doi:10.1021/jp012085b.
- [47] Cheung CL, Kurtz A, Park H, Lieber CM. Diameter-controlled synthesis of carbon nanotubes. *J Phys Chem B* 2002;106:2429–33. doi:10.1021/jp0142278.
- [48] Li Y, Liu J, Wang Y, Wang ZL. Preparation of monodispersed Fe–Mo nanoparticles as the catalyst for CVD synthesis of carbon nanotubes. *Chem Mater* 2001;13:1008–14. doi:10.1021/cm000787s.
- [49] Nasibulin AG, Brown DP, Queipo P, Gonzalez D, Jiang H, Kauppinen EI. An essential role of CO<sub>2</sub> and H<sub>2</sub>O during single-walled CNT synthesis from carbon monoxide. *Chem Phys Lett* 2006;417:179–84. doi:10.1016/j.cplett.2005.10.022.
- [50] Kuwana K, Endo H, Saito K, Qian D, Andrews R, Grulke EA. Catalyst deactivation in CVD synthesis of carbon nanotubes. *Carbon* 2005;43:253–60. doi:10.1016/j.carbon.2004.09.008.
- [51] Castro C, Pinault M, Coste-Leconte S, Porterat D, Bendiab N, Reynaud C, et al. Dynamics of catalyst particle formation and multi-walled carbon nanotube growth in aerosol-assisted catalytic chemical vapor deposition. *Carbon* 2010;48:3807–16. doi:10.1016/j.carbon.2010.06.045.
- [52] Kunadian I, Andrews R, Qian D, Pinar Mengüç M. Growth kinetics of MWCNTs synthesized by a continuous-feed CVD method. *Carbon* 2009;47:384–95. doi:10.1016/j.carbon.2008.10.022.
- [53] Delmas M, Pinault M, Patel S, Porterat D, Reynaud C, Mayne-L’Hermite M. Growth of long and aligned multi-walled carbon nanotubes on carbon and metal substrates. *Nanotechnology* 2012;23:N.105604: 1–8. doi:10.1088/0957-4484/23/10/105604.
- [54] Kanchan M. Samant, Santosh K. Haram, Sudhir Kapoor. Synthesis of carbon nanotubes by catalytic vapor decomposition (CVD) method: Optimization of various parameters for the maximum yield. *Pramana - J Phys* 2007;68:51–60.
- [55] Yao BD, Wang N. Carbon Nanotube Arrays Prepared by MWCVD. *J Phys Chem B* 2001;105:11395–8. doi:10.1021/jp011849k.
- [56] Kim J-P, Kim Y-K, Park C-K, Choi H-Y, Kim J-U, Park J-S. Direct growth of carbon nanotubes on a micro-sized cobalt tip and characterization of electron-emission properties. *Thin Solid Films* 2008;517:1136–40. doi:10.1016/j.tsf.2008.08.174.
- [57] Ma Y-R, Cheng K-W, Shee C-H, Tsai C-C, Cheng C-L, Liu H-L, et al. Effect of field power on growth of multiwall carbon nanotubes. *J Magn Magn Mater* 2004;282:61–4. doi:10.1016/j.jmmm.2004.04.014.
- [58] Reddy NK, Meunier J-L, Coulombe S. Growth of carbon nanotubes directly on a nickel surface by thermal CVD. *Mater Lett* 2006;60:3761–5. doi:10.1016/j.matlet.2006.03.109.
- [59] Huang ZP, Xu JW, Ren ZF, Wang JH, Siegal MP, Provencio PN. Growth of highly oriented carbon nanotubes by plasma-enhanced hot filament chemical vapor deposition. *Appl Phys Lett* 1998;73:3845–7. doi:10.1063/1.122912.
- [60] Camilli L, Scarselli M, Del Gobbo S, Castrucci P, Nanni F, Gautron E, et al. The synthesis and characterization of carbon nanotubes grown by chemical vapor deposition using a stainless steel catalyst. *Carbon* 2011;49:3307–15. doi:10.1016/j.carbon.2011.04.014.
- [61] Baddour CE, Fadlallah F, Nasuhoglu D, Mitra R, Vandsburger L, Meunier J-L. A simple thermal CVD method for carbon nanotube synthesis on stainless steel 304 without the addition of an external catalyst. *Carbon* 2009;47:313–8. doi:10.1016/j.carbon.2008.10.038.

- [62] Baddour CE, Meunier J. Carbon Nanotube Synthesis on Stainless Steel for use in a Nanotube-Titanium Nitride Nanocomposite. 8th IEEE Conf. Nanotechnol. 2008 NANO 08, 2008, p. 752–5. doi:10.1109/NANO.2008.225.
- [63] Baddour CE, Upham DC, Meunier J-L. Direct and repetitive growth cycles of carbon nanotubes on stainless steel particles by chemical vapor deposition in a fluidized bed. *Carbon* 2010;48:2652–6. doi:10.1016/j.carbon.2010.03.031.
- [64] Nguyen XH, Lee YB, Lee CH, Lim D-S. Synthesis of sea urchin-like particles of carbon nanotubes directly grown on stainless steel cores and their effect on the mechanical properties of polymer composites. *Carbon* 2010;48:2910–6. doi:10.1016/j.carbon.2010.04.027.
- [65] Sabeti Nejad N, Larjani MM, Ghoranneviss M, Balashabadi P, Shokouhy A. Direct growth of carbon nanotubes on Ar ion bombarded AISI 304 stainless steel substrates. *Surf Coat Technol* 2009;203:2510–3. doi:10.1016/j.surfcoat.2009.02.047.
- [66] Sano N, Hori Y, Yamamoto S, Tamon H. A simple oxidation–reduction process for the activation of a stainless steel surface to synthesize multi-walled carbon nanotubes and its application to phenol degradation in water. *Carbon* 2012;50:115–22. doi:10.1016/j.carbon.2011.07.059.
- [67] Vander Wal RL, Hall LJ. Carbon nanotube synthesis upon stainless steel meshes. *Carbon* 2003;41:659–72. doi:10.1016/S0008-6223(02)00369-X.
- [68] Martínez-Hansen V, Latorre N, Royo C, Romeo E, García-Bordejé E, Monzón A. Development of aligned carbon nanotubes layers over stainless steel mesh monoliths. *Catal Today* 2009;147:S71–5. doi:10.1016/j.cattod.2009.07.010.
- [69] Karwa M, Iqbal Z, Mitra S. Scaled-up self-assembly of carbon nanotubes inside long stainless steel tubing. *Carbon* 2006;44:1235–42. doi:10.1016/j.carbon.2005.10.046.
- [70] Ko Y-K, Lee W-B, Lee C-W, Yoo S. Nanocrystallized steel surface by micro-shot peening for catalyst-free carbon nanotube growth. *Mater Res Bull* 2010;45:343–7. doi:10.1016/j.materresbull.2009.12.026.
- [71] Baker RTK. Catalytic growth of carbon filaments. *Carbon* 1989;27:315–23. doi:10.1016/0008-6223(89)90062-6.
- [72] Talapatra S, Kar S, Pal SK, Vajtai R, Ci L, Victor P, et al. Direct growth of aligned carbon nanotubes on bulk metals: *Nat Nanotechnol* 2006;1:112–6. doi:10.1038/nnano.2006.56.
- [73] Li X, Imin P, Adronov A, Zhitomirsky I. Effect of 5-sulfosalicylic acid and poly[2,5-bis(3-sulfonatopropoxy)-1,4-ethynylphenylene-alt-1,4-ethynylphenylene] on electrodeposition of polypyrrole–carbon nanotube films on stainless steel. *Mater Lett* 2012;68:24–7. doi:10.1016/j.matlet.2011.10.010.
- [74] Moore JJ, Kang JH, Wen JZ. Fabrication and characterization of single walled nanotube supercapacitor electrodes with uniform pores using electrophoretic deposition. *Mater Chem Phys* 2012;134:68–73. doi:10.1016/j.matchemphys.2012.02.030.
- [75] Wang Y, Liu H, Sun X, Zhitomirsky I. Manganese dioxide–carbon nanotube nanocomposites for electrodes of electrochemical supercapacitors. *Scr Mater* 2009;61:1079–82. doi:10.1016/j.scriptamat.2009.08.040.
- [76] Chen YM, Cai JH, Huang YS, Lee KY, Tsai DS. Preparation and characterization of iridium dioxide–carbon nanotube nanocomposites for supercapacitors. *Nanotechnology* 2011;22:N.115706:1–7. doi:10.1088/0957-4484/22/11/115706.
- [77] Lamp JL, Guest JS, Naha S, Radavich KA, Love NG, Ellis MW, et al. Flame synthesis of carbon nanostructures on stainless steel anodes for use in microbial fuel cells. *J Power Sources* 2011;196:5829–34. doi:10.1016/j.jpowsour.2011.02.077.
- [78] Lee Y-B, Lee C-H, Kim K-M, Lim D-S. Preparation and properties on the graphite/polypropylene composite bipolar plates with a 304 stainless steel by compression molding for PEM fuel cell. *Int J Hydrog Energy* 2011;36:7621–7. doi:10.1016/j.ijhydene.2011.03.108.
- [79] Show Y, Takahashi K. Stainless steel bipolar plate coated with carbon nanotube (CNT)/polytetrafluoroethylene (PTFE) composite film for proton exchange membrane fuel cell (PEMFC). *J Power Sources* 2009;190:322–5. doi:10.1016/j.jpowsour.2009.01.027.
- [80] Chen Y, Lv Z, Xu J, Peng D, Liu Y, Chen J, et al. Stainless steel mesh coated with MnO<sub>2</sub>/carbon nanotube and polymethylphenyl siloxane as low-cost and high-performance microbial fuel cell cathode materials. *J Power Sources* 2012;201:136–41. doi:10.1016/j.jpowsour.2011.10.134.
- [81] Lee Y-B, Lee C-H, Lim D-S. The electrical and corrosion properties of carbon nanotube coated 304 stainless steel/polymer composite as PEM fuel cell bipolar plates. *Int J Hydrog Energy* 2009;34:9781–7. doi:10.1016/j.ijhydene.2009.08.065.
- [82] Oren Y. Capacitive deionization (CDI) for desalination and water treatment — past, present and future (a review). *Desalination* 2008;228:10–29. doi:10.1016/j.desal.2007.08.005.

- [83] Anderson MA, Cudero AL, Palma J. Capacitive deionization as an electrochemical means of saving energy and delivering clean water. Comparison to present desalination practices: Will it compete? *Electrochimica Acta* 2010;55:3845–56. doi:10.1016/j.electacta.2010.02.012.
- [84] Boon N, van Roij R. “Blue energy” from ion adsorption and electrode charging in sea and river water. *Mol Phys* 2011;109:1229–41. doi:10.1080/00268976.2011.554334.
- [85] Brogioli D, Zhao R, Biesheuvel PM. A prototype cell for extracting energy from a water salinity difference by means of double layer expansion in nanoporous carbon electrodes. *Energy Environ Sci* 2011;4:772–7. doi:10.1039/C0EE00524J.
- [86] Brogioli D. Extracting Renewable Energy from a Salinity Difference Using a Capacitor. *Phys Rev Lett* 2009;103:N.058501: 1–4. doi:10.1103/PhysRevLett.103.058501.
- [87] Lin C-L, Chen C-F, Shi S-C. Field emission properties of aligned carbon nanotubes grown on stainless steel using CH<sub>4</sub>/CO<sub>2</sub> reactant gas. *Diam Relat Mater* 2004;13:1026–31. doi:10.1016/j.diamond.2003.10.056.
- [88] Sinha N, Sun Y, Yeow J. Field Emission Properties of Carbon Nanotube Thin Films Grown on Different Substrate Materials. 8th IEEE Conf. Nanotechnol. 2008 NANO 08, 2008, p. 270–3. doi:10.1109/NANO.2008.86.
- [89] Wang N, Yao BD. Nucleation and growth of well-aligned, uniform-sized carbon nanotubes by microwave plasma chemical vapor deposition. *Appl Phys Lett* 2001;78:4028–30. doi:10.1063/1.1381036.
- [90] Yeow JTW, She JPM. Carbon nanotube-enhanced capillary condensation for a capacitive humidity sensor. *Nanotechnology* 2006;17:5441–8. doi:10.1088/0957-4484/17/21/026.
- [91] Yun Y, Gollapudi R, Shanov V, Schulz MJ, Dong Z, Jazieh A, et al. Carbon nanotubes grown on stainless steel to form plate and probe electrodes for chemical/biological sensing. *J Nanosci Nanotechnol* 2007;7:891–7.
- [92] Minnikanti S, Skeath P, Peixoto N. Electrochemical characterization of multi-walled carbon nanotube coated electrodes for biological applications. *Carbon* 2009;47:884–93. doi:10.1016/j.carbon.2008.11.045.
- [93] Abad MD, Sánchez-López JC, Berenguer-Murcia A, Golovko VB, Cantoro M, Wheatley AEH, et al. Catalytic growth of carbon nanotubes on stainless steel: Characterization and frictional properties. *Diam Relat Mater* 2008;17:1853–7. doi:10.1016/j.diamond.2008.03.021.
- [94] Carrión FJ, Sanes J, Bermúdez M-D, Arribas A. New single-walled carbon nanotubes–ionic liquid lubricant. application to Polycarbonate–stainless steel sliding contact. *Tribol Lett* 2011;41:199–207. doi:10.1007/s11249-010-9700-7.
- [95] Hu JJ, Jo SH, Ren ZF, Voevodin AA, Zabinski JS. Tribological behavior and graphitization of carbon nanotubes grown on 440C stainless steel. *Tribol Lett* 2005;19:119–25. doi:10.1007/s11249-005-5091-6.
- [96] Park D, Kim YH, Lee JK. Pretreatment of stainless steel substrate surface for the growth of carbon nanotubes by PECVD. *J Mater Sci* 2003;38:4933–9. doi:10.1023/B:JMSS.000004416.60953.07.
- [97] Park D, Hoon Kim Y, Kee Lee J. Synthesis of carbon nanotubes on metallic substrates by a sequential combination of PECVD and thermal CVD. *Carbon* 2003;41:1025–9. doi:10.1016/S0008-6223(02)00432-3.
- [98] Esconjauregui S, Whelan CM, Maex K. The reasons why metals catalyze the nucleation and growth of carbon nanotubes and other carbon nanomorphologies. *Carbon* 2009;47:659–69. doi:10.1016/j.carbon.2008.10.047.
- [99] R. T. K. Baker, P. S. Harris. In: Philip L. Walker Jr, Peter A. Thrower, editors. *Chem. Phys. Carbon*, vol. 14. 1st ed., New York/Basel: Marcel Dekker Inc.; 1978, p. 83.
- [100] Grabke HJ. *Carburization: A High Temperature Corrosion Phenomenon*. St. Louis, MO: Material Technology Institute of the Chemical Process Industries; 1998.
- [101] W.B. Hoyt, R.H. Caughey. High temperature metal deterioration in atmospheres containing carbon-monoxide and hydrogen. *Corros NACE* 1959;15:21–4 (627t – 630t).
- [102] H.J. Grabke. Carburization, carbide formation, metal dusting, coking. *Mater Tehnol* 2002;36:297–305.
- [103] Szakálos P. Mechanisms of metal dusting. PhD Dissertation. Kungl. Tekniska högskolan (KTH), Institutionen för materialvetenskap, 2004.
- [104] Horcas I, Fernández R, Gómez-Rodríguez JM, Colchero J, Gómez-Herrero J, Baro AM. WSXM: A software for scanning probe microscopy and a tool for nanotechnology. *Rev Sci Instrum* 2007;78:013705–013705 – 8. doi:10.1063/1.2432410.

- [105] Wang H, Sweikart MA, Turner JA. Stainless steel as bipolar plate material for polymer electrolyte membrane fuel cells. *J Power Sources* 2003;115:243–51. doi:10.1016/S0378-7753(03)00023-5.
- [106] Wang Y, Northwood DO. Effects of O<sub>2</sub> and H<sub>2</sub> on the corrosion of SS316L metallic bipolar plate materials in simulated anode and cathode environments of PEM fuel cells. *Electrochimica Acta* 2007;52:6793–8. doi:10.1016/j.electacta.2007.05.001.
- [107] Wu J, Yuan XZ, Martin JJ, Wang H, Zhang J, Shen J, et al. A review of PEM fuel cell durability: Degradation mechanisms and mitigation strategies. *J Power Sources* 2008;184:104–19. doi:10.1016/j.jpowsour.2008.06.006.
- [108] E. Beraha. *New Metallographic Reagents for Stainless Steel and Heat-Resisting Alloys*. *J Iron Steel Inst Jpn* 1966;204:248–51.
- [109] Shakerzadeh M, Loh GC, Xu N, Chow WL, Tan CW, Lu C, et al. Re-ordering Chaotic Carbon: Origins and Application of Textured Carbon. *Adv Mater* 2012;24:4112–23. doi:10.1002/adma.201104991.
- [110] Szakálos P. *Mechanisms of metal dusting*. PhD Dissertation. Kungl. Tekniska högskolan (KTH), Institutionen för materialvetenskap, 2004.
- [111] Szakálos P, Pettersson R, Hertzman S. An active corrosion mechanism for metal dusting on 304L stainless steel. *Corros Sci* 2002;44:2253–70. doi:10.1016/S0010-938X(02)00053-7.
- [112] Stevens KJ, Levi T, Minchington I, Briggs N, Keast V, Bulcock S. Transmission electron microscopy of high pressure metal dusted 316 stainless steel. *Mater Sci Eng A* 2004;385:292–9. doi:10.1016/j.msea.2004.06.057.
- [113] Yoshida H, Takeda S, Uchiyama T, Kohno H, Homma Y. Atomic-Scale In-situ Observation of Carbon Nanotube Growth from Solid State Iron Carbide Nanoparticles. *Nano Lett* 2008;8:2082–6. doi:10.1021/nl080452q.
- [114] Schaper AK, Hou H, Greiner A, Philipp F. The role of iron carbide in multiwalled carbon nanotube growth. *J Catal* 2004;222:250–4. doi:10.1016/j.jcat.2003.11.011.
- [115] Chen X, Wang R, Xu J, Yu D. TEM investigation on the growth mechanism of carbon nanotubes synthesized by hot-filament chemical vapor deposition. *Micron* 2004;35:455–60. doi:10.1016/j.micron.2004.02.006.
- [116] Kibria AKMF, Mo YH, Nahm KS. Synthesis of carbon nanotubes over nickel–iron catalysts supported on alumina under controlled conditions. *Catal Lett* 2001;71:229–36. doi:10.1023/A:1009019624640.
- [117] Ducati C, Alexandrou I, Chhowalla M, Amaratunga GAJ, Robertson J. Temperature selective growth of carbon nanotubes by chemical vapor deposition. *J Appl Phys* 2002;92:3299–303. doi:10.1063/1.1499746.
- [118] R.F. Hochman. *Basic studies of metal dusting deterioration in carbonaceous environments at elevated temperatures*. Proc. 4th International Congr. Met. Corros., Amsterdam, Netherlands: NACE; 1969, p. 258–63.
- [119] Young DJ, Zhang J, Geers C, Schütze M. Recent advances in understanding metal dusting: A review. *Mater Corros* 2011;62:7–28. doi:10.1002/maco.201005675.
- [120] Pippel E, Woltersdorf J, Schneider R. Micromechanisms of metal dusting on Fe-base and Ni-base alloys. *Mater Corros* 1998;49:309–16. doi:10.1002/(SICI)1521-4176(199805)49:5<309::AID-MACO309>3.0.CO;2-1.
- [121] Pippel E, Woltersdorf J, Grabke HJ, Strauss S. Microprocesses of metal dusting on iron. *Steel Res* 1995;66:217–21.
- [122] Lin C-Y, Tsai W-T. Nano-sized carbon filament formation during metal dusting of stainless steel. *Mater Chem Phys* 2003;82:929–36. doi:10.1016/j.matchemphys.2003.08.019.
- [123] Madix RJ, Benziger J. Kinetic Processes on Metal Single-Crystal Surfaces. *Annu Rev Phys Chem* 1978;29:285–306. doi:10.1146/annurev.pc.29.100178.001441.
- [124] Yao Y, Falk LKL, Morjan RE, Nerushev OA, Campbell EEB. Synthesis of carbon nanotube films by thermal CVD in the presence of supported catalyst particles. Part II: the nanotube film. *J Mater Sci Mater Electron* 2004;15:583–94. doi:10.1023/B:JMSE.0000036037.84271.f0.
- [125] Behr MJ, Mkhoyan KA, Aydil ES. Orientation and Morphological Evolution of Catalyst Nanoparticles During Carbon Nanotube Growth. *ACS Nano* 2010;4:5087–94. doi:10.1021/nn100944n.
- [126] Behr MJ, Andre Mkhoyan K, Aydil ES. Catalyst rotation, twisting, and bending during multiwall carbon nanotube growth. *Carbon* 2010;48:3840–5. doi:10.1016/j.carbon.2010.06.049.

- [127] Behr MJ, Mkhoyan KA, Aydil ES. Carbon Diffusion from Methane into Walls of Carbon Nanotube through Structurally and Compositionally Modified Iron Catalyst. *Microsc Microanal* 2011;17:582–6. doi:10.1017/S1431927611000286.
- [128] Bard AJ, Faulkner LR. *Electrochemical methods: fundamentals and applications*. New York: Wiley; 1980.
- [129] Devine TM. The mechanism of sensitization of austenitic stainless steel. *Corros Sci* 1990;30:135–51. doi:10.1016/0010-938X(90)90068-G.
- [130] Staicopolus DN. The Role of Cementite in the Acidic Corrosion of Steel. *J Electrochem Soc* 1963;110:1121–4. doi:10.1149/1.2425602.
- [131] Streicher MA. General and Intergranular Corrosion of Austenitic Stainless Steels in Acids. *J Electrochem Soc* 1959;106:161–80. doi:10.1149/1.2427304.
- [132] J.S. Armijo. Intergranular Corrosion of Nonsensitized Austenitic Stainless Steels; Part 1 - Environmental Variables. *Corros NACE* 1965;21:235–44.
- [133] Schweitzer PA. *Corrosion of Stainless Steels. Fundam. Met. Corros. Atmospheric Media Corros. Met. Corros. Eng. Handb.* 2nd ed., Boca Raton: CRC Press; 2007, p. 114–6.
- [134] Kasparova OV, Baldokhin YV. New concept of the mechanism of intergranular corrosion of stainless steels. *Prot Met* 2007;43:235–40. doi:10.1134/S0033173207030058.
- [135] Tedmon CS, Vermilyea DA, Rosolowski JH. Intergranular Corrosion of Austenitic Stainless Steel. *J Electrochem Soc* 1971;118:192–202. doi:10.1149/1.2407966.
- [136] Devine TM. Influence of carbon content and ferrite morphology on the sensitization of duplex stainless steel. *Metall Trans A* 1980;11:791–800. doi:10.1007/BF02661208.
- [137] Hsu H-W, Tsai W-T. High temperature corrosion behavior of siliconized 310 stainless steel. *Mater Chem Phys* 2000;64:147–55. doi:10.1016/S0254-0584(99)00264-3.
- [138] Jones DA. *Principles and prevention of corrosion*. Prentice Hall; 1996.
- [139] Greene DL, Hopson JL, Li J. Running out of and into oil: Analyzing global oil depletion and transition through 2050. Prepared by the OAK RIDGE NATIONAL LABORATORY, Tennessee for the U.S. DEPARTMENT OF ENERGY; 2003.
- [140] Global Atmosphere Watch. The State of Greenhouse Gases in the Atmosphere Based on Global Observations through 2013. World Meteorological Organization GREENHOUSE GAS BULLETIN; 2014.
- [141] Grove WR. LVI. On a new voltaic combination. *Philos Mag Ser 3* 1838;13:430–1. doi:10.1080/14786443808649618.
- [142] Steele BCH. Material science and engineering: The enabling technology for the commercialisation of fuel cell systems. *J Mater Sci* 2001;36:1053–68. doi:10.1023/A:1004853019349.
- [143] Bar-On I, Kirchain R, Roth R. Technical cost analysis for PEM fuel cells. *J Power Sources* 2002;109:71–5. doi:10.1016/S0378-7753(02)00062-9.
- [144] Carlson EJ, Kopf P, Sinha J, Sriramulu S, Yang Y. Cost Analysis of PEM Fuel Cell Systems for Transportation. National Renewable Energy Laboratory, Operated for the U.S. Department of Energy; 2005.
- [145] Lokurlu A, Grube T, H hlein B, Stolten D. Fuel cells for mobile and stationary applications—cost analysis for combined heat and power stations on the basis of fuel cells. *Int J Hydrog Energy* 2003;28:703–11. doi:10.1016/S0360-3199(02)00242-2.
- [146] Tsuchiya H, Kobayashi O. Mass production cost of PEM fuel cell by learning curve. *Int J Hydrog Energy* 2004;29:985–90. doi:10.1016/j.ijhydene.2003.10.011.
- [147] Borup R, Meyers J, Pivovar B, Kim YS, Mukundan R, Garland N, et al. Scientific Aspects of Polymer Electrolyte Fuel Cell Durability and Degradation. *Chem Rev* 2007;107:3904–51. doi:10.1021/cr050182l.
- [148] Shao Y, Yin G, Wang Z, Gao Y. Proton exchange membrane fuel cell from low temperature to high temperature: Material challenges. *J Power Sources* 2007;167:235–42. doi:10.1016/j.jpowsour.2007.02.065.
- [149] Shao Y, Yin G, Gao Y. Understanding and approaches for the durability issues of Pt-based catalysts for PEM fuel cell. *J Power Sources* 2007;171:558–66. doi:10.1016/j.jpowsour.2007.07.004.
- [150] Auer E, Freund A, Pietsch J, Tacke T. Carbons as supports for industrial precious metal catalysts. *Appl Catal Gen* 1998;173:259–71. doi:10.1016/S0926-860X(98)00184-7.
- [151] Shao Y, Liu J, Wang Y, Lin Y. Novel catalyst support materials for PEM fuel cells: current status and future prospects. *J Mater Chem* 2009;19:46. doi:10.1039/b808370c.

- [152] Sharma S, Pollet BG. Support materials for PEMFC and DMFC electrocatalysts—A review. *J Power Sources* 2012;208:96–119. doi:10.1016/j.jpowsour.2012.02.011.
- [153] Dicks AL. The role of carbon in fuel cells. *J Power Sources* 2006;156:128–41. doi:10.1016/j.jpowsour.2006.02.054.
- [154] Cameron DS, Cooper SJ, Dodgson IL, Harrison B, Jenkins JW. Carbons as supports for precious metal catalysts. *Catal Today* 1990;7:113–37. doi:10.1016/0920-5861(90)85012-D.
- [155] Pierson HO. *Handbook of Carbon, Graphite, Diamond and Fullerenes: Properties, Processing and Applications*. 1 edition. Park Ridge, N.J., U.S.A: Noyes Publications; 1994.
- [156] McBreen J, Olender H, Srinivasan S, Kordesch KV. Carbon supports for phosphoric acid fuel cell electrocatalysts: alternative materials and methods of evaluation. *J Appl Electrochem* 1981;11:787–96. doi:10.1007/BF00615184.
- [157] Takasu Y, Kawaguchi T, Sugimoto W, Murakami Y. Effects of the surface area of carbon support on the characteristics of highly-dispersed PtRu particles as catalysts for methanol oxidation. *Electrochimica Acta* 2003;48:3861–8. doi:10.1016/S0013-4686(03)00521-8.
- [158] Watanabe M, Saegusa S, Stonehart P. Electro-catalytic activity on supported platinum crystallites for oxygen reduction in sulphuric acid. *Chem Lett* 1988;1487–90. doi:10.1246/cl.1988.1487.
- [159] Antolini E. Formation, microstructural characteristics and stability of carbon supported platinum catalysts for low temperature fuel cells. *J Mater Sci* 2003;38:2995–3005. doi:10.1023/A:1024771618027.
- [160] Uchida M, Aoyama Y, Tanabe M, Yanagihara N, Eda N, Ohta A. Influences of Both Carbon Supports and Heat-Treatment of Supported Catalyst on Electrochemical Oxidation of Methanol. *J Electrochem Soc* 1995;142:2572–6. doi:10.1149/1.2050055.
- [161] Gharibi H, Mirzaie RA, Shams E, Zhiani M, Khairmand M. Preparation of platinum electrocatalysts using carbon supports for oxygen reduction at a gas-diffusion electrode. *J Power Sources* 2005;139:61–6. doi:10.1016/j.jpowsour.2004.06.075.
- [162] Fraga MA, Jordão E, Mendes MJ, Freitas MMA, Faria JL, Figueiredo JL. Properties of Carbon-Supported Platinum Catalysts: Role of Carbon Surface Sites. *J Catal* 2002;209:355–64. doi:10.1006/jcat.2002.3637.
- [163] Antolini E, Cardellini F, Giacometti E, Squadrito G. Study on the formation of Pt/C catalysts by non-oxidized active carbon support and a sulfur-based reducing agent. *J Mater Sci* 2002;37:133–9. doi:10.1023/A:1013166429216.
- [164] Rao V, Simonov PA, Savinova ER, Plaksin GV, Cherepanova SV, Kryukova GN, et al. The influence of carbon support porosity on the activity of PtRu/Sibunit anode catalysts for methanol oxidation. *J Power Sources* 2005;145:178–87. doi:10.1016/j.jpowsour.2004.12.064.
- [165] Watanabe M, Sei H, Stonehart P. The influence of platinum crystallite size on the electroreduction of oxygen. *J Electroanal Chem Interfacial Electrochem* 1989;261:375–87. doi:10.1016/0022-0728(89)85006-5.
- [166] Antolini E. Carbon supports for low-temperature fuel cell catalysts. *Appl Catal B Environ* 2009;88:1–24. doi:10.1016/j.apcatb.2008.09.030.
- [167] Gallezot P, Chaumet S, Perrard A, Isnard P. Catalytic Wet Air Oxidation of Acetic Acid on Carbon-Supported Ruthenium Catalysts. *J Catal* 1997;168:104–9. doi:10.1006/jcat.1997.1633.
- [168] Guerrero-Ruiz A, Badenes P, Rodríguez-Ramos I. Study of some factors affecting the Ru and Pt dispersions over high surface area graphite-supported catalysts. *Appl Catal Gen* 1998;173:313–21. doi:10.1016/S0926-860X(98)00187-2.
- [169] Díaz E, Ordóñez S, Vega A. Adsorption of volatile organic compounds onto carbon nanotubes, carbon nanofibers, and high-surface-area graphites. *J Colloid Interface Sci* 2007;305:7–16. doi:10.1016/j.jcis.2006.09.036.
- [170] Ferreira-Aparicio P, Folgado MA, Daza L. High surface area graphite as alternative support for proton exchange membrane fuel cell catalysts. *J Power Sources* 2009;192:57–62. doi:10.1016/j.jpowsour.2008.12.003.
- [171] Díaz E, Ordóñez S, Bueres RF, Asedegbega-Nieto E, Sastre H. High-surface area graphites as supports for hydrodechlorination catalysts: Tuning support surface chemistry for an optimal performance. *Appl Catal B Environ* 2010;99:181–90. doi:10.1016/j.apcatb.2010.06.016.
- [172] Bansal RC. *Active carbon*. New York: M. Dekker; 1988.
- [173] Stiles AB. *Catalyst supports and supported catalysts: theoretical and applied concepts*. Butterworths; 1987.
- [174] Marsh H, Reinoso FR. *Activated Carbon*. 1 edition. Amsterdam ; Boston: Elsevier Science; 2005.

- [175] Rodríguez-Reinoso F, Molina-Sabio M. Activated carbons from lignocellulosic materials by chemical and/or physical activation: an overview. *Carbon* 1992;30:1111–8. doi:10.1016/0008-6223(92)90143-K.
- [176] Noh JS, Schwarz JA. Effect of HNO<sub>3</sub> treatment on the surface acidity of activated carbons. *Carbon* 1990;28:675–82. doi:10.1016/0008-6223(90)90069-B.
- [177] Suh DJ, Tae-Jin P, Son-Ki I. Effect of surface oxygen groups of carbon supports on the characteristics of Pd/C catalysts. *Carbon* 1993;31:427–35. doi:10.1016/0008-6223(93)90130-3.
- [178] Torres GC, Jablonski EL, Baronetti GT, Castro AA, de Miguel SR, Scelza OA, et al. Effect of the carbon pre-treatment on the properties and performance for nitrobenzene hydrogenation of Pt/C catalysts. *Appl Catal Gen* 1997;16:1213–26. doi:10.1016/S0926-860X(97)00071-9.
- [179] Sepúlveda-Escribano A, Coloma F, Rodríguez-Reinoso F. Platinum catalysts supported on carbon blacks with different surface chemical properties. *Appl Catal Gen* 1998;17:3247–57. doi:10.1016/S0926-860X(98)00183-5.
- [180] Van Dam HE, Van Bekkum H. Preparation of platinum on activated carbon. *J Catal* 1991;131:335–49. doi:10.1016/0021-9517(91)90269-A.
- [181] Coloma F, Sepúlveda-Escribano A, Fierro JLG, Rodríguez-Reinoso F. Preparation of Platinum Supported on Pregraphitized Carbon Blacks. *Langmuir* 1994;10:750–5. doi:10.1021/la00015a025.
- [182] Derbyshire FJ, de Beer VHJ, Abotsi GMK, Scaroni AW, Solar JM, Kirovanev DJ. The influence of surface functionality on the activity of carbon-supported catalysts. *Appl Catal* 1986;2:117–31. doi:10.1016/S0166-9834(00)81051-9.
- [183] Ehrburger P, Mahajan OP, Walker Jr. PL. Carbon as a support for catalysts: I. Effect of surface heterogeneity of carbon on dispersion of platinum. *J Catal* 1976;43:61–7. doi:10.1016/0021-9517(76)90293-1.
- [184] Pinheiro ALN, Oliveira-Neto A, De Souza EC, Perez J, Paganin VA, Ticianelli EA, et al. Electrocatalysis on Noble Metal and Noble Metal Alloys Dispersed on High Surface Area Carbon. *J New Mater Electrochem Syst* 2003;6:1–8.
- [185] Ryoo R, Joo SH, Jun S. Synthesis of Highly Ordered Carbon Molecular Sieves via Template-Mediated Structural Transformation. *J Phys Chem B* 1999;103:7743–6. doi:10.1021/jp991673a.
- [186] Jun S, Sang Hoon Joo, Ryoo R, Kruk M, Jaroniec M, Liu Z, et al. Synthesis of new, nanoporous carbon with hexagonally ordered mesostructure [5]. *J Am Chem Soc* 2000;122:10710–3. doi:10.1021/ja002261e.
- [187] Ryoo R, Joo SH, Kruk M, Jaroniec M. Ordered Mesoporous Carbons. *Adv Mater* 2001;13:677–81. doi:10.1002/1521-4095(200105)13:9<677::AID-ADMA677>3.0.CO;2-C.
- [188] Chang H, Joo SH, Pak C. Synthesis and characterization of mesoporous carbon for fuel cell applications. *J Mater Chem* 2007;17:3078. doi:10.1039/b700389g.
- [189] Liang C, Li Z, Dai S. Mesoporous Carbon Materials: Synthesis and Modification. *Angew Chem Int Ed* 2008;47:3696–717. doi:10.1002/anie.200702046.
- [190] Raghuvver V, Manthiram A. Mesoporous Carbon with Larger Pore Diameter as an Electrocatalyst Support for Methanol Oxidation. *Electrochem Solid-State Lett* 2004;7:A336–9. doi:10.1149/1.1792264.
- [191] Ding J, Chan K-Y, Ren J, Xiao F. Platinum and platinum–ruthenium nanoparticles supported on ordered mesoporous carbon and their electrocatalytic performance for fuel cell reactions. *Electrochimica Acta* 2005;50:3131–41. doi:10.1016/j.electacta.2004.11.064.
- [192] Calvillo L, Lázaro MJ, García-Bordejé E, Moliner R, Cabot PL, Esparbé I, et al. Platinum supported on functionalized ordered mesoporous carbon as electrocatalyst for direct methanol fuel cells. *J Power Sources* 2007;169:59–64. doi:10.1016/j.jpowsour.2007.01.042.
- [193] Su F, Zeng J, Bao X, Yu Y, Lee JY, Zhao XS. Preparation and Characterization of Highly Ordered Graphitic Mesoporous Carbon as a Pt Catalyst Support for Direct Methanol Fuel Cells. *Chem Mater* 2005;17:3960–7. doi:10.1021/cm050222z.
- [194] Joo SH, Pak C, You DJ, Lee S-A, Lee HI, Kim JM, et al. Ordered mesoporous carbons (OMC) as supports of electrocatalysts for direct methanol fuel cells (DMFC): Effect of carbon precursors of OMC on DMFC performances. *Electrochimica Acta* 2006;52:1618–26. doi:10.1016/j.electacta.2006.03.092.
- [195] Vengatesan S, Kim H-J, Kim S-K, Oh I-H, Lee S-Y, Cho E, et al. High dispersion platinum catalyst using mesoporous carbon support for fuel cells. *Electrochimica Acta* 2008;54:856–61. doi:10.1016/j.electacta.2008.05.072.
- [196] Yamada H, Hirai T, Moriguchi I, Kudo T. A highly active Pt catalyst fabricated on 3D porous carbon. *J Power Sources* 2007;164:538–43. doi:10.1016/j.jpowsour.2006.10.074.

- [197] Joo SH, Choi SJ, Oh I, Kwak J, Liu Z, Terasaki O, et al. Ordered nanoporous arrays of carbon supporting high dispersions of platinum nanoparticles. *Nature* 2001;412:169–72. doi:10.1038/35084046.
- [198] Song S, Liang Y, Li Z, Wang Y, Fu R, Wu D, et al. Effect of pore morphology of mesoporous carbons on the electrocatalytic activity of Pt nanoparticles for fuel cell reactions. *Appl Catal B Environ* 2010;98:132–7. doi:10.1016/j.apcatb.2010.05.021.
- [199] Lin M-L, Lo M-Y, Mou C-Y. PtRu Nanoparticles Supported on Ozone-Treated Mesoporous Carbon Thin Film As Highly Active Anode Materials for Direct Methanol Fuel Cells. *J Phys Chem C* 2009;113:16158–68. doi:10.1021/jp904611p.
- [200] Salgado JRC, Alcaide F, Álvarez G, Calvillo L, Lázaro MJ, Pastor E. Pt–Ru electrocatalysts supported on ordered mesoporous carbon for direct methanol fuel cell. *J Power Sources* 2010;195:4022–9. doi:10.1016/j.jpowsour.2010.01.001.
- [201] Cui X, Shi J, Zhang L, Ruan M, Gao J. PtCo supported on ordered mesoporous carbon as an electrode catalyst for methanol oxidation. *Carbon* 2009;47:186–94. doi:10.1016/j.carbon.2008.09.054.
- [202] Hwang S, Park G-G, Yim S-D, Park S-H, Yang T-H, Kim H, et al. Synthesis of the electro-catalyst supported on mesoporous carbon via imprinting method for polymer electrolyte fuel cells. *Curr Appl Phys* 2010;10:569–72. doi:10.1016/j.cap.2009.11.045.
- [203] Choi J-S, Chung WS, Ha HY, Lim T-H, Oh I-H, Hong S-A, et al. Nano-structured Pt–Cr anode catalyst over carbon support, for direct methanol fuel cell. *J Power Sources* 2006;156:466–71. doi:10.1016/j.jpowsour.2005.05.075.
- [204] Fuertes AB, Alvarez S. Graphitic mesoporous carbons synthesised through mesostructured silica templates. *Carbon* 2004;42:3049–55. doi:10.1016/j.carbon.2004.06.020.
- [205] DE JONG KP, GEUS JW. Carbon Nanofibers: Catalytic Synthesis and Applications. *Catal Rev* 2000;42:481–510. doi:10.1081/CR-100101954.
- [206] Lee K, Zhang J, Wang H, Wilkinson DP. Progress in the synthesis of carbon nanotube- and nanofiber-supported Pt electrocatalysts for PEM fuel cell catalysis. *J Appl Electrochem* 2006;36:507–22. doi:10.1007/s10800-006-9120-4.
- [207] Fu R, Zeng H, Lu Y, Lai SY, Chan WH, Ng CF. The reduction of Pt(IV) with activated carbon fibers—An XPS study. *Carbon* 1995;33:657–61. doi:10.1016/0008-6223(94)00152-P.
- [208] Macías Pérez MC, Salinas Martínez de Lecea C, Linares Solano A. Platinum supported on activated carbon cloths as catalyst for nitrobenzene hydrogenation. *Appl Catal Gen* 1997;151:461–75. doi:10.1016/S0926-860X(96)00303-1.
- [209] De Miguel SR, Vilella JI, Jablonski EL, Scelza OA, Salinas-Martinez de Lecea C, Linares-Solano A. Preparation of Pt catalysts supported on activated carbon felts (ACF). *Appl Catal Gen* 2002;232:237–46. doi:10.1016/S0926-860X(02)00112-6.
- [210] Zheng HT, Li Y, Chen S, Shen PK. Effect of support on the activity of Pd electrocatalyst for ethanol oxidation. *J Power Sources* 2006;163:371–5. doi:10.1016/j.jpowsour.2006.09.062.
- [211] Huang HX, Chen SX, Yuan C. Platinum nanoparticles supported on activated carbon fiber as catalyst for methanol oxidation. *J Power Sources* 2008;175:166–74. doi:10.1016/j.jpowsour.2007.08.107.
- [212] Rodriguez NM, Kim M-S, Baker RTK. Carbon Nanofibers: A Unique Catalyst Support Medium. *J Phys Chem* 1994;98:13108–11. doi:10.1021/j100101a003.
- [213] Hoogenraad MS, van Leeuwarden RAGMM, van Breda Vriesman GJB, Broersma A, van Dillen AJ, Geus JW. Metal catalysts supported on a novel carbon support. In: G. Poncelet JM, B. Delmon, P. A. Jacobs and P. Grange, editor. *Stud. Surf. Sci. Catal.*, vol. 91, Elsevier; 1995, p. 263–71.
- [214] Hoogenraad MS, Onwezen MF, van Dillen AJ, Geus JW. Supported catalysts based on carbon fibrils. In: Joe W. Hightower WND, Enrique Iglesia and Alexis T. Bell, editor. *Stud. Surf. Sci. Catal.*, vol. 101, Elsevier; 1996, p. 1331–9.
- [215] Chambers A, Nemes T, Rodriguez NM, Baker RTK. Catalytic Behavior of Graphite Nanofiber Supported Nickel Particles. 1. Comparison with Other Support Media. *J Phys Chem B* 1998;102:2251–8. doi:10.1021/jp973462g.
- [216] Park C, Baker RTK. Catalytic Behavior of Graphite Nanofiber Supported Nickel Particles. 2. The Influence of the Nanofiber Structure. *J Phys Chem B* 1998;102:5168–77. doi:10.1021/jp981210p.
- [217] Park C, Baker RTK. Catalytic Behavior of Graphite Nanofiber Supported Nickel Particles. 3. The Effect of Chemical Blocking on the Performance of the System. *J Phys Chem B* 1999;103:2453–9. doi:10.1021/jp983802d.
- [218] Bessel CA, Lauberndrns K, Rodriguez NM, Baker RTK. Graphite Nanofibers as an Electrode for Fuel Cell Applications. *J Phys Chem B* 2001;105:1115–8. doi:10.1021/jp003280d.

- [219] Steigerwalt ES, Deluga GA, Cliffler DE, Lukehart CM. A Pt-Ru/Graphitic Carbon Nanofiber Nanocomposite Exhibiting High Relative Performance as a Direct-Methanol Fuel Cell Anode Catalyst. *J Phys Chem B* 2001;105:8097–101. doi:10.1021/jp011633i.
- [220] Steigerwalt ES, Deluga GA, Lukehart CM. Pt-Ru/Carbon Fiber Nanocomposites: Synthesis, Characterization, and Performance as Anode Catalysts of Direct Methanol Fuel Cells. A Search for Exceptional Performance. *J Phys Chem B* 2002;106:760–6. doi:10.1021/jp0212707.
- [221] Zhang L, Cheng B, Samulski ET. In situ fabrication of dispersed, crystalline platinum nanoparticles embedded in carbon nanofibers. *Chem Phys Lett* 2004;398:505–10. doi:10.1016/j.cplett.2004.09.120.
- [222] Zheng J-S, Zhang X-S, Li P, Zhu J, Zhou X-G, Yuan W-K. Effect of carbon nanofiber microstructure on oxygen reduction activity of supported palladium electrocatalyst. *Electrochem Commun* 2007;9:895–900. doi:10.1016/j.elecom.2006.12.006.
- [223] Zheng J-S, Zhang X-S, Li P, Zhou X-G, Yuan W-K. Microstructure effect of carbon nanofiber on electrocatalytic oxygen reduction reaction. *Catal Today* 2008;131:270–7. doi:10.1016/j.cattod.2007.10.104.
- [224] Zheng J-S, Wang M-X, Zhang X-S, Wu Y-X, Li P, Zhou X-G, et al. Platinum/carbon nanofiber nanocomposite synthesized by electrophoretic deposition as electrocatalyst for oxygen reduction. *J Power Sources* 2008;175:211–6. doi:10.1016/j.jpowsour.2007.09.058.
- [225] Hsin YL, Hwang KC, Yeh C-T. Poly(vinylpyrrolidone)-Modified Graphite Carbon Nanofibers as Promising Supports for PtRu Catalysts in Direct Methanol Fuel Cells. *J Am Chem Soc* 2007;129:9999–10010. doi:10.1021/ja072367a.
- [226] Maiyalagan T. Pt-Ru nanoparticles supported PAMAM dendrimer functionalized carbon nanofiber composite catalysts and their application to methanol oxidation. *J Solid State Electrochem* 2009;13:1561–6. doi:10.1007/s10008-008-0730-0.
- [227] Yuan F, Ryu H. The synthesis, characterization, and performance of carbon nanotubes and carbon nanofibres with controlled size and morphology as a catalyst support material for a polymer electrolyte membrane fuel cell. *Nanotechnology* 2004;15:S596. doi:10.1088/0957-4484/15/10/017.
- [228] Gangeri M, Centi G, Malfa AL, Perathoner S, Vieira R, Pham-Huu C, et al. Electrocatalytic performances of nanostructured platinum-carbon materials. *Catal Today* 2005;102–103:50–7. doi:10.1016/j.cattod.2005.02.035.
- [229] Park I-S, Park K-W, Choi J-H, Park CR, Sung Y-E. Electrocatalytic enhancement of methanol oxidation by graphite nanofibers with a high loading of PtRu alloy nanoparticles. *Carbon* 2007;45:28–33. doi:10.1016/j.carbon.2006.08.011.
- [230] Knupp SL, Li W, Paschos O, Murray TM, Snyder J, Haldar P. The effect of experimental parameters on the synthesis of carbon nanotube/nanofiber supported platinum by polyol processing techniques. *Carbon* 2008;46:1276–84. doi:10.1016/j.carbon.2008.05.007.
- [231] Planeix JM, Coustel N, Coq B, Brotons V, Kumbhar PS, Dutartre R, et al. Application of Carbon Nanotubes as Supports in Heterogeneous Catalysis. *J Am Chem Soc* 1994;116:7935–6. doi:10.1021/ja00096a076.
- [232] Iijima S. Helical microtubules of graphitic carbon. *Nature* 1991;354:56–8. doi:10.1038/354056a0.
- [233] Freemantle M. Filled carbon nanotubes could lead to improved catalysts and biosensors. *Chem Eng News Arch* 1996;74:62–4. doi:10.1021/cen-v074n029.p062.
- [234] Baum RM. Nurturing nanotubes. *Chem Eng News Arch* 1997;75:39–41. doi:10.1021/cen-v075n026.p039.
- [235] Sloan J, Cook J, Green MLH, Hutchison JL, Tenne R. Crystallisation inside fullerene related structures. *J Mater Chem* 1997;7:1089–95. doi:10.1039/A700035I.
- [236] Che G, Lakshmi BB, Fisher ER, Martin CR. Carbon nanotubule membranes for electrochemical energy storage and production. *Nature* 1998;393:346–9. doi:10.1038/30694.
- [237] Britto PJ, Santhanam KSV, Rubio A, Alonzo JA, Ajayan PM. Improved Charge Transfer at Carbon Nanotube Electrodes. *Adv Mater* 1999;11:154–7. doi:10.1002/(SICI)1521-4095(199902)11:2<154::AID-ADMA154>3.0.CO;2-B.
- [238] Li W, Liang C, Qiu J, Zhou W, Han H, Wei Z, et al. Carbon nanotubes as support for cathode catalyst of a direct methanol fuel cell. *Carbon* 2002;40:791–4. doi:10.1016/S0008-6223(02)00039-8.
- [239] Li W, Liang C, Zhou W, Qiu J, Zhou, Sun G, et al. Preparation and Characterization of Multiwalled Carbon Nanotube-Supported Platinum for Cathode Catalysts of Direct Methanol Fuel Cells. *J Phys Chem B* 2003;107:6292–9. doi:10.1021/jp022505c.

- [240] Liu Z, Lin X, Lee JY, Zhang W, Han M, Gan LM. Preparation and Characterization of Platinum-Based Electrocatalysts on Multiwalled Carbon Nanotubes for Proton Exchange Membrane Fuel Cells. *Langmuir* 2002;18:4054–60. doi:10.1021/la0116903.
- [241] Rajesh B, Karthik V, Karthikeyan S, Ravindranathan Thampi K, Bonard J-M, Viswanathan B. Pt-WO<sub>3</sub> supported on carbon nanotubes as possible anodes for direct methanol fuel cells. *Fuel* 2002;81:2177–90. doi:10.1016/S0016-2361(02)00162-X.
- [242] Wang C, Waje M, Wang X, Tang JM, Haddon RC, Yan. Proton Exchange Membrane Fuel Cells with Carbon Nanotube Based Electrodes. *Nano Lett* 2003;4:345–8. doi:10.1021/nl034952p.
- [243] Matsumoto T, Komatsu T, Nakano H, Arai K, Nagashima Y, Yoo E, et al. Efficient usage of highly dispersed Pt on carbon nanotubes for electrode catalysts of polymer electrolyte fuel cells. *Catal Today* 2004;90:277–81. doi:10.1016/j.cattod.2004.04.038.
- [244] Kim C, Kim YJ, Kim YA, Yanagisawa T, Park KC, Endo M, et al. High performance of cup-stacked-type carbon nanotubes as a Pt–Ru catalyst support for fuel cell applications. *J Appl Phys* 2004;96:5903–5. doi:10.1063/1.1804242.
- [245] Xing Y. Synthesis and Electrochemical Characterization of Uniformly-Dispersed High Loading Pt Nanoparticles on Sonochemically-Treated Carbon Nanotubes. *J Phys Chem B* 2004;108:19255–9. doi:10.1021/jp046697i.
- [246] Carmo M, Paganin VA, Rosolen JM, Gonzalez ER. Alternative supports for the preparation of catalysts for low-temperature fuel cells: the use of carbon nanotubes. *J Power Sources* 2005;142:169–76. doi:10.1016/j.jpowsour.2004.10.023.
- [247] Liang Y, Zhang H, Yi B, Zhang Z, Tan Z. Preparation and characterization of multi-walled carbon nanotubes supported PtRu catalysts for proton exchange membrane fuel cells. *Carbon* 2005;43:3144–52. doi:10.1016/j.carbon.2005.06.017.
- [248] Guo D-J, Li H-L. Electrocatalytic oxidation of methanol on Pt modified single-walled carbon nanotubes. *J Power Sources* 2006;160:44–9. doi:10.1016/j.jpowsour.2006.01.026.
- [249] Wildgoose GG, Banks CE, Compton RG. Metal Nanoparticles and Related Materials Supported on Carbon Nanotubes: Methods and Applications. *Small* 2006;2:182–93. doi:10.1002/sml.200500324.
- [250] Jiang Z, Jiang Z-J. Carbon Nanotubes Supported Metal Nanoparticles for the Applications in Proton Exchange Membrane Fuel Cells (PEMFCs). In: Naraghi M, editor. *Carbon Nanotub. - Growth Appl., InTech*; 2011, p. 567–604.
- [251] Wang X, Waje M, Yan Y. CNT-Based Electrodes with High Efficiency for PEMFCs. *Electrochem Solid-State Lett* 2005;8:A42–4. doi:10.1149/1.1830397.
- [252] Kongkanand A, Kuwabata S, Girishkumar G, Kamat P. Single-Wall Carbon Nanotubes Supported Platinum Nanoparticles with Improved Electrocatalytic Activity for Oxygen Reduction Reaction. *Langmuir* 2006;22:2392–6. doi:10.1021/la052753a.
- [253] Liao S, Holmes K-A, Tsapralis H, Birss VI. High Performance PtRu Catalysts Supported on Carbon Nanotubes for the Anodic Oxidation of Methanol. *J Am Chem Soc* 2006;128:3504–5. doi:10.1021/ja0578653.
- [254] Prabhuram J, Zhao TS, Tang ZK, Chen R, Liang ZX. Multiwalled Carbon Nanotube Supported PtRu for the Anode of Direct Methanol Fuel Cells. *J Phys Chem B* 2006;110:5245–52. doi:10.1021/jp0567063.
- [255] Ke K, Waki K. Fabrication and Characterization of Multiwalled Carbon Nanotubes-Supported Pt/SnO<sub>x</sub> Nanocomposites as Catalysts for Electro-oxidation of Methanol. *J Electrochem Soc* 2007;154:A207–12. doi:10.1149/1.2426873.
- [256] Paschos O, Knupp SL, Choi P, Snyder J, Buelte SJ, Merchant N, et al. Carbon Nanotube-Supported Platinum Electrode for ORR in Phosphoric Acid Solution Effect of PTFE Content and Annealing Temperature. *Electrochem Solid-State Lett* 2007;10:B147–9. doi:10.1149/1.2752452.
- [257] Wang JJ, Yin GP, Zhang J, Wang ZB, Gao YZ. High utilization platinum deposition on single-walled carbon nanotubes as catalysts for direct methanol fuel cell. *Electrochimica Acta* 2007;52:7042–50. doi:10.1016/j.electacta.2007.05.038.
- [258] Yoo E, Okada T, Kizuka T, Nakamura J. Effect of carbon substrate materials as a Pt–Ru catalyst support on the performance of direct methanol fuel cells. *J Power Sources* 2008;180:221–6. doi:10.1016/j.jpowsour.2008.01.065.
- [259] Guo D-J, Zhao L, Qiu X-P, Chen L-Q, Zhu W-T. Novel hollow PtRu nanospheres supported on multi-walled carbon nanotube for methanol electrooxidation. *J Power Sources* 2008;177:334–8. doi:10.1016/j.jpowsour.2007.11.087.

- [260] Wei ZD, Yan C, Tan Y, Li L, Sun CX, Shao ZG, et al. Spontaneous Reduction of Pt(IV) onto the Sidewalls of Functionalized Multiwalled Carbon Nanotubes as Catalysts for Oxygen Reduction Reaction in PEMFCs. *J Phys Chem C* 2008;112:2671–7. doi:10.1021/jp709936p.
- [261] Bekyarova E, Itkis ME, Cabrera N, Zhao B, Yu A, Gao J, et al. Electronic Properties of Single-Walled Carbon Nanotube Networks. *J Am Chem Soc* 2005;127:5990–5. doi:10.1021/ja043153l.
- [262] Maiyalagan T, Viswanathan B, Varadaraju UV. Nitrogen containing carbon nanotubes as supports for Pt – Alternate anodes for fuel cell applications. *Electrochem Commun* 2005;7:905–12. doi:10.1016/j.elecom.2005.07.007.
- [263] Rajesh B, Ravindranathan Thampi K, Bonard J-M, Xanthopoulos N, Mathieu HJ, Viswanathan B. Carbon Nanotubes Generated from Template Carbonization of Polyphenyl Acetylene as the Support for Electrooxidation of Methanol. *J Phys Chem B* 2003;107:2701–8. doi:10.1021/jp0219350.
- [264] Fang H-T, Liu C-G, Liu C, Li F, Liu M, Cheng H-M. Purification of Single-Wall Carbon Nanotubes by Electrochemical Oxidation. *Chem Mater* 2004;16:5744–50. doi:10.1021/cm035263h.
- [265] Shao Y, Yin G, Zhang J, Gao Y. Comparative investigation of the resistance to electrochemical oxidation of carbon black and carbon nanotubes in aqueous sulfuric acid solution. *Electrochimica Acta* 2006;51:5853–7. doi:10.1016/j.electacta.2006.03.021.
- [266] Li L, Xing Y. Electrochemical Durability of Carbon Nanotubes in Noncatalyzed and Catalyzed Oxidations. *J Electrochem Soc* 2006;153:A1823–8. doi:10.1149/1.2234659.
- [267] Wang J, Yin G, Shao Y, Wang Z, Gao Y. Investigation of Further Improvement of Platinum Catalyst Durability with Highly Graphitized Carbon Nanotubes Support. *J Phys Chem C* 2008;112:5784–9. doi:10.1021/jp800186p.
- [268] Matsumoto T, Komatsu T, Arai K, Yamazaki T, Kijima M, Shimizu H, et al. Reduction of Pt usage in fuel cell electrocatalysts with carbon nanotube electrodes. *Chem Commun* 2004:840. doi:10.1039/b400607k.
- [269] Li X, Hsing I-M. The effect of the Pt deposition method and the support on Pt dispersion on carbon nanotubes. *Electrochimica Acta* 2006;51:5250–8. doi:10.1016/j.electacta.2006.01.046.
- [270] Baglio V, Blasi AD, D'Urso C, Antonucci V, Aricò AS, Ornelas R, et al. Development of Pt and Pt – Fe Catalysts Supported on Multiwalled Carbon Nanotubes for Oxygen Reduction in Direct Methanol Fuel Cells. *J Electrochem Soc* 2008;155:B829–33. doi:10.1149/1.2938368.
- [271] Liu Z, Lee JY, Chen W, Han M, Gan LM. Physical and Electrochemical Characterizations of Microwave-Assisted Polyol Preparation of Carbon-Supported PtRu Nanoparticles. *Langmuir* 2003;20:181–7. doi:10.1021/la035204i.
- [272] Chen W-X, Lee JY, Liu Z. Preparation of Pt and PtRu nanoparticles supported on carbon nanotubes by microwave-assisted heating polyol process. *Mater Lett* 2004;58:3166–9. doi:10.1016/j.matlet.2004.06.008.
- [273] Liu Z, Gan LM, Hong L, Chen W, Lee JY. Carbon-supported Pt nanoparticles as catalysts for proton exchange membrane fuel cells. *J Power Sources* 2005;139:73–8. doi:10.1016/j.jpowsour.2004.07.012.
- [274] Li X, Chen W-X, Zhao J, Xing W, Xu Z-D. Microwave polyol synthesis of Pt/CNTs catalysts: Effects of pH on particle size and electrocatalytic activity for methanol electrooxidation. *Carbon* 2005;43:2168–74. doi:10.1016/j.carbon.2005.03.030.
- [275] Jeng K-T, Chien C-C, Hsu N-Y, Yen S-C, Chiou S-D, Lin S-H, et al. Performance of direct methanol fuel cell using carbon nanotube-supported Pt–Ru anode catalyst with controlled composition. *J Power Sources* 2006;160:97–104. doi:10.1016/j.jpowsour.2006.01.057.
- [276] Tian ZQ, Jiang SP, Liang YM, Shen PK. Synthesis and Characterization of Platinum Catalysts on Multiwalled Carbon Nanotubes by Intermittent Microwave Irradiation for Fuel Cell Applications. *J Phys Chem B* 2006;110:5343–50. doi:10.1021/jp056401o.
- [277] Wang S, Jiang SP, White TJ, Guo J, Wang X. Electrocatalytic Activity and Interconnectivity of Pt Nanoparticles on Multiwalled Carbon Nanotubes for Fuel Cells. *J Phys Chem C* 2009;113:18935–45. doi:10.1021/jp906923z.
- [278] Guo Z, Chen Y, Li L, Wang X, Haller GL, Yang Y. Carbon nanotube-supported Pt-based bimetallic catalysts prepared by a microwave-assisted polyol reduction method and their catalytic applications in the selective hydrogenation. *J Catal* 2010;276:314–26. doi:10.1016/j.jcat.2010.09.021.
- [279] Zhang W, Chen J, Swiegers GF, Ma Z-F, Wallace GG. Microwave-assisted synthesis of Pt/CNT nanocomposite electrocatalysts for PEM fuel cells. *Nanoscale* 2010;2:282. doi:10.1039/b9nr00140a.

- [280] Sakthivel M, Schlange A, Kunz U, Turek T. Microwave assisted synthesis of surfactant stabilized platinum/carbon nanotube electrocatalysts for direct methanol fuel cell applications. *J Power Sources* 2010;195:7083–9. doi:10.1016/j.jpowsour.2010.05.002.
- [281] Hsieh C-T, Hung W-M, Chen W-Y, Lin J-Y. Microwave-assisted polyol synthesis of Pt–Zn electrocatalysts on carbon nanotube electrodes for methanol oxidation. *Int J Hydrog Energy* 2011;36:2765–72. doi:10.1016/j.ijhydene.2010.11.030.
- [282] Kim H-T, Lee J-K, Kim J. Platinum-sputtered electrode based on blend of carbon nanotubes and carbon black for polymer electrolyte fuel cell. *J Power Sources* 2008;180:191–4. doi:10.1016/j.jpowsour.2008.02.031.
- [283] Soin N, Roy SS, Karlsson L, McLaughlin JA. Sputter deposition of highly dispersed platinum nanoparticles on carbon nanotube arrays for fuel cell electrode material. *Diam Relat Mater* 2010;19:595–8. doi:10.1016/j.diamond.2009.10.029.
- [284] Yang C, Hu X, Wang D, Dai C, Zhang L, Jin H, et al. Ultrasonically treated multi-walled carbon nanotubes (MWCNTs) as PtRu catalyst supports for methanol electrooxidation. *J Power Sources* 2006;160:187–93. doi:10.1016/j.jpowsour.2006.05.015.
- [285] Guha A, Lu W, Zawodzinski Jr. TA, Schiraldi DA. Surface-modified carbons as platinum catalyst support for PEM fuel cells. *Carbon* 2007;45:1506–17. doi:10.1016/j.carbon.2007.03.023.
- [286] Shao Y, Yin G, Wang J, Gao Y, Shi P. Multi-walled carbon nanotubes based Pt electrodes prepared with in situ ion exchange method for oxygen reduction. *J Power Sources* 2006;161:47–53. doi:10.1016/j.jpowsour.2006.03.064.
- [287] Guo D-J, Li H-L. High dispersion and electrocatalytic properties of Pt nanoparticles on SWNT bundles. *J Electroanal Chem* 2004;573:197–202. doi:10.1016/j.jelechem.2004.07.006.
- [288] He Z, Chen J, Liu D, Zhou H, Kuang Y. Electrodeposition of Pt–Ru nanoparticles on carbon nanotubes and their electrocatalytic properties for methanol electrooxidation. *Diam Relat Mater* 2004;13:1764–70. doi:10.1016/j.diamond.2004.03.004.
- [289] Yudasaka M, Iijima S, Crespi VH. Single-Wall Carbon Nanohorns and Nanocones. In: Jorio A, Dresselhaus G, Dresselhaus MS, editors. *Carbon Nanotub., Springer Berlin Heidelberg*; 2008, p. 605–29.
- [290] Fejes D, Hernádi K. A Review of the Properties and CVD Synthesis of Coiled Carbon Nanotubes. *Materials* 2010;3:2618–42. doi:10.3390/ma3042618.
- [291] McDonough JK, Gogotsi Y. Carbon onions: synthesis and electrochemical applications. *Electrochem Soc Interface* 2013;22:61–5.
- [292] Bartelmeß J, Giordani S. Carbon nano-onions (multi-layer fullerenes): chemistry and applications. *Beilstein J Nanotechnol* 2014;5:1980–98. doi:10.3762/bjnano.5.207.
- [293] Sano N, Wang H, Alexandrou I, Chhowalla M, Teo KBK, Amaratunga G a. J, et al. Properties of carbon onions produced by an arc discharge in water. *J Appl Phys* 2002;92:2783–8. doi:10.1063/1.1498884.
- [294] Huang Q, Yu D, Xu B, Hu W, Ma Y, Wang Y, et al. Nanotwinned diamond with unprecedented hardness and stability. *Nature* 2014;510:250–3. doi:10.1038/nature13381.
- [295] Iijima S, Yudasaka M, Yamada R, Bandow S, Suenaga K, Kokai F, et al. Nano-aggregates of single-walled graphitic carbon nano-horns. *Chem Phys Lett* 1999;309:165–70. doi:10.1016/S0009-2614(99)00642-9.
- [296] Harris PJF, Tsang SC, Claridge JB, Green MLH. High-resolution electron microscopy studies of a microporous carbon produced by arc-evaporation. *J Chem Soc Faraday Trans* 1994;90:2799–802. doi:10.1039/FT9949002799.
- [297] Motojima S, Kawaguchi M, Nozaki K, Iwanaga H. Preparation of coiled carbon fibers by catalytic pyrolysis of acetylene, and its morphology and extension characteristics. *Carbon* 1991;29:379–85. doi:10.1016/0008-6223(91)90207-Y.
- [298] Ihara S, Itoh S, Kitakami J. Helically coiled cage forms of graphitic carbon. *Phys Rev B* 1993;48:5643–7. doi:10.1103/PhysRevB.48.5643.
- [299] Itoh S, Ihara S, Kitakami J. Toroidal form of carbon C360. *Phys Rev B* 1993;47:1703–4. doi:10.1103/PhysRevB.47.1703.
- [300] Itoh S, Ihara S. Toroidal forms of graphitic carbon. II. Elongated tori. *Phys Rev B* 1993;48:8323–8. doi:10.1103/PhysRevB.48.8323.
- [301] Zhang XB, Zhang XF, Bernaerts D, Tendeloo G van, Amelinckx S, Landuyt J van, et al. The Texture of Catalytically Grown Coil-Shaped Carbon Nanotubules. *EPL Europhys Lett* 1994;27:141. doi:10.1209/0295-5075/27/2/011.

- [302] Hyeon T, Han S, Sung Y-E, Park K-W, Kim Y-W. High-Performance Direct Methanol Fuel Cell Electrodes using Solid-Phase-Synthesized Carbon Nanocoils. *Angew Chem* 2003;115:4488–92. doi:10.1002/ange.200250856.
- [303] Sevilla M, Sanchis C, Valdés-Solís T, Morallón E, Fuertes AB. Highly dispersed platinum nanoparticles on carbon nanocoils and their electrocatalytic performance for fuel cell reactions. *Electrochimica Acta* 2009;54:2234–8. doi:10.1016/j.electacta.2008.10.042.
- [304] Yoshitake T, Shimakawa Y, Kuroshima S, Kimura H, Ichihashi T, Kubo Y, et al. Preparation of fine platinum catalyst supported on single-wall carbon nanohorns for fuel cell application. *Phys B Condens Matter* 2002;323:124–6. doi:10.1016/S0921-4526(02)00871-2.
- [305] Sano N, Ukita S. One-step synthesis of Pt-supported carbon nanohorns for fuel cell electrode by arc plasma in liquid nitrogen. *Mater Chem Phys* 2006;99:447–50. doi:10.1016/j.matchemphys.2005.11.019.
- [306] GUO J, YANG X, YAO Y, WANG X, LIU X, XU B. Pt/onion-like fullerenes as catalyst for direct methanol fuel cell. *Rare Met* 2006;25:305–8. doi:10.1016/S1001-0521(07)60094-1.
- [307] Xu B, Yang X, Wang X, Guo J, Liu X. A novel catalyst support for DMFC: Onion-like fullerenes. *J Power Sources* 2006;162:160–4. doi:10.1016/j.jpowsour.2006.06.063.
- [308] Wu G, Dai C, Wang D, Li D, Li N. Nitrogen-doped magnetic onion-like carbon as support for Pt particles in a hybrid cathode catalyst for fuel cells. *J Mater Chem* 2010;20:3059. doi:10.1039/b924010a.
- [309] Wu G, Nelson M, Ma S, Meng H, Cui G, Shen PK. Synthesis of nitrogen-doped onion-like carbon and its use in carbon-based CoFe binary non-precious-metal catalysts for oxygen-reduction. *Carbon* 2011;49:3972–82. doi:10.1016/j.carbon.2011.05.036.
- [310] Eguchi U, Takikawa H, Suda Y. Electromagnetic wave absorption characteristics of multiwalled carbon nanocoils. *Jpn J Appl Phys* 2014;53:045102. doi:10.7567/JJAP.53.045102.
- [311] Danilenko VV. On the history of the discovery of nanodiamond synthesis. *Phys Solid State* 2004;46:595–9. doi:10.1134/1.1711431.
- [312] Greiner NR, Phillips DS, Johnson JD, Volk F. Diamonds in detonation soot. *Nature* 1988;333:440–2. doi:10.1038/333440a0.
- [313] Mochalin VN, Shenderova O, Ho D, Gogotsi Y. The properties and applications of nanodiamonds. *Nat Nanotechnol* 2012;7:11–23. doi:10.1038/nnano.2011.209.
- [314] Banhart F, Ajayan PM. Carbon onions as nanoscopic pressure cells for diamond formation. *Nature* 1996;382:433–5. doi:10.1038/382433a0.
- [315] Xu J, Granger MC, Chen Q, Strojek JW, Lister TE, Swain GM. Peer Reviewed: Boron-Doped Diamond Thin-Film Electrodes. *Anal Chem* 1997;69:591A – 597A. doi:10.1021/ac971791z.
- [316] Hupert M, Muck A, Wang J, Stotter J, Cvackova Z, Haymond S, et al. Conductive diamond thin-films in electrochemistry. *Diam Relat Mater* 2003;12:1940–9. doi:10.1016/S0925-9635(03)00260-7.
- [317] Martin HB, Argoitia A, Landau U, Anderson AB, Angus JC. Hydrogen and Oxygen Evolution on Boron-Doped Diamond Electrodes. *J Electrochem Soc* 1996;143:L133–6. doi:10.1149/1.1836901.
- [318] Yano T, Tryk DA, Hashimoto K, Fujishima A. Electrochemical Behavior of Highly Conductive Boron-Doped Diamond Electrodes for Oxygen Reduction in Alkaline Solution. *J Electrochem Soc* 1998;145:1870–6. doi:10.1149/1.1838569.
- [319] Wang J, Swain GM, Tachibana T, Kobashi K. Incorporation of Pt Particles in Boron-Doped Diamond Thin Films Applications in Electrocatalysis. *Electrochem Solid-State Lett* 2000;3:286–9. doi:10.1149/1.1391126.
- [320] Honda K, Yoshimura M, Rao TN, Tryk DA, Fujishima A, Yasui K, et al. Electrochemical properties of Pt-modified nano-honeycomb diamond electrodes. *J Electroanal Chem* 2001;514:35–50. doi:10.1016/S0022-0728(01)00614-3.
- [321] Zhang Y, Asahina S, Yoshihara S, Shirakashi T. Oxygen reduction on Au nanoparticle deposited boron-doped diamond films. *Electrochimica Acta* 2003;48:741–7. doi:10.1016/S0013-4686(02)00743-0.
- [322] Montilla F, Morallón E, Duo I, Comninellis C, Vázquez JL. Platinum particles deposited on synthetic boron-doped diamond surfaces. Application to methanol oxidation. *Electrochimica Acta* 2003;48:3891–7. doi:10.1016/S0013-4686(03)00526-7.
- [323] Fischer AE, Swain GM. Preparation and Characterization of Boron-Doped Diamond Powder A Possible Dimensionally Stable Electrocatalyst Support Material. *J Electrochem Soc* 2005;152:B369–75. doi:10.1149/1.1984367.

- [324] Suffredini HB, Tricoli V, Vatasias N, Avaca LA. Electro-oxidation of methanol and ethanol using a Pt–RuO<sub>2</sub>/C composite prepared by the sol–gel technique and supported on boron-doped diamond. *J Power Sources* 2006;158:124–8. doi:10.1016/j.jpowsour.2005.09.040.
- [325] Siné G, Fóti G, Comminellis C. Boron-doped diamond (BDD)-supported Pt/Sn nanoparticles synthesized in microemulsion systems as electrocatalysts of ethanol oxidation. *J Electroanal Chem* 2006;595:115–24. doi:10.1016/j.jelechem.2006.07.012.
- [326] Salazar-Banda GR, Suffredini HB, Calegaro ML, Tanimoto ST, Avaca LA. Sol–gel-modified boron-doped diamond surfaces for methanol and ethanol electro-oxidation in acid medium. *J Power Sources* 2006;162:9–20. doi:10.1016/j.jpowsour.2006.06.045.
- [327] Salazar-Banda GR, Eguiluz KIB, Avaca LA. Boron-doped diamond powder as catalyst support for fuel cell applications. *Electrochem Commun* 2007;9:59–64. doi:10.1016/j.elecom.2006.08.038.
- [328] Salazar-Banda GR, Suffredini HB, Avaca LA, Machado SAS. Methanol and ethanol electro-oxidation on Pt–SnO<sub>2</sub> and Pt–Ta<sub>2</sub>O<sub>5</sub> sol–gel-modified boron-doped diamond surfaces. *Mater Chem Phys* 2009;117:434–42. doi:10.1016/j.matchemphys.2009.06.027.
- [329] Spätaru N, Zhang X, Spätaru T, Tryk DA, Fujishima A. Platinum Electrodeposition on Conductive Diamond Powder and Its Application to Methanol Oxidation in Acidic Media. *J Electrochem Soc* 2008;155:B264–9. doi:10.1149/1.2830857.
- [330] Hutton LA, Vidotti M, Patel AN, Newton ME, Unwin PR, Macpherson JV. Electrodeposition of Nickel Hydroxide Nanoparticles on Boron-Doped Diamond Electrodes for Oxidative Electrocatalysis. *J Phys Chem C* 2010;115:1649–58. doi:10.1021/jp109526b.
- [331] Moore A, Celorrio V, de Oca MM, Plana D, Hongthani W, Lázaro MJ, et al. Insulating diamond particles as substrate for Pd electrocatalysts. *Chem Commun* 2011;47:7656. doi:10.1039/c1cc12387d.
- [332] Lu X, Hu J, Foord JS, Wang Q. Electrochemical deposition of Pt–Ru on diamond electrodes for the electrooxidation of methanol. *J Electroanal Chem* 2011;654:38–43. doi:10.1016/j.jelechem.2011.01.034.
- [333] Novoselov KS, Geim AK, Morozov SV, Jiang D, Zhang Y, Dubonos SV, et al. Electric Field Effect in Atomically Thin Carbon Films. *Science* 2004;306:666–9. doi:10.1126/science.1102896.
- [334] Novoselov KS, Geim AK, Morozov SV, Jiang D, Katsnelson MI, Grigorieva IV, et al. Two-dimensional gas of massless Dirac fermions in graphene. *Nature* 2005;438:197–200. doi:10.1038/nature04233.
- [335] Wick P, Louw-Gaume AE, Kucki M, Krug HF, Kostarelos K, Fadeel B, et al. Classification Framework for Graphene-Based Materials. *Angew Chem Int Ed* 2014;53:7714–8. doi:10.1002/anie.201403335.
- [336] Bianco A, Cheng H-M, Enoki T, Gogotsi Y, Hurt RH, Koratkar N, et al. All in the graphene family – A recommended nomenclature for two-dimensional carbon materials. *Carbon* 2013;65:1–6. doi:10.1016/j.carbon.2013.08.038.
- [337] Si Y, Samulski ET. Exfoliated Graphene Separated by Platinum Nanoparticles. *Chem Mater* 2008;20:6792–7. doi:10.1021/cm801356a.
- [338] Xu C, Wang X, Zhu J. Graphene–Metal Particle Nanocomposites. *J Phys Chem C* 2008;112:19841–5. doi:10.1021/jp807989b.
- [339] Shang NG, Papakonstantinou P, Sharma S, Lubarsky G, Li M, McNeill DW, et al. Controllable selective exfoliation of high-quality graphene nanosheets and nanodots by ionic liquid assisted grinding. *Chem Commun* 2012;48:1877. doi:10.1039/c2cc17185f.
- [340] Paton KR, Varria E, Backes C, Smith RJ, Khan U, O'Neill A, et al. Scalable production of large quantities of defect-free few-layer graphene by shear exfoliation in liquids. *Nat Mater* 2014;13:624–30. doi:10.1038/nmat3944.
- [341] Hernandez Y, Nicolosi V, Lotya M, Blighe FM, Sun Z, De S, et al. High-yield production of graphene by liquid-phase exfoliation of graphite. *Nat Nanotechnol* 2008;3:563–8. doi:10.1038/nnano.2008.215.
- [342] Zhao W, Fang M, Wu F, Wu H, Wang L, Chen G. Preparation of graphene by exfoliation of graphite using wet ball milling. *J Mater Chem* 2010;20:5817. doi:10.1039/c0jm01354d.
- [343] Geng J, Kong B-S, Yang SB, Jung H-T. Preparation of graphene relying on porphyrin exfoliation of graphite. *Chem Commun* 2010;46:5091. doi:10.1039/c001609h.
- [344] Zhao L, Rim KT, Zhou H, He R, Heinz TF, Pinczuk A, et al. Influence of copper crystal surface on the CVD growth of large area monolayer graphene. *Solid State Commun* 2011;151:509–13. doi:10.1016/j.ssc.2011.01.014.

- [345] Panchakarla LS, Subrahmanyam KS, Saha SK, Govindaraj A, Krishnamurthy HR, Waghmare UV, et al. Synthesis, Structure, and Properties of Boron- and Nitrogen-Doped Graphene. *Adv Mater* 2009;21:4726–30. doi:10.1002/adma.200901285.
- [346] Li N, Wang Z, Zhao K, Shi Z, Gu Z, Xu S. Large scale synthesis of N-doped multi-layered graphene sheets by simple arc-discharge method. *Carbon* 2010;48:255–9. doi:10.1016/j.carbon.2009.09.013.
- [347] Berger C, Song Z, Li T, Li X, Ogbazghi AY, Feng R, et al. Ultrathin Epitaxial Graphite: 2D Electron Gas Properties and a Route toward Graphene-based Nanoelectronics. *J Phys Chem B* 2004;108:19912–6. doi:10.1021/jp040650f.
- [348] Kosynkin DV, Higginbotham AL, Sinitskii A, Lomeda JR, Dimiev A, Price BK, et al. Longitudinal unzipping of carbon nanotubes to form graphene nanoribbons. *Nature* 2009;458:872–6. doi:10.1038/nature07872.
- [349] Stankovich S, Dikin DA, Piner RD, Kohlhaas KA, Kleinhammes A, Jia Y, et al. Synthesis of graphene-based nanosheets via chemical reduction of exfoliated graphite oxide. *Carbon* 2007;45:1558–65. doi:10.1016/j.carbon.2007.02.034.
- [350] Kamat PV. Graphene-Based Nanoarchitectures. Anchoring Semiconductor and Metal Nanoparticles on a Two-Dimensional Carbon Support. *J Phys Chem Lett* 2009;1:520–7. doi:10.1021/jz900265j.
- [351] Seger B, Kamat PV. Electrocatalytically Active Graphene-Platinum Nanocomposites. Role of 2-D Carbon Support in PEM Fuel Cells. *J Phys Chem C* 2009;113:7990–5. doi:10.1021/jp900360k.
- [352] Yoo E, Okata T, Akita T, Kohyama M, Nakamura J, Honma I. Enhanced Electrolytic Activity of Pt Subnanoclusters on Graphene Nanosheet Surface. *Nano Lett* 2009;9:2255–9. doi:10.1021/nl900397t.
- [353] Kou R, Shao Y, Wang D, Engelhard MH, Kwak JH, Wang J, et al. Enhanced activity and stability of Pt catalysts on functionalized graphene sheets for electrocatalytic oxygen reduction. *Electrochem Commun* 2009;11:954–7. doi:10.1016/j.elecom.2009.02.033.
- [354] Imran Jafri R, Rajalakshmi N, Ramaprabhu S. Nitrogen doped graphene nanoplatelets as catalyst support for oxygen reduction reaction in proton exchange membrane fuel cell. *J Mater Chem* 2010;20:7114. doi:10.1039/c0jm00467g.
- [355] Zhang L-S, Liang X-Q, Song W-G, Wu Z-Y. Identification of the nitrogen species on N-doped graphene layers and Pt/NG composite catalyst for direct methanol fuel cell. *Phys Chem Chem Phys* 2010;12:12055. doi:10.1039/c0cp00789g.
- [356] Zhu C, Guo S, Zhai Y, Dong S. Layer-by-Layer Self-Assembly for Constructing a Graphene/Platinum Nanoparticle Three-Dimensional Hybrid Nanostructure Using Ionic Liquid as a Linker. *Langmuir* 2010;26:7614–8. doi:10.1021/la904201j.
- [357] Dong L, Gari RRS, Li Z, Craig MM, Hou S. Graphene-supported platinum and platinum–ruthenium nanoparticles with high electrocatalytic activity for methanol and ethanol oxidation. *Carbon* 2010;48:781–7. doi:10.1016/j.carbon.2009.10.027.
- [358] Li Y, Gao W, Ci L, Wang C, Ajayan PM. Catalytic performance of Pt nanoparticles on reduced graphene oxide for methanol electro-oxidation. *Carbon* 2010;48:1124–30. doi:10.1016/j.carbon.2009.11.034.
- [359] Qiu J-D, Wang G-C, Liang R-P, Xia X-H, Yu H-W. Controllable Deposition of Platinum Nanoparticles on Graphene As an Electrocatalyst for Direct Methanol Fuel Cells. *J Phys Chem C* 2011;115:15639–45. doi:10.1021/jp200580u.
- [360] Venkateswara Rao C, Cabrera CR, Ishikawa Y. Graphene-Supported Pt–Au Alloy Nanoparticles: A Highly Efficient Anode for Direct Formic Acid Fuel Cells. *J Phys Chem C* 2011;115:21963–70. doi:10.1021/jp202561n.
- [361] Zhang S, Shao Y, Liao H, Liu J, Aksay IA, Yin G, et al. Graphene Decorated with PtAu Alloy Nanoparticles: Facile Synthesis and Promising Application for Formic Acid Oxidation. *Chem Mater* 2011;23:1079–81. doi:10.1021/cm101568z.
- [362] Xin Y, Liu J, Zhou Y, Liu W, Gao J, Xie Y, et al. Preparation and characterization of Pt supported on graphene with enhanced electrocatalytic activity in fuel cell. *J Power Sources* 2011;196:1012–8. doi:10.1016/j.jpowsour.2010.08.051.
- [363] Rao CV, Reddy ALM, Ishikawa Y, Ajayan PM. Synthesis and electrocatalytic oxygen reduction activity of graphene-supported Pt<sub>3</sub>Co and Pt<sub>3</sub>Cr alloy nanoparticles. *Carbon* 2011;49:931–6. doi:10.1016/j.carbon.2010.10.056.
- [364] Qu L, Liu Y, Baek J-B, Dai L. Nitrogen-Doped Graphene as Efficient Metal-Free Electrocatalyst for Oxygen Reduction in Fuel Cells. *ACS Nano* 2010;4:1321–6. doi:10.1021/nn901850u.
- [365] Shang N, Papakonstantinou P, Wang P, Silva SRP. Platinum Integrated Graphene for Methanol Fuel Cells. *J Phys Chem C* 2010;114:15837–41. doi:10.1021/jp105470s.

- [366] Soin N, Roy SS, Lim TH, McLaughlin JAD. Microstructural and electrochemical properties of vertically aligned few layered graphene (FLG) nanoflakes and their application in methanol oxidation. *Mater Chem Phys* 2011;129:1051–7. doi:10.1016/j.matchemphys.2011.05.063.
- [367] Maiyalagan T, Dong X, Chen P, Wang X. Electrodeposited Pt on three-dimensional interconnected graphene as a free-standing electrode for fuel cell application. *J Mater Chem* 2012;22:5286. doi:10.1039/c2jm16541d.
- [368] Li Y, Tang L, Li J. Preparation and electrochemical performance for methanol oxidation of Pt/graphene nanocomposites. *Electrochem Commun* 2009;11:846–9. doi:10.1016/j.elecom.2009.02.009.
- [369] Sharma S, Ganguly A, Papakonstantinou P, Miao X, Li M, Hutchison JL, et al. Rapid Microwave Synthesis of CO Tolerant Reduced Graphene Oxide-Supported Platinum Electrocatalysts for Oxidation of Methanol. *J Phys Chem C* 2010;114:19459–66. doi:10.1021/jp107872z.
- [370] Shao Y, Zhang S, Wang C, Nie Z, Liu J, Wang Y, et al. Highly durable graphene nanoplatelets supported Pt nanocatalysts for oxygen reduction. *J Power Sources* 2010;195:4600–5. doi:10.1016/j.jpowsour.2010.02.044.
- [371] Kulla T, Bose S, Mishra AK, Khanra P, Kim NH, Lee JH. Chemical functionalization of graphene and its applications. *Prog Mater Sci* 2012;57:1061–105. doi:10.1016/j.pmatsci.2012.03.002.
- [372] Zhang L, Xia Z. Mechanisms of Oxygen Reduction Reaction on Nitrogen-Doped Graphene for Fuel Cells. *J Phys Chem C* 2011;115:11170–6. doi:10.1021/jp201991j.
- [373] Jafri RI, Arockiadoss T, Rajalakshmi N, Ramaprabhu S. Nanostructured Pt Dispersed on Graphene-Multiwalled Carbon Nanotube Hybrid Nanomaterials as Electrocatalyst for PEMFC. *J Electrochem Soc* 2010;157:B874–9. doi:10.1149/1.3374353.
- [374] Yang S-Y, Chang K-H, Lee Y-F, Ma C-CM, Hu C-C. Constructing a hierarchical graphene-carbon nanotube architecture for enhancing exposure of graphene and electrochemical activity of Pt nanoclusters. *Electrochem Commun* 2010;12:1206–9. doi:10.1016/j.elecom.2010.06.020.
- [375] Lv R, Cui T, Jun M-S, Zhang Q, Cao A, Su DS, et al. Open-Ended, N-Doped Carbon Nanotube-Graphene Hybrid Nanostructures as High-Performance Catalyst Support. *Adv Funct Mater* 2011;21:999–1006. doi:10.1002/adfm.201001602.
- [376] Jha N, Jafri RI, Rajalakshmi N, Ramaprabhu S. Graphene-multi walled carbon nanotube hybrid electrocatalyst support material for direct methanol fuel cell. *Int J Hydrog Energy* 2011;36:7284–90. doi:10.1016/j.ijhydene.2011.03.008.
- [377] Hsieh C-T, Liu Y-Y, Tzou D-Y, Chen W-Y. Atomic Layer Deposition of Platinum Nanocatalysts onto Three-Dimensional Carbon Nanotube/Graphene Hybrid. *J Phys Chem C* 2012;116:26735–43. doi:10.1021/jp303552j.
- [378] Ye F, Cao X, Yu L, Chen S, Lin W. Synthesis and catalytic performance of PtRuMo nanoparticles supported on graphene-carbon nanotubes nanocomposites for methanol electro-oxidation. *Int J Electrochem Sci* 2012;7:1251–65.
- [379] Yang S, Shen C, Lu X, Tong H, Zhu J, Zhang X, et al. Preparation and electrochemistry of graphene nanosheets-multiwalled carbon nanotubes hybrid nanomaterials as Pd electrocatalyst support for formic acid oxidation. *Electrochimica Acta* 2012;62:242–9. doi:10.1016/j.electacta.2011.12.022.
- [380] Wang Y-S, Yang S-Y, Li S-M, Tien H-W, Hsiao S-T, Liao W-H, et al. Three-dimensionally porous graphene-carbon nanotube composite-supported PtRu catalysts with an ultrahigh electrocatalytic activity for methanol oxidation. *Electrochimica Acta* 2013;87:261–9. doi:10.1016/j.electacta.2012.09.013.
- [381] Yao Z, Yue R, Zhai C, Jiang F, Wang H, Du Y, et al. Electrochemical layer-by-layer fabrication of a novel three-dimensional Pt/graphene/carbon fiber electrode and its improved catalytic performance for methanol electrooxidation in alkaline medium. *Int J Hydrog Energy* 2013;38:6368–76. doi:10.1016/j.ijhydene.2013.02.140.
- [382] Sahoo M, Vinayan BP, Ramaprabhu S. Platinum-decorated chemically modified reduced graphene oxide-multiwalled carbon nanotube sandwich composite as cathode catalyst for a proton exchange membrane fuel cell. *RSC Adv* 2014;4:26140. doi:10.1039/c4ra02542c.
- [383] Pham K-C, Chua DHC, McPhail DS, Wee ATS. The Direct Growth of Graphene-Carbon Nanotube Hybrids as Catalyst Support for High-Performance PEM Fuel Cells. *ECS Electrochem Lett* 2014;3:F37–40. doi:10.1149/2.009406eel.
- [384] Antolini E, Gonzalez ER. Ceramic materials as supports for low-temperature fuel cell catalysts. *Solid State Ion* 2009;180:746–63. doi:10.1016/j.ssi.2009.03.007.
- [385] Antolini E, Gonzalez ER. Polymer supports for low-temperature fuel cell catalysts. *Appl Catal Gen* 2009;365:1–19. doi:10.1016/j.apcata.2009.05.045.

- [386] Wang M, Guo D, Li H. High activity of novel Pd/TiO<sub>2</sub> nanotube catalysts for methanol electro-oxidation. *J Solid State Chem* 2005;178:1996–2000. doi:10.1016/j.jssc.2005.04.006.
- [387] Musthafa OTM, Sampath S. High performance platinumized titanium nitride catalyst for methanol oxidation. *Chem Commun* 2008;6:7–9. doi:10.1039/b715859a.
- [388] Yin S, Mu S, Lv H, Cheng N, Pan M, Fu Z. A highly stable catalyst for PEM fuel cell based on durable titanium diboride support and polymer stabilization. *Appl Catal B Environ* 2010;93:233–40. doi:10.1016/j.apcatb.2009.09.034.
- [389] Manasilp A, Gulari E. Selective CO oxidation over Pt/alumina catalysts for fuel cell applications. *Appl Catal B Environ* 2002;37:17–25. doi:10.1016/S0926-3373(01)00319-8.
- [390] Okanishi T, Matsui T, Takeguchi T, Kikuchi R, Eguchi K. Chemical interaction between Pt and SnO<sub>2</sub> and influence on adsorptive properties of carbon monoxide. *Appl Catal Gen* 2006;298:181–7. doi:10.1016/j.apcata.2005.09.035.
- [391] Chhina H, Campbell S, Kesler O. An oxidation-resistant indium tin oxide catalyst support for proton exchange membrane fuel cells. *J Power Sources* 2006;161:893–900. doi:10.1016/j.jpowsour.2006.05.014.
- [392] Min K-B, Tanaka S, Esashi M. Fabrication of novel MEMS-based polymer electrolyte fuel cell architectures with catalytic electrodes supported on porous SiO<sub>2</sub>. *J Micromechanics Microengineering* 2006;16:505. doi:10.1088/0960-1317/16/3/005.
- [393] Seger B, Kongkanand A, Vinodgopal K, Kamat PV. Platinum dispersed on silica nanoparticle as electrocatalyst for PEM fuel cell. *J Electroanal Chem* 2008;621:198–204. doi:10.1016/j.jelechem.2007.09.037.
- [394] Kulesza PJ, Faulkner LR. Electrodeposition and characterization of three-dimensional tungsten(VI, V)-oxide films containing spherical Pt microparticles. *J Electrochem Soc* 1989;136:707–13.
- [395] Kulesza PJ, Faulkner LR. Electrocatalytic properties of bifunctional Pt/W(VI,V) oxide microstructures electrodeposited on carbon substrates. *J Electroanal Chem Interfacial Electrochem* 1989;259:81–98. doi:10.1016/0022-0728(89)80040-3.
- [396] Ganesan R, Lee JS. An electrocatalyst for methanol oxidation based on tungsten trioxide microspheres and platinum. *J Power Sources* 2006;157:217–21. doi:10.1016/j.jpowsour.2005.07.069.
- [397] Weigert EC, Stottlemeyer AL, Zellner MB, Chen JG. Tungsten monocarbide as potential replacement of platinum for methanol electrooxidation. *J Phys Chem C* 2007;111:14617–20. doi:10.1021/jp075504z.
- [398] Bosco JP, Sasaki K, Sadakane M, Ueda W, Chen JG. Synthesis and characterization of three-dimensionally ordered macroporous (3DOM) tungsten carbide: Application to direct methanol fuel cells. *Chem Mater* 2010;22:966–73. doi:10.1021/cm901855y.
- [399] Suzuki Y, Ishihara A, Mitsushima S, Kamiya N, Ota K-I. Sulfated-zirconia as a support of Pt catalyst for polymer electrolyte fuel cells. *Electrochem Solid-State Lett* 2007;10:B105–7. doi:10.1149/1.2730625.
- [400] Guo D-J, Qiu X-P, Zhu W-T, Chen L-Q. Synthesis of sulfated ZrO<sub>2</sub>/MWCNT composites as new supports of Pt catalysts for direct methanol fuel cell application. *Appl Catal B Environ* 2009;89:597–601. doi:10.1016/j.apcatb.2009.01.025.
- [401] Karakoti AS, King JES, Vincent A, Seal S. Synthesis dependent core level binding energy shift in the oxidation state of platinum coated on ceria–titania and its effect on catalytic decomposition of methanol. *Appl Catal Gen* 2010;388:262–71. doi:10.1016/j.apcata.2010.08.060.
- [402] Rajesh B, Thampi KR, Bonard JM, Mathieu HJ, Xanthopoulos N, Viswanathan B. Nanostructured Conducting Polyaniline Tubules as Catalyst Support for Pt Particles for Possible Fuel Cell Applications. *Electrochem Solid-State Lett* 2004;7:A404–7. doi:10.1149/1.1799955.
- [403] Huang S-Y, Ganesan P, Popov BN. Development of conducting polypyrrole as corrosion-resistant catalyst support for polymer electrolyte membrane fuel cell (PEMFC) application. *Appl Catal B Environ* 2009;93:75–81. doi:10.1016/j.apcatb.2009.09.014.
- [404] Roncali J. Conjugated poly(thiophenes): Synthesis, functionalization, and applications. *Chem Rev* 1992;92:711–38.
- [405] Swathirajan S, Mikhail YM. Methanol Oxidation on Platinum-Tin Catalysts Dispersed on Poly(3-methyl)thiophene Conducting Polymer. *J Electrochem Soc* 1992;139:2105–10. doi:10.1149/1.2221186.
- [406] Drillet J-F, Dittmeyer R, Jüttner K. Activity and long-term stability of PEDOT as Pt catalyst support for the DMFC anode. *J Appl Electrochem* 2007;37:1219–26. doi:10.1007/s10800-007-9393-2.

- [407] Lefebvre M, Qi Z, Rana D, Pickup PG. Chemical synthesis, characterization, and electrochemical studies of poly(3,4-ethylenedioxythiophene)/ Poly(styrene-4-sulfonate) composites. *Chem Mater* 1999;11:262–8.
- [408] Choi J-H, Park K-W, Lee H-K, Kim Y-M, Lee J-S, Sung Y-E. Nano-composite of PtRu alloy electrocatalyst and electronically conducting polymer for use as the anode in a direct methanol fuel cell. *Electrochimica Acta* 2003;48:2781–9. doi:10.1016/S0013-4686(03)00412-2.
- [409] Jiang SP, Liu Z, Tang HL, Pan M. Synthesis and characterization of PDDA-stabilized Pt nanoparticles for direct methanol fuel cells. *Electrochimica Acta* 2006;51:5721–30. doi:10.1016/j.electacta.2006.03.006.
- [410] Román-Martínez MC, Cazorla-Amorós D, Linares-Solano A, De Lecea CS-M, Yamashita H, Anpo M. Metal-support interaction in Pt/C catalysts. Influence of the support surface chemistry and the metal precursor. *Carbon* 1995;33:3–13. doi:10.1016/0008-6223(94)00096-1.
- [411] Rodríguez-reinoso F. The role of carbon materials in heterogeneous catalysis. *Carbon* 1998;36:159–75. doi:10.1016/S0008-6223(97)00173-5.
- [412] Yu X, Ye S. Recent advances in activity and durability enhancement of Pt/C catalytic cathode in PEMFC: Part I. Physico-chemical and electronic interaction between Pt and carbon support, and activity enhancement of Pt/C catalyst. *J Power Sources* 2007;172:133–44. doi:10.1016/j.jpowsour.2007.07.049.
- [413] Yu X, Ye S. Recent advances in activity and durability enhancement of Pt/C catalytic cathode in PEMFC: Part II: Degradation mechanism and durability enhancement of carbon supported platinum catalyst. *J Power Sources* 2007;172:145–54. doi:10.1016/j.jpowsour.2007.07.048.
- [414] Montes-Morán MA, Menéndez JA, Fuente E, Suárez D. Contribution of the Basal Planes to Carbon Basicity: An Ab Initio Study of the H<sub>3</sub>O<sup>+</sup>- $\pi$  Interaction in Cluster Models. *J Phys Chem B* 1998;102:5595–601. doi:10.1021/jp972656t.
- [415] Fabish TJ, Schleifer DE. Surface chemistry and the carbon black work function. *Carbon* 1984;22:19–38. doi:10.1016/0008-6223(84)90129-5.
- [416] Leon y Leon CA, Solar JM, Calemma V, Radovic LR. Evidence for the protonation of basal plane sites on carbon. *Carbon* 1992;30:797–811. doi:10.1016/0008-6223(92)90164-R.
- [417] Menéndez JA, Phillips J, Xia B, Radovic LR. On the Modification and Characterization of Chemical Surface Properties of Activated Carbon: In the Search of Carbons with Stable Basic Properties. *Langmuir* 1996;12:4404–10. doi:10.1021/la9602022.
- [418] Menéndez JA, Radovic LR, Xia B, Phillips J. Low-Temperature Generation of Basic Carbon Surfaces by Hydrogen Spillover. *J Phys Chem* 1996;100:17243–8. doi:10.1021/jp961243+.
- [419] Leon y Leon CA, Radovic LR. Interfacial Chemistry and Electrochemistry of Carbon Surfaces. In: Thrower PA, editor. *Chem. Phys. Carbon*, vol. 25, CRC Press; 1996, p. 213–310.
- [420] De Miguel SR, Scelza OA, Román-Martínez MC, Salinas-Martínez de Lecea C, Cazorla-Amorós D, Linares-Solano A. States of Pt in Pt/C catalyst precursors after impregnation, drying and reduction steps. *Appl Catal Gen* 1998;170:93–103. doi:10.1016/S0926-860X(98)00029-5.
- [421] Lambert J-F, Che M. The molecular approach to supported catalysts synthesis: state of the art and future challenges. *J Mol Catal Chem* 2000;162:5–18. doi:10.1016/S1381-1169(00)00318-6.
- [422] Wieckowski A, Savinova E, Vayenas C, editors. *Catalysis and Electrocatalysis at Nanoparticle Surfaces*. CRC Press; 2003.
- [423] Calvillo L, Celorrio V, Moliner R, Lázaro MJ. Influence of the support on the physicochemical properties of Pt electrocatalysts: Comparison of catalysts supported on different carbon materials. *Mater Chem Phys* 2011;127:335–41. doi:10.1016/j.matchemphys.2011.02.014.
- [424] Prado-Burguete C, Linares-Solano A, Rodríguez-Reinoso F, de Lecea CS-M. The effect of oxygen surface groups of the support on platinum dispersion in Pt/carbon catalysts. *J Catal* 1989;115:98–106. doi:10.1016/0021-9517(89)90010-9.
- [425] Kim S, Park S-J. Effect of acid/base treatment to carbon blacks on preparation of carbon-supported platinum nanoclusters. *Electrochimica Acta* 2007;52:3013–21. doi:10.1016/j.electacta.2006.09.060.
- [426] Choi B, Yoon H, Park I-S, Jang J, Sung Y-E. Highly dispersed Pt nanoparticles on nitrogen-doped magnetic carbon nanoparticles and their enhanced activity for methanol oxidation. *Carbon* 2007;45:2496–501. doi:10.1016/j.carbon.2007.08.028.
- [427] Chen Z, Higgins D, Tao H, Hsu RS, Chen Z. Highly Active Nitrogen-Doped Carbon Nanotubes for Oxygen Reduction Reaction in Fuel Cell Applications. *J Phys Chem C* 2009;113:21008–13. doi:10.1021/jp908067v.
- [428] Tang Y, Allen BL, Kauffman DR, Star A. Electrocatalytic Activity of Nitrogen-Doped Carbon Nanotube Cups. *J Am Chem Soc* 2009;131:13200–1. doi:10.1021/ja904595t.

- [429] Gong K, Du F, Xia Z, Durstock M, Dai L. Nitrogen-Doped Carbon Nanotube Arrays with High Electrocatalytic Activity for Oxygen Reduction. *Science* 2009;323:760–4. doi:10.1126/science.1168049.
- [430] Zhou Y, Neyerlin K, Olson TS, Pylypenko S, Bult J, Dinh HN, et al. Enhancement of Pt and Pt-alloy fuel cell catalyst activity and durability via nitrogen-modified carbon supports. *Energy Environ Sci* 2010;3:1437. doi:10.1039/c003710a.
- [431] Ahmadi R, Amini MK. Synthesis and characterization of Pt nanoparticles on sulfur-modified carbon nanotubes for methanol oxidation. *Int J Hydrog Energy* 2011;36:7275–83. doi:10.1016/j.ijhydene.2011.03.013.
- [432] Ahmadi R, Amini MK, Bennett JC. Pt–Co alloy nanoparticles synthesized on sulfur-modified carbon nanotubes as electrocatalysts for methanol electrooxidation reaction. *J Catal* 2012;292:81–9. doi:10.1016/j.jcat.2012.05.001.
- [433] Xu Z, Qi Z, Kaufman A. High performance carbon-supported catalysts for fuel cells via phosphonation. *Chem Commun* 2003:878–9. doi:10.1039/b211969b.
- [434] Xu Z, Qi Z, Kaufman A. Advanced Fuel Cell Catalysts Sulfonation of Carbon-Supported Catalysts Using 2-Aminoethanesulfonic Acid. *Electrochem Solid-State Lett* 2003;6:A171–3. doi:10.1149/1.1592373.
- [435] Xu Z, Qi Z, Kaufman A. Superior Catalysts for Proton Exchange Membrane Fuel Cells Sulfonation of Carbon-Supported Catalysts Using Sulfate Salts. *Electrochem Solid-State Lett* 2005;8:A313–5. doi:10.1149/1.1912018.
- [436] Kim H, Lee W, Yoo D. Functionalized carbon support with sulfonated polymer for direct methanol fuel cells. *Electrochimica Acta* 2007;52:2620–4. doi:10.1016/j.electacta.2006.09.017.
- [437] Selvarani G, Sahu AK, Choudhury NA, Sridhar P, Pitchumani S, Shukla AK. A phenyl-sulfonic acid anchored carbon-supported platinum catalyst for polymer electrolyte fuel cell electrodes. *Electrochimica Acta* 2007;52:4871–7. doi:10.1016/j.electacta.2006.12.080.
- [438] Yang S, Zhang X, Mi H, Ye X. Pd nanoparticles supported on functionalized multi-walled carbon nanotubes (MWCNTs) and electrooxidation for formic acid. *J Power Sources* 2008;175:26–32. doi:10.1016/j.jpowsour.2007.09.080.
- [439] Du CY, Zhao TS, Liang ZX. Sulfonation of carbon-nanotube supported platinum catalysts for polymer electrolyte fuel cells. *J Power Sources* 2008;176:9–15. doi:10.1016/j.jpowsour.2007.10.016.
- [440] Coloma F, Sepulvedaescrignano A, Rodriguezreinoso F. Heat-Treated Carbon-Blacks as Supports for Platinum Catalysts. *J Catal* 1995;154:299–305. doi:10.1006/jcat.1995.1171.
- [441] Kang M, Bae Y-S, Lee C-H. Effect of heat treatment of activated carbon supports on the loading and activity of Pt catalyst. *Carbon* 2005;43:1512–6. doi:10.1016/j.carbon.2005.01.035.
- [442] Cerro-Alarcón M, Maroto-Valiente A, Rodríguez-Ramos I, Guerrero-Ruiz A. Further insights into the Ru nanoparticles–carbon interactions and their role in the catalytic properties. *Carbon* 2005;43:2711–22. doi:10.1016/j.carbon.2005.05.031.
- [443] Nunga S, Tito A, Bianco F, Bestetti M, Mazzocchia V. Production of carbon nanotubes using CVD with a Fe/Al<sub>2</sub>O<sub>3</sub> catalyst in fluidized bed. 12nd SFGP Conf., Marseille, France: 2009, p. 617–23.
- [444] Acierno D, Bestetti M, Mazzocchia CV, Tito A. A process for the preparation of a catalyst, a catalyst obtained thereby, and its use in the production of nanotubes. EP2213369 A1, 2010.
- [445] Hirata M, Gotou T, Horiuchi S, Fujiwara M, Ohba M. Thin-film particles of graphite oxide 1: High-yield synthesis and flexibility of the particles. *Carbon* 2004;42:2929–37. doi:10.1016/j.carbon.2004.07.003.
- [446] Garsany Y, Baturina OA, Swider-Lyons KE, Kocha SS. Experimental Methods for Quantifying the Activity of Platinum Electrocatalysts for the Oxygen Reduction Reaction. *Anal Chem* 2010;82:6321–8. doi:10.1021/ac100306c.
- [447] Moulder JF, Stickle WF, Sobol PE, Bomben KD. Handbook of X Ray Photoelectron Spectroscopy: A Reference Book of Standard Spectra for Identification and Interpretation of Xps Data. Eden Prairie, Minn.: Physical Electronics; 1995.
- [448] Hontoria-Lucas C, López-Peinado AJ, López-González J de D, Rojas-Cervantes ML, Martín-Aranda RM. Study of oxygen-containing groups in a series of graphite oxides: Physical and chemical characterization. *Carbon* 1995;33:1585–92. doi:10.1016/0008-6223(95)00120-3.
- [449] Szabó T, Berkesi O, Forgó P, Josepovits K, Sanakis Y, Petridis D, et al. Evolution of Surface Functional Groups in a Series of Progressively Oxidized Graphite Oxides. *Chem Mater* 2006;18:2740–9. doi:10.1021/cm060258+.
- [450] Jeong H-K, Lee YP, Lahaye RJWE, Park M-H, An KH, Kim IJ, et al. Evidence of Graphitic AB Stacking Order of Graphite Oxides. *J Am Chem Soc* 2008;130:1362–6. doi:10.1021/ja0764730.

- [451] Pei S, Cheng H-M. The reduction of graphene oxide. *Carbon* 2012;50:3210–28. doi:10.1016/j.carbon.2011.11.010.
- [452] Gao W, Alemany LB, Ci L, Ajayan PM. New insights into the structure and reduction of graphite oxide. *Nat Chem* 2009;1:403–8. doi:10.1038/nchem.281.
- [453] Gupta V, Ganegoda H, Engelhard MH, Terry J, Linford MR. Assigning Oxidation States to Organic Compounds via Predictions from X-ray Photoelectron Spectroscopy: A Discussion of Approaches and Recommended Improvements. *J Chem Educ* 2013;91:232–8. doi:10.1021/ed400401c.
- [454] Casa Software Ltd. C. CasaXPS Manual, CasaXPS Processing Software for XPS Spectra (Orange Book). Ed. 2.3.15 rev 1.3. 2009.
- [455] Walton J, Wincott P, Fairley N. Peak Fitting with CasaXPS: A Casa PocketBook. Knutsford: Acolyte Science; 2010.
- [456] Prabhuram J, Zhao TS, Wong CW, Guo JW. Synthesis and physical/electrochemical characterization of Pt/C nanocatalyst for polymer electrolyte fuel cells. *J Power Sources* 2004;134:1–6. doi:10.1016/j.jpowsour.2004.02.021.
- [457] Liu S-H, Lu R-F, Huang S-J, Lo A-Y, Chien S-H, Liu S-B. Controlled synthesis of highly dispersed platinum nanoparticles in ordered mesoporous carbons. *Chem Commun* 2006;3435. doi:10.1039/b607449a.
- [458] Liu S-H, Yu W-Y, Chen C-H, Lo A-Y, Hwang B-J, Chien S-H, et al. Fabrication and Characterization of Well-Dispersed and Highly Stable PtRu Nanoparticles on Carbon Mesoporous Material for Applications in Direct Methanol Fuel Cell. *Chem Mater* 2008;20:1622–8. doi:10.1021/cm702777j.
- [459] Sellin R, Clacens J-M, Coutanceau C. A thermogravimetric analysis/mass spectroscopy study of the thermal and chemical stability of carbon in the Pt/C catalytic system. *Carbon* 2010;48:2244–54. doi:10.1016/j.carbon.2010.02.034.
- [460] Xie L, Brault P, Coutanceau C, Bauchire J-M, Caillard A, Baranton S, et al. Efficient amorphous platinum catalyst cluster growth on porous carbon: A combined molecular dynamics and experimental study. *Appl Catal B Environ* 2015;162:21–6. doi:10.1016/j.apcatb.2014.06.032.
- [461] Prabhuram J, Wang X, Hui CL, Hsing I-M. Synthesis and Characterization of Surfactant-Stabilized Pt/C Nanocatalysts for Fuel Cell Applications. *J Phys Chem B* 2003;107:11057–64. doi:10.1021/jp0357929.
- [462] Kundu P, Nethravathi C, Deshpande PA, Rajamathi M, Madras G, Ravishankar N. Ultrafast Microwave-Assisted Route to Surfactant-Free Ultrafine Pt Nanoparticles on Graphene: Synergistic Co-reduction Mechanism and High Catalytic Activity. *Chem Mater* 2011;23:2772–80. doi:10.1021/cm200329a.
- [463] He D, Cheng K, Li H, Peng T, Xu F, Mu S, et al. Highly Active Platinum Nanoparticles on Graphene Nanosheets with a Significant Improvement in Stability and CO Tolerance. *Langmuir* 2012;28:3979–86. doi:10.1021/la2045493.
- [464] Biegler T, Rand DAJ, Woods R. Limiting oxygen coverage on platinumized platinum; Relevance to determination of real platinum area by hydrogen adsorption. *J Electroanal Chem Interfacial Electrochem* 1971;29:269–77. doi:10.1016/S0022-0728(71)80089-X.
- [465] Mayrhofer KJJ, Strmcnik D, Blizanac BB, Stamenkovic V, Arenz M, Markovic NM. Measurement of oxygen reduction activities via the rotating disc electrode method: From Pt model surfaces to carbon-supported high surface area catalysts. *Electrochimica Acta* 2008;53:3181–8. doi:10.1016/j.electacta.2007.11.057.
- [466] Gasteiger HA, Kocha SS, Sompalli B, Wagner FT. Activity benchmarks and requirements for Pt, Pt-alloy, and non-Pt oxygen reduction catalysts for PEMFCs. *Appl Catal B Environ* 2005;56:9–35. doi:10.1016/j.apcatb.2004.06.021.
- [467] Conway BE. *Electrochemical Supercapacitors*. Boston, MA: Springer US; 1999.
- [468] Simon P, Gogotsi Y. Materials for electrochemical capacitors. *Nat Mater* 2008;7:845–54. doi:10.1038/nmat2297.
- [469] Miller JR, Simon P. Electrochemical capacitors for energy management. *Sci Mag* 2008;321:651–2.
- [470] Frackowiak E, Abbas Q, Béguin F. Carbon/carbon supercapacitors. *J Energy Chem* 2013;22:2226–40. doi:10.1016/S2095-4956(13)60028-5.
- [471] Miller JR. Market and Applications of Electrochemical Capacitors. In: Béguin F, Frackowiak E, editors. *Supercapacitors*, Wiley-VCH Verlag GmbH & Co. KGaA; 2013, p. 509–26.
- [472] Becker HI. Low voltage electrolytic capacitor. US2800616 A, 1957.
- [473] Rightmire RA. Electrical energy storage apparatus. US3288641 A, 1966.
- [474] Boos DL. Electrolytic capacitor having carbon paste electrodes. US3536963 A, 1970.

- [475] Miller JR. A brief history of supercapacitors. *Batter Storage Technol* 2007;61–78.
- [476] Qu D, Shi H. Studies of activated carbons used in double-layer capacitors. *J Power Sources* 1998;74:99–107. doi:10.1016/S0378-7753(98)00038-X.
- [477] Salitra G, Soffer A, Eliad L, Cohen Y, Aurbach D. Carbon Electrodes for Double-Layer Capacitors I. Relations Between Ion and Pore Dimensions. *J Electrochem Soc* 2000;147:2486–93. doi:10.1149/1.1393557.
- [478] Endo M, Maeda T, Takeda T, Kim YJ, Koshiba K, Hara H, et al. Capacitance and Pore-Size Distribution in Aqueous and Nonaqueous Electrolytes Using Various Activated Carbon Electrodes. *J Electrochem Soc* 2001;148:A910–4. doi:10.1149/1.1382589.
- [479] Kierzek K, Frackowiak E, Lota G, Gryglewicz G, Machnikowski J. Electrochemical capacitors based on highly porous carbons prepared by KOH activation. *Electrochimica Acta* 2004;49:515–23. doi:10.1016/j.electacta.2003.08.026.
- [480] Barbieri O, Hahn M, Herzog A, Kötz R. Capacitance limits of high surface area activated carbons for double layer capacitors. *Carbon* 2005;43:1303–10. doi:10.1016/j.carbon.2005.01.001.
- [481] Raymundo-Piñero E, Kierzek K, Machnikowski J, Béguin F. Relationship between the nanoporous texture of activated carbons and their capacitance properties in different electrolytes. *Carbon* 2006;44:2498–507. doi:10.1016/j.carbon.2006.05.022.
- [482] Raymundo-Piñero E, Leroux F, Béguin F. A High-Performance Carbon for Supercapacitors Obtained by Carbonization of a Seaweed Biopolymer. *Adv Mater* 2006;18:1877–82. doi:10.1002/adma.200501905.
- [483] Azaïs P, Duclaux L, Florian P, Massiot D, Lillo-Rodenas M-A, Linares-Solano A, et al. Causes of supercapacitors ageing in organic electrolyte. *J Power Sources* 2007;171:1046–53. doi:10.1016/j.jpowsour.2007.07.001.
- [484] Largeot C, Portet C, Chmiola J, Taberna P-L, Gogotsi Y, Simon P. Relation between the Ion Size and Pore Size for an Electric Double-Layer Capacitor. *J Am Chem Soc* 2008;130:2730–1. doi:10.1021/ja7106178.
- [485] Pandolfo AG, Hollenkamp AF. Carbon properties and their role in supercapacitors. *J Power Sources* 2006;157:11–27. doi:10.1016/j.jpowsour.2006.02.065.
- [486] Seredych M, Hulicova-Jurcakova D, Lu GQ, Bandosz TJ. Surface functional groups of carbons and the effects of their chemical character, density and accessibility to ions on electrochemical performance. *Carbon* 2008;46:1475–88. doi:10.1016/j.carbon.2008.06.027.
- [487] Shashurin A, Keidar M. Factors affecting the size and deposition rate of the cathode deposit in an anodic arc used to produce carbon nanotubes. *Carbon* 2008;46:1826–8. doi:10.1016/j.carbon.2008.08.002.
- [488] Pan H, Li J, Feng YP. Carbon Nanotubes for Supercapacitor. *Nanoscale Res Lett* 2010;5:654–68. doi:10.1007/s11671-009-9508-2.
- [489] Lu W, Dai L. Carbon Nanotube Supercapacitors. In: Mauricio J, editor. *Carbon Nanotub., InTech*; 2010.
- [490] Obreja VVN. On the performance of supercapacitors with electrodes based on carbon nanotubes and carbon activated material—A review. *Phys E Low-Dimens Syst Nanostructures* 2008;40:2596–605. doi:10.1016/j.physe.2007.09.044.
- [491] Futaba DN, Hata K, Yamada T, Hiraoka T, Hayamizu Y, Kakudate Y, et al. Shape-engineerable and highly densely packed single-walled carbon nanotubes and their application as super-capacitor electrodes. *Nat Mater* 2006;5:987–94. doi:10.1038/nmat1782.
- [492] Frackowiak E, Jurewicz K, Delpeux S, Béguin F. Nanotubular materials for supercapacitors. *J Power Sources* 2001;97-98:822–5. doi:10.1016/S0378-7753(01)00736-4.
- [493] Niu C, Sichel EK, Hoch R, Moy D, Tennent H. High power electrochemical capacitors based on carbon nanotube electrodes. *Appl Phys Lett* 1997;70:1480–2. doi:10.1063/1.118568.
- [494] Zhang H, Cao G, Yang Y, Gu Z. Comparison Between Electrochemical Properties of Aligned Carbon Nanotube Array and Entangled Carbon Nanotube Electrodes. *J Electrochem Soc* 2008;155:K19–22. doi:10.1149/1.2811864.
- [495] Bordjiba T, Mohamedi M, Dao LH. New Class of Carbon-Nanotube Aerogel Electrodes for Electrochemical Power Sources. *Adv Mater* 2008;20:815–9. doi:10.1002/adma.200701498.
- [496] Zhi M, Xiang C, Li J, Li M, Wu N. Nanostructured carbon-metal oxide composite electrodes for supercapacitors: a review. *Nanoscale* 2013;5:72. doi:10.1039/c2nr32040a.
- [497] Zhang LL, Zhou R, Zhao XS. Graphene-based materials as supercapacitor electrodes. *J Mater Chem* 2010;20:5983. doi:10.1039/c000417k.

- [498] Ruoff R. Graphene: Calling all chemists. *Nat Nanotechnol* 2008;3:10–1. doi:10.1038/nnano.2007.432.
- [499] Vivekchand SRC, Rout CS, Subrahmanyam KS, Govindaraj A, Rao CNR. Graphene-based electrochemical supercapacitors. *J Chem Sci* 2008;120:9–13. doi:10.1007/s12039-008-0002-7.
- [500] Stoller MD, Park S, Zhu Y, An J, Ruoff RS. Graphene-Based Ultracapacitors. *Nano Lett* 2008;8:3498–502. doi:10.1021/nl802558y.
- [501] Rao CNR, Sood AK, Subrahmanyam KS, Govindaraj A. Graphene: The New Two-Dimensional Nanomaterial. *Angew Chem Int Ed* 2009;48:7752–77. doi:10.1002/anie.200901678.
- [502] Zhao X, Tian H, Zhu M, Tian K, Wang JJ, Kang F, et al. Carbon nanosheets as the electrode material in supercapacitors. *J Power Sources* 2009;194:1208–12. doi:10.1016/j.jpowsour.2009.06.004.
- [503] Xia J, Chen F, Li J, Tao N. Measurement of the quantum capacitance of graphene. *Nat Nanotechnol* 2009;4:505–9. doi:10.1038/nnano.2009.177.
- [504] Stankovich S, Dikin DA, Dommett GHB, Kohlhaas KM, Zimney EJ, Stach EA, et al. Graphene-based composite materials. *Nature* 2006;442:282–6. doi:10.1038/nature04969.
- [505] Wang D-W, Li F, Zhao J, Ren W, Chen Z-G, Tan J, et al. Fabrication of Graphene/Polyaniline Composite Paper via In Situ Anodic Electropolymerization for High-Performance Flexible Electrode. *ACS Nano* 2009;3:1745–52. doi:10.1021/nn900297m.
- [506] Murugan AV, Muraliganth T, Manthiram A. Rapid, Facile Microwave-Solvothermal Synthesis of Graphene Nanosheets and Their Polyaniline Nanocomposites for Energy Storage. *Chem Mater* 2009;21:5004–6. doi:10.1021/cm902413c.
- [507] Yan J, Wei T, Shao B, Fan Z, Qian W, Zhang M, et al. Preparation of a graphene nanosheet/polyaniline composite with high specific capacitance. *Carbon* 2010;48:487–93. doi:10.1016/j.carbon.2009.09.066.
- [508] Zhang K, Zhang LL, Zhao XS, Wu J. Graphene/Polyaniline Nanofiber Composites as Supercapacitor Electrodes. *Chem Mater* 2010;22:1392–401. doi:10.1021/cm902876u.
- [509] Huang Y, Liang J, Chen Y. An Overview of the Applications of Graphene-Based Materials in Supercapacitors. *Small* 2012;8:1805–34. doi:10.1002/smll.201102635.
- [510] Zhao XS, Su F, Yan Q, Guo W, Bao XY, Lv L, et al. Templating methods for preparation of porous structures. *J Mater Chem* 2006;16:637–48. doi:10.1039/B513060C.
- [511] Ania CO, Khomenko V, Raymundo-Piñero E, Parra JB, Béguin F. The Large Electrochemical Capacitance of Microporous Doped Carbon Obtained by Using a Zeolite Template. *Adv Funct Mater* 2007;17:1828–36. doi:10.1002/adfm.200600961.
- [512] Li W, Chen D, Li Z, Shi Y, Wan Y, Wang G, et al. Nitrogen-containing carbon spheres with very large uniform mesopores: The superior electrode materials for EDLC in organic electrolyte. *Carbon* 2007;45:1757–63. doi:10.1016/j.carbon.2007.05.004.
- [513] Wang D-W, Li F, Liu M, Lu GQ, Cheng H-M. 3D Aperiodic Hierarchical Porous Graphitic Carbon Material for High-Rate Electrochemical Capacitive Energy Storage. *Angew Chem Int Ed* 2008;47:373–6. doi:10.1002/anie.200702721.
- [514] Liu H-J, Wang X-M, Cui W-J, Dou Y-Q, Zhao D-Y, Xia Y-Y. Highly ordered mesoporous carbon nanofiber arrays from a crab shell biological template and its application in supercapacitors and fuel cells. *J Mater Chem* 2010;20:4223–30. doi:10.1039/B925776D.
- [515] Zhao HJ, Zhao DL, Zhang JM, Zhang DD. Ordered Mesoporous Carbon Nano Spheres as Electrode Material for Supercapacitors. *Appl Mech Mater* 2013;320:661–4. doi:10.4028/www.scientific.net/AMM.320.661.
- [516] Li N, Xu J, Chen H, Wang X. Supercapacitors based on ordered mesoporous carbon derived from furfuryl alcohol: effect of the carbonized temperature. *J Nanosci Nanotechnol* 2014;14:5157–65. doi:10.1002/jnnm.201402233.
- [517] Frackowiak E. Carbon materials for supercapacitor application. *Phys Chem Chem Phys* 2007;9:1774–85. doi:10.1039/B618139M.
- [518] Huang J, Sumpter BG, Meunier V. A Universal Model for Nanoporous Carbon Supercapacitors Applicable to Diverse Pore Regimes, Carbon Materials, and Electrolytes. *Chem – Eur J* 2008;14:6614–26. doi:10.1002/chem.200800639.
- [519] Yamada H, Nakamura H, Nakahara F, Moriguchi I, Kudo T. Electrochemical Study of High Electrochemical Double Layer Capacitance of Ordered Porous Carbons with Both Meso/Macropores and Micropores. *J Phys Chem C* 2007;111:227–33. doi:10.1021/jp063902g.
- [520] Xu B, Wu F, Chen R, Cao G, Chen S, Zhou Z, et al. Highly mesoporous and high surface area carbon: A high capacitance electrode material for EDLCs with various electrolytes. *Electrochem Commun* 2008;10:795–7. doi:10.1016/j.elecom.2008.02.033.

- [521] Fang B, Binder L. A modified activated carbon aerogel for high-energy storage in electric double layer capacitors. *J Power Sources* 2006;163:616–22. doi:10.1016/j.jpowsour.2006.09.014.
- [522] Brodie BC. On the Atomic Weight of Graphite. *Philos Trans R Soc Lond* 1859;149:249–59.
- [523] Staudenmaier L. Preparation of Graphitic Acid. *J Chem Soc Abstr* 1898;74:B472–8. doi:10.1039/CA8987405472.
- [524] Hummers WS, Offeman RE. Preparation of Graphitic Oxide. *J Am Chem Soc* 1958;80:1339–1339. doi:10.1021/ja01539a017.
- [525] Marcano DC, Kosynkin DV, Berlin JM, Sinitskii A, Sun Z, Slesarev A, et al. Improved Synthesis of Graphene Oxide. *ACS Nano* 2010;4:4806–14. doi:10.1021/nn1006368.
- [526] Celzard A, Maréché JF, Payot F, Furdin G. Electrical conductivity of carbonaceous powders. *Carbon* 2002;40:2801–15. doi:10.1016/S0008-6223(02)00196-3.
- [527] Marinho B, Ghislandi M, Tkalya E, Koning CE, de With G. Electrical conductivity of compacts of graphene, multi-wall carbon nanotubes, carbon black, and graphite powder. *Powder Technol* 2012;221:351–8. doi:10.1016/j.powtec.2012.01.024.
- [528] Magistris A, Mustarelli P, Parazzoli F, Quartarone E, Piaggio P, Bottino A. Structure, porosity and conductivity of PVdF films for polymer electrolytes. *J Power Sources* 2001;97–98:657–60. doi:10.1016/S0378-7753(01)00644-9.
- [529] Bhatt AS, Bhat DK, Santosh MS. Crystallinity, conductivity, and magnetic properties of PVDF-Fe<sub>3</sub>O<sub>4</sub> composite films. *J Appl Polym Sci* 2011;119:968–72. doi:10.1002/app.32796.
- [530] Tripathi SK, Gupta A, Kumari M. Studies on electrical conductivity and dielectric behaviour of PVdF–HFP–PMMA–NaI polymer blend electrolyte. *Bull Mater Sci* 2012;35:969–75. doi:10.1007/s12034-012-0387-2.
- [531] Bonnefoi L, Simon P, Fauvarque JF, Sarrazin C, Sarrau JF, Dugast A. Electrode compositions for carbon power supercapacitors. *J Power Sources* 1999;80:149–55. doi:10.1016/S0378-7753(99)00069-5.
- [532] Gamby J, Taberna PL, Simon P, Fauvarque JF, Chesneau M. Studies and characterisations of various activated carbons used for carbon/carbon supercapacitors. *J Power Sources* 2001;101:109–16. doi:10.1016/S0378-7753(01)00707-8.
- [533] Frackowiak E, Béguin F. Carbon materials for the electrochemical storage of energy in capacitors. *Carbon* 2001;39:937–50. doi:10.1016/S0008-6223(00)00183-4.
- [534] Portet C, Taberna PL, Simon P, Flahaut E. Influence of carbon nanotubes addition on carbon–carbon supercapacitor performances in organic electrolyte. *J Power Sources* 2005;139:371–8. doi:10.1016/j.jpowsour.2004.07.015.
- [535] Pumera M. Electrochemistry of graphene: new horizons for sensing and energy storage. *Chem Rec* 2009;9:211–23. doi:10.1002/tcr.200900008.
- [536] Chu A, Braatz P. Comparison of commercial supercapacitors and high-power lithium-ion batteries for power-assist applications in hybrid electric vehicles: I. Initial characterization. *J Power Sources* 2002;112:236–46. doi:10.1016/S0378-7753(02)00364-6.
- [537] Zhang H, Cao G, Wang Z, Yang Y, Shi Z, Gu Z. Growth of Manganese Oxide Nanoflowers on Vertically-Aligned Carbon Nanotube Arrays for High-Rate Electrochemical Capacitive Energy Storage. *Nano Lett* 2008;8:2664–8. doi:10.1021/nl800925j.
- [538] Bi R-R, Wu X-L, Cao F-F, Jiang L-Y, Guo Y-G, Wan L-J. Highly Dispersed RuO<sub>2</sub> Nanoparticles on Carbon Nanotubes: Facile Synthesis and Enhanced Supercapacitance Performance. *J Phys Chem C* 2010;114:2448–51. doi:10.1021/jp9116563.
- [539] Lee SW, Kim J, Chen S, Hammond PT, Shao-Horn Y. Carbon Nanotube/Manganese Oxide Ultrathin Film Electrodes for Electrochemical Capacitors. *ACS Nano* 2010;4:3889–96. doi:10.1021/nn100681d.
- [540] Chen Z, Augustyn V, Wen J, Zhang Y, Shen M, Dunn B, et al. High-Performance Supercapacitors Based on Intertwined CNT/V<sub>2</sub>O<sub>5</sub> Nanowire Nanocomposites. *Adv Mater* 2011;23:791–5. doi:10.1002/adma.201003658.
- [541] Lang J, Yan X, Xue Q. Facile preparation and electrochemical characterization of cobalt oxide/multi-walled carbon nanotube composites for supercapacitors. *J Power Sources* 2011;196:7841–6. doi:10.1016/j.jpowsour.2011.04.010.
- [542] Lee G-J, Pyun S-I. Synthesis and Characterization of Nanoporous Carbon and its Electrochemical Application to Electrode Material for Supercapacitors. In: Vayenas C, White RE, Gamboa-Aldeco ME, editors. *Mod. Asp. Electrochem.*, Springer New York; 2007, p. 139–95.

- [543] Taberna PL, Portet C, Simon P. Electrode surface treatment and electrochemical impedance spectroscopy study on carbon/carbon supercapacitors. *Appl Phys A* 2005;82:639–46. doi:10.1007/s00339-005-3404-0.
- [544] Du C, Pan N. Supercapacitors using carbon nanotubes films by electrophoretic deposition. *J Power Sources* 2006;160:1487–94. doi:10.1016/j.jpowsour.2006.02.092.
- [545] Basiricò L, Lanzara G. Moving towards high-power, high-frequency and low-resistance CNT supercapacitors by tuning the CNT length, axial deformation and contact resistance. *Nanotechnology* 2012;23:305401. doi:10.1088/0957-4484/23/30/305401.
- [546] Zhao F. Synthesis of nanostructured carbon materials for electrochemical energy storage. PhD Dissertation. Politecnico di Milano, 2014.
- [547] Thompson SP. *Dynamo-Electricity Machinery: A Manual for Students of Electrotechnics*. 1 edition. Cambridge: Cambridge University Press; 2011.
- [548] Gualous H, Gallay R. Supercapacitor Module Sizing and Heat Management under Electric, Thermal, and Aging Constraints. In: Béguin F, Frackowiak E, editors. *Supercapacitors*, Wiley-VCH Verlag GmbH & Co. KGaA; 2013, p. 373–436.

# Appendix A

## Catalyst amount calculation and ink composition

### Vulcan 30wt% Pt

This sample was synthesized based on 30wt%Pt target (reported Pt ratio for this commercial sample) and a  $17.5 \mu\text{g}_{\text{Pt}} \text{cm}^{-2}$  loading decision.

#### Calculations based on which the primary experiments were performed:

Generally, the Pt loading on the glassy carbon should be 7-30  $\mu\text{g}_{\text{Pt}} \text{cm}^{-2}$  for catalysts having concentrations of 10-50 wt% Pt on carbon.

In our case, Pt/C weight percent is 30 (in the range mentioned above). If we decide to have a  $17.5 \mu\text{g}_{\text{Pt}} \text{cm}^{-2}$  loading, considering the area of glassy carbon electrode ( $(0.5 \times 0.5 \times \pi) / 4 = 0.196 \text{cm}^2$ ), we will need ( $0.196 \times 17.5 = 3.43 \mu\text{g}_{\text{Pt}}$ ) Pt.

$$\text{Weight percent}=30 \Rightarrow \frac{\text{Pt}}{\text{Pt}+\text{Carbon Support}} = \frac{30}{100} = 0.3$$

$$\Rightarrow 3.43 \mu\text{g}_{\text{Pt}} \text{ is found in } \frac{3.43}{0.3} = 11.43 \mu\text{g} \text{ of "catalyst+support mixture"}.$$

\*\*\*\*\*

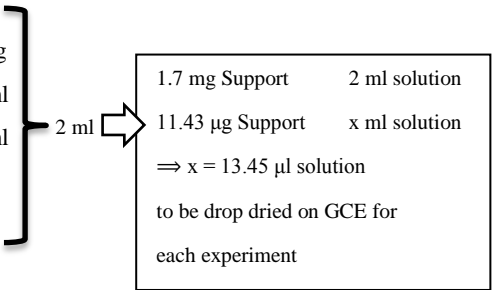
Ink composition:

Support (Carbon+Pt): 1.7 mg

IPA: 0.494 ml

H<sub>2</sub>O: 1.496 ml

Nafion: 0.01 ml



### CNT-Pt

This sample was synthesized based on 30wt%Pt target and a  $17.5 \mu\text{g}_{\text{Pt}} \text{cm}^{-2}$  loading decision.

#### Calculations based on which the primary experiments were performed:

Based on a 30wt% Pt concentration, if we decide to have a  $17.5 \mu\text{g}_{\text{Pt}} \text{cm}^{-2}$  loading, considering the area of glassy carbon electrode ( $(0.5 \times 0.5 \times \pi) / 4 = 0.196 \text{ cm}^2$ ), we will need ( $0.196 \times 17.5 = 3.43 \mu\text{g}_{\text{Pt}}$ ) Pt.

$$\text{Weight percent}=30 \Rightarrow \frac{\text{Pt}}{\text{Pt}+\text{Carbon Support}} = \frac{30}{100} = 0.3$$

$$\Rightarrow 3.43 \mu\text{g}_{\text{Pt}} \text{ is found in } \frac{3.43}{0.3} = 11.43 \mu\text{g} \text{ of "catalyst+support mixture"}.$$

\*\*\*\*\*

Ink composition:

Support (Carbon+Pt): 1.7 mg

IPA: 0.247 ml

H<sub>2</sub>O: 0.748 ml

Ethanol: 1 ml

Nafion: 0.01 ml

2 ml →

1.7 mg Support      2 ml solution

11.43 μg Support      x ml solution

⇒ x = 13.45 μl solution

to be drop dried on GCE for  
each experiment

\*\*\*\*\*

However, after the TGA test it was found that there is a 28.388wt% residue, from which, 5wt% is attributed to the residues not removed after CNT purification. Therefore, there is a residue of 23.388wt% related to Pt, that as can be seen in the following, would result in a  $13.64 \mu\text{g}_{\text{Pt}} \text{cm}^{-2}$  Pt loading on GCE.

$$\text{Weight percent}=23.38 \Rightarrow \frac{\text{Pt}}{\text{Pt}+\text{Carbon Support}} = \frac{23.388}{100} = 0.2339$$

11.43 μg Support used, so  $11.43 \mu\text{g} \times 23.38\% = 2.67 \mu\text{g}$  Pt is used to cover  $0.196 \text{ cm}^2$  GCE. So,

$$\begin{array}{l} 2.67 \qquad \qquad 0.196 \text{ cm}^2 \\ \times \qquad \qquad \qquad 1 \text{ cm}^2 \qquad \qquad \Rightarrow \end{array}$$

$$x = 13.64 \mu\text{g} = \text{the real loading used}$$

**RGO-Pt**

This sample was synthesized based on 30wt%Pt target and a 17.5  $\mu\text{g}_{\text{Pt}} \text{cm}^{-2}$  loading decision.

**Calculations based on which the primary experiments were performed:**

Based on a 30wt% Pt concentration, if we decide to have a 17.5  $\mu\text{g}_{\text{Pt}} \text{cm}^{-2}$  loading, considering the area of glassy carbon electrode  $((0.5 \times 0.5 \times \pi) / 4 = 0.196 \text{ cm}^{-2})$ , we will need  $(0.196 \times 17.5 = 3.43 \mu\text{g}_{\text{Pt}})$  Pt.

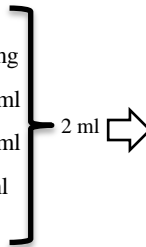
$$\text{Weight percent} = 30 \Rightarrow \frac{\text{Pt}}{\text{Pt} + \text{Carbon Support}} = \frac{30}{100} = 0.3$$

$$\Rightarrow 3.43 \mu\text{g}_{\text{Pt}} \text{ is found in } \frac{3.43}{0.3} = 11.43 \mu\text{g} \text{ of "catalyst+support mixture"}.$$

\*\*\*\*\*

Ink composition:

- Support (Carbon+Pt): 1.7 mg
- IPA: 0.494 ml
- H<sub>2</sub>O: 1.496 ml
- Nafion: 0.01 ml



1.7 mg Support      2 ml solution

11.43  $\mu\text{g}$  Support      x ml solution

$\Rightarrow x = 13.45 \mu\text{l}$  solution

to be drop dried on GCE for each experiment

\*\*\*\*\*

However, after the TGA test it was found that there is a 46.799wt% residue. Therefore, there is a residue of 46.799wt% related to Pt, that as can be seen in the following, would result in a 27.3  $\mu\text{g}_{\text{Pt}} \text{cm}^{-2}$  Pt loading on GCE.

$$\text{Weight percent} = 46.799 \Rightarrow \frac{\text{Pt}}{\text{Pt} + \text{Carbon Support}} = \frac{46.799}{100} = 0.46799$$

11.43  $\mu\text{g}$  Support used, so  $11.43 \mu\text{g} \times 46.799\% = 5.35 \mu\text{g}$  Pt is used to cover  $0.196 \text{ cm}^{-2}$  GCE. So,

$$\begin{array}{lcl} 5.35 & 0.196 \text{ cm}^{-2} & \\ x & 1 \text{ cm}^{-2} & \Rightarrow \\ & & x = 27.30 \mu\text{g} = \text{the real loading used} \end{array}$$

## CNT-RGO-Pt

This sample was synthesized based on 30wt%Pt target and a  $17.5 \mu\text{g}_{\text{Pt}} \text{cm}^{-2}$  loading decision.

### Calculations based on which the primary experiments were performed:

Based on a 30wt% Pt concentration, if we decide to have a  $17.5 \mu\text{g}_{\text{Pt}} \text{cm}^{-2}$  loading, considering the area of glassy carbon electrode ( $(0.5 \times 0.5 \times \pi) / 4 = 0.196 \text{ cm}^2$ ), we will need ( $0.196 \times 17.5 = 3.43 \mu\text{g}_{\text{Pt}}$ ) Pt.

$$\text{Weight percent}=30 \Rightarrow \frac{\text{Pt}}{\text{Pt}+\text{Carbon Support}} = \frac{30}{100} = 0.3$$

$$\Rightarrow 3.43 \mu\text{g}_{\text{Pt}} \text{ is found in } \frac{3.43}{0.3} = 11.43 \mu\text{g} \text{ of "catalyst+support mixture".}$$

\*\*\*\*\*

Ink composition:

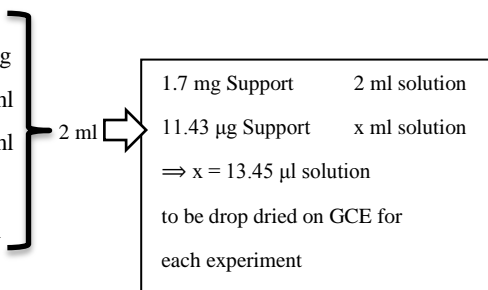
Support (Carbon+Pt): 1.7 mg

IPA: 0.247 ml

H<sub>2</sub>O: 0.748 ml

Ethanol: 1 ml

Nafion: 0.01 ml



\*\*\*\*\*

However, after the TGA test it was found that there is a 33.12wt% residue, from which, approximately 3% is attributed to the residues not removed after CNT purification. Therefore, there is a residue of almost 30wt% related to Pt, that as can be seen in the following, would result in a  $17.5 \mu\text{g}_{\text{Pt}} \text{cm}^{-2}$  Pt loading on GCE, exactly as was intended at the beginning.

$$\text{Weight percent}=30 \Rightarrow \frac{\text{Pt}}{\text{Pt}+\text{Carbon Support}} = \frac{30}{100} = 0.3$$

11.43 μg Support used, so  $11.43 \mu\text{g} \times 30\% = 3.43 \mu\text{g}$  Pt is used to cover  $0.196 \text{ cm}^2$  GCE. So,

$$3.43 \quad 0.196 \text{ cm}^2$$

$$x \quad 1 \text{ cm}^2 \quad \Rightarrow$$

$$x = 17.5 \mu\text{g} = \text{the real loading used}$$

